STATE OF THE CLIMATE IN 2007

D. H. Levinson and J. H. Lawrimore, Eds.
Associate Eds.: A. Arguez, H. J. Diamond, F. Fetterer, A. Horvitz, J. M. Levy

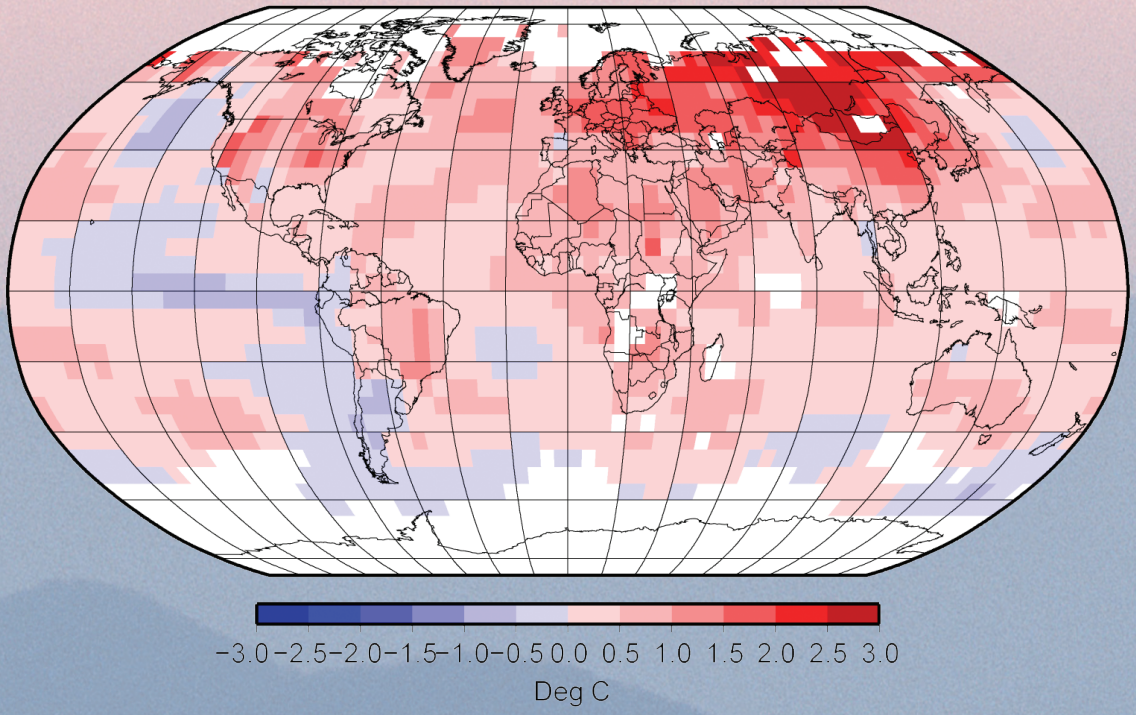

Geographic distribution of global surface temperature anomalies in 2007, relative to the 1961 to 1990 average.

Special Supplement to the *Bulletin of the American Meteorological Society*
Vol. 89, No. 7, July 2008

On the front cover: Geographic distribution of temperature anomalies in 2007. Departure from the 1961 to 1990 average. (Source: NOAA/NCDC.) More information on global surface temperatures can be found in section 2b of the report.

On the back cover: The annual mean latent plus sensible heat fluxes in 2007 (in W m^{-2}). (Source: Woods Hole Oceanographic Institution.) More information on global ocean heat fluxes can be found in section 3b of the report.

STATE OF THE CLIMATE IN 2007

AFFILIATIONS (ALPHABETICAL BY AUTHOR)

1. Aceituno, Patricio, Universidad de Chile, Santiago, Chile
2. Achberger, Christine, Earth Sciences Centre, University of Gothenburg, Gothenburg, Sweden
3. Arguez, Anthony, NOAA/NESDIS National Climatic Data Center, Asheville, North Carolina
4. Armstrong, R., CIRES/NSIDC, University of Colorado, Boulder, Colorado
5. Ashik, I., Arctic and Antarctic Research Institute, St. Petersburg, Russia
6. Attaher, Samar M., Ministry of Agriculture and Land Reclamation, Cairo, Egypt
7. Bader, Stephan, MeteoSwiss, Zurich, Switzerland
8. Báez, Julián, Dirección Nacional de Aeronáutica Civil, Asunción, Paraguay
9. Bai, L.-S., Byrd Polar Research Center, The Ohio State University, Columbus, Ohio
10. Baringer, Molly O., NOAA/OAR Atlantic Oceanographic and Meteorological Laboratory, Physical Oceanography Division, Miami, Florida
11. Barreira, S., Argentine Navy Meteorological Service, Argentine Hydrographic Service, Buenos Aires, Argentina
12. Baum, Bryan, Space Science and Engineering Center, University of Wisconsin—Madison, Madison, Wisconsin
13. Behrenfeld, Michael J., Oregon State University, Corvallis, Oregon
14. Bell, Gerald D., NOAA/NWS/NCEP Climate Prediction Center, Camp Springs, Maryland
15. Beswick, Mark, Met Office, Exeter, United Kingdom
16. Bidegain, Mario, Universidad de la República, Montevideo, Uruguay
17. Bissolli, Peter, German Meteorological Service, Offenbach, Germany
18. Blake, Eric, NOAA/NWS/NCEP National Hurricane Center, Miami, Florida
19. Boudet-Roco, Dagne, Instituto de Meteorología, La Habana, Cuba
20. Bourassa, Mark, Center for Ocean–Atmosphere Prediction Studies, The Florida State University, Tallahassee, Florida
21. Box, J., Byrd Polar Research Center, The Ohio State University, Columbus, Ohio
22. Bromwich, D., Byrd Polar Research Center, The Ohio State University, Columbus, Ohio
23. Buchel, Denise, Meteorological Service of Luxembourg, Luxembourg, Luxembourg
24. Bulygina, Olga N., All-Russian Research Institute of Hydrometeorological Information, Obninsk, Russia
25. Burgess, Stuart M., National Institute of Water and Atmospheric Research, Ltd., Wellington, New Zealand
26. Busuioc, Aristata, National Meteorological Administraion, Bucharest, Romania
27. Camargo, Suzana J., Lamont-Doherty Earth Observatory, The Earth Institute at Columbia University, Palisades, New York
28. Cappelen, John, Danish Meteorological Institute, Copenhagen, Denmark
29. Carmack, E., Arctic and Antarctic Research Institute, St. Petersburg, Russia
30. Carrión Romero, Ana M., Instituto de Meteorología, La Habana, Cuba
31. Cegnar, Tanja, Environmental Agency of the Republic of Slovenia, Ljubljana, Slovenia
32. Chen, Deliang, Earth Sciences Centre, University of Gothenburg, Gothenburg, Sweden
33. Chen, Yu, National Climate Center, China Meteorological Administration, Beijing, China
34. Christy, John R., University of Alabama in Huntsville, Huntsville, Alabama
35. Coelho, Caio A. S., CPTEC/INPE, Center for Weather Forecasts and Climate Studies, Cachoeira Paulista, Brazil
36. Colombo, Tiziano, CNMCA, Pomezia/Rome, Italy
37. Colwell, S., British Antarctic Survey, Cambridge, England, United Kingdom
38. Comiso, J., NASA Goddard Space Flight Center, Greenbelt, Maryland
39. Croci-Maspoli, Mischa, Zurich, Switzerland
40. Cupo, Jeffrey P., NOAA/NWS, San Juan, Puerto Rico
41. Cutié Cansino, Virgen, Instituto de Meteorología, La Habana, Cuba
42. Davydova-Belitskaya, Valentina, National Meteorological Service (SMN/CONAGUA), Mexico City, Mexico
43. Demircan, Mesut, Turkish State Meteorological Service, Kalaba/Ankara, Turkey
44. Derka, Helmut, ZAMG, Vienna, Austria
45. Diamond, Howard J., NOAA/NESDIS National Climatic Data Center, Silver Spring, Maryland
46. Djordjevic, Smilija, Republic Hydrometeorological Service of Serbia, Belgrade, Serbia
47. Dlugokencky, Edward, NOAA/OAR Earth Systems Research Laboratory, Boulder, Colorado
48. Dutton, Geoff S., NOAA/OAR Earth Systems Research Laboratory, Boulder, Colorado
49. Elkins, James W., NOAA/OAR Earth Systems Research Laboratory, Boulder, Colorado
50. Evan, Amato T., Cooperative Institute for Meteorological Satellite Studies, University of Wisconsin—Madison, Madison, Wisconsin
51. Feely, Richard A., NOAA/OAR Pacific Marine Environmental Laboratory, Seattle, Washington
52. Fetterer, F., CIRES National Snow and Ice Data Center, University of Colorado, Boulder, Colorado
53. Fogt, R. L., NOAA/Earth Systems Research Laboratory, Boulder, Colorado
54. Fonseca Rivera, Cecilia, Instituto de Meteorología, La Habana, Cuba
55. Free, Melissa P., NOAA/OAR/Air Resources Laboratory, Silver Spring, Maryland
56. Fritsch, Rick, NOAA/NWS, Anchorage, Alaska
57. Frolov, I., Arctic and Antarctic Research Institute, St. Petersburg, Russia
58. Frutos, Ramon, National Meteorological/Hydrological Service, Belize City, Belize

59. García-Herrera, Ricardo, Universidad Complutense, Madrid, Spain
60. Gascard, J. C., Université Pierre et Marie Curie, Paris, France
61. Gill, Stephen, NOAA/NOS Center for Operational Oceanographic Products and Services, Silver Spring, Maryland
62. Gleason, Karin L., NOAA/NESDIS National Climatic Data Center, Asheville, North Carolina
63. Goldenberg, Stanley B., NOAA/OAR Atlantic Oceanographic and Meteorological Laboratory, Miami, Florida
64. Gomboluudev, Purevjav, Institute of Meteorology and Hydrology, Ulaanbaatar, Mongolia
65. Goni, Gustavo Jorge, NOAA/OAR Atlantic Oceanographic and Meteorological Laboratory, Physical Oceanography Division, Miami, Florida
66. Gordon, Ann, National Meteorological/Hydrological Service, Belize City, Belize
67. Gottschalck, Jonathan C., NOAA/NWS/NCEP Climate Prediction Center, Camp Springs, Maryland
68. Gouveia, Célia C., Instituto Politécnico de Setúbal and Universidade de Lisboa, Lisbon, Portugal
69. Grooters, Frank, KNMI, De Bilt, Netherlands
70. Guard, Charles, NOAA National Weather Service, Barrigada, Guam
71. Guo, Yanjun, National Climate Center, Beijing, China
72. Haimberger, Leopold, University of Vienna, Vienna, Austria
73. Halpert, Michael S., NOAA/NWS/NCEP Climate Prediction Center, Camp Springs, Maryland
74. Hardwick, Jen, Met Office, Exeter, United Kingdom
75. Hechler, Peer, German Meteorological Service, Offenbach, Germany
76. Heidinger, Andrew K., NOAA/NESDIS Center for Satellite Applications and Research, Cooperative Research Program, University of Wisconsin—Madison, Madison, Wisconsin
77. Heim, Richard R., Jr., NOAA/NESDIS National Climatic Data Center, Asheville, North Carolina
78. Hellström, Sverker, Swedish Meteorological and Hydrological Institute, Norrköping, Sweden
79. Hoerling, M. P., NOAA/CIRES Climate Diagnostics Center, Boulder, Colorado
80. Horvitz, Andy, NOAA/NWS/Office of Climate Water and Weather Services, Silver Spring, Maryland
81. Hotanova, Eva, Czech Hydrometeorological Institute, Prague, Czech Republic
82. Hovsepyan, Anahit, Armstatehydromet, Yerevan, Armenia
83. Hughes, Paul J., Center for Ocean-Atmospheric Prediction Studies, Florida State University, Tallahassee, Florida
84. Hurtado, Gonzalo, Instituto de Hidrología, Meteorología y Estudios Ambientales de Colombia, Bogotá, Colombia
85. Iden, Knut A., Norwegian Meteorological Office, Oslo, Norway
86. Itoh, M., Institute of Observational Research for Global Change, Japan Agency for Marine-Earth Science and Technology, Yokosuka, Japan
87. Jaimes Espinoza, Ena M., Servicio Nacional de Meteorología e Hidrología (SENAMHI), Lima, Perú
88. Janowiak, John E., NOAA/NWS/NCEP Climate Prediction Center, Camp Springs, Maryland
89. Jezek, Ken, Byrd Polar Research Center, The Ohio State University, Columbus, Ohio
90. Jia, G., RCE/TEA, Chinese Academy of Science, Beijing, China
91. Johnson, Gregory C., NOAA/OAR Pacific Marine Environmental Laboratory, Seattle, Washington
92. Jonsson, Magnus, The Icelandic Meteorological Office, Reykjavik, Iceland
93. Kabidi, Khadija, Direction de la Météorologie Nationale, Rabat, Morocco
94. Kadi, Mohamed, African Centre of Meteorological Applications for Development, Niamey, Niger
95. Karkozas, Juozas, Lithuanian Hydrometeorological Service, Vilnius, Lithuania
96. Katusin, Zvonimir, Meteorological and Hydrological Service, Zagreb, Croatia
97. Kennedy, John J., Hadley Centre for Climate Change, Met Office, Exeter, United Kingdom
98. Khoshkam, Mahbobeh, Islamic Republic of Iran Meteorological Organization, Tehran, Iran
99. Kimberlain, Todd, NOAA/NWS/NCEP National Hurricane Center, Miami, Florida
100. Korshunova, Natalia N., All-Russian Research Institute of Hydrometeorological Information, Obninsk, Russia
101. Krishfield, R., Woods Hole Oceanographic Institution, Woods Hole, Massachusetts
102. Kruger, Andries C., South African Weather Service, Pretoria, South Africa
103. Kruk, Michael C., NOAA/NESDIS/NCDC, Asheville, North Carolina
104. Kulbida, Mykola, Ukrainian Hydrometeorological Center, Kiev, Ukraine
105. L'Heureux, Michelle L., NOAA/NWS/NCEP Climate Prediction Center, Camp Springs, Maryland
106. Lander, Mark A., Water and Environmental Research Institute, University of Guam, Mangilao, Guam
107. Landsea, Chris W., NOAA/NWS/NCEP National Hurricane Center, Miami, Florida
108. Lapinel Pedroso, Braulio, Instituto de Meteorología, La Habana, Cuba
109. Lawrimore, Jay H., NOAA/NESDIS National Climatic Data Center, Asheville, North Carolina
110. Lennon, Peter, Met Éireann, Dublin, Ireland
111. Levinson, David H., NOAA/NESDIS National Climatic Data Center, Asheville, North Carolina
112. Levy, Joel M., NOAA/OAR Climate Program Office, Silver Spring, Maryland
113. Liang, Xiaoyun, China Meteorological Administration, Beijing China
114. Lindsey, Scott, NOAA/NWS, Anchorage, Alaska
115. Liu, H., Department of Geography, Texas A&M University, College Station, Texas

116. Liu, Y., Cooperative Institute of Meteorological Satellite Studies, University of Wisconson—Madison, Madison, Wisconsin
117. López Carmona, Patricio, Centro Internacional para la Investigación del Fenómeno de El Niño (CIIFEN), Guayaquil, Ecuador
118. Lukac, Ivan, Meteorological and Hydrological Service, Zagreb, Croatia
119. Lumpkin, Rick, NOAA/OAR Atlantic Oceanographic and Meteorological Laboratory, Physical Oceanography Division, Miami, Florida
120. Luo, Jing-Jia, Frontier Research Center for Global Change, JAMSTEC, Yokohama, Japan
121. Lyman, John M., NOAA/OAR Pacific Marine Environmental Laboratory, Seattle, Washington, and Joint Institute for Marine and Atmospheric Research, University of Hawaii, Honolulu, Hawai
122. Maddux, B., Department of Atmospheric and Oceanic Science, University of Wisconsin—Madison, Madison, Wisconsin
123. Marengo, Jose A., Instituto Nacional de Pesquisas Espaciais, Cachoeira Paulista, Brazil
124. Martínez Güingla, Rodney, Centro Internacional para la Investigación del Fenómeno de El Niño (CIIFEN), Guayaquil, Ecuador
125. Massom, R. A., Australian Government Antarctic Division and Antarctic Climate and Ecosystems CRC, University of Tasmania, Hobart, Tasmania, Australia
126. Maue, Ryan N., Center for Ocean–Atmospheric Prediction Studies, The Florida State University, Tallahassee, Florida
127. McLaughlin, F., Institute of Ocean Sciences, Sidney, Canada
128. Mears, Carl A., Remote Sensing Systems, San Rafael, California
129. Medany, Mahmoud A., Ministry of Agriculture and Land Reclamation, Cairo, Egypt
130. Meier, W., CIRES/NSIDC, University of Colorado, Boulder, Colorado
131. Meinen, Christopher S., NOAA/OAR Atlantic Oceanographic and Meteorological Laboratory, Physical Oceanography Division, Miami, Florida
132. Menne, Matthew J., NOAA/NESDIS National Climatic Data Center, Asheville, North Carolina
133. Merrifield, Mark A., University of Hawaii at Manoa, Honolulu, Hawaii
134. Mikkelsen, N., Geologic Survey of Denmark and Greenland (GEUS), Copenhagen, Denmark
135. Mitchum, Gary T., University of South Florida, College of Marine Science, St. Petersburg, Florida
136. Monaghan, A., Byrd Polar Research Center, The Ohio State University, Columbus, Ohio
137. Montzka, Stephen A., NOAA/OAR Earth Systems Research Laboratory, Boulder, Colorado
138. Morales, Ernesto, NOAA/NWS, San Juan, Puerto Rico
139. Morison, J., Polar Science Center, University of Washington, Seattle, Washington
140. Mote, T., Department of Geography, University of Georgia, Atlanta, Georgia
141. Mullan, A. Brett, National Institute of Water and Atmospheric Research, Ltd., Wellington, New Zealand
142. Müller-Westermeier, Gerhard, German Meteorological Service, Offenbach, Germany
143. Newman, P. A., Laboratory for Atmospheres, NASA Goddard Space Flight Center, Greenbelt, Maryland
144. Nghiem, S., Jet Propulsion Laboratory, Pasadena, California
145. Njau, Leonard, African Centre of Meteorological Applications for Development, Niamey, Niger
146. Obregón, André, Laboratory for Climatology and Remote Sensing (LCRS), University of Marburg, Marburg, Germany
147. Ogallo, Laban, IGAD Climate Prediction and Applications Centre (ICPAC), Nairobi, Kenya
148. Oludhe, Christopher, University of Nairobi, Nairobi, Kenya
149. O'Malley, Robert T., Oregon State University, Corvallis, Oregon
150. Overland, J., NOAA, Pacific Marine Environmental Laboratory, Seattle, Washington
151. Ozcan, Halis, Turkish State Meteorological Service, Istanbul, Turkey
152. Papineau, John, NOAA/NWS, Anchorage, Alaska
153. Parker, David E., Hadley Centre for Climate Change, Met Office, Exeter, United Kingdom
154. Pasch, Richard, NOAA/NWS/NCEP National Hurricane Center, Miami, Florida
155. Pashiardis, Stelios, Meteorological Service Cyprus, Nicosia, Cyprus
156. Patricio, Domingos M., Instituto Nacional de Meteorologia (INAM), Maputo, Mozambique
157. Pavan, Valentina, ARPA-SIM, Bologna, Italy
158. Pérez Suárez, Ramón, Instituto de Meteorología, La Habana, Cuba
159. Perovich, D., ERDC-Cold Regions Research and Engineering Laboratory, Hanover, New Hampshire
160. Perry, Matthew, Met Office, Exeter, United Kingdom
161. Pezza, Alexandre B., The University of Melbourne, Melbourne, Victoria, Australia
162. Phillips, David, Environment Canada, Ottawa, Ontario, Canada
163. Pires, Oliveira, Portuguese Meteorological Institute, Lisbon, Portugal
164. Polyakov, I., International Arctic Research Center, Fairbanks, Alaska
165. Prior, John, Met Office, Exeter, United Kingdom
166. Proshutinsky, A., Woods Hole Oceanographic Institution, Woods Hole, Massachusetts
167. Quintana, Juan M., Dirección Meteorológica de Chile, Santiago, Chile
168. Quintero Mercado, Alexander, Servicio de Meteorología dela Aviación Militar de Venezuela, Maracay, Venezuela
169. Rahimzadeh, Fatemeh, Atmospheric Science and Meteorological Research Center (ASMERC), Tehran, Iran

170. Rajeevan, Madhavan, National Climate Centre, India Meteorological Department, Pune, India
171. Ramírez, Patricia, Comité Regional de Recursos Hidráulicos (CRRH/SICA), San José, Costa Rica
172. Razuvaev, Vyacheslav N., All-Russian Research Institute of Hydrometeorological Information, Obninsk, Russia
173. Reid, P., Australian Bureau of Meteorology and Antarctic Climate and Ecosystems CRC, University of Tasmania, Hobart, Tasmania, Australia
174. Revadekar, Jayashree, Indian Institute of Tropical Meteorology, Pune, India
175. Reynolds, Richard W., NOAA/NESDIS National Climatic Data Center, Asheville, North Carolina
176. Richter-Menge, J., ERDC-Cold Regions Research and Engineering Laboratory, Hanover, New Hampshire
177. Robinson, David A., Department of Geography, Rutgers–The State University of New Jersey, Piscataway, New Jersey
178. Romanovsky, V., Geophyiscal Institute, University of Alaska, Fairbanks, Fairbanks, Alaska
179. Romero-Cruz, Fernando, National Meteorological Service (SMN/CONAGUA), Mexico City, Mexico
180. Rudels, B., Finnish Institute of Marine Research, Helsinki, Finland
181. Rusticucci, Matilde, Universidad de Buenos Aires, Buenos Aires, Argentina
182. Sabine, Christopher L., NOAA/OAR Pacific Marine Environmental Laboratory, Seattle, Washington
183. Saku, Seppo, Finnish Meteorological Office, Helsinki, Finland
184. Salinger, M. James, National Institute of Water and Atmospheric Research, Ltd., Newmarket, Auckland, New Zealand
185. Sánchez-Lugo, Ahira M., NOAA/NESDIS/NCDC, Asheville, North Carolina
186. Sayouri, Amal, Direction de la Météorologie Nationale, Rabat, Morocco
187. Scambos, T. A., National Snow and Ice Data Center, University of Colorado, Boulder, Colorado
188. Schauer, U., Alfred-Wegener-Institut für Polar- und Meeresforschung, Bremer-haven, Germany
189. Schnell, Russell C., NOAA/OAR Earth Systems Research Laboratory, Boulder, Colorado
190. Sensoy, Serhat, Turkish State Meteorological Service, Ankara, Turkey
191. Shiklomanov, A., University of New Hampshire, Durham, New Hampshire
192. Shimada, K., Institute of Observational Research for Global Change, Japan Agency for Marine-Earth Science and Technology, Yokosuka, Japan
193. Siegel, David A., University of California, Santa Barbara, Santa Barbara, California
194. Skansi, María de los Milagros, Servicio Meteorológico Nacional, Buenos Aires, Argentina
195. Smith, Shawn R., Center for Ocean–Atmosphere Prediction Studies, The Florida State University, Tallahassee, Florida
196. Sokolov, V., Arctic and Antarctic Research Institute, St. Petersburg, Russia
197. Spence, Jacqueline M., Department of Physics, University of the West Indies, Mona, Jamaica
198. Stammerjohn, S., Lamont-Doherty Earth Observatory, Columbia University, Palisades, New York
199. Steele, M., Polar Science Center, University of Washington, Seattle, Washington
200. Suda, Kazuto, Japan Meteorological Agency, Tokyo, Japan
201. Svabik, Otto, ZAMG, Vienna, Austria
202. Takahashi, Taro, Lamont-Doherty Earth Observatory, Columbia University, Palisades, New York
203. Taylor, Michael A., Department of Physics, University of the West Indies, Mona, Jamaica
204. Thiaw, Wassila M., NOAA/NWS/NCEP Climate Prediction Center, Camp Springs, Maryland
205. Thoman, Rick, NOAA/NWS, Anchorage, Alaska
206. Thorne, Peter, Met Office Hadley Centre, Exeter, United Kingdom
207. Timmermans, M.-L., Woods Hole Oceanographic Institu tion, Woods Hole, Massachusetts
208. Tinni, Seydou, African Centre of Meteorological Applications for Development, Niamey, Niger
209. Titchner, Holly, Met Office Hadley Centre, Exeter, United Kingdom
210. Toole, J., Woods Hole Oceanographic Institution, Woods Hole, Massachusetts
211. Trewin, Blair C., National Climate Centre, Australian Bureau of Meteorology, Melbourne, Victoria, Australia
212. Trigo, Ricardo M., CGUL, IDL, Universidade de Lisboa and Universidade Lusófona, Lisbon, Portugal
213. Turner, J., British Antarctic Survey, Cambridge, United Kingdom
214. Veenhuis, B., Department of Meteorology, The Florida State University, Tallahassee, Florida
215. Velden, Chris, Cooperative Institute for Meteorological Satellite Studies, University of Wisconsin— Madison, Madison, Wisconsin
216. Vinit, Francois, Météo France, Toulouse, France
217. Walker, D., Institute of Arctic Biology, University of Alaska–Fairbanks, Fairbanks, Alaska
218. Walsh, J., International Arctic Research Center, Fairbanks, Alaska
219. Wang, L., Department of Geography and Anthropology, Louisiana State University, Baton Rouge, Louisiana
220. Wang, M., Joint Institute for the Study of the Atmosphere and Ocean, University of Washington, Seattle, Washington
221. Wanninkhof, Rik, NOAA/OAR Atlantic Oceanographic and Meteorological Laboratory, Ocean Chemistry Division, Miami, Florida
222. Watkins, Andrew B., National Climate Centre, Australian Bureau of Meteorology, Melbourne, Australia
223. Weidick, A., Geologic Survey of Denmark and Greenland (GEUS), Copenhagen, Denmark
224. Weller, Robert A., Woods Hole Oceanographic Institution, Woods Hole, Massachusetts

225. Weyman, James, NOAA/NWS/central Pacific Hurricane Center, Honolulu, Hawaii
226. Whitewood, Robert, Environment Canada, Ottawa, Ontario, Canada
227. Willis, Joshua K., NASA/Jet Propulsion Laboratory, Pasadena, California
228. Woodworth, Philip L., Proudman Oceanographic Laboratory, Liverpool, United Kingdom
229. Xie, Pingping, NOAA/NWS/NCEP, Climate Prediction Center, Camp Springs, Maryland
230. Xue, Yan, NOAA/NWS Climate Prediction Center, National Centers for Environmental Prediction, Camp Springs, Maryland
231. Yu, Lisan, Woods Hole Oceanographic Institution, Woods Hole, Massachusetts
232. Yun, Won-Tae, Korea Meteorological Administration, Seoul, South Korea
233. Zimmer, Jacques, Meteorological Service of Luxemburg, Luxemburg
234. Zou, Xukai, National Climate Center, China Meteorological Administration, Beijing, China
235. Zubair, Lareef, International Research Institute for Climate and Society, Palisades, New York

TABLE OF CONTENTS

ABSTRACT—
D. H. LEVINSON AND J. H. LAWRIMORE

The combined land and ocean surface temperature in 2007 fell within the 10 highest on record, while the average land temperature was the warmest since global records began in 1880. In the low to midtroposphere, the annual global mean temperature was among the five warmest since reliable global records began in 1958, but still cooler than the record warmest year of 1998. For the fourth consecutive year, the annual precipitation averaged over global land surfaces was above the long-term mean, although the anomaly was significantly less than in 2006 when the annual value was the eighth wettest since 1901.

The globally averaged concentration of carbon dioxide (CO_2) continued to increase in 2007, having risen to 382.7 ppm at the Mauna Loa Observatory in Hawaii. The average rate of rise of CO_2 has been 1.6 ppm yr^{-1} since 1980; however, since 2000 this has increased to 1.9 ppm yr^{-1}. In addition, both methane (CH_4) and carbon monoxide (CO) concentrations were also higher in 2007.

Over the oceans, global SST during 2007 showed significant departures from the 1971–2000 climatology. Annual average upper-ocean heat content anomalies declined between 2006 and 2007 in the eastern equatorial Pacific and increased in off-equatorial bands in that ocean basin. These changes were consistent with the transition from an El Niño in 2006 to a La Niña in 2007. The global mean sea level anomaly (SLA) in 2007 was 1.1 mm higher than in 2006, which is about one standard deviation below what would be expected from the 15-yr trend value of 3.4 mm yr^{-1}.

In the tropics, the Atlantic hurricane season was near normal in 2007, although slightly more active than in 2006. In the north and south Indian Ocean Basins, both the seasonal totals and intensity of tropical cyclones (TC) were significantly above average, and included two Saffir–Simpson category 5 TCs in the north Indian Ocean and a world record rainfall amount of 5510 mm over a 3–8-day period on the island of Reunion in the south Indian Ocean.

In the polar regions 2007 was the warmest on record for the Arctic, and continued a general, Arctic-wide warming trend that began in the mid-1960s. An unusually strong high pressure region in the Beaufort Sea during summer contributed to a record minimum Arctic sea ice cover in September. Measurements of the mass balance of glaciers and ice caps indicate that in most of the world, glaciers are shrinking in mass. The Greenland ice sheet experienced records in both the duration and extent of the summer surface melt. From the continental scale, as a whole the Antarctic was warmer than average in 2007, although the Antarctic Peninsula was considerably cooler than average. The size of the ozone hole was below the record levels of 2006, and near the average of the past 15 yr, due to warmer springtime temperatures in the Antarctic stratosphere.

1. INTRODUCTION—J. H. Lawrimore and D. H. Levinson

This special section represents the 18th annual State of the Climate report, the 12th year the report has been included in *BAMS,* and the third year it has appeared as a separate supplement. NOAA's NCDC (see the appendix for a complete list of acronym expansions) has been responsible for the report's publication for the past eight years, although the report is truly an interagency and international effort. For the 2007 article, over 200 scientists from around the world participated, as the editorial team continued to focus on expanding international participation.

The purpose of this annual summary is to highlight the most salient events and overall climate conditions of 2007, which include noteworthy weather events (e.g., floods, tropical cyclones, tornadoes, and heat waves), assessment of temperature and precipitation anomalies, and reports on some of the primary features and parameters of the global climate system: global temperature and precipitation, trace gases in the Earth's atmosphere, climate conditions in the ocean basins, climate-related conditions in the tropics and polar regions, details of continental and regional climates, etc.

One of the main goals of this and past State of the Climate articles has been to put the observed climate and weather events over the previous year into historical perspective, with a focus on long-term trends and variability of the primary climatic elements over the period of instrumental observations (since the late 1800s), and, if possible, to extend back in time through the use of paleoclimate data. Due to the large number of data sources, it was impossible to refer to a standard base period for each climatic element in the article. Therefore, the base period for each dataset varied according to scientific convention, and those noted for each dataset herein were chosen by the authors and contributors based on a number of practical and scientific factors. It should also be noted that the data and analyses contained herein represent the best available as of early 2008; the data included in each section are susceptible to updates by the source agencies, although it is not expected that any key findings would be significantly affected.

As in the past, a determined effort was made to ensure that all participants were acknowledged for their efforts. Therefore, authorship has been noted for individual sections where appropriate. In addition to authors, numerous reviewers and other facilitators made this publication possible, and these individuals are also listed in the acknowledgments section.

As with each subsequent State of the Climate report, new topics and special features have been incorporated. For 2007, a section on the Indian Ocean dipole was added in the tropics chapter, analysis of conditions on the Greenland ice sheet was greatly expanded, and a number of sidebar features were included to highlight specific events and climate-related milestones that occurred in 2007. Also new this year is the inclusion of a number of new countries in the chapter 6, including Belize, Jamaica, and Puerto Rico in the Central America/Caribbean section; Japan, South Korea, and Mongolia in the East Asia section; Micronesia in the Oceania section; and Egypt in the Africa section. In addition, the section on Europe was expanded and includes a much wider participation of scientists from that continent.

The following is a summary of the report's five main sections:

Section 2: Global climate

- The global land and ocean combined surface temperature for 2007 fell within the 10 highest on record, while the average land temperature was the warmest since global records began in 1880, with an annual departure of +0.64°C (+1.15°F).
- The annual global mean temperature in the low to midtroposphere was among the five warmest since records began in 1958, ~0.2°C (~0.36°F) cooler than the warmest year of 1998.
- The 12-month running mean of Northern Hemisphere snow cover extent was below the long-term average throughout 2007. Overall, there had been no negative annual anomaly of snow cover extent for the Northern Hemisphere as large as the one at the end of 2007 since the record lows of the satellite era were observed between 1988 and 1990.
- For the fourth consecutive year, the annual precipitation averaged over global land surfaces was above the long-term mean, although the anomaly was significantly less than in 2006 when the annual value was the eighth wettest since 1901. Since the start of the twentieth century land-based precipitation has increased globally, with the greatest increases in the mid- and high latitudes of the Northern Hemisphere.
- The globally averaged concentration of CO_2 continued to increase in 2007, having risen to 382.7 ppm at the Mauna Loa Observatory in Hawaii. This represents an increase of ~1.8 ppm above the 2006 global annual mean (380.9 ppm). The atmospheric concentration was around 280 ppm prior to the Industrial Revolution (ca 1850).
- Both CH_4 and CO concentrations were also higher in 2007.
- The average rate of rise of CO_2 has been 1.6 ppm yr^{-1} since 1980; however, since 2000 this has increased to 1.9 ppm yr^{-1}. This suggests that the fraction of CO_2 emitted from sources that remain in the atmosphere may be increasing.
- The 2006 elevated aerosol levels seen at the far northern latitudes or around Indonesia were absent in 2007, and smoke from biomass burning over the Amazon basin, an indication of regional deforestation, exhibited levels that were in agreement with the increasing aerosol trend observed from 2000 through 2005.
- In the Southern Ocean, above average wind speeds in March through August suggested an atypically strong surface manifestation of the polar vortex during the austral winter (June–August).

Section 3: Global oceans

- Global SST during 2007 showed significant departures from the 1971–2000 climatology in four regions: a positive anomaly in the high latitude North Atlantic that has persisted since 2002 continued into 2007; positive anomalies that have occurred each boreal summer since 2002 in the Arctic Ocean adjacent to the North Pacific reached their highest value of about 2.5°C in 2007; the positive anomaly in the tropical North Atlantic, which has had a downward trend from its highest value in 2005, returned to near-normal conditions in the summer of 2007; and positive anomalies in the central and eastern equatorial Pacific associated with the 2006 El Niño ended in February, and a moderate-strength La Niña developed in the fall.
- Annual average upper-ocean heat content anomalies declined between 2006 and 2007 in the eastern equatorial Pacific and increased in off-equatorial bands in that ocean basin. These changes were consistent with the transition from an El Niño in 2006 to a La Niña in 2007.
- Ocean heat fluxes demonstrated a coherent pattern of change in the tropical Pacific, in response to the east–west SST pattern of the 2007 La Niña episode. Evaporation decreased over the cooler SST region in the eastern Pacific and increased over the warmer SST region in the western Pacific.
- The tropical cyclone heat potential, a parameter proportional to the upper-ocean heat content that is linked to hurricane intensification, exhibited

high variability within each ocean basin. On average, all basins, except the eastern Pacific basin, showed areas of positive anomalies, with the largest anomalies in the west Pacific.
- Global sea surface salinity anomalies in 2007 continued to accentuate climatological patterns; fresh areas of the ocean have generally become fresher and salty areas have generally become saltier in recent years relative to a long-term climatology.
- The global mean SLA in 2007 was 1.1 mm higher than in 2006, which is about one standard deviation below what would be expected from the 15-yr trend value of 3.4 mm yr^{-1}. Dominant spatial patterns of sea level variability during 2007 included the strengthening La Niña in the tropical Pacific Ocean, and zonal anomalies in the tropical Indian Ocean, particularly south of the equator.
- A revised climatology of global surface pCO_2, which was assembled from over 3 million measurements spanning 36 yr, suggests a 30% larger inter-annual variability in ocean CO_2 uptake than that inferred from the previous climatology.
- Chlorophyll concentrations during 2007 were close to the mean value derived from 10 yr of climate-quality ocean color measurements, but exhibited significant deviations from the mean that were largely due to global changes in phytoplankton physiology rather than phytoplankton biomass.

Section 4: The tropics
- The year was characterized by a transition to La Niña conditions that, while not developed until August, resulted in suppressed convection near the date line beginning in early June. Therefore, La Niña–like impacts on the upper-tropospheric circulation were already evident during June–August across the subtropical South Pacific.
- The 2007 Atlantic hurricane season was near normal, although slightly more active than in 2006. In the north and south Indian Ocean Basins, both the seasonal totals and intensity of TCs were significantly above average, and included two Saffir–Simpson category 5 TCs in the north Indian Ocean and a world-record rainfall amount of 5,510 mm over a 3–8-day period on the island of Reunion in the south Indian Ocean.
- A very strong, positive phase of the Indian Ocean dipole occurred during 2007. This pattern likely contributed to the lack of a traditional La Niña signal in the Northern Hemisphere subtropics during the peak of the Atlantic hurricane season.

Section 5: The Poles
- The year 2007 was the warmest on record for the Arctic, continuing a general, Arctic-wide warming trend that began in the mid-1960s.
- A dramatic signal related to the anomalous warming was the significant reduction in the extent of the summer sea ice cover and in the relative amount of older, thicker ice, both showing signs of an increase in their relative rates of reduction.
- An unusually strong high pressure region in the Beaufort Sea during summer contributed to a record minimum Arctic sea ice cover in September. Accompanying the reduction in sea ice cover was an increase in the temperature and a decrease in the salinity of the surface ocean layer.
- Due to more open water at the end of the boreal summer, surface air temperature anomalies for 2005–07 remained above +6°C (+10.8°F) during October–November compared with the 1982–2007 mean over the central Arctic.
- Measurements of the mass balance of glaciers and ice caps indicate that in most of the world, glaciers are shrinking in mass. The Greenland ice sheet experienced records in both the duration and extent of the summer surface melt.
- The AO circulation regime, widely considered the main source of Arctic climate variability during the twentieth century, returned to a strongly positive wintertime index value for the first time in more than a decade.
- As a whole, Antarctica was warmer than average in 2007, although the Antarctic Peninsula was considerably cooler than average.
- The cool temperatures over the Antarctic Peninsula resulted in extensive fast ice accumulation on the eastern peninsula coast by the end of the calendar year, and an unusually late start to the summer melt season there.
- Ozone activity was below the record levels of last year, and near the average of the past 15 yr, due to warmer springtime temperatures in the stratosphere.

Section 6: Regional climates

Numerous noteworthy climate events occurred in 2007 on the regional scale (Fig. 1.1):

- The end of a weak El Niño episode in February 2007 followed by a transition to moderate-to-strong La Niña conditions during the latter half

of the year influenced climate conditions in many parts of the world.

- *Africa*: In East Africa, unusually wet conditions during the summer rainy season brought the level of the Blue Nile at Khartoum, the capital of Sudan, far above the record levels seen in 1988. The 2007 rainy season in West Africa featured above average rainfall across most areas of the Sahel and portions of the Gulf of Guinea region.
- *North America*: In Canada, 2007 was warmer and wetter than normal, with the country as a whole having its 13th warmest year on record, 0.9°C (1.6°F) above normal. For the United States, 2007 tied with 2005 as the ninth warmest year on record with a nationally averaged temperature of 12.4°C (54.3°F), the 10th consecutive year with temperatures much warmer than the long-term average. Continuing a string of record or near-record fire seasons, the wildfire season in 2007 had the second most acres burned in the historical record for the United States as a whole (9.3 million acres; ~3.8 million hectares). Above average temperatures prevailed across Mexico, as the nationwide mean was 21.8°C (71.2°F) in 2007, 1.1°C (~2°F) above the long-term average.
- *Central America and the Caribbean*: Much of the region was warm and wet in 2007. The above normal rainfall was attributable in part to the tropical cyclones that impacted the region, as well as the emergence of a La Niña during the latter half of the year. Cuba had its eighth warmest year since 1951, with a mean temperature of 25.99°C (78.78°F), ~0.5°C (~0.9°F) above normal.
- *South America*: Precipitation over South America during 2007 was below normal in the southern and eastern parts of the continent, very dry over the west, and near normal to wetter than normal in the region north of the equator and parts of the Amazon basin. An unusually cold winter was reported over the southern portion of the continent, while warmer-than-normal conditions prevailed in the Amazonian region.
- *Asia*: It was the warmest year on record in Russia, with a mean annual air temperature of 2.0°C (3.6°F) above normal. Winter and summer were also the warmest on record in 2007, registering anomalies of +3.2°C (+5.8°F) and +1.8°C (+3.2°F), respectively (meteorological observations in Russia date back to 1891). It was also record warm in China and near-record warm in Japan in 2007. The annual mean temperature in China was 1.3°C (~2.3°F) above normal, with all four seasons warmer than average, making 2007 the warmest year since reliable country-wide records began in 1951. In Japan, the annual mean temperature was 0.85°C (~1.5°F) above normal, the fourth highest on record since 1898.
- *Europe*: Based on data from the Hadley Centre in the United Kingdom, the annual average land surface temperature was +1.23 ± 0.08°C (+2.21 ± 0.14°F) above the 1961–90 mean for the European region between 35°–75°N and 10°W–30°E, and is virtually certain to be one of the five warmest years in the 1850–2007 period of record. It was the warmest year on record in the Netherlands, Belgium, the Czech Republic, and several countries in eastern and southeastern Europe. In addition, Denmark had its warmest and sunniest year on record in 2007, 1.8°C (3.2°F) above the 1961–90 mean. Since 1870, Danish temperatures have increased by 1.5°C (2.7°F).
- *Oceania*: Large areas of Australia continued to be impacted by both long- and short-term drought in 2007. In terms of mean temperatures it was Australia's sixth warmest year since high quality Australia-wide records commenced in 1950, 0.7°C (1.3°F) above the 1961–90 mean. For 2007 as a whole, above average SSTs were observed throughout much of the tropical southwest Pacific, south and west of the date line.

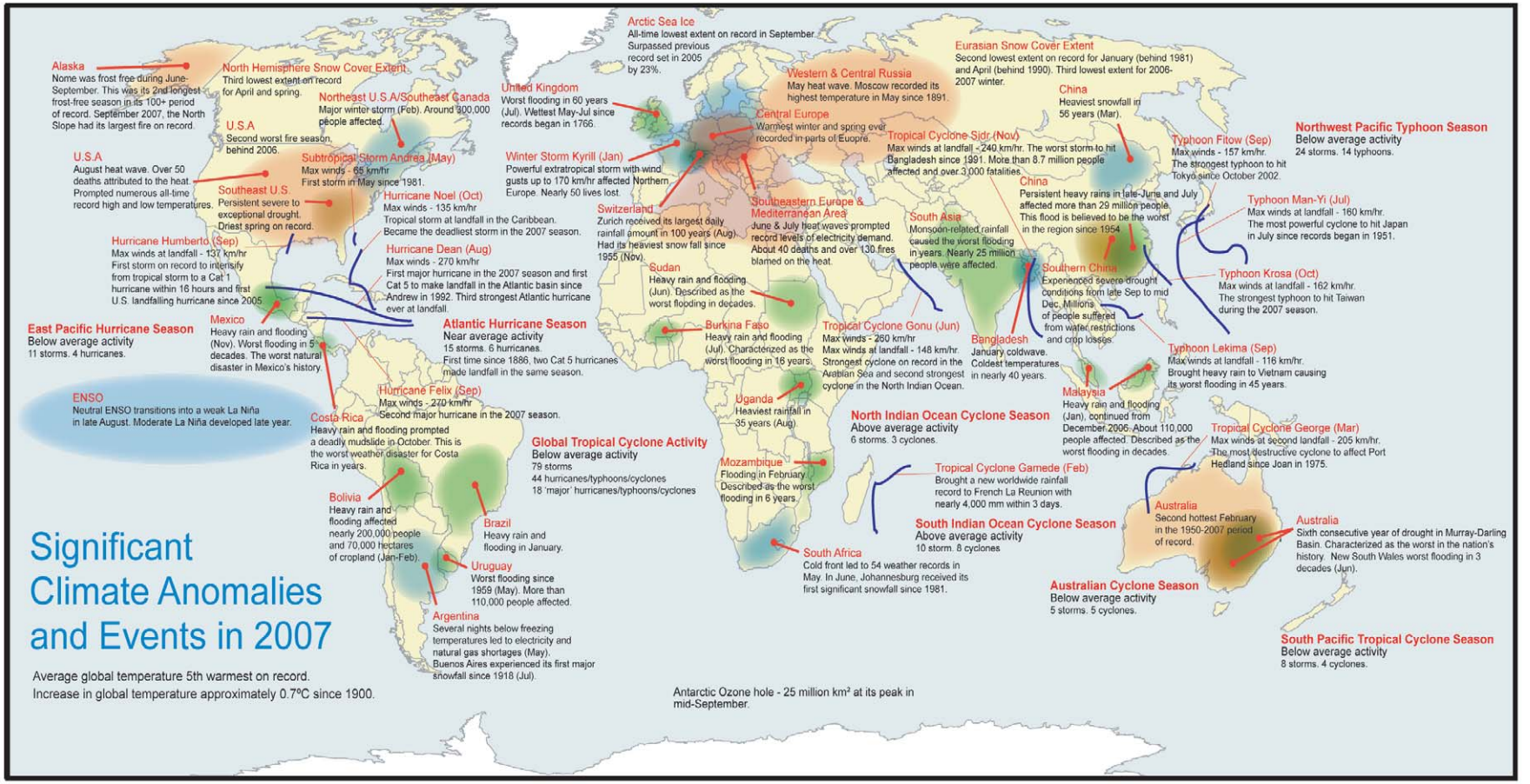

Fig. 1.1. Geographical distribution of notable climate anomalies and events occurring around the planet in 2007.

2. GLOBAL CLIMATE—A. Horvitz, Ed.

a. Overview—A. Horvitz

The year 2007 was notable for pronounced warmth at the surface and throughout the troposphere. The global land and ocean combined surface temperature ranked within the 10 highest on record, while the average land temperature was the warmest since records began in 1880, with an annual departure of +0.64°C. The annual global mean temperature in the low to midtroposphere was among the five warmest since records began in 1958, about 0.2°C cooler than the warmest year of 1998.

For the fourth consecutive year, the annual precipitation averaged over global land surfaces was above the 1961–90 base period mean, with a wet anomaly of approximately 8 mm (0.7%) in 2007. Over the tropical Pacific, the 2006 El Niño ended abruptly in February 2007. During the second half of the year negative SST anomalies expanded westward from the equatorial eastern Pacific as a moderate-to-strong La Niña episode developed by year's end.

The 12-month running mean of Northern Hemisphere snow cover extent was below the long-term average throughout the year. The negative 12-month anomaly at year's end had not occurred since the record lows of the satellite era were observed between 1988 and 1990. The Arctic and the Amazon basin and its environs both exhibited strong deviations in total cloud cover in 2007, which may have resulted from changes in atmospheric moisture and surface temperatures (for the Arctic) and land use change (for the Amazon).

The globally averaged concentration of CO_2 continued to increase in 2007, rising to 382.7 ppm, an increase of 1.6 ppm over the 2006 global mean value. CH_4 and CO concentrations were also higher in 2007, with the preliminary global averages increasing to 1,782.2 ppb and 84 ppb, respectively. The global mean mixing ratios at the end of 2007 for N_2O was 321.4 ppb while SF_6 was 6.29 ppt, an increase of 1.4 ppb and 0.29 ppt, respectively, over 2006. Additionally, HCFCs continued to increase and by mid-2007 chlorine accounted for by the three most abundant HCFCs amounted to 237 ppt, or 8.8% of all chlorine carried by long-lived halocarbons of anthropogenic chlorine (not including Cl from CH_3Cl).

The 2006 elevated aerosol levels seen at the far northern latitudes or around Indonesia were absent in 2007, and smoke from biomass burning over the Amazon basin, an indication of regional deforestation, exhibited levels that were inline with the increasing aerosol trend observed from 2000 through 2005. Over the Southern Ocean, long bands of greater wind speeds in March through August suggested an atypically strong surface manifestation of the polar vortex during the austral winter. This chapter concludes with a discussion of teleconnection patterns including the mean December–February 2006–07 500-hPa circulation pattern, which was characterized by a large degree of zonal symmetry that projected strongly onto the Arctic Oscillation.

b. Global temperature

1) Surface temperature—M. J. Menne

The global average surface temperature in 2007 was among the 10 warmest years on record. As shown in Fig. 2.1, the 2007 annual average temperature ranked from second to eighth highest on record based on three global datasets maintained independently by NOAA's NCDC (fifth highest), NASA's GISS (second highest), and the University of East Anglia–CRU/UKMO (eighth highest). Calculated as a linear trend, the rates of temperature change are 0.065°, 0.066°, and 0.074°C decade^{-1} since 1901 for the NOAA, NASA, and CRU/UKMO analyses, respectively. However, as Fig. 2.1 shows, the change in global temperature has been nonlinear, with the rise from 1979 to 2007 nearly 3 times greater than the century-scale trend. In addition, the pattern of warming has not been uniform, as shown in Fig. 2.2.

All three global temperature analyses shown in Fig. 2.1 are based on air temperature data over land and SST derived from ship reports, buoys, and satellite observations. The NOAA surface temperature analysis is described in Smith and Reynolds (2005), the NASA analysis is described in Hansen et al. (2001), and the CRU/UKMO analysis (HadCRUT3) is described in Brohan et al. (2006). Because the three groups use different reconstruction and interpola-

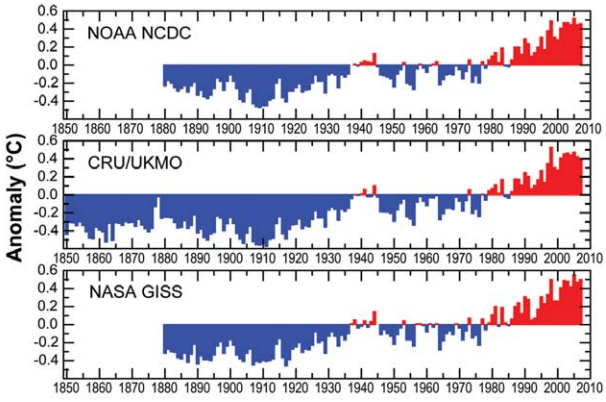

Fig. 2.1. Annual global surface temperature departures from the 1961 to 1990 average. [Sources: NOAA/NCDC; CRU/UKMO (HadCRUT3); and NASA GISS.]

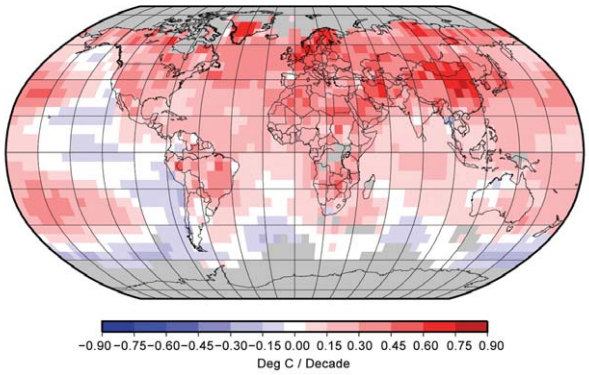

Fig. 2.2. Pattern of linear temperature trends for the period 1979 to 2007. Gray areas indicate data-sparse regions. [Source: NOAA/NCDC.]

tion approaches, the analyses differ most in regions with sparse data. In terms of the global averages, and where observations are plentiful, the three surface temperature reconstructions are in good agreement. The differences in annual rankings in recent years are caused in part by how the different groups treat data sparse regions. For example, the NASA analysis expands estimates of temperature anomalies across the Arctic where values were at or near record levels in 2007. Despite these differences, the uncertainty in the calculations implies that the value for 2007 in all three datasets is effectively indistinguishable from values in several of the other high ranking years. The addition of error bars to the NCDC global surface temperature time series (Fig. 2.3a) illustrates the uncertainty in calculations of annual global temperature rankings.

Warming has occurred in both land and sea surface temperatures. As might be expected given the tremendous thermal capacity of the oceans, land temperatures have risen at over twice the rate of the ocean surface since 1979 (about 0.30° versus 0.12°C decade^{-1}). Worldwide, land surface temperatures in 2007 ranked as highest on record according to the NOAA record while SSTs ranked as ninth highest (Fig. 2.4b). (A preliminary analysis of the influence of SSTs on land surface temperatures in 2007 is provided in the adjoining sidebar discussion.) The top 10 ranking for SSTs is noteworthy because it occurred at a time when the equatorial Pacific Ocean was in the cool phase of the El Niño–La Niña cycle. The geographic distribution of the 2007 annual temperature anomalies is shown in Fig. 2.4 (see chapter 6 for additional details of regional temperatures in 2007).

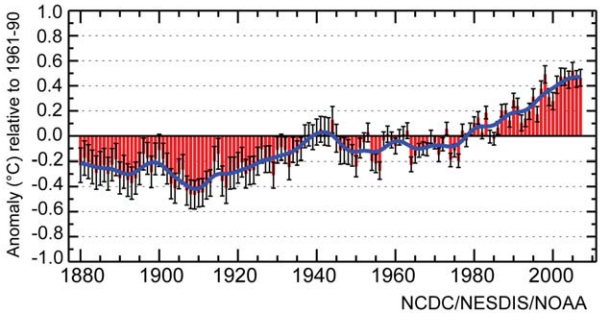

Fig. 2.3a. Annual global surface temperature departures (red bars) from the 1901 to 2000 average with error estimates (black lines). [Source: NOAA/NCDC (Smith and Reynolds 2005).]

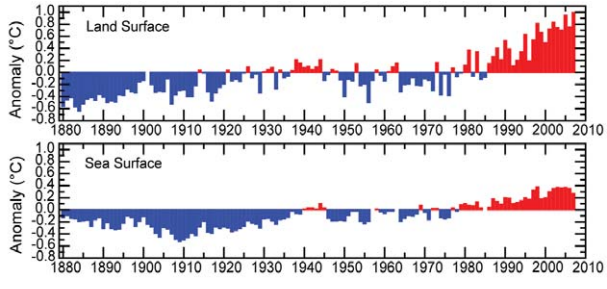

Fig. 2.3b. Global land and sea surface temperature anomalies with respect to the 1961 to 1990 average. [Source: NOAA/NCDC.]

2) Upper-air temperatures—J. R. Christy

The temperature variations of three broad atmospheric layers, the LT to MT (Sfc–300 hPa), the MT to LS (Sfc–70 hPa), and the upper troposphere to LS (150–20 hPa) are monitored by two observing systems, radiosondes, and satellites. Three radiosonde-based products are available, HadAT2 (Thorne et al. 2005) based on about 650 stations, RATPAC (Free et al. 2005) based on 85 stations, and RAOBCORE based on about 1,100 stations (Haimberger 2007).

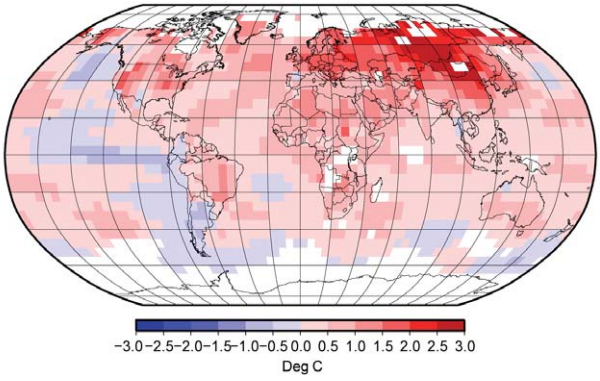

Fig. 2.4. Geographic distribution of temperature anomalies in 2007. Departure from the 1961 to 1990 average. [Source: NOAA/NCDC.]

Satellite products are the latest versions updated from last year, LT, MT, and LS from the UAH (Christy et al. 2003; Spencer et al. 2006; v5.2 LT, v5.1 MT, and LS) and RSS (Mears et al. 2003; Mears and Wentz 2005; v3.1 LT, v3.0 MT, and LS). Here "annual" is defined as December to November, otherwise known as the meteorological year.

The annual, global mean LT anomaly for 2007 was second to fifth warmest (for reference: HadAT2:2nd, RATPAC:4th, RAOBCORE:2nd, UAH:4th, RSS:5th) among the datasets since records began (1958 for radiosondes or 1979 for the satellite record, Fig. 2.5). On average, this was about 0.2°C cooler than the warmest year 1998. Some datasets also ranked the NH anomaly as second warmest following 1998. All datasets are consistent with global trend values of +0.16 ± 0.03°C decade^{-1} since 1979 and +0.16 ±0.02°C decade^{-1} since 1958 (Fig. 2.5; Table 2.1).

Regionally, the tropical LT values began the year warmer than the 1979–98 average during a minor El Niño while the global LT temperature in January was the warmest monthly anomaly since the 1998 El Niño in some datasets. By the end of the year, however, a developing and substantial La Niña dropped tropical temperatures below average. The north polar regions continued to be above average with trends since 1979 above +0.4°C decade^{-1} while the south polar regions were near the long-term average.

A similar picture is indicated for the MT layer (not shown), which includes some stratospheric influence. The rankings for 2007 placed this layer from third to sixth warmest (for reference: HadAT2:3rd, RATPAC:6th, RAOBCORE:3rd, UAH:5th, RSS:5th) depending on the datasets. Linear trends are more negative than LT due to the influence of the cooling stratosphere (Table 2.1).

The quasi-biennial oscillation shifted to the easterly or cold phase in 2007 and thus tropical stratospheric temperatures (LS) in the latter half of 2007 were cooler than the similar period in 2006 by about 1.2°C. Globally, among the datasets, the 2007 annual anomaly ranked from the second to sixth coldest (for reference: HadAT2:2nd, RATPAC:2nd, RAOBCORE:6th, UAH:2nd, RSS:3nd). As has been

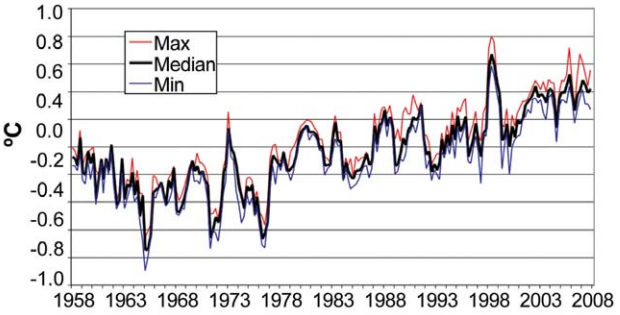

Fig. 2.5. Time series of seasonal anomalies of the lower troposphere, LT, as the median of the various datasets, with respect to 1979–88 (black). The red and blue lines represent the highest and lowest values, respectively, reported by any of the sources.

Table 2.1. Linear trends (°C decade^{-1}) of global and tropical (20°S–20°N) anomalies for 1958–2007. In parentheses are trends for 1979–2007.

	HadAT2*	RATPAC*	RAOBCORE*	UAH**	RSS**
Global LT	+0.16 (+0.18)	+0.16 (+0.17)	+0.14 (+0.17)	(+0.14)	(+0.18)
Tropical LT	+0.12 (+0.09)	+0.14 (+0.13)	+0.13 (+0.12)	(+0.08)	(+0.18)
Global MT	+0.09 (+0.07)	+0.08 (+0.05)	+0.10 (+0.12)	(+0.06)	(+0.12)
Tropical MT	+0.09 (+0.02)	+0.08 (+0.03)	+0.12 (+0.12)	(+0.05)	(+0.15)
Global LS	−0.36 (−0.53)	−0.39 (−0.62)	−0.30 (−0.39)	(−0.43)	(−0.31)
Tropical LS	−0.34 (−0.54)	−0.44 (−0.65)	−0.25 (−0.34)	(−0.38)	(−0.31)

* Radiosonde datasets are characterized by more limited coverage with few data south of 50°S latitude and little in oceanic areas.

** UAH coverage is 85°S to 85°N, RSS 70°S to 85°N. Since less warming has been observed in the high southern latitudes, their inclusion tends to reduce "global" trends, e.g., the UAH global LT trend is 0.02°C decade^{-1} more positive when excluding latitudes south of 50°S.

THE INFLUENCE OF SSTs ON GLOBAL LAND SURFACE TEMPERATURES—
M. P. HOERLING IN CONJUNCTION WITH THE NOAA CSI TEAM

Globally averaged land temperatures for 2007 were the warmest since records began in 1880, with a mean annual departure of +0.64°C above the 1971–2000 average based on the CRU/UKMO analysis. Land temperatures were anomalously warm almost everywhere over the globe (Fig. 2.6, top panel).

The connection between the record global land temperatures of 2007 and global SST conditions was investigated with three AGCM simulations forced with the monthly evolution of observed SSTs (so-called AMIP experiments; Gates 1992). For each AGCM, an ensemble of 50 realizations was made without the effects of radiative forcing due to changes in atmospheric chemical composition. The multimodel ensemble averaged land surface temperature response in 2007 is warm at virtually all locations (Fig. 2.6, middle panel), with a mean annual globally averaged land temperature departure of +0.26°C computed with respect to the 1971–2000 climatological mean. The PDF of simulated globally averaged 2007 land surface temperature departures for each of the 150 AMIP runs is shown in Fig. 2.7 (left panel), along with the PDF of 150 members of the control runs that used 1971–2000 climatological SSTs. The PDF indicates that 1) a majority of simulations for 2007 had a positive land surface temperature anomaly and 2) while SSTs in 2007 greatly elevated the chances that global land surface temperatures would be above normal, no single run generated a departure as large as observed. This SST-only-forced analysis suggests that the SST-forced response, although of the same sign as the 2007 observed record land temperatures, was not the leading cause.

The relationship between the record global land temperature of 2007 and GHG forcing was investigated using the coupled model simulations that were used in the IPCC Fourth Assessment

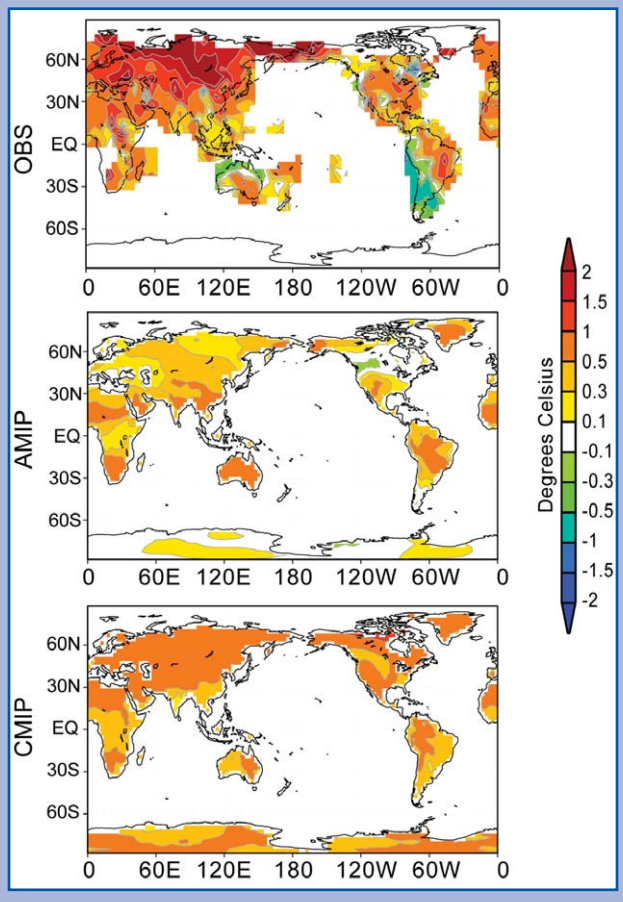

Fig. 2.6. (top) Observed and simulated 2007 annually averaged land surface temperature departure based on (middle) AMIP ensemble and (bottom) CMIP ensemble experiments. Reference is 1971–2000 climatologies. AMIP refers to atmospheric climate models forced with the monthly varying observed 2007 global sea surface temperatures. CMIP refers to coupled ocean–atmosphere climate models forced with estimated 2007 greenhouse gas concentrations. See text for details on model runs. [Source: NOAA CSI Team.]

the case for most of the last few years, there was not a dramatic cooling of the south polar region in the austral spring. Even so, all datasets indicate significant cooling over the period on a global basis (Table 2.1), though since about 1995, the global trends have not been remarkable (Fig. 2.8).

c. Hydrologic cycle

1) Global precipitation

(i) Over land—D. H. Levinson and J. H. Lawrimore

The focus of this section is on land-based precipitation and the spatiotemporal variations observed in 2007 using in situ gauge data from the GHCN dataset (Peterson and Vose 1997). The annual and seasonal

Report. This "CMIP archive" of model data (which included 22 coupled atmosphere–ocean models and a total ensemble size of 48 simulations for 2007) used projected GHG concentrations based on a business-as-usual scenario (A1B) extended from the historical climate of the twentieth century runs that ended in 1999. The 2007 land surface temperature anomalies averaged across all 48 model simulations are shown in Fig. 2.7 (right panel). Warm surface temperature departures (relative to the CMIP model climatologies of 1971–2000) occur over all land points, with a mean annual globally average land temperature departure of +0.40°C. The PDF of simulated globally averaged land surface temperature departures for each of the 48 runs is shown in Fig. 2.7 (right panel), along with the distribution of all CMIP simulated global land surface temperatures during the reference period of 1971–2000 (comprising 1,440 samples; 30 yr × 48 runs). The PDF indicates that 1) almost all simulations for 2007 had a positive land surface temperature anomaly and 2) 2007 GHG forcing greatly elevated the chances that global land surface temperatures would be above normal, with a few runs generating 2007 departures larger than the record observed warmth. The magnitude of the land surface warmth is appreciably greater in the CMIP ensemble than in the AMIP ensemble, suggesting that GHG forcing was a leading cause for the 2007 record land temperatures.

In conclusion, the analysis indicates that greenhouse gas forcing was a likely attributing factor raising global mean land temperatures in 2007. That signal (defined as the multimodel mean response) alone, however, cannot explain the record warmth that was observed. Further, the increase of GHG forcing in 2007 led to a 100-fold increase in the probability of land temperatures exceeding the 2007 observed +0.64°C record (from a less than 0.1% chance for 1971–2000 GHG forcing to a 10% probability under the 2007 GHG forcing scenario). At least one pathway by which GHG forcing raised land temperature was via their influence on the observed SSTs, although as judged from the AMIP simulations this alone cannot explain the record warmth.

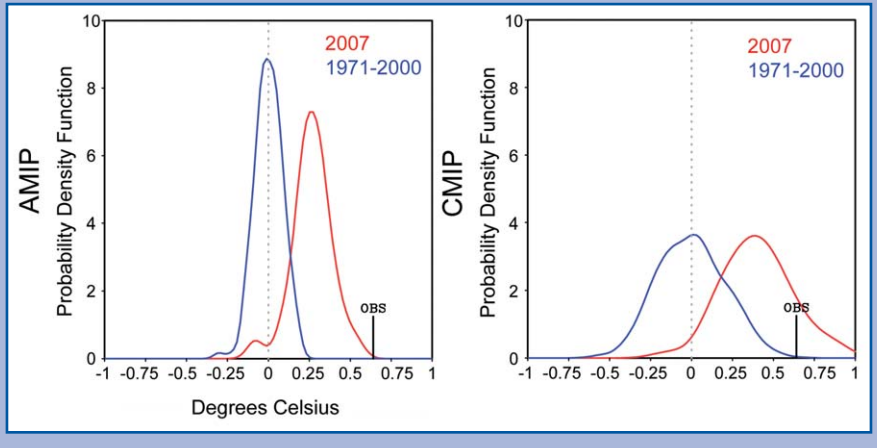

Fig. 2.7. PDFs of the simulated globally averaged 2007 (red) annual land surface temperatures based on (left) individual 150 AMIP runs and (right) the individual 48 CMIP runs. The PDFs of simulated globally averaged annual land surface temperatures during the reference period of 1971–2000 are shown as the blue PDF curves. The observed globally averaged 2007 annual land surface temperature departure of +0.64°C is plotted by the vertical tic mark. [Source: NOAA CSI Team.]

departures covering the period 1901 to 2007 were analyzed, and precipitation anomalies determined with respect to the 1961–90 mean for those stations with a minimum of 25 yr of data during the 30-yr base period (Vose et al. 1992). In addition, highlights of selected regional precipitation anomalies are also included below (see chapter 6 for more complete details of regional precipitation patterns and variability).

In 2007, the annual precipitation averaged over all global land surfaces was approximately 8 mm (0.7%) above the 1961–90 base period mean (Fig. 2.9a). It was the fourth consecutive year with above average global precipitation, although the anomaly was sig-

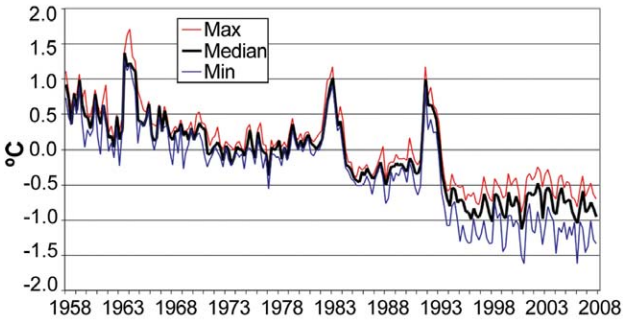

Fig. 2.8. Time series of seasonal anomalies of the LS as the median of the various datasets, with respect to 1979–88 (black). The three warm events are volcanically induced (Agung, El Chichón, and Mt. Pinatubo, respectively). The red and blue lines represent the highest and lowest values, respectively, reported by any of the sources.

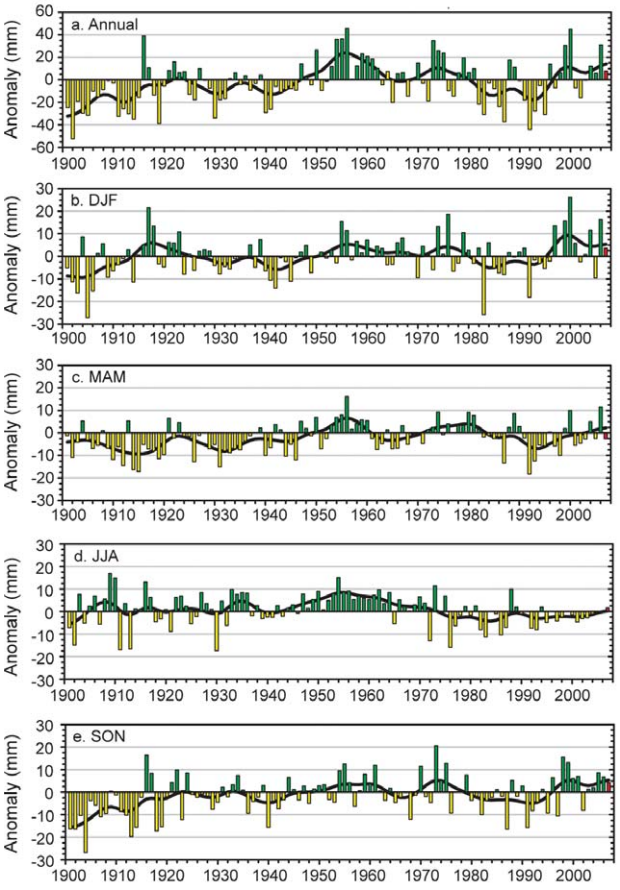

Fig. 2.9. Time series of annual and seasonal global land surface precipitation anomalies (mm) over the period 1900–2007, based on observations from the Global Historical Climatology Network dataset (Vose et al. 1992): (a) annual, (b) Dec–Feb, (c) Mar–May, (d) Jun–Aug, and (e) Sep–Nov. The precipitation anomalies were calculated with respect to the 1961–90 base period mean: green bars = positive anomalies, yellow bars = negative anomalies, and red bar = 2007 anomaly. In addition, the black line in each time series denotes the smoothed annual or seasonal values using a 13-point binomial filter.

nificantly less than in 2006 when the annual value was the eighth wettest (~31 mm above average) since the beginning of the twentieth century.

From a seasonal perspective, only the March–May period (boreal spring) was drier than average globally, with an anomaly of –2.7 mm (–1.1%) below the mean (Fig. 2.9c). Of special note, the global anomaly for the June–August period (boreal summer) was +1.67 mm (+0.6%), which was the largest positive precipitation anomaly for that season since 1994. In fact, of the past 15 yr only 2007 had above average precipitation globally during the June–August period. In contrast, 9 of the past 10 yr have been wetter than average during September–November (Fig. 2.9e), and 2007 continued this pattern with a global anomaly of +4.2 mm (+1.7%) above the long-term mean.

From a hemispheric perspective, the Southern Hemisphere was drier than average for the year (–20 mm, –1.7%), while the Northern Hemisphere was wetter than average (+18.4 mm, +2.2%) in 2007 (not shown). The seasonal variations reflected these annual anomalies, with only the December–February season (austral summer) wetter than average in the Southern Hemisphere (+25.9 mm), while the same 3-month period (boreal winter) was drier than average in the Northern Hemisphere (–5.2 mm, –6.3%). The summer (June–August) was anomalously wet in the Northern Hemisphere (+11.7 mm, +3.7%), which was only the eighth time in the past 20 yr with above average precipitation.

Regional-scale precipitation patterns in 2007 were influenced by the El Niño–Southern Oscillation, as the year began with a weak El Niño event and ended in a moderate-to-strong La Niña episode. Precipitation patterns during the period December 2006 to February 2007 were in a number of places consistent with El Niño (warm event) conditions (Ropelewski and Halpert 1987). Dry conditions occurred across much of Australia, the islands of the western tropical Pacific, and Hawaii, while wet conditions were observed in parts of central South America (Bolivia, southern Brazil, northern Argentina, Uruguay and Paraguay). Additional details on ENSO conditions are available in section 4b.

In the central United States, unusually wet conditions intensified during March–May, generating widespread flooding across the southern plains. The excessive rainfall in the region persisted into summer

(June–August), and both Oklahoma and Texas had their wettest summer on record (historical records began in 1895). Excessive rainfall and flooding also affected large areas of the United Kingdom during the summer, and a number of long-term rainfall records were broken. In southern Australia, long-term rainfall deficits continued during the austral winter (June–August), where over six years of drought has affected the Murray–Darling basin (see chapter 6 for additional details). The tropical western North Pacific was significantly wetter than average during September–November 2007, especially the Philippines and Borneo, which contributed to the wetter-than-average seasonal anomaly for the Northern Hemisphere during that period (~11 mm).

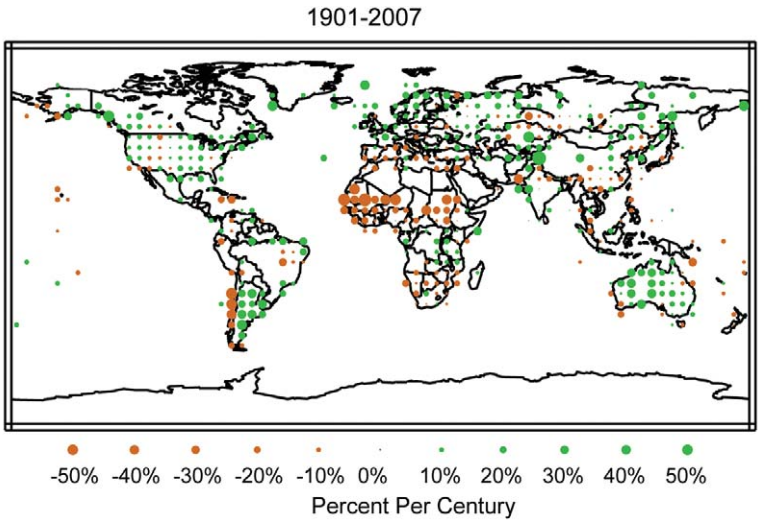

Fig. 2.10. Annual precipitation trends for the period 1901–2007 depicted in the percent change per century. Calculation of grid cell trends required at least two-thirds (66%) of the years without missing data. Stations with more than one-third of their data missing during the 1961–90 reference period were excluded from the analysis.

The wetter-than-average global conditions in 2007 are consistent with a long-term increasing trend in precipitation. Global land surface precipitation has increased approximately 2% since the start of the twentieth century, with the greatest contribution to this rise occurring in mid- and high-latitude regions (Fig. 2.10). Although there has been pronounced decadal variability, with all regions of the world experiencing multiyear periods of both increasing and decreasing trends during the past century, the overall trend has been toward greater precipitation amounts in much of the world. A notable exception has occurred in the Northern Hemisphere tropics, where rainfall has decreased at a rate near 0.8% per decade, largely due to a recent multidecadal period of drier-than-average conditions in western and eastern Africa.

In many places, the positive precipitation trends also have been accompanied by even larger increases in heavy and extreme precipitation events, as warming temperatures have increased the water-holding capacity of the atmosphere (Trenberth et al. 2003). In the United States, for example, the amount of precipitation falling in the heaviest 1% of rain events has increased by 20% during the twentieth century, while total precipitation has increased by only 7% (Groisman et al. 2004). Similar trends have occurred in other regions of the world, as precipitation from heavy events has increased while light-to-moderate events have exhibited much less change (Groisman et al. 2005).

(ii) Over oceans—P. Xie and J. E. Janowiak

Real-time monitoring of global oceanic precipitation is routinely conducted at NOAA's CPC with the use of the rain gauge–satellite merged "CAMS-OPI" dataset (Janowiak and Xie 1999). By combining gauge observations of precipitation collected and archived by CPC via the CAMS (Ropelewski et al. 1985) with the satellite-based OPI (Xie and Arkin 1998), the CAMS-OPI provides monthly precipitation estimates over global land and ocean on a real-time basis. As shown in Fig. 2.11 (middle panel), several large-scale anomalies (departures from normal) were observed over the global oceans, which are discussed below.

The mean precipitation amount over the global oceans during 2007 (Fig. 2.11, top panel) was 2.890 mm day^{-1}, which is equivalent to a freshwater influx of 1040.3 Kg m^{-2}. This was an increase over 2006, when the global mean was 2.812 mm day^{-1} and the equivalent freshwater influx was 1,026.4 Kg m^{-2}. Maximum annual precipitation rates of over 9 mm day^{-1} are observed during the year over the tropical western Pacific where the ITCZ merges with the SPCZ near the equator and 150°E, and over the tropical eastern Indian Ocean. Meanwhile, relatively light precipitation was recorded, as expected, over the oceanic dry zones in the southeast Pacific, northeast Pacific off the coast of the southwestern United States, southeast Atlantic, tropical North Atlantic near western Africa, and the southeastern Indian Ocean.

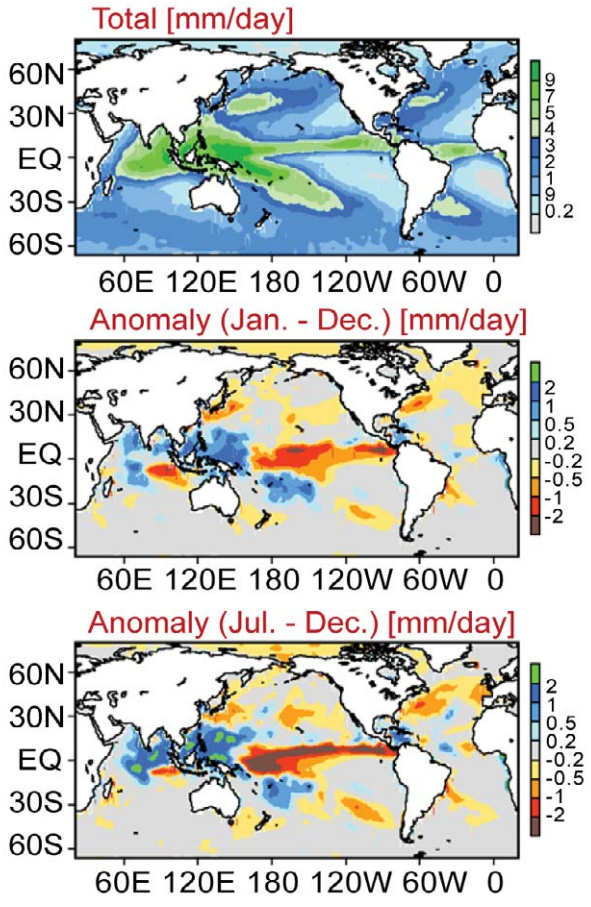

Fig. 2.11. (top) Annual mean total precipitation (mm day^{-1}), (middle) annual mean precipitation anomaly (mm day^{-1}), and (bottom) Jul–Dec precipitation anomaly (mm day^{-1}) for 2007 as observed by the gauge-satellite merged dataset of CAMS-OPI (Janowiak and Xie 1999). Precipitation anomalies were calculated using 1979–95 as the base period.

Over the tropical Pacific, the 2006/07 El Niño ended abruptly in February 2007. Negative SST anomalies expanded from the equatorial eastern Pacific and developed into a moderate-to-strong La Niña during the second half of the year (Climate Prediction Center 2007). Associated with the evolution of this La Niña event, the precipitation anomaly for 2007 exhibited a canonical horseshoe-shaped distribution pattern (Ropelewski and Halpert 1989; Xie and Arkin 1997), with depressed precipitation over the equatorial eastern and central Pacific surrounded by enhanced precipitation over the western Pacific and central South Pacific (Fig. 2.11, middle and bottom panels).

Over the Indian Ocean, the precipitation distribution during 2007 was characterized by a large positive precipitation anomaly over the northern portion of the ocean. This strong precipitation anomaly is associated with the intensified Asian monsoon circulation observed during summer 2007, as indicated by the South Asian monsoon index of Goswami et al. (1999). Hurricane activity over the Atlantic Ocean was close to normal during 2007, with a total of 17 tropical storms and 5 hurricanes recorded. Two category 5 hurricanes (Dean and Felix) passed through the Caribbean Sea, contributing to the above normal precipitation anomaly over the region during the second half of the year. Precipitation deficits were observed over the northwestern Atlantic Ocean off the North America continent.

Strong precipitation variations at intraseasonal time scales were recorded over the eastern Indian Ocean and western Pacific during November and December 2007 (Fig. 2.12). A positive precipitation anomaly of larger than 5 mm day^{-1} progressed eastward from the central equatorial Indian Ocean to the date line. These intraseasonal variations were associated with MJO (Madden and Julian 1971) activity, which in 2007 exhibited the strongest intensity in the past 4–5 yr (Climate Prediction Center 2008).

2) Northern Hemisphere continental snow cover extent—D. A. Robinson

Annual SCE over Northern Hemisphere lands averaged 24.0 million km^2 in 2007, a decrease of 0.9 million km^2 compared with the 2006 annual mean. This is 1.5 million km^2 less than the 38-yr average and ranks 2007 as having the third least extensive cover of record (Table 2.2). This evaluation considers snow over the continents, including the Greenland ice sheet. The SCE in 2007 ranged from 45.3 million km^2 in January to 2.0 million km^2 in August. Monthly snow extent values are calculated at the Rutgers Global Snow Lab[1] from weekly SCE maps produced by NOAA meteorologists, who rely primarily on daily visible satellite imagery to construct the maps (Robinson and Frei 2000).

Hemispheric SCE was below the long-term mean in every month except December. Departures were as large as –3.0 million km^2 in May, followed closely by June (–2.6) and April (–2.5). In conjunction with the lower than average extents in most of 2006, the 12-month running means of Northern Hemisphere extent were below the long-term average throughout

[1] Maps depicting daily, weekly, and monthly conditions, daily and monthly anomalies, and climatologies for the entire period of record may be viewed at the Rutgers Global Snow Lab Web site (http://climate.rutgers.edu/snowcover).

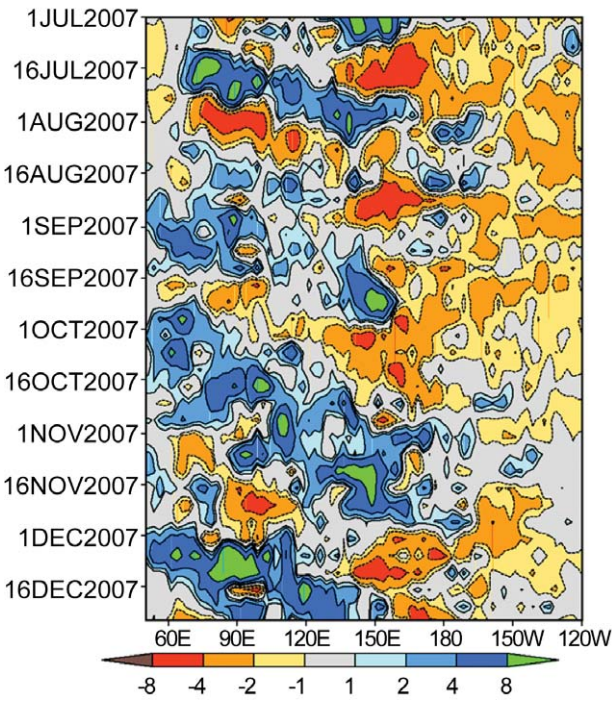

Fig. 2.12. Time–longitude section of precipitation anomaly averaged over the tropical Pacific (5°S–5°N) as observed by the GPCP pentad precipitation dataset (Xie et al. 2003). Precipitation anomaly is calculated using 1979–95 as the base period.

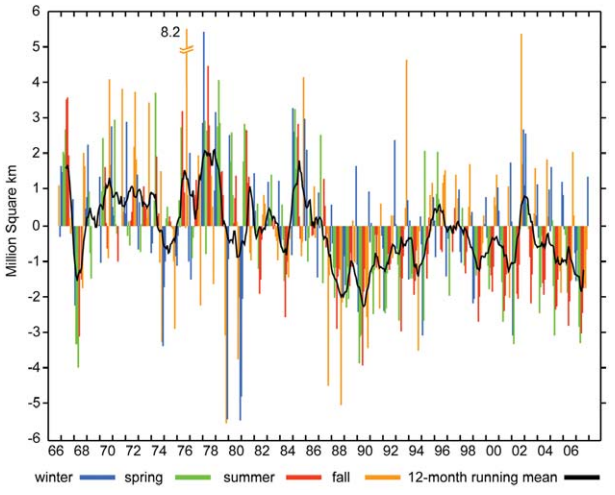

Fig. 2.13. Anomalies of monthly snow cover extent over Northern Hemisphere lands (including Greenland) between Nov 1966 and Dec 2007. Also shown are 12-month running anomalies of hemispheric snow extent, plotted on the seventh month of a given interval. Anomalies are calculated from NOAA snow maps. Mean hemispheric snow extent is 25.5 million km^2 for the full period of record. Monthly means for the period of record are used for nine missing months between 1968 and 1971 to create a continuous series of running means. Missing months fall between Jun and Oct, and no winter months are missing.

the year (Fig. 2.13). In fact, the negative 12-month anomaly at years end had not been reached since the record lows of the satellite era were observed during 1988–90. Eurasian SCE was well below the long-term average in 2007 and ranked as the second least extensive cover of the satellite era. North American SCE was similar, ranking the eighth least extensive.

The 2007 SCE exhibited some variability on temporal and spatial scales. Eurasian SCE was at near record lows until the fall, when extents came close to the long-term average. North American SCE was above average in January and February, but fell below average in March, a tendency that persisted through November. December cover over North America was the third most extensive, the major factor contributing to the ninth most extensive ranking over Northern Hemisphere land areas. Spring and summer snow cover continues to be less extensive in the second half of the satellite record than in the first half, with 2007 spring SCE the third lowest on record (Fig. 2.14).

Over the contiguous United States, SCE was above average in January and February and well below average the remainder of the year, with the exception of December, which was third most extensive. Alaskan snow cover ran well below average from April through September, and was relatively close to average from October through December.

3) Global cloudiness—A. T. Evan, Y. Liu, and B. Maddux

(i) Introduction

Global patterns of cloudiness in 2007 were largely dominated by modest fluctuations in ENSO, which consisted of a positive anomaly during the beginning of the year that was followed by the development of a negative one in the boreal fall. While high cloud cover anomalies associated with even weak ENSO events can be upward of 20% across the tropical Pacific, none of the observed cloudiness anomalies associated with the ENSO events of 2007 represented a statistically significant departure from the mean state (here, a statistically significant departure from average is estimated as an anomaly that is more than two standard deviations from the climatological mean). With that being said, the Arctic and the Amazon basin and its environs both exhibited strong deviations in total cloud cover over 2007 (see Figs. 2.15–2.17), which may have resulted from changes in atmospheric moisture and surface temperatures (for the case of the Arctic) and land use change (for the case of the Amazon).

Table 2.2. Monthly and annual climatological information on Northern Hemisphere and continental snow extent between Nov 1966 and Dec 2007. Included 2007 values and rankings. Areas are in millions km^2. Years 1968, 1969, and 1971 have one, five, and three missing months, respectively, and thus are not included in the annual (Ann) calculations; North America (N. Am.) includes Greenland. Ranks are from most extensive (1) to least (ranges from 38 to 42 depending on the month).

	Years	Mean	Std dev	2007	2007 Northern Hemisphere rank	Eurasia rank	N. Am. rank
Jan	41	46.9	1.5	45.3	38	40	14
Feb	41	45.9	1.8	45.2	28	33	12
Mar	41	41.0	1.8	39.6	33	31	29
Apr	41	31.3	1.7	28.8	39	40	27
May	41	20.4	1.9	17.4	40	38	37
Jun	40	10.9	2.1	8.3	38	39	29
Jul	38	4.8	1.5	2.8	38	36	37
Aug	39	3.5	1.0	2.0	39	38	39
Sep	39	5.6	1.0	4.1	37	37	34
Oct	40	18.3	2.6	16.4	33	33	26
Nov	42	34.1	2.0	33.4	29	27	29
Dec	42	43.5	1.8	44.6	9	25	3
Ann	38	25.5	1.0	24.0	36	37	31

(ii) Data description

To investigate the global pattern of cloudiness in 2007, we use the long-term cloud climatology from the AVHRR from the Pathfinder Atmospheres Extended (PATMOS-x) project (PATMOS-x data acquired from http://cimms.ssec.wisc.edu/clavr/patmosx.html). Cloud cover extent is defined as the percentage of 4-km pixels that are cloudy within each 55-km grid cell. Cloud is detected within each pixel through the use of spatial and spectral tests. PATMOS-x results are available twice daily from each operational NOAA satellite from 1981 to 2007.

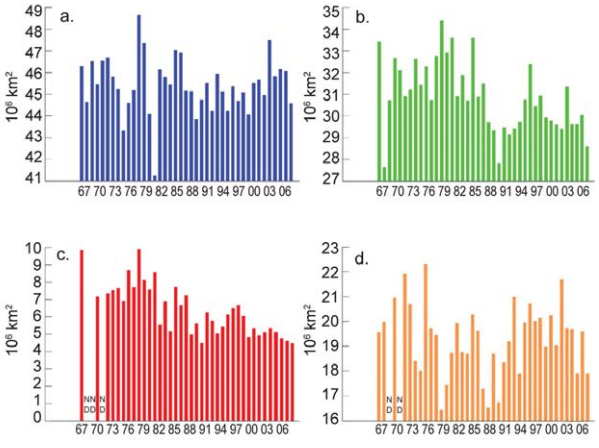

Fig. 2.14. Extent of (a) winter (DJF), (b) spring (MAM), (c) summer (JJA), and (d) autumn (SON) seasonal snow cover over Northern Hemisphere lands (including Greenland) from the winter of 1966–67 through the autumn of 2007.

(iii) Amazon basin and environs

There was a strong negative anomaly in cloud cover over northern Bolivia, parts of Paraguay, and much of Brazil (Fig. 2.15). This anomaly was largely confined to regions surrounding the dense tropical forests of the Amazon basin, along the so-called arc of deforestation, and the agricultural lands farther to the south and east. For the most part the decreases in cloudiness that were statistically significant were on the order of 5% to 10%. According to data from the *Terra* MODIS instrument, aerosol cover in 2007 over this same region was the highest on record (Evan 2008), and is an indication of fire activity in these same areas (Koren et al. 2007). Heavy smoke cover has an adverse effect on cumulus cloud development directly via warming, and therefore stabilization, of

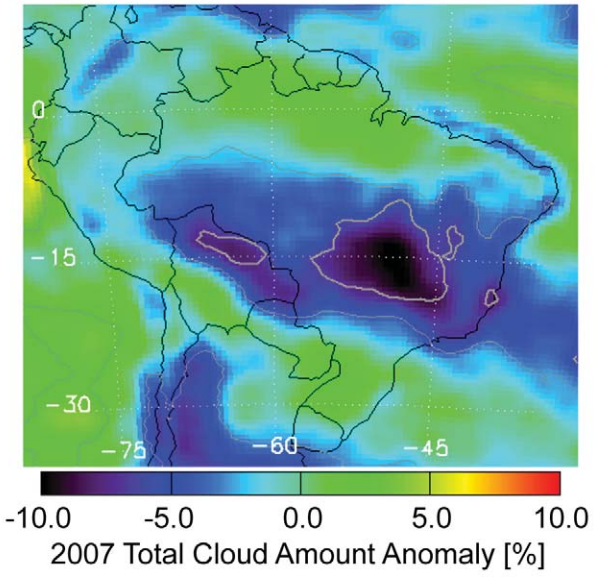

Fig. 2.15. Total cloud cover anomaly for 2007 over Brazil. The thin gray contour represents anomalies that are one standard deviation from the climatological mean value, and the thick gray contour represents anomalies that are two standard deviations from the mean state.

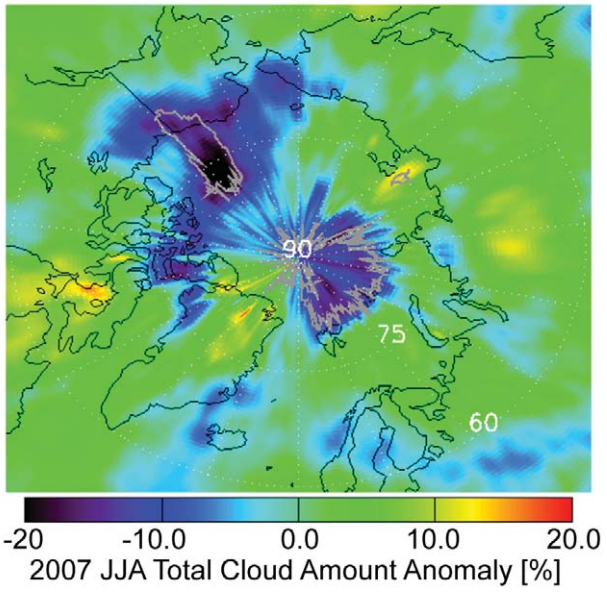

Fig. 2.16. Total Arctic summer cloud cover anomaly 2007. Cloud cover anomaly for the months of Jun, Jul, and Aug over the northern polar regions. The thick gray contour represents anomalies that are two standard deviations from the mean state.

the boundary layer, and indirectly via reductions in surface heating and evapotranspiration (Koren et al. 2004). The same pattern and intensity of the total cloud cover anomaly is not repeated for high cloud cover, but this is not surprising since most deep convection occurs in the more central regions of the Amazon basin.

(iv) Arctic

Figure 2.16 is a map of the Arctic summer total cloud cover anomaly. There were widespread negative anomalies in cloudiness that extended north from Alaska, and around much of the pole, representing deficits in cloudiness of 10% to 20%. According to data from the NCEP–NCAR reanalysis (data acquired from www.cdc.noaa.gov/) (Kalnay et al. 1996), during the boreal summer months there existed a strong high pressure anomaly over much of the western Arctic (sea level pressure and 500-hPa geopotential heights; not shown). It is likely that this high pressure directly contributed to the reduction of cloudiness over the same time period. There has been a long-term upward trend in Arctic cloud cover during the spring and summer that is thought to be associated with surface warming in the same region (Wang and Key 2003). It is possible that discontinuation of this general cloud cover trend in 2007 is also linked to summertime surface temperatures in this same region (Wang and Key 2003), as data from the NCEP reanalysis do not show a strong positive anomaly for temperatures at the surface in 2007 (not shown here).

Although this high pressure anomaly did persist into the fall, the summertime cloud cover deficit gave way to a strongly positive cloudiness anomaly that was much more spatially expansive, particularly in the eastern Arctic (Fig. 2.17). Here, the region of above average cloudiness extended northward from much of Siberia, and the Bering Strait, and for the most part consisted of increases in cloudiness that are upward of 30%. There has been a modest downward trend in Arctic cloud cover during autumn (Wang and Key 2003), which may be linked to decreases in moisture convergence for the same region (Liu et al. 2007). At the same time, according to NCEP reanalysis data, in 2007 an anomalously low sea level pressure over the eastern Arctic and resulting northward flow penetrated the Arctic from North America and the North Pacific (850-hPa vector winds). Surface temperatures in the region of the positive cloud anomalies were also above average. Therefore, it is likely that the northerly flow, possibly combined with a warmer surface, strongly encouraged cloud development here.

However, there may also be a linkage between the positive cloud anomaly and the negative sea ice extent anomaly over the eastern Arctic Ocean.

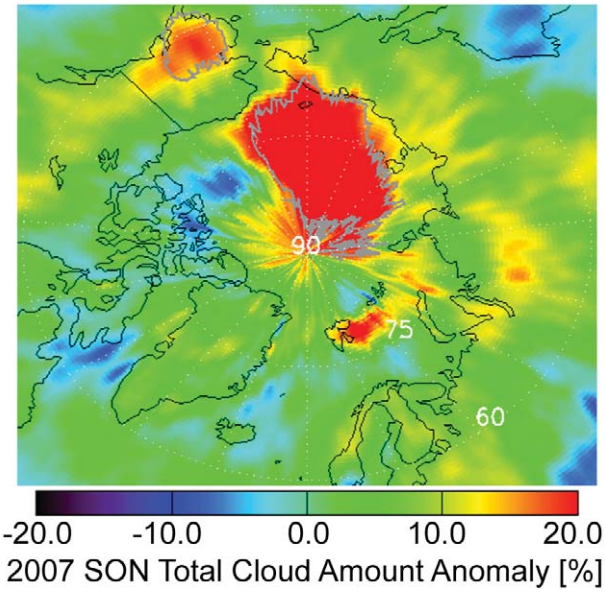

Fig. 2.17. Total Arctic autumn cloud cover anomaly in 2007. Cloud cover anomaly for the months of Sep, Oct, and Nov over the northern polar regions. The thick gray contour represents anomalies that are two standard deviations from the mean state.

Data from the CloudSat cloud profiling radar and the CALIPSO instruments show that during 2007, low clouds had somewhat lower base heights, but midlevel cloud amount increased. The increase in the midlevel cloud might in part be a result of an increase in the vertical extent of the low-level clouds associated with the less stable atmosphere of the open water region.

Since cloud detection with the AVHRR over ice is difficult, it is possible that the anomalies in cloudiness here are artifacts of the cloud detection methodology that are initiated by changes in sea ice. Therefore, the above analysis was also repeated with the MODIS cloud climatology (data acquired from http://daac.gsfc.nasa.gov) (Platnick et al. 2003), since this 36-channel imager is better suited for cloud detection over ice. Analysis of these data showed very similar results, suggesting that the anomalies are robust.

d. Trace gases and aerosols

1) Carbon dioxide—R. C. Schnell

CO_2 emitted from fossil fuel burning is partitioned into three mobile reservoirs: the atmosphere, oceans, and terrestrial biosphere. One result of fossil fuel combustion has been that atmospheric CO_2 has increased from about 280 ppm (ppm = parts in 10^6 by dry-air mole fraction) at the start of the industrial revolution to more than 380 ppm today.[2] Since high-accuracy measurements began more than 50 yr ago, ~57% of the emitted CO_2 has remained in the atmosphere and the remainder has gone into two "sinks," oceans and land biosphere (which include plants and soil carbon).

Currently, more than 8 Pg (Pg = 10^{15}g) of carbon is emitted to the atmosphere by fossil fuel combustion each year (Marland et al. 2007). Global emissions have increased since 2000, surpassing even the most pessimistic of the IPCC emission scenarios used to test climate models. During the 1990s, net uptake by the oceans was estimated as 1.7 ± 0.5 Pg yr^{-1} and by the land biosphere as 1.4 ± 0.7 Pg yr^{-1} (Prentice et al. 2001). The gross fluxes between atmosphere and oceans, and atmosphere and terrestrial biosphere (photosynthesis and respiration), are approximately 100 Pg yr^{-1}. Interannual variations in the atmospheric increase of CO_2 (see Fig. 2.18a, based on Conway et al. 1994) are due to small changes in these net fluxes, and not due to variations in fossil fuel emissions. Most attempts to explain the interannual variability of the atmospheric CO_2 increase have focused on short-term climate fluctuations (e.g., ENSO and post-Pinatubo cooling), but the mechanisms, especially the role of the terrestrial biosphere, are not well understood. To date, about 5% of conventional fossil fuels have been combusted. If combustion were stopped today, after a few hundred years, 15% of the total carbon emitted would remain in the atmosphere, and the remainder would be in the oceans (Maier-Reimer and Hasselmann 1987).

The preliminary globally averaged atmospheric CO_2 mole fraction in 2007 was 382.7 ppm, which was ~1.8 ppm greater than the 2006 global annual mean (380.9 ppm). While an average annual increase of 1.6 ppm yr^{-1} has occurred since 1980, the average rate of increase since 2000 has been 1.9 ppm yr^{-1}. This suggests that the fraction of CO_2 emitted from sources that remain in the atmosphere may be increasing.

Because of the policy implications surrounding the fate of fossil fuel CO_2, NOAA/ESRL launched

[2] Note that fossil fuels are primarily responsible for the observed increase in CO_2 over the past half century. In the nineteenth century, land use change emissions dominated, but since ~1940 cumulative CO_2 emissions from fossil fuel burning overtook cumulative emissions from land use change (Marland et al. 2007). Approximately 87% of fossil fuel emissions have occurred since 1940, and currently the terrestrial biosphere is a small net sink.

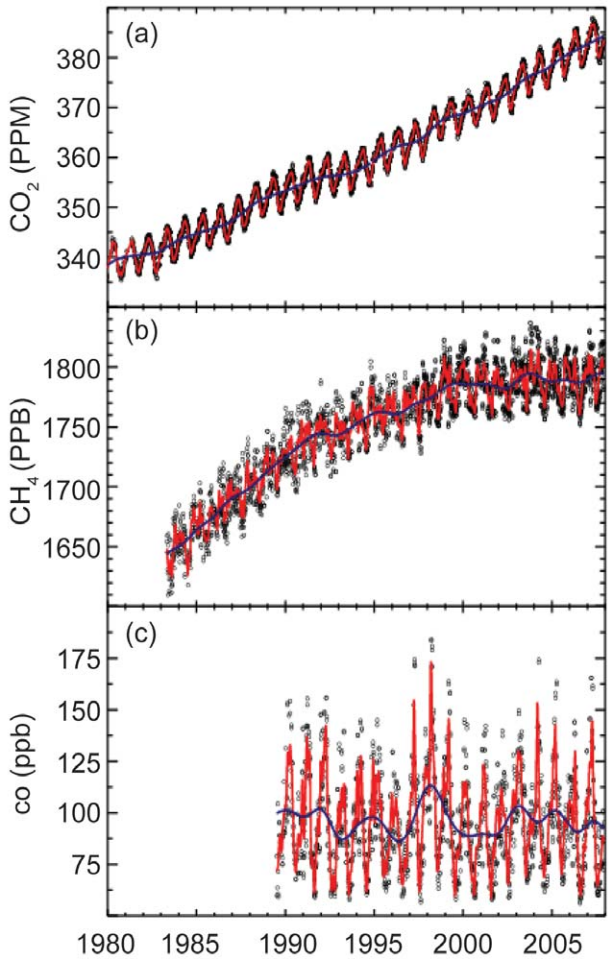

Fig. 2.18. Trace gas mole fractions (black symbols) determined from weekly discrete samples collected at the NOAA/ESRL Mauna Loa Observatory for (a) CO_2 (courtesy: T. J. Conway, NOAA), (b) CH_4 (courtesy: E. J. Dlugokencky, NOAA), and (c) CO (courtesy: P. C. Novelli, NOAA). In all panels, the solid blue line is the deseasonalized trend and the red line is a smooth curve fitted to the black symbols. (Current CO_2 trends at MLO are available online at www.esrl.noaa.gov/gmd/ccgg/trends/. Additional plots can be found online at www.esrl.noaa.gov/gmd/ccgg/iadv/ and www.esrl.noaa.gov/gmd/Photo_Gallery/GMD_Figures/ccgg_figures/.)

"Carbon Tracker," a new tool that uses observations and a state-of-the-art model to keep track of time-dependent emissions and uptake of atmospheric CO_2, from both natural and anthropogenic processes. For the period January 2001 to December 2006, Carbon Tracker (available online at http://carbontracker.noaa.gov) estimated that uptake of carbon by North American ecosystems averaged –0.65 Pg C yr^{-1}, varying between –0.4 and –1.00 Pg C yr^{-1} (Peters et al. 2007); this can be compared to the total North American fossil fuel emissions of 1.9 Pg C yr^{-1}.

2) Methane—R. C. Schnell and E. Dlugokencky

Methane's contribution to anthropogenic radiative forcing, including direct and indirect effects, is about 0.7 W m^{-2}, about half that of CO_2. Changes in the burden of methane also feed back into atmospheric chemistry, affecting the concentrations of OH and O_3. The increase in methane since the preindustrial era is responsible for approximately one-half the estimated increase in background tropospheric O_3 during that time. Changes in OH concentration affect the lifetimes of other greenhouse gases such as the replacement refrigerants (HFCs, HCFCs).

High-precision measurements of atmospheric methane provide climate modelers with current and past rates of CH_4 increase, and they are also useful in constraining the global CH_4 budget, and how it is changing with time. This "top-down" approach can determine total global emissions to within ±10%, but background atmospheric observations alone can not effectively quantify emissions from individual sources. A recent surprise in the global CH_4 budget was the report that vegetation can be a significant source of atmospheric CH_4, even under aerobic conditions (Keppler et al. 2006), but the original emission estimates are likely overestimated. (The inability to identify this source sooner shows the limitations of the observations, particularly in the tropics, for quantifying weakly emitting, diffuse sources.)

In Fig. 2.18b, CH_4 mole fractions from the NOAA observatory at Mauna Loa, Hawaii, are plotted as a function of time. During more than 20 yr of measurements, CH_4 has increased by nearly 10%, but the rate of increase has slowed in recent years. A large increase in 1998 and a smaller one in 2003 were likely the result of climatic conditions that resulted in increased emissions from biomass burning and natural wetlands. Otherwise, atmospheric CH_4 has remained nearly constant since the late 1990s (Dlugokencky et al. 2003). Possible causes for the recent lack of growth in atmospheric CH_4 burden are decreased emissions from natural wetlands because of widespread drought in the tropics (Bousquet et al. 2006) and a change in the CH_4 sink because of increased lightning (Fiore et al. 2006), but the exact causes are still unclear. The preliminary 2007 global annual CH_4 average of 1782.2 ppb is 7 ppb greater than the concentration observed in 2006. The reasons for the increase in 2007 are not yet known, but analysis of CO measurements suggests it is not from biomass burning.

3) Carbon monoxide—R. C. Schnell

Unlike CO_2 and CH_4, carbon monoxide does not strongly absorb terrestrial IR radiation, but it still im-

pacts climate through its chemistry. The chemistry of CO affects OH (which influences the lifetimes of CH_4 and HFCs) and tropospheric O_3 (itself a greenhouse gas), so emissions of CO can be considered equivalent to emissions of CH_4 (Prather 1996). Current emissions of CO may contribute more to radiative forcing over decadal time scales than emissions of anthropogenic N_2O (Daniel and Solomon 1998).

Carbon monoxide mole fractions from Mauna Loa (symbols) are plotted as a function of time in Fig. 2.18c and show little trend over the period of these measurements (Novelli et al. 2003). Superimposed on the flat trend are significant increases during 1997 to 1998, and again in 2002 to 2003, which were likely the result of tropical (Langenfelds et al. 2002) and boreal biomass burning (Kasischke et al. 2000). Since the lifetime of CO is relatively short (few months), the anomaly quickly disappeared and CO returned to pre-1997 levels shortly afterward. In 2007, CO levels are comparable to those found in the early 2000s.

The preliminary globally averaged CO mole fraction in 2007 was 84.0 ppb, 2 ppb greater than the 2006 global annual mean, and 11 ppb lower than 1998, which had a large contribution from CO that was emitted by biomass burning.

4) Halocarbons—R. C. Schnell and S. A. Montzka
Decreases in ozone-depleting gases and their replacements

Long-lived halocarbons affect the radiative balance of the atmosphere because they efficiently absorb terrestrial IR radiation (see section 2d5). Long-lived halocarbons containing bromine and chlorine also influence the radiative atmospheric balance indirectly through their destruction of stratospheric ozone.

Because of concern over stratospheric ozone depletion, production of many halocarbons has become restricted over the past two decades. The phase out of human-produced halocarbons internationally was brought about through amendments and adjustments to the 1987 Montreal Protocol on Substances that Deplete the Ozone Layer. As a result of these efforts, mixing ratios of most of the potent ozone-depleting gases have been declining at the Earth's surface in recent years. These declines continued in 2007 as shown in Fig. 2.19. Of the main ozone-depleting substances measured in the global NOAA/ESRL sampling network and not considered to be replacement chemicals, only H-1301 was still increasing in the background atmosphere in 2007.

The NOAA/ESRL data show that mixing ratios of some halogenated gases continue to increase globally (Fig. 2.19). The most rapid increases are observed for HCFCs and HFCs, which are chemicals commonly used as replacements for chlorofluorocarbons (CFCs), halons, and other ozone-depleting gases. Although HCFCs contain chlorine and deplete ozone with a reduced efficiency compared to CFCs, HFCs do not participate in ozone-destroying reactions.

Increases in HCFCs have continued so that by mid-2007 chlorine accounted for by the three most abundant HCFCs amounted to 237 ppt, or 8.8% of all chlorine carried by long-lived halocarbons of anthropogenic Chlorine (not including Cl from CH_3Cl). Mixing ratios of HFC-134a, the most abundant HFC in the global background atmosphere, increased nonlinearly in the 1990s during the period of early production and use. From 2004 through 2007, however, it increased in the global troposphere at a fairly constant linear rate of 4.5 (±0.3) ppt yr^{-1}. Concern over increases in HFCs stems in large part because these gases are efficient absorbers of infrared radiation.

The influence of these disparate trends on future levels of stratospheric ozone can be gauged roughly from a sum of Cl and Br in long-lived halocarbons provided the enhanced efficiency for Br to destroy ozone is considered (note that this efficiency factor has been updated here to 60 based upon a reanalysis appearing in the latest WMO Scientific Assessment of Ozone Depletion (Clerbaux and Cunnold et al. 2007). This sum is expressed here as EECl (Fig. 2.19) and is derived from surface-based measurements. EECl provides an estimate of the ozone-depleting power of trace gases a few years in the future, when air at Earth's surface will have become mixed into the midlatitude stratosphere where the ozone layer resides. A second metric, ECl, provides an estimate of the ozone-depleting power of trace gases in the near future for the stratosphere over the polar regions (not shown).

The observations indicate that through 2007 the ECl and EECl content of the lower atmosphere declined fairly steadily since the peak in 1994 at a mean rate of 25 to 28 ppt yr^{-1}. Scenarios projecting future halocarbon mixing ratios have been derived elsewhere based upon full compliance with the fully amended and revised Montreal Protocol and our understanding of atmospheric lifetimes of these gases (Clerbaux and Cunnold et al. 2007). These analyses suggest that it will take 40 to 60 yr for EECl and ECl to decline to the levels present in 1980, which is before ozone depletion was first observed. This 1980 level is notable, given that one might expect nearly full recovery of stratospheric ozone once atmospheric EECl or ECl returns back to this level. The time scale for ozone recovery will depend upon other factors as well, however, such

as stratospheric temperatures and atmospheric aerosol loading. Nonetheless, the declines in EECl from 1994 to the present time represent a significant drop in the atmospheric EECl burden; as of 2007 EECl had declined 26% of the way back down to the 1980 level (lower panel of Fig. 2.19).

Progress toward EECl returning to the abundance in 1980 can be readily assessed with the NOAA ODGI (see www.cmdl.noaa.gov/odgi/). This index is derived from EECl and ECl data for the midlatitude and Antarctic stratosphere. The index is scaled so that a value of 100 represents the EECl or ECl abundance at its peak, and 0 represents the 1980 level (the level at which no ozone depletion is expected assuming constancy in all other variables). In 2007 the ODGI-Midlatitudes was 73.4, indicating that the abundance of ozone-depleting substances have decreased over 26% of the way toward the levels that were present in 1980 (Fig. 2.19). Less progress is evident for Antarctica where the ODGI-Antarctica was 86.0 in 2007. This suggests halocarbon abundances have declined slightly more than 14% of the way toward 1980 levels.

Changes in the direct radiative influence of long-lived halocarbons can be estimated from observed changes in atmospheric mixing ratios with knowledge of trace gas radiative efficiencies. Such an analysis suggests that the direct radiative forcing of these gases was still increasing in 2007, though at a much slower rate than observed from 1970 to 1990 (see below).

5) Nitrous oxide and sulfur hexafluoride—J. W. Elkins and G. S. Dutton

Nitrous oxide and SF_6 absorb infrared radiation in the atmospheric window (8 to 14 μm) and contribute to the radiation budget of the Earth's surface. NOAA/ESRL scientists have been measuring their mixing ratios on the same channel of electron-capture gas chromatographs using both in situ and flask sampling since 1977 for N_2O and since 1995 for SF_6. On a per molecule basis, N_2O

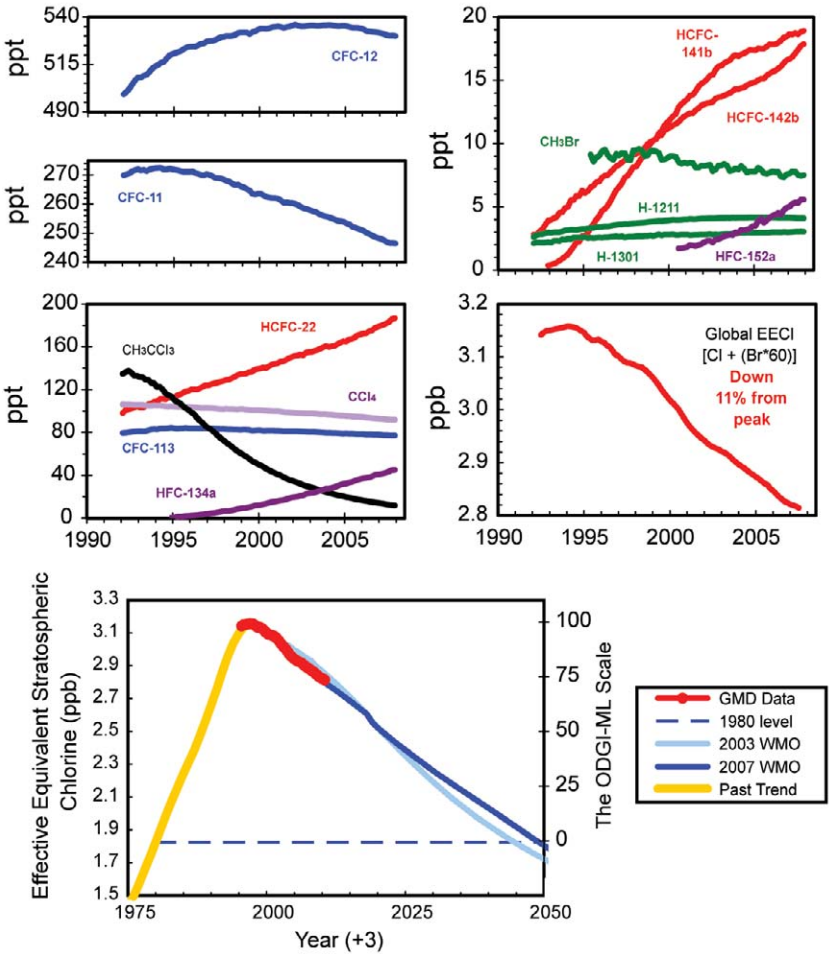

Fig. 2.19. Changes in global mean tropospheric mixing ratios (in ppt or pmol mol^{-1}) of the most abundant CFCs, HCFCs, HFCs, chlorinated solvents, and brominated gases. These global changes are estimated from atmospheric measurements made at remote sites in both the Northern and Southern Hemispheres (from the NOAA/ESRL Cooperative Air Sampling Network). The middle right-hand panel shows secular changes in atmospheric equivalent chlorine (EECl; in ppb or nmol mol^{-1}), which is an estimate of the ozone-depleting power of atmospheric halocarbons. EECl is derived from observed mixing ratios of ozone-depleting gases appearing in the other four panels, and it is derived from the sum of [Cl + (Br×60)] contained in these gases. The bottom panel shows the recent changes in EESC observed by the NOAA/ESRL global network relative to the secular changes observed in the past, including the level observed in 1980 when the ozone hole was first observed, and a projected future. The Ozone Depleting Gas Index for midlatitudes is derived (right-hand axis) from rescaling EESC. EESC is derived from EECl by simply adding 3 yr to the time axis to represent the lag associated with mixing air from the troposphere to the middle stratosphere, where the ozone layer resides. [Source: Montzka et al. (1996, 1999).]

is about 298 times and SF_6 is about 22,800 times more effective than carbon dioxide as a greenhouse gas (Forster et al. 2007, p. 212). The global mean mixing ratios at the end of 2007 for N_2O was 321.4 ppb while SF_6 was 6.29 ppt (Fig. 2.20). The atmospheric concentrations of these potent infrared absorbers, N_2O and SF_6, are approximately 1,000 and 60 million times less than atmospheric CO_2 (382.7 ppm), respectively. But since the beginning of the industrial revolution, increases in the burden of atmospheric N_2O have added 0.16 ± 0.02 W m^{-2}, and increases in SF_6 have added 0.0029 W m^{-2} to the Earth's surface radiation budget (Forster et al. 2007, p. 141). Atmospheric N_2O also is involved in stratospheric O_3 depletion, because it is a major source of stratospheric NO that forms nitrogen dioxide quickly, which in turn destroys O_3 in a catalytic cycle.

Like CO_2, N_2O and SF_6 have been growing at a relatively linear rate of 0.778 ± 0.003 ppb yr^{-1} since 1977 and 0.218 ± 0.001 ppt yr^{-1} since 1995 as shown in Fig. 2.20 (top panel). Sulfur hexafluoride is the sixth fastest growing greenhouse gas in percentage of all Montreal and Kyoto Protocol gases since 1998. Examining the instantaneous growth rates, there exist variations of greater than ±25% throughout their respective periods for both gases shown at the bottom of Fig. 2.20. The growth rate of SF_6 increased to a high of 0.28 ppt yr^{-1} in mid-2007, however, more data are required to determine if this increased growth will be sustained in the subsequent year. The growth rate of N_2O exhibits considerable inter-annual changes that may result from transport or changes in the magnitudes of emissions. The budget of atmospheric N_2O is about 30% out of balance because of major anthropogenic sources from the application of nitrogen fertilizers on crops, by products of chemical manufacturing processes, and catalytic reduction of oxides of nitrogen generated from fossil fuel emissions. Emissions of N_2O are expected to increase as the world population grows. The gas, SF_6, is primarily used as a gaseous dielectric for high-voltage power applications and is emitted where power grids and populations are located. Its emissions are largely due to leakage from power applications, and there is no available substitute compound with similar dielectric properties that is more climate-friendly than SF_6.

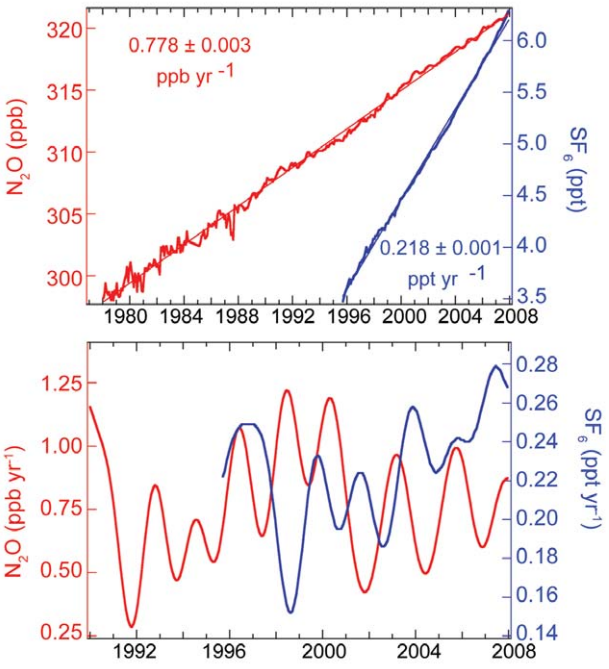

Fig. 2.20. (top) Atmospheric concentrations for global monthly means vs time for N_2O (in ppb, red) and SF_6 (in ppt, blue) with linear regressions as thin lines displayed for the NOAA/ESRL baseline observatories located at Pt. Barrow, AK; Niwot Ridge, CO; Mauna Loa Observatory, HI; American Samoa; and South Pole. Concentrations for N_2O are determined from flask samples during 1977–87 and in situ GCs from 1987 to the present. Atmospheric SF_6 concentrations are measured from flask samples during 1996–98 and in situ GCs from 2000 to the present. (bottom) Instantaneous growth rates for the same datasets since 1990.

6) The combined influence of long-lived trace gases on the radiative balance of the atmosphere

Changes in the abundance of long-lived trace gases have a direct and indirect influence on the energy balance of the atmosphere. The direct radiative influence of a trace gas is directly proportional to its atmospheric abundance and how efficiently it absorbs infrared radiation in specific regions of the electromagnetic radiation spectrum (its radiative forcing). High-precision measurements of CO_2, CH_4, N_2O, CFC-12, CFC-11 (the major long-lived greenhouse gases), and 10 minor greenhouse gases obtained from the NOAA global air sampling network were used to calculate the overall change in the direct radiative climate forcing arising from the sum of all of these long-lived gases (Hofmann et al. 2006; Fig. 2.21). This forcing is calculated by considering changes in the abundances of these gases since 1750, which are coarsely derived from ice cores prior to the instrumental record. By mid-2006, the increases in the abundances of all these gases above 1750 levels amounted to an additional direct radiative forcing to the atmosphere totaling approximately 2.66 W m^{-2}. Changes in the abundance of CO_2 since 1750 accounted for nearly two-thirds of this enhanced radiative forcing (63%).

The NOAA AGGI is based upon the direct radiative forcing calculated from these NOAA measurements (Hofmann et al. 2006). The index is a ratio of direct radiative forcing from all these gases (based upon changes since 1750) relative to the direct radiative forcing calculated from these gases for 1990, the Kyoto Protocol baseline year; indirect effects are not considered in this index. By 2007, the AGGI was 1.242, indicating that the direct radiative forcing arising from increases in the abundance of these trace gases had increased by 24.2% from 1990 to 2007 (Fig. 2.21). Increases in the atmospheric abundance of CO_2 accounted for ~80% of the observed increase in the AGGI from 1990 to 2007.

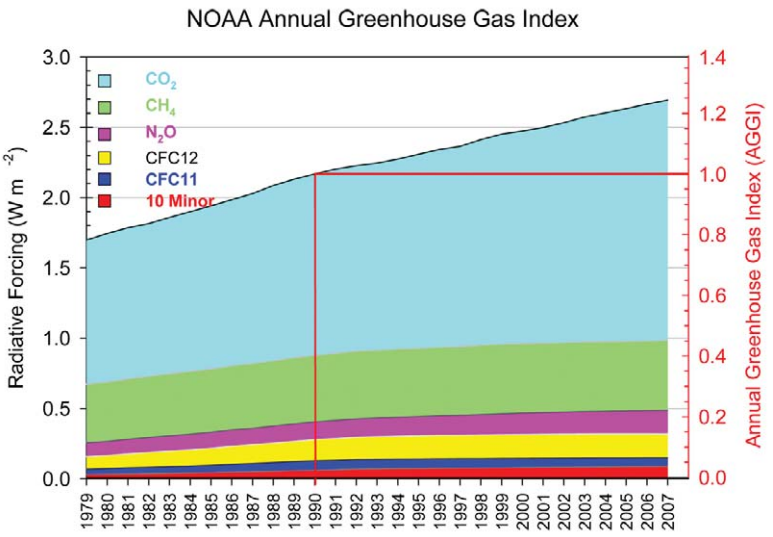

Fig. 2.21. The direct radiative forcing arising from increases in the abundance of long-lived trace gases in the atmosphere since 1750 and the AGGI (Hofmann et al. 2006). The colored bands indicate the radiative forcing from subsets of gases listed in the caption. Also shown is the NOAA AGGI, which is calculated from the total direct radiative forcing normalized to 1.0 in 1990 (red line), the baseline year of the Kyoto Protocol. [Source: D. Hofmann, NOAA/ESRL.]

7) Global aerosols—A. T. Evan

Aerosols in 2007 were generally in line with recent "climatological" norms. Many of the aerosol anomalies related to smoke from biomass burning observed in 2006 (Evan et al. 2007) did not persist. For example, the 2006 elevated aerosol levels seen at the far northern latitudes or around Indonesia were absent this year. In contrast, smoke from biomass burning over the Amazon basin, an indication of regional deforestation, exhibited levels that were inline with the increasing aerosol trend seen from 2000 through 2005, a stark contrast to the much clearer skies noted in 2006 (Koren et al. 2007).

The analysis of aerosols in this year's report focuses on the examination of satellite AOD retrievals from the MODIS onboard the *Terra* satellite at 550 nm[3] (Remer et al. 2005) and the AVHRR at 670 nm (AVHRR date were obtained through the PATMOS-x project Web site: http://cimms.ssec.wisc.edu/clavr/patmosx.html) (Ignatov and Stowe 2002a, 2002b). Although the coverage for these polar orbiting satellites is nearly global, retrievals are only made for cloud-free conditions and are limited to oceanic regions (for the AVHRR) or are not retrieved over bright reflecting land surfaces (for the MODIS). Additionally, the MODIS and AVHRR products do not measure particle composition, although information about the particle's nature can be inferred from the MODIS aerosol size modes (small or coarse). Despite these limitations, the 7-yr MODIS and 26-yr AVHRR records are reliable indicators of change on inter-annual to multidecadal time scales.

Figure 2.22 is a map of the global mean aerosol optical depth from the MODIS *Terra* satellite, where the global mean AOD is 0.15. The spatial distribution of global AOD in 2007 was similar to recent years. High AOD associated with mineral dust over the tropical Atlantic, West Africa, the Middle East, and the north Indian Ocean dominated much of the aerosol loadings. High aerosol loadings were also concentrated along the northern boundary of the Indian subcontinent and eastern China. These aerosols were likely anthropogenic in nature, as evidenced by higher values of the small mode fraction here (a measure of the fractional composition of the aerosol optical depth by small particles, not shown). The Taklimakan Desert is a major dust source region that resides in western China, upwind of Beijing and the Yellow Sea. Therefore, the AOD values there are a mix of anthropogenic and mineral aerosols (Kaufman et al. 2002). Biomass burning in the Amazon basin along the so-called arc of deforestation dominated the aerosol signal in South America.

[3] MODIS data used in this paper were obtained through the Giovanni online data system, developed and maintained by the NASA Goddard Earth Sciences (GES) Data and Information Services Center (DISC).

Figure 2.23 is a 1982 to 2007 time series of global, oceanic, AOD retrievals from the AVHRR. This previously reported downward trend in aerosol loadings (Mishchenko et al. 2007), superimposed over spikes in AOD in 1982 and 1991 associated with the eruptions of El Chichón and Mt. Pinatubo, respectively, is likely a reflection of reduction in Saharan/Sahel dust storm activity. It may also, more importantly, reflect reductions in anthropogenic sulfate aerosols by some industrialized nations over the same time period.

Comparison of aerosol optical depths in 2007 with measurements in 2006 indicates three regions with notable variability: the Amazon basin, Indonesia, and the northern boreal forests of Eurasia. In 2006 aerosol loadings in the Amazon were at their lowest point since at least 2000 (Koren et al. 2007), but in 2007 these measurements were the highest on record, at about 1.5 times the 2006 estimations (Fig. 2.24). It is unclear if these low 2006 AOD levels, and the subsequent high 2007 values, are the result of policy shifts or reflect variability in the local meteorology (Koren et al. 2007). For example, cloudiness has a significant effect on the AOD record and may have played some role in these annual values. In addition when low-level winds are predominately easterly in this region, aerosols from the Amazon basin are not easily advected past the Andes and over the South Pacific. Therefore, the long-term AVHRR oceanic record of aerosols is currently of little help in identifying the interannual to decadal variability in aerosols from this region.

In Indonesia, aerosols associated with biomass burning in 2007 were significantly lower than the previous year. In 2006, there was an increase in biomass burning, associated with drier than average conditions. This was associated in part with an El Niño event that developed late in the year (Evan et al. 2007). In 2007, a moderate La Niña event developed in September, and these conditions contributed to higher precipitation totals across Indonesia and a reduction in biomass burning episodes compared to 2006 (van der Werf et al. 2004). When considering the longer AVHRR aerosol record, which includes several positive and negative ENSO events, there were no statistically significant aerosol anomalies in this region for 2007. Last, aerosols associated with the northern boreal forests of Eurasia returned to mean climatological levels in 2007, for both the MODIS and AVHRR data, following the elevated activity associated with biomass burning that was observed in 2006 (Stohl et al. 2006).

e. *Global winds*—S. R. Smith, R. N. Maue, and M. A. Bourassa

Monthly global wind speed and sea level pressure anomalies (Fig. 2.25) with respect to the long-term mean (1968–96) are constructed from the NCEP–NCAR reanalysis (Kalnay et al. 1996). Overall, the global wind speed and sea level pressure anomalies are weaker in the tropics and stronger in the midlatitude and polar regions. With a few exceptions, larger anomalies occur over the oceans.

1) Ocean winds

Wind anomalies were most pronounced over the Southern Ocean throughout 2007. The wind anomaly pattern associated with the building La Niña pattern was present in the tropical Pacific and a stronger summer Indian monsoon pattern occurred. Elsewhere, the anomaly patterns lacked spatial and temporal consistency from month to month.

(i) Southern Ocean

In a pattern similar to 2006, the atmospheric circulation over the circumpolar Southern Ocean exhibited a series of positive and negative wind speed anomalies for all months, with the possible exception of January and February. A pattern of alternating pressure anomalies in the circumpolar trough (~40° to 60°S) results in stronger pressure gradients, which are associated with the large wind speed anomalies. The wind and pressure patterns are indicators of anomalous

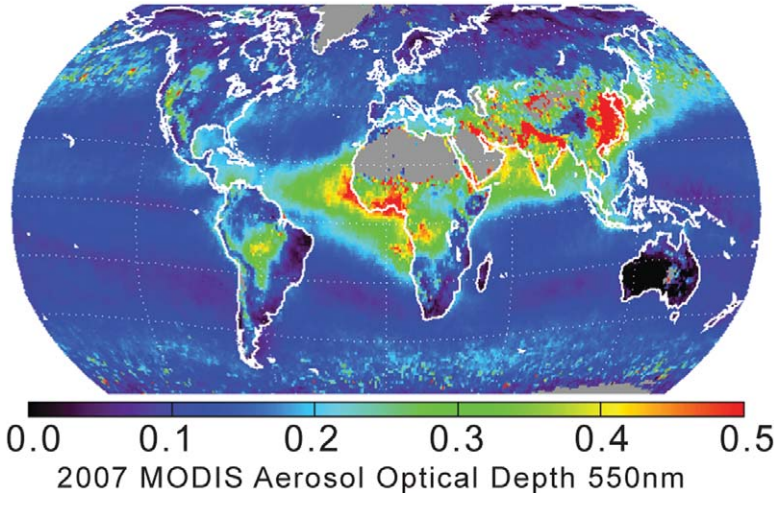

Fig. 2.22. Global map of mean AOD values at 550 nm from the MODIS *Terra* satellite.

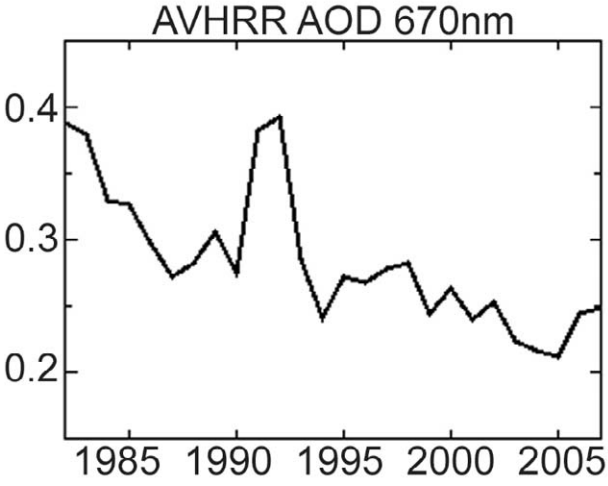

Fig. 2.23. Time series of global oceanic AOD values at 670 nm from the AVHRR.

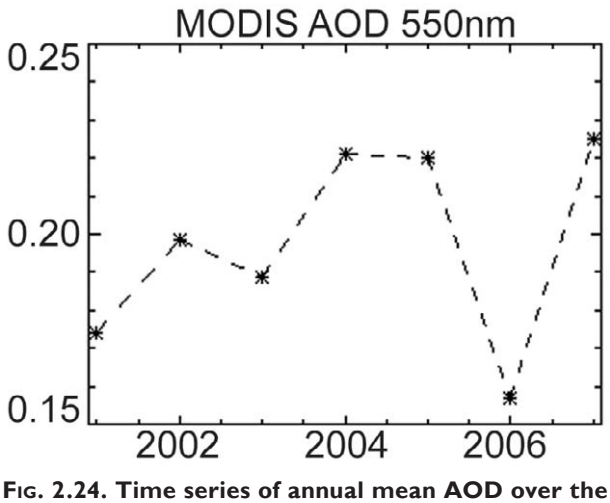

Fig. 2.24. Time series of annual mean AOD over the Amazon basin from MODIS.

storm activity in the Southern Ocean. The patterns do not necessarily indicate more or less storms: they could be related to a shift in the location of the storm tracks. However, the long bands of greater wind speeds in March through August suggest an atypically strong surface manifestation of the polar vortex during the austral winter.

(ii) Tropics

Starting in June, a pattern of stronger winds appeared in the equatorial Pacific Ocean near the date line. This was the onset of the easterly anomalies associated with La Niña. The easterly anomalies became more prominent in August through December, with a drop in strength in October. The location and monthly variation of the NCEP–NCAR anomalies match well with the monthly Florida State University wind analysis based on ship and mooring observations (available in the Climate Diagnostics Bulletin, www.cpc.ncep.noaa.gov/products/CDB/).

2) Continental winds

Winds over the land surface showed very few notable anomalies during 2007. Although many individual months showed anomalies over the land surface (e.g., stronger winds in Central America in November), these anomalies rarely persisted from month to month. The exceptions occurred around the North Atlantic region over Europe and Greenland.

(i) Europe

During January, lower pressure over the Russian Arctic and higher pressure to the southwest resulted in stronger winds over most of northern Europe. A similar pressure pattern existed in March through May, but the impacts on European winds varied from month to month. High pressure anomalies during October and November resulted in weaker winds over northwestern Europe.

(ii) Greenland

Positive wind anomalies persisted over Greenland throughout 2007. The wind anomalies peaked in strength during February and July (with anomalies near 4 m s^{-1}) and were weakest during September and October. With the exception of February, the wind anomalies were not clearly associated with gradients in the sea level pressure anomalies. This may, in part, be due to the sea level pressures not being a representative measure over the high ice plateau of interior Greenland. The reduction of surface pressures to sea level is problematic over very high terrain.

f. Major modes of Northern Hemisphere variability: The Arctic Oscillation and the Pacific–North American pattern—M. L. L'Heureux, J. C. Gottschalck, and M. S. Halpert

The two leading patterns of Northern Hemisphere climate variability are the AO and the PNA pattern. These patterns collectively explain nearly one-third of the month-to-month variations in SLP, and nearly half of the variance in the wintertime mean SLP (Quadrelli and Wallace 2004). The AO, which is the first leading mode, features a "zonally symmetric" pattern featuring anomalous atmospheric pressure in the polar region and opposite-signed anomalies focused over the northern Pacific and Atlantic Oceans (Thompson and Wallace 2000). In contrast, the PNA is the second-leading mode and is consid-

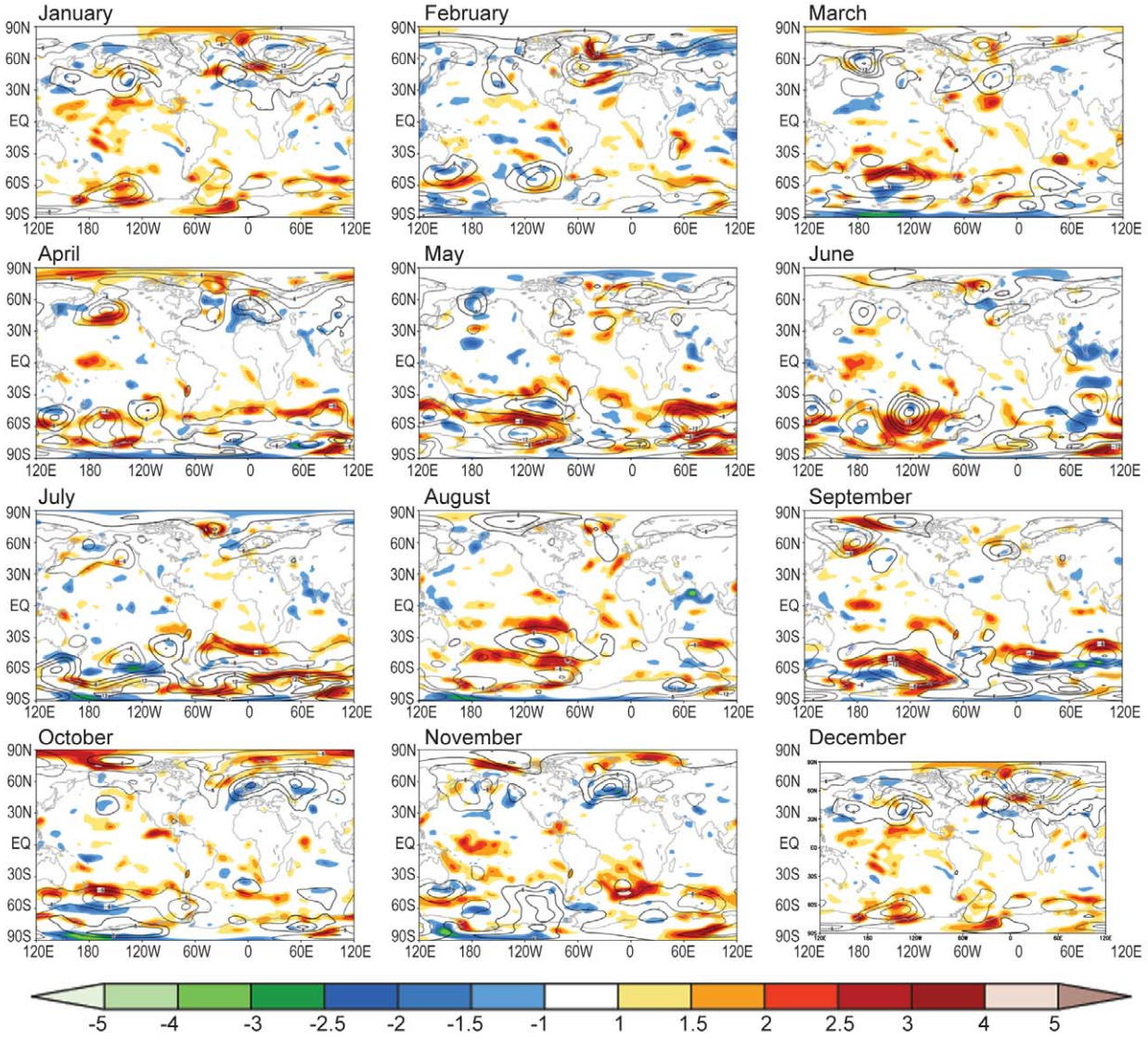

Fig. 2.25. Wind speed (m s^{-1}) and sea level pressure (hPa) anomalies during each month of 2007. Sea level pressure contoured every 3 hPa with negative anomalies dashed.

ered a "zonally asymmetric" pattern with alternating centers of anomalous pressure that arc northeastward through the North Pacific Ocean and then curve southeastward into North America (Wallace and Gutzler 1981).

1) Record PNA pattern during July–September

The positive phase of the wintertime PNA at 500 hPa is typically characterized by a "wave train" of above-average heights in the vicinity of Hawaii and over western Canada, and below-average heights over the North Pacific and southeastern United States The positive polarity of the PNA is often cited to describe the midlatitude response to El Niño, which implies the PNA can be externally forced (e.g., tropical SSTs), but other research has indicated that the PNA pattern is a distinct natural mode of climate variability arising from internal atmospheric dynamics (Simmons et al. 1983; Mo and Livezey 1986; Straus and Shukla 2002).

The PNA is calculated using a rotated empirical orthogonal function procedure and has its strongest amplitude during the winter season. The PNA has a signal throughout the year, with the wave train varying in location and strength depending on the season. In particular, the wave train is weaker and shifts poleward during the summer months JAS (Fig. 2.26a), with weaker centers of action arcing through the Pacific Ocean and stronger centers of action arcing through the western Arctic Circle toward the Hudson

Bay. However, even when considering the muted PNA pattern, the JAS 2007 PNA featured an unusually strong signal in the observed circulation anomalies, and may have helped to modify the Pacific storm track during the period.

During JAS 2007, the positive polarity of the PNA pattern projected very strongly onto the observed 500-hPa height pattern (Fig. 2.26b). Anomalous ridging was observed at lower latitudes in the North Pacific Ocean and more notably just north of Alaska. Weak anomalous troughs were observed just to the west of the Aleutian Islands and near Hudson Bay over northern Canada. Accordingly, the PNA index for JAS 2007 was three standard deviations above the 1950–2007 JAS mean, constituting a 1 in 333 yr chance of occurrence (Fig. 2.26c) and is the largest departure recorded in the historical record.

The observed upper-level circulation over the Pacific was conducive to a stronger jet stream and downstream divergence in the jet exit region, which helped to enhance storminess across a wide swath of the central and eastern North Pacific Ocean. During JAS 2007, at least a 25% increase in those storms was observed across a west–east trajectory in the central North Pacific with a nearly 300% increase observed in the eastern North Pacific.

2) The AO flips sign during the 2006–07 winter

The AO, or the NAM, is the leading mode of variability in the Northern Hemisphere and is characterized by north–south shifts of circumpolar westerly flow in the Northern Hemisphere. The high index polarity is defined by a poleward shift of the westerly midlatitude jet, while the low index polarity occurs when the jet is equatorward of its average position (Thompson and Wallace 1998, 2000). While distinguished by a hemispheric-wide pattern, the AO has its greatest teleconnection in the Atlantic basin, where it is highly correlated with the regional NAO pattern (Thompson et al. 2003). The AO, however, describes more of the hemispheric trends and interannual variability of temperature, with the high index phase associated with less frequent cold air outbreaks into the midlatitudes and more cold air outbreaks for the low index phase (Thompson and Wallace 2001).

The mean 500-hPa circulation pattern during DJF 2006–07 was characterized by a large degree of zonal symmetry that projected strongly onto the AO. The pattern featured the positive phase of the AO from December 2006 to mid-January 2007 and the negative phase from mid-January through the end of February 2007 (Fig. 2.27). Correspondingly, anomalous temperatures also had a hemispheric-wide signal, with anomalies of like sign observed over the midlatitudes in North America and Eurasia during both halves of the winter.

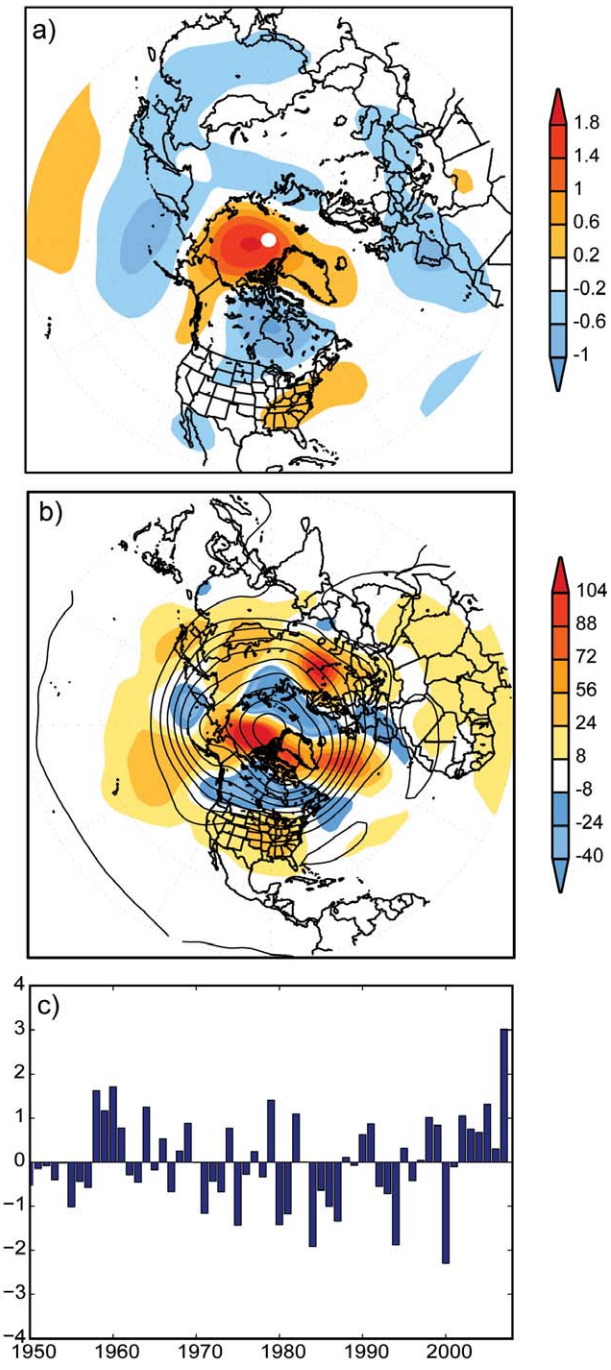

Fig. 2.26. (a) Jul–Sep PNA loading pattern (dimensionless) based on a rotated empirical orthogonal function calculation using 500-hPa geopotential height anomalies. (b) Mean 500-hPa height (contours, contour interval 50 m) and height anomalies (shading, units are in m) for Jul–Sep 2007. (c) Jul–Sep seasonally averaged PNA index values standardized based on all Jul–Sep values from 1950 to 2007.

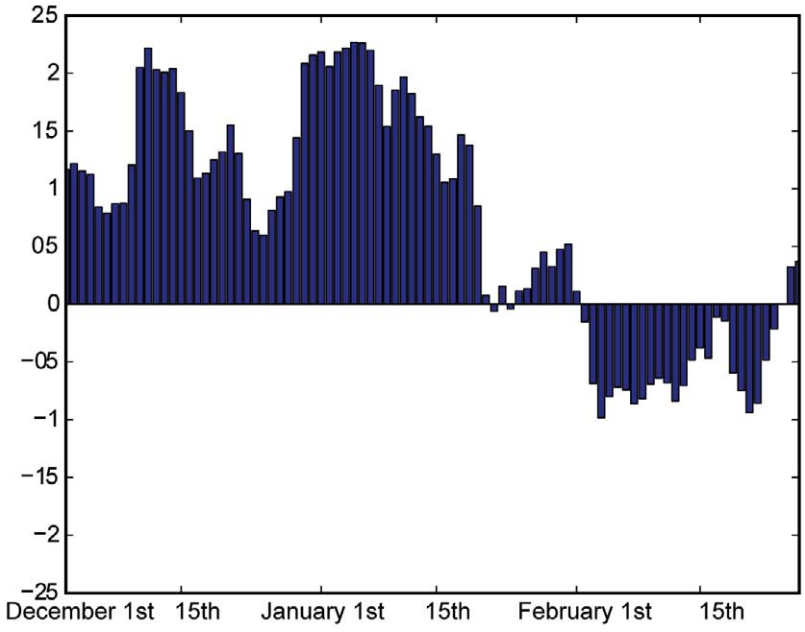

Fig. 2.27. Standardized time series of the AO index for daily values between 1 Dec 2006 and 28 Feb 2007.

Consistent with the positive phase of the AO, the 500-hPa geopotential heights during 1 December 2006–15 January 2007 featured negative anomalies throughout the polar latitudes stretching from Greenland toward Alaska, and positive anomalies throughout the midlatitudes (Fig. 2.28a). During this period, the midlatitude jet streams were displaced poleward and high-latitude blocking was minimal, which limited cold air outbreaks into the middle latitudes. Consequently, this pattern was linked to above-average surface temperatures across much of Eurasia, Canada, and the central and eastern United States (Fig. 2.28b).

In contrast, during the latter half of the winter season (15 January–28 February 2007), the 500-hPa circulation shifted with positive height anomalies prevailing over the Arctic Circle and negative height anomalies over northern Eurasia and from the north-central/eastern United States eastward through the Atlantic Ocean (Fig. 2.28c). This pattern was associated with increased high-latitude blocking, and numerous cold air outbreaks into both North America and the northern half of Eurasia. These conditions were consistent with the negative polarity of the AO and led to an abrupt end to the exceptionally mild winter conditions seen in these regions during December and early January, with below-average temperatures dominating these regions during the second half of the winter (Fig. 2.28d).

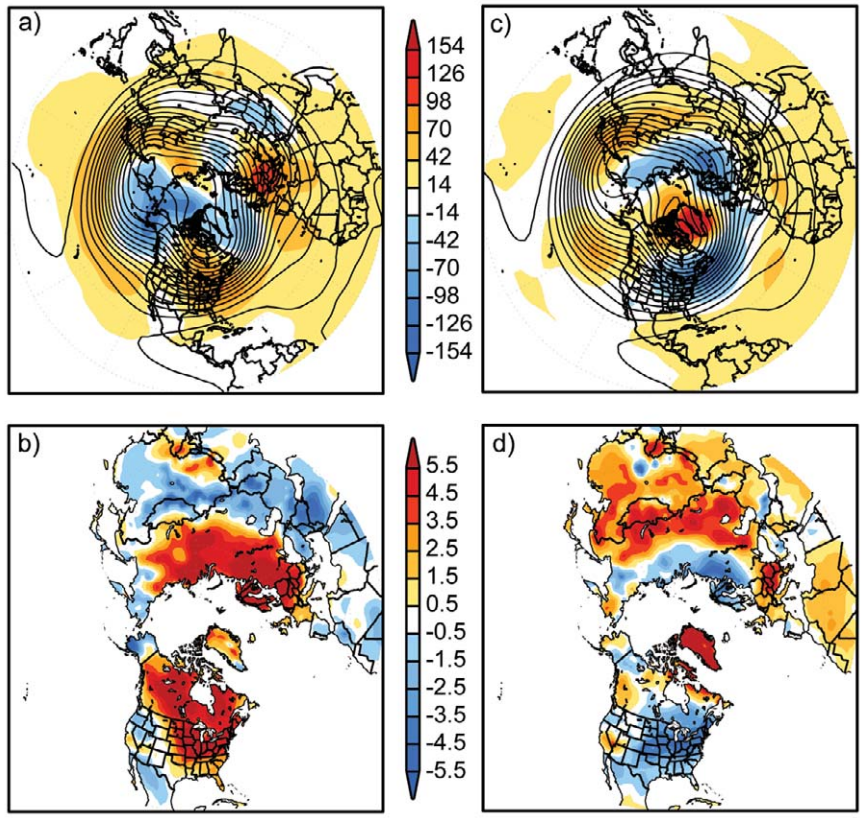

Fig. 2.28. (a) Mean 500-hPa height (contours, contour interval 50 m) and height anomalies (shading, units are in m) for 1 Dec 2006–15 Jan 2007. (b) Surface temperature anomalies based on CDAS (Kalnay et al. 1996) for 1 Dec 2006–15 Jan 2007 (climatology calculated using the first four harmonics during 1979–95). (c) Same as (a) except for 15 Jan–28 Feb 2007. (d) Same as (b) except for 15 Jan–28 Feb 2007.

3. GLOBAL OCEANS—J. M. Levy, Ed.

a. Overview—J. M. Levy

As the global ocean observing system matures and climatologies of essential climate variables grow more robust, observations of anomalous departures continue to shed light on the evolving behavior of the coupled ocean–atmosphere system. The year 2007, while less anomalous than 2006, was characterized by the following key findings:

- Global sea surface temperature during 2007 showed significant departures from the 1971–2000 climatology in four regions: the positive anomaly in the high-latitude North Atlantic that has persisted since 2002 continued into 2007; positive anomalies that have occurred each boreal summer since 2002 in the Arctic Ocean adjacent to the North Pacific reached their highest value of about 2.5°C in 2007; the positive anomaly in the tropical North Atlantic that has been trending downward from its highest value in 2005 returned to near-normal conditions in the summer of 2007; and positive anomalies in the central and eastern equatorial Pacific associated with the 2006 El Niño ended in February 2007, and a moderate-strength La Niña developed in the fall of 2007.
- Annual average upper-ocean heat content anomalies declined between 2006 and 2007 in the eastern equatorial Pacific and increased in off-equatorial bands in that ocean. These changes were consistent with the transition from El Niño in 2006 to La Niña in 2007.
- Ocean heat fluxes demonstrated a coherent pattern of change in the tropical Pacific, in response to the east–west SST pattern of the 2007 La Niña episode. Evaporative heat loss decreased over the cooler SST region in the eastern Pacific and increased over the warmer SST region in the western Pacific. Variations of ocean heat fluxes in the tropical Pacific on ENSO time scales are a dominant interannual signal.
- The tropical cyclone heat potential, a parameter proportional to the upper-ocean heat content that is linked to hurricane intensification, exhibited high variability within each ocean basin. On average, all basins, except the eastern Pacific basin, showed areas of positive values. The west Pacific Ocean had the largest anomaly values of this parameter.
- Global sea surface salinity anomalies in 2007 continued to accentuate climatological patterns; fresh areas of the ocean have generally become fresher and salty areas have generally become saltier in recent years relative to a long-term climatology. These changes suggest a possible increase in the strength of the hydrological cycle.
- Westward surface current anomalies dominated the equatorial Pacific basin, reflecting the La Niña conditions that developed in the second half of 2007. Long-term trends in eddy kinetic energy reveal that major ocean currents such as the Gulf Stream, Kuroshio, Brazil, and Malvinas Currents are shifting in position and/or strength; these decadal-scale changes may reflect longer-term fluctuations or secular trends.
- A new basinwide time series capturing the entire Atlantic meridional overturning circulation at 26.5°N demonstrated that the variability of the MOC is much higher at time scales of weeks to months than had previously been believed. Consistent with observations that Florida Current transport, representing the upper limb of the MOC, was at its climatological mean in 2007, the high degree of observed variability makes it impossible at this time to rule in or out any long-term trend in the MOC.
- The global mean SLA in 2007 was 1.1 mm higher than in 2006, which is about one standard deviation below what would be expected from the 15-yr trend value of 3.4 mm yr^{-1}. However, when combined with the SLA of 6 mm in 2006, the 2-yr increase matches the 15-yr trend. Dominant spatial patterns of sea level variability during 2007 included the strengthening La Niña in the tropical Pacific Ocean, and zonal anomalies in the tropical Indian Ocean, particularly south of the equator.
- A revised global surface pCO_2 climatology, assembled from over 3 million measurements spanning 36 yr, suggests a 30% larger inter-annual variability in ocean CO_2 uptake than that inferred from the previous climatology, which incorporated far fewer observations.
- Chlorophyll concentrations during 2007 were close to the mean value derived from 10 yr of climate-quality ocean color measurements, but exhibited significant climate-related deviations from the mean that were largely due to global changes in phytoplankton physiology rather than phytoplankton biomass.

b. Temperature

1) Sea Surface Temperatures in 2007—R. W. Reynolds and Y. Xue

SSTs have been derived as monthly fields interpolated from the weekly 1° OI analyses of Reynolds et al. (2002) and as daily fields from the daily 1/4° OI

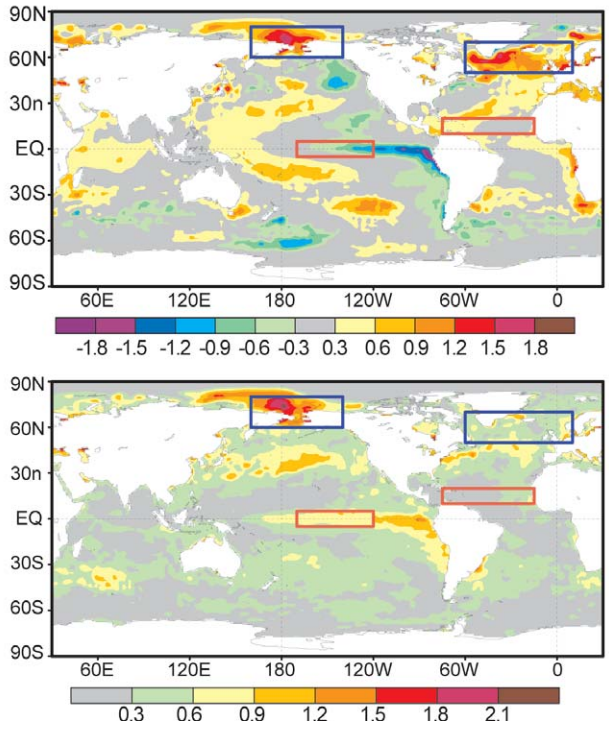

Fig. 3.1. Mean and standard deviation of monthly SST anomalies for 2007 on a 1° spatial grid. The anomalies are computed relative to a 1971–2000 base period. Boxes indicate time-series regions discussed in Fig. 3.2.

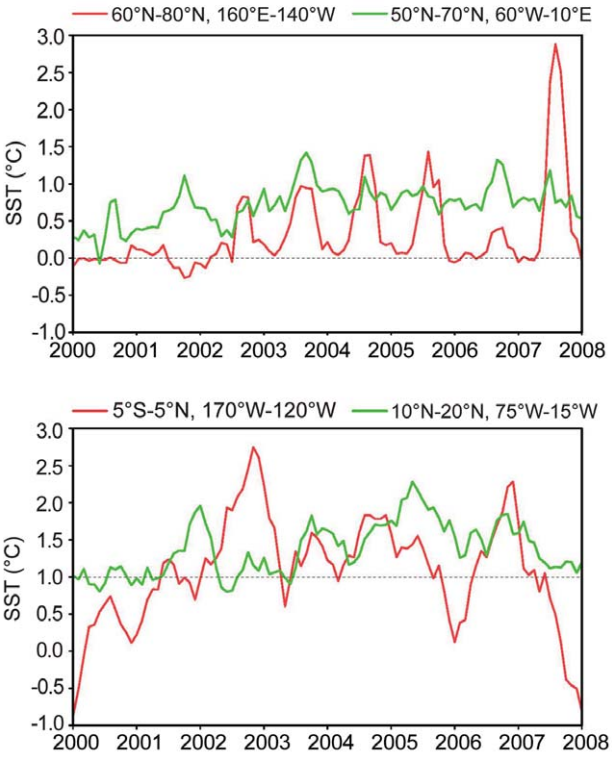

Fig. 3.2. Time series of monthly SST anomalies (top) for two northern high-latitude regions (blue boxes in Fig. 3.1) and (bottom) for two tropical regions (red boxes in Fig. 3.1).

analyses of Reynolds of et al. (2007). Both analyses use ship and buoy in situ SST data as well as satellite SST retrievals. The weekly OI analysis uses satellite retrievals from the IR AVHRR; the daily OI analysis uses satellite retrievals from AVHRR and microwave retrievals from the AMSR. All anomalies are defined as departures from the 1971–2000 climatology described by Xue et al. (2003). Although either analysis is adequate to describe large-scale changes in SST, the daily analysis becomes more useful, on smaller time and space scales.

To illustrate the overall changes in 2007, the yearly average and standard deviation of the monthly anomalies derived from the weekly analysis are shown in Fig. 3.1. As expected, the anomalies are primarily positive due to an overall global warming relative to the climatological base period. There are four important features that are indicated by boxes and shown as time series in Fig. 3.2 for 2000–07. The first feature is due to the strong positive boreal summer anomalies in the North Pacific/Arctic near the Bering Strait. The positive anomalies are mostly due to summer warming that occurred each year beginning in 2002. The summer warming weakened substantially in 2006, but was enhanced in 2007, consistent with the record low summer sea ice coverage. Figure 3.2 shows strong boreal summer anomaly peaks of 1°–1.5°C in 2003–05 and a record maximum above 2.5°C in 2007. The second feature is the strong positive anomaly in the high-latitude North Atlantic, which has persisted since 2001. The strongest Atlantic peak occurred in the summer of 2003 and was associated with high European summer temperatures at that time. The third feature is the tropical North Atlantic positive anomaly that has persisted since mid-2003, although it weakened substantially in 2007. This region is important for summer and fall hurricane formation. Finally, the fourth feature is the El Niño, which peaked in December 2006, terminated dramatically in February, and transitioned into a moderate-strength La Niña by the fall of 2007. The Niño-3.4 region in Fig. 3.2 shows positive anomalies during the second half of 2006 from the El Niño. The positive anomalies transitioned into normal conditions during February 2007. Weak La Niña conditions (Niño-3.4 index < –0.5°C) did not occur until August and continued to strengthen from August through December 2007 into a moderate-to-strong La Niña (see, also, Figs. 3.15 and 3.20). This change is also indicated in the mean

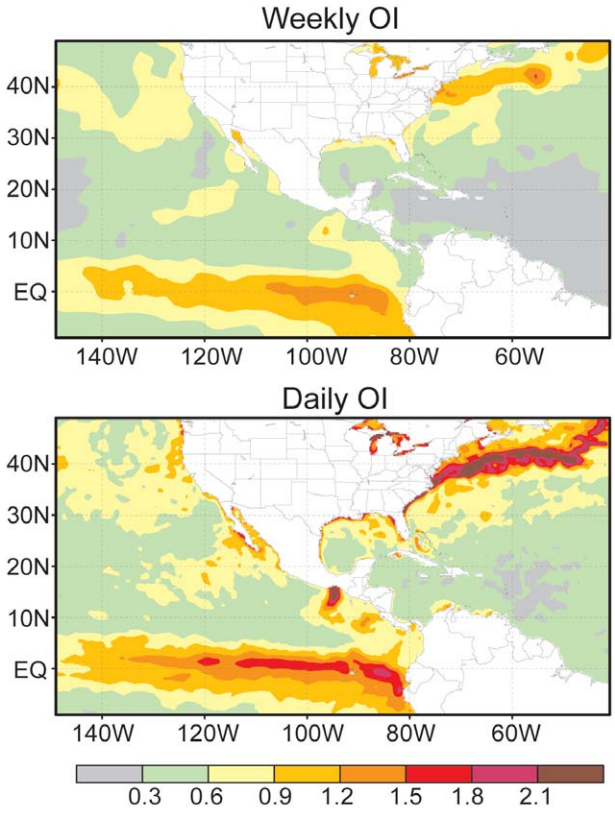

Fig. 3.3. Standard deviation of (top) weekly and (bottom) daily SST anomalies for 2007 on a 1/4° spatial grid. The anomalies are computed relative to a 1971–2000 base period.

by the overall negative anomaly in Fig. 3.1 along the equator in the Pacific and the anomaly standard deviation near 1°C between 120° and 80°W. In addition to these features it is important to point out that a negative Pacific decadal oscillation pattern developed in August 2007 and has persisted into early 2008 (for updated information see http://jisao.washington.edu/pdo/PDO.latest).

Although the large-scale differences between the weekly and daily OI are small, the variability in the daily OI is much larger. This difference can be seen in Fig. 3.3, which shows the daily standard deviation for 2007 for the two analyses. Here the weekly analysis is linearly interpolated in time and space to the day and to the daily analysis grid. The daily OI shows greater variability in the eastern Pacific along the equator and in the Gulf Stream. Compared to the weekly OI, the variability in the Gulf Stream doubles in the daily OI and increases more moderately along the equator in the Pacific. In addition, the daily OI shows greater variability along the coasts and in the Great Lakes. Note in particular, the region of variability in the daily OI off the west coast of Mexico near 15°N. Time series of upwelling off the Oregon coast and in the Niño-1+2 region (10°S–0°, 80°–90°W) show more variability in the daily OI as expected.

To examine one coastal region in more detail, daily and weekly OI time series are shown in Fig. 3.4 off the coast of South Carolina (32°–34°N, 81°–79°W) for 2006 to 2007. This region is chosen to sample the gradients between the Gulf Stream and the coast. These gradients are strongest in the winter when coastal waters are much cooler than the Gulf Stream. The results show that the weekly OI can be up to 5°C warmer than the daily OI during February 2007. The weekly OI has average spatial error correlation scales of 700 km while the daily OI has scales of 100 km. Thus, the difference occurs because the weekly OI is not able to resolve the coastal SST gradients.

2) Ocean Heat Content—G. C. Johnson, J. M. Lyman, and J. K. Willis

Storage and transport of heat in the ocean are central to such aspects of climate as El Niño (e.g., Zebiak 1989), the North Atlantic Oscillation (e.g., Curry and McCartney 2001), hurricane seasons (e.g., Emanuel 2005), and global warming (e.g., Levitus et al. 2005; Hansen et al. 2005).

Here we discuss an estimate of upper (0–750 m) OHCA for the period 1 January–31 December 2007 (Fig. 3.5) analyzed following Willis et al. (2004), but relative to a 1993–2007 baseline. We also discuss changes in OHCA between 2007 and 2006 (Fig. 3.6). In situ ocean temperature data and real-time satellite altimetry are combined using the techniques of Willis et al. (2004) to produce these real-time estimates. In

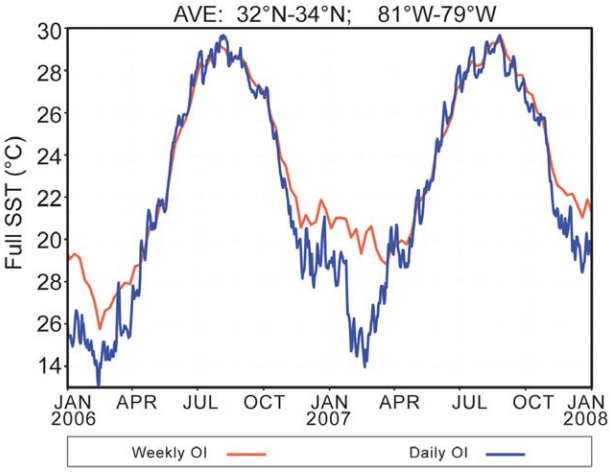

Fig. 3.4. Time series of daily SSTs for the weekly and daily OI analyses for a region just offshore of South Carolina for 1 Jan 2006 through 1 Jan 2008.

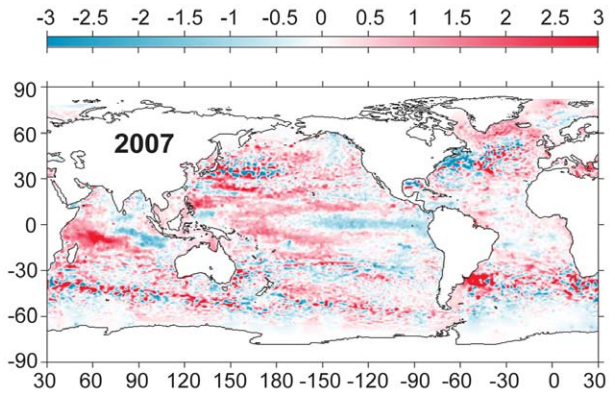

FIG. 3.5. Combined satellite altimeter and in situ ocean temperature data upper (0–750 m) OHCA (10^9 J m^{-2}) map for 2007 analyzed following Willis et al. (2004), but relative to a 1993–2007 baseline.

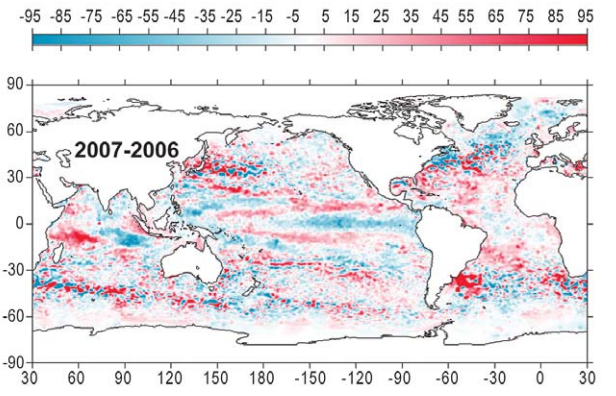

FIG. 3.6. The difference of 2007 and 2006 combined OHCA maps expressed as a local surface heat flux equivalent (W m^{-2}). For purposes of direct comparison with Fig. 3.5, note that 95 W m^{-2} applied over one year would result in 3×10^9 J m^{-2} of OHCA.

recent years many of the globally distributed in situ data are from Argo (Roemmich et al. 2004). Data from Argo floats with a recently detected systematic bias in reported pressure values that were not corrected prior to this analysis have been removed from the estimates discussed here. In addition, annual estimates of XBT fall rate corrections have been applied for deep and shallow probe data (e.g., Wijffels et al. 2008). Details of the fields analyzed here may change after data with corrected pressures from the few remaining floats with outstanding pressure-reporting issues are corrected and made available, after more real-time data are subject to delayed-mode scientific quality control, and as XBT fall rate corrections improve.

The 2007 combined OHCA map (Fig. 3.5) shows eddy and meander variability down to the 100-km mapping scales, as does, to a greater extent, the difference of the 2007 and 2006 combined OHCA maps (Fig. 3.6). There is a great deal of small-scale spatial variability in OHCA fields associated with the western boundary currents in every gyre, as well as the Antarctic Circumpolar Current. The difference in combined OHCA maps between 2007 and 2006 (Fig. 3.6) illustrates the large year-to-year variability in ocean heat storage, with changes reaching or exceeding the equivalent of a 95 W m^{-2} magnitude surface flux applied over one year (~3×10^9 J m^{-2}). Ocean advection likely plays a significant role in many of these changes. While one would not expect OHCA (Fig. 3.5) and SST (Fig. 3.1) anomalies to be tightly coupled, there are some large-scale visual similarities between the two fields in 2007, even relative to their differing baseline periods.

Large-scale patterns are also evident in OHCA for 2007 (Fig. 3.5) and its difference from 2006 (Fig. 3.6). Along the equatorial Pacific, where there was a band of high heat content in 2006 (Arguez et al. 2007), heat content is below the mean in 2007 east of 180°. In addition to the cooling along the equator in the Pacific (Fig. 3.6), there are bands of cooling along 15°N from the western Pacific to about 180° and reaching from 150°E on the equator to around 90°W and 30°S. The result is that OHCA in these off-equatorial regions, while still above mean values, is much diminished with respect to 2006 values (Arguez et al. 2007). While the annual averaging period presented here is too long for detailed study of the movement of heat associated with the transition from El Niño in 2006 to La Niña in 2007, certainly the change on the equator and perhaps those in the off-equatorial regions as well may be related to those processes (e.g., Zebiak 1989).

The North Atlantic largely warmed south of 40°N and cooled north of 40°N between 2006 and 2007 (Fig. 3.6), suggesting either a southward shift in the subtropical–subpolar gyre boundary or intensification of the North Atlantic Current in 2007 relative to the previous year. This intensification arises because subpolar cooling and subtropical warming increase the dynamic height difference between the gyres, hence strengthening the North Atlantic Current (Curry and McCartney 2001). Despite this subpolar cooling in 2007 relative to 2006, much of the North Atlantic subpolar gyre remains warm in 2007 relative to the baseline period (Fig. 3.5). Although weaker than in 2006, this pattern in 2007 is still consistent with a lower than normal strength of the North Atlantic Current and is probably related to decadal changes in the North Atlantic Oscillation index, including atmospheric forcing of ocean circulation

(Curry and McCartney 2001). This climate index has oscillated during the baseline period, including a relatively high wintertime value in DJFM 2007, but has generally trended toward lower values from 1993 through 2007.

In addition, in 2007 a large and strong cool patch coalesces north of 40°N and west of 55°W in the North Atlantic, as does a warm patch east of the cool one (Fig. 3.5). In the South Atlantic, a warm patch of similar geographical extent centered near 35°S, 50°W develops. Large-scale shifts in the locations or strengths of western boundary current extensions in these basins seem the most likely explanations of these patterns.

In the Indian Ocean the largest changes are centered near 10°S, with cooling in the eastern half of the basin along this parallel, and warming in the western half (Fig. 3.6). These changes cause a warm patch centered near this latitude to shift westward in 2007 (Fig. 3.5) from its position in 2006 (Arguez et al. 2007).

In 2007 (Fig. 3.5), as in 2006 (Arguez et al. 2007), OHCA remains high in the Southern Oceans, in a belt located north of the Antarctic Circumpolar Current. In 2007, from west to east, this high band in OHCA is evident near 40°S south of Africa, trending southward to 55°S south of Tasmania. Similarly, from west to east in the Pacific this ridge in OHCA starts near 40°S east of New Zealand and shifts slowly southward to about 55°S near Drake Passage. Finally, in the Atlantic, there is a region of high OCHA across the basin around 35°S. This change has recently been studied on decadal time scales in the South Pacific (Roemmich et al. 2007) and appears to be related to changes in the wind stress field associated with an increase in the Antarctic Oscillation index. This index reached a peak in 1999, fell into a shallow valley in 2002, and has been near neutral since. It is difficult to discern much large-scale trend in OHCA between 2006 and 2007 in this region (Fig. 3.6), with smaller spatial-scale changes of varying sign predominating in the subpolar regions of the Southern Hemisphere.

3) Global ocean heat fluxes—L. Yu and R. A. Weller

Solar radiation, being the only significant external heat source for Earth, is the primary factor that affects the Earth's climate. Most of the solar energy absorbed by Earth is taken up in the top ocean layer, and the ability of the oceans to store, release, and redistribute the heat ensures that the oceans play a key role in moderating the Earth's climate.

Not all absorbed heat is stored and transported by the oceans; much of the heat is released back to the atmosphere by two heat exchange processes at the air–sea interface: evaporation that releases latent heat and conduction and convection that release sensible heat. These air–sea heat exchanges cool the ocean but warm the air, supplying the heat energy needed to drive the atmospheric circulation and global weather patterns. Clearly, air–sea heat fluxes (i.e., the amount of air–sea heat exchange) are a key measure of the role that the ocean plays in global climate, and their changes on short- and long-term time scales may have important climate implications.

The global LHF+SHF in 2007 and the differences from the year 2006 are shown in Fig. 3.7. The flux estimates were produced by the OAFlux project (Yu and Weller 2007) at WHOI.

The OAFlux products used the state-of-the-art bulk flux algorithm version 3.0 developed from the COARE (Fairall et al. 2003), with input surface meteorological variables from an optimal blending of satellite retrievals (e.g., SSMI, QuikSCAT, AVHRR, TMI, and AMSR-E) and the outputs of surface me-

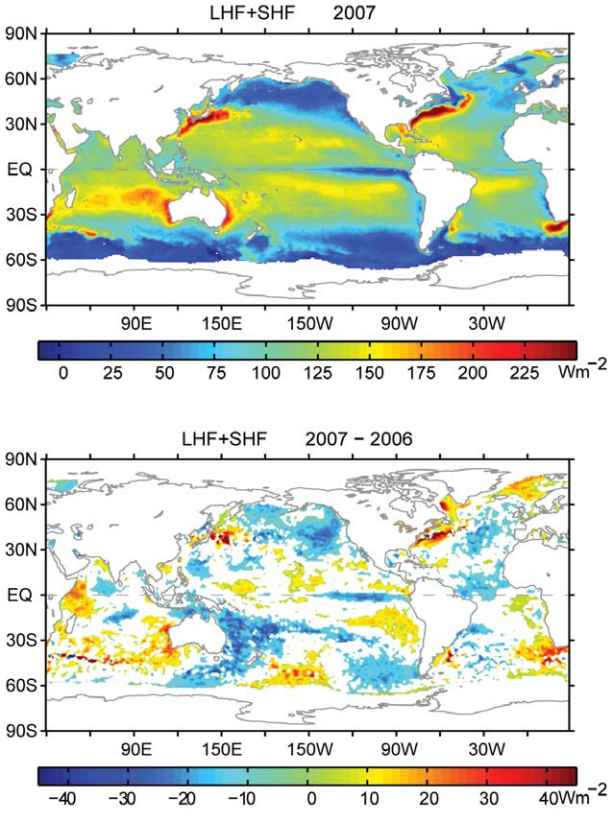

Fig. 3.7. (top) Annual mean latent plus sensible heat fluxes in 2007 (in W m^{-2}). (bottom) Differences between the 2007 and 2006 annual mean latent plus sensible heat fluxes (in W m^{-2}). The sign is defined as upward (downward) positive (negative). The differences significant at the 90% confidence level are plotted.

teorology from reanalysis/forecast models of NCEP and ECMWF (Yu et al. 2008).

The global distribution of latent and sensible heat fluxes is controlled by air–sea temperature/humidity gradients and near-surface atmospheric circulation. On an annual basis, the largest ocean heat losses occur over the regions that are associated with major WBCs and their extensions, the most noted of which are the Kuroshio off Japan, the Gulf Stream off the United States, and the Agulhas Current off the African coast. The magnitude of the annual mean LHF+SHF in these regions exceeds 250 W m^{-2}, produced largely during the fall-to-winter seasons by strong winds and cold and dry air masses coming from the lands. The second largest heat loss (~180 W m^{-2}) is located over the broad subtropical southern Indian Ocean, where the large air–sea heat exchange is sustained primarily by the strong southeast trade winds in the monsoon months June–September.

The LHF+SHF mean difference between 2007 and 2006 shows large-scale, coherent changes over the global basins, with the magnitude of the change within ±50 W m^{-2}. The major change in the tropical oceans is the reduction in LHF+SHF in the central and eastern equatorial Pacific and a slight increase in the western Pacific. This broad east–west contrast is a reflection of the 2007 equatorial Pacific SST structure associated with the La Niña episode of the ENSO cycle. During La Niña, the trade winds in the Pacific Ocean are stronger than normal, driving warm surface waters toward the western Pacific. Meanwhile, the stronger trade winds enhance upwelling of cold deep water near Peru that produces colder than normal SSTs in the eastern basin. As sea surface evaporates more (less) readily over warmer (colder) water, the result is a decrease of latent heat over the colder SST region in the east and an increase of latent heat over the warmer SST region in the west. Variations of ocean heat fluxes in the tropical Pacific on ENSO time scales are a dominant interannual signal in the OAFlux multidecade time series (e.g., Yu and Weller 2007).

The tropical Indian Ocean experienced a short-lived IOD mode event in September–November 2007, which is very unusual during the Pacific La Niña phase. The IOD is characterized by cold SST anomalies off the south Java coast and warm SST anomalies in the western equatorial basin, similar to the La Niña SST pattern in the Pacific. Like the tropical Pacific, the changes in LHF+SHF in the tropical Indian Ocean reflected primarily the changes in SST, and the large increase in LHF+SHF in the western equatorial Indian Ocean is the most notable feature. For the tropical North Atlantic Ocean, the 2007 LHF+SHF was reduced considerably compared to 2006, which was consistent with the regional cooling of SSTs in the two years. The cooling was associated with a persistent high pressure pattern over the Atlantic Ocean, which brought strong northeasterly winds into the tropics that cooled the SSTs through increased upwelling and evaporation. In summary, the close relationship between SST and LHF+SHF in the tropical oceans suggests a response of the atmosphere to the oceanic forcing.

Outside of the tropics, the departure of the 2007 LHF+SHF from 2006 was most pronounced in the vicinity of the WBCs, that is, the Kuroshio, the Gulf Stream, the Agulhas Current, and their extensions. In addition, the increase in LHF+SHF in the northern North Atlantic is worth noting. The enhanced LHF+SHF over the Kuroshio Extension and the Agulhas Current and extension were in phase with the warmer SST difference anomalies (see Fig. 3.1), a further indication of the dominance of the oceanic forcing on the regional air–sea heat exchange. By contrast, the SSTs over the Gulf Stream and its extension were cooler in 2007 than in 2006, as was the case for the SSTs in the northern North Atlantic Ocean. This raises the question of whether SST cooling in the North Atlantic was induced by enhanced evaporative heat loss: In other words, was the change in the Atlantic SST caused by the atmospheric forcing? Further investigation is certainly needed to elucidate the role of air–sea fluxes in the 2007 Atlantic SST variability.

The long-term context of the change in 2007 LHF+SHF is shown in the plot of year-to-year variations of the annual mean averaged over the global oceans from 1958 to 2007 (Fig. 3.8). The 2007 LHF+SHF is at a level similar to the 2006 mean, indicative of insignificant net change. Nevertheless, the two recent years are situated at the high end of a long-term upward trend that started in 1977–78. The upward trend has been driven primarily by LHF, with a minor positive contribution from SHF in the 1990s. Over the past 20 yr from 1978 to 2007, the LHF+SHF has increased by ~ 10 W m^{-2}, from a low at 99 W m^{-2} in 1997 to a high at 109 W m^{-2} in 1999. Since 2000, however, the trend in the time series of the annual mean LHF+SHF has been largely flat.

The oceans, being the source of 86% of the global evaporation and the receiver of 78% of global precipitation, are a key component of the global water cycle. The apparent increase in LHF is consistent with the scenario that evaporation increases as climate warms and hence supports the hypothesized intensification

of the water cycle under global warming. With the availability of continuous satellite-based ocean precipitation records from 1979, a link of evaporation with precipitation records would lead to a better understanding as to how global water cycle has changed in past decades.

4) Tropical Cyclone Heat Potential—G. J. Goni

The role of the ocean in TC formation has been largely recognized and accepted. The formation of Atlantic hurricanes has been linked to the SST, where values of this parameter larger than approximately 26°C have been shown to be a necessary but insufficient condition for hurricane cyclogenesis. Additionally, the intensification of hurricanes involves a combination of favorable atmospheric conditions, such as trough interactions and small vertical shear (DeMaria et al. 1993). After a series of events where the sudden intensification of hurricanes occurred when their path passed over oceanic warm features, it became clear that the upper ocean may play an important role in this process.

Although the sea surface temperature provides a measure of the surface ocean conditions, it gives no information about the subsurface (first tens of meters) ocean thermal structure. It is known that the oceanic skin temperature erodes when the sea surface is affected by strong winds, creating a well-mixed layer that can reach depths of several tens of meters. As the TC progresses, it travels above waters with mixed layer temperatures similar to their skin sea surface temperatures. This provides the motivation to investigate and monitor the upper-ocean thermal structure, which has become a key element in the study of tropical cyclone–ocean interactions focused on prediction of sudden tropical cyclone intensification. Warm ocean features, mainly anticyclonic rings and eddies, are characterized by a deepening of the isotherms toward their centers with a markedly different temperature and salinity structure than the surrounding water mass. We present here results that are used to a) monitor the upper-ocean heat content in all basins where TCs occur, and b) investigate any possible link between this parameter and the growth of intense TCs during 2007.

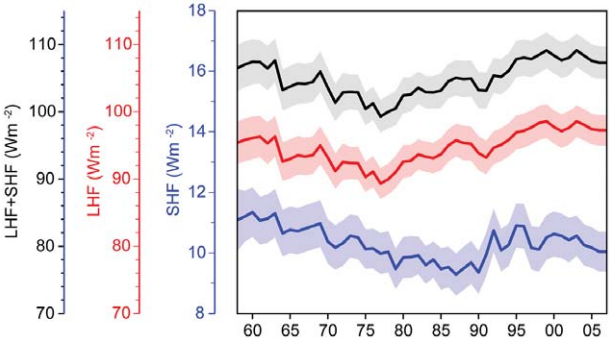

Fig. 3.8. Year-to-year variations of global averaged annual mean latent plus sensible heat flux (upper curve, black), latent heat flux (middle curve, red), and sensible heat flux (bottom curve, blue). The shaded areas indicate the upper and lower limits at the 90% confidence level.

The TCHP is the heat contained in the upper ocean from the sea surface to the depth of the 26°C isotherm. Hydrographic observations cannot provide TCHP fields needed to monitor this parameter on a daily to weekly basis with global coverage. Consequently, a methodology based on a combination of hydrographic and satellite-derived observations is used to create daily global fields of TCHP (Goni et al. 1996; Shay et al. 2000). Statistical analyses of these fields have shown that values of 50 kJ cm^{-2} are usually needed for the ocean to have an effect on the intensification of an Atlantic hurricane (Mainelli et al. 2008). Clearly, areas with high values of TCHP may be important only when TCs travel over them.

There are seven basins where TCs occur: North Atlantic, east Pacific, west Pacific, north Indian, southeast Indian, southwest Indian, and South Pacific. Results presented separate the North Atlantic basin into tropical Atlantic and Gulf of Mexico. The TCHP anomalies are computed during the months of TC activity in each hemisphere: June through November in the Northern Hemisphere and November through April in the Southern Hemisphere. Anomalies are defined as departures from the mean TCHP obtained for the same months from 1993 to 2007. These anomalies show large variability within and among the basins (Fig. 3.9, left).

In the Pacific Ocean, the largest anomalies showed the signature of the negative phase of the 2007 ENSO event (La Niña). However, these anomalies are mostly outside regions where TCs occur, with the exception of the west Pacific and South Pacific basins. The west Pacific showed positive anomalies only, while the South Pacific showed both large positive and negative anomalies. The north Indian Basin exhibited positive values in the Arabian Sea and negative values in the Bay of Bengal. In the mean, the Gulf of Mexico and the tropical Atlantic exhibited small positive anomalies. Nevertheless, within the tropical Atlantic the anomalies were positive (negative) to the south (north) of approximately 25°N. The analysis of the monthly TCHP anomalies averaged over each basin since 1993 (Fig. 3.9) showed that the only two basins

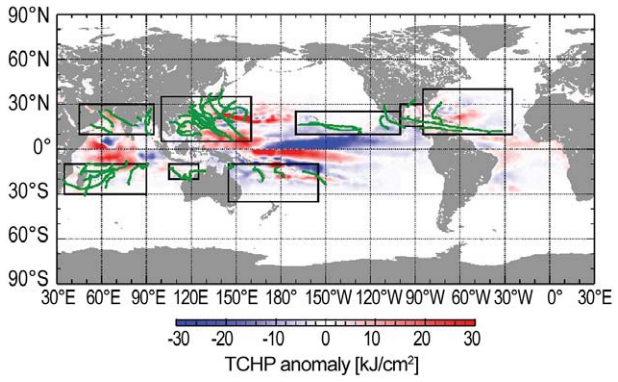

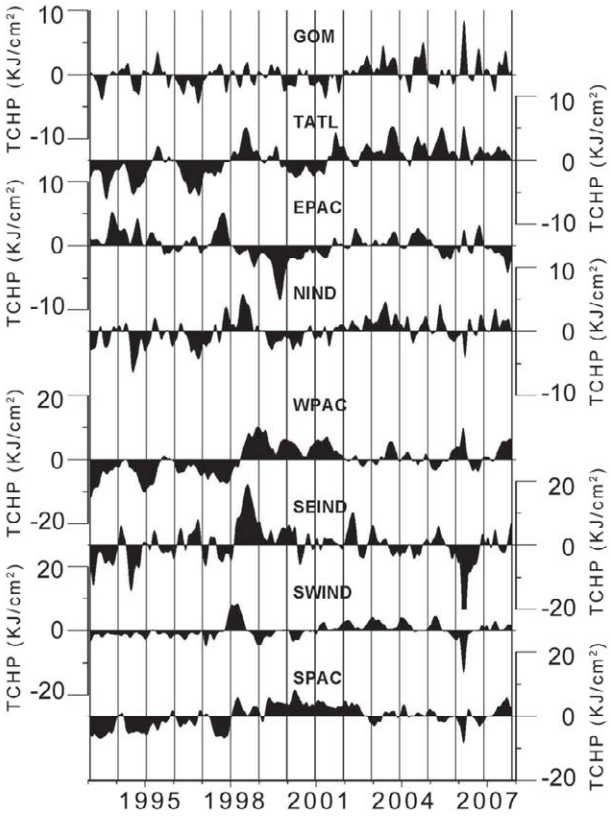

Fig. 3.9. (left) Global anomalies of TCHP corresponding to 2007 computed as described in the text. The boxes indicate the seven regions where TCs occur: from left to right, SWIND, NIND, WPAC, SEIND, SPAC, EPAC, and North Atlantic (shown as GOM and TATL separately). The green lines indicate the trajectories of all tropical cyclones category 1 and above from Nov 2006 to Apr 2007 in the Southern Hemisphere and Jun–Nov 2007 in the Northern Hemisphere. (right) Time series of monthly TCHP anomalies corresponding to each of the seven basins. Note that two different vertical scales are used in this figure.

exhibiting large monthly anomalies (within 75% of their historical extreme values) are the west Pacific and the South Pacific (Fig. 3.9, right). In the mean, all basins, except the eastern Pacific, showed mean positive annual values of TCHP during 2007.

Several TCs were identified to have gained strength when traveling into regions of very high values of TCHP. Some examples of these intensification events are shown in Fig. 3.10. The results presented here correspond to three intense (category 4 and 5) TCs, where the location of their intensification coincided with an increase of the values of TCHP along their tracks. Additionally, the cooling associated with the wake of the TCs is important since it influences the upper-ocean thermal structure on regional time scales within weeks to months after the passage of the cyclones. These TCs were Gonu in the north Indian Basin (Fig. 3.10, top three panels); Krosa in the west Pacific basin (Fig. 3.10, middle three panels); and Felix in the Caribbean Sea (Fig. 3.10, bottom three panels).

(i) Cyclone Gonu

During 3 June to 4 June 2007, cyclone Gonu, a storm with maximum winds of 104 mph (category 2), intensified to maximum sustained winds of 133 mph (category 4). This cyclone intensified when traveling from a region with TCHP value of 60 kJ cm^{-2} over a mesoscale feature with TCHP values averaging 110 kJ cm^{-2}. The average decrease of TCHP and SST under the wake of this cyclone were of 25 kJ cm^{-2} and 3°C, respectively.

(ii) Typhoon Krosa

On 3 October 2007, Typhoon Krosa, a storm with maximum winds of 86 mph (category 1), intensified to one with maximum sustained winds of 138 mph (category 4). This typhoon traveled from a region with TCHP values of 30 kJ cm^{-2} over a mesoscale feature with TCHP values of 75 kJ cm^{-2}. The average decrease of TCHP and SST values under the wake of this typhoon were 50 kJ cm^{-2} and 3°C, respectively.

(iii) Hurricane Felix

On September 2, 2007, hurricane Felix, a cyclone with maximum winds of 104 mph (category 2), intensified to a hurricane with maximum sustained winds of 138 mph (category 4). This hurricane traveled from a region in the Caribbean Sea with TCHP values of 50 kJ cm^{-2} into a region with TCHP values of 110 kJ cm^{-2}. The average decrease of TCHP and SST values under the wake of this hurricane were

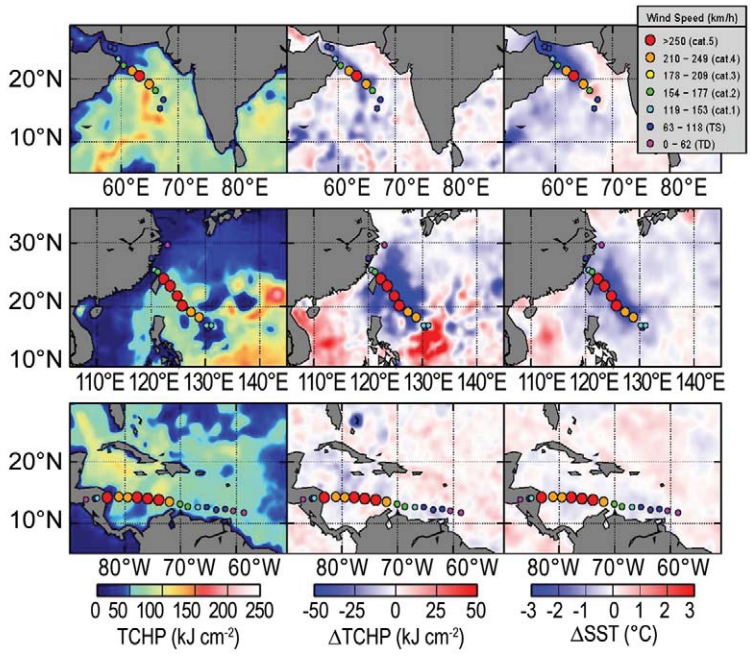

Fig. 3.10. (left) TCHP during three 2007 TCs: (top) Cyclone Gonu, (middle) Typhoon Krosa, and (bottom) Hurricane Felix; (center) TCHP cooling; and (right) SST cooling associated with the wake produced by each TC.

approximately 10 kJ cm^{-2} and 1°C, respectively. The cooling produced by this hurricane is substantially less than that produced by Cyclone Gonu and Typhoon Krosa, probably due to several factors such as translation speed of the storm and vertical ocean stratification.

Altimetry-derived fields of tropical cyclone heat potential provide a measure of the heat contained in warm mesoscale features. The examples presented here show the value of satellite-derived and in situ upper-ocean thermal observations for tropical cyclone intensity studies, suggesting that the inclusion of information on the upper-ocean thermal conditions in air–sea coupled models could help reduce the errors in intensity forecast.

c. *Sea surface salinity*—G. C. Johnson and J. M. Lyman

Ocean storage and transport of freshwater are intrinsic to many aspects of climate, including the global water cycle (e.g., Wijffels et al. 1992), El Niño (e.g., Maes et al. 2006), and global climate change (e.g., Held and Soden 2006). In the past, in situ ocean salinity data have been too sparse and their reporting too delayed for an annual global perspective of ocean freshwater, and its complement, salinity. However, over the past few years, the now mature Argo array of profiling floats, which measures temperature and salinity year-round in the upper 2 km of the ice-free global ocean (Roemmich et al. 2004), has remedied this situation. The near-global Argo data are analyzed here to determine an annual average SSS anomaly for 2007 relative to a long-term climatology and to describe how annual SSS anomalies have changed in 2007 relative to 2006. Remote sensing of SSS by satellite is planned for 2010 (http://aquarius.nasa.gov/).

In this work the shallowest near-surface (<25 m) salinity data flagged as good from each available Argo profile for 2006 and 2007 were subjected to a statistical check to discard outliers. After this statistical check, the remaining data were then cast as differences from a long-term climatological mean surface salinity field from the *World Ocean Atlas* based on historical data reported through 2001 (*WOA2001*; Boyer et al. 2002). The resulting anomalies were then mapped (Bretherton et al. 1976) assuming a Gaussian covariance function with 6° latitude and longitude decorrelation length scales and a noise-to-signal variance ratio of 2.2. While some delayed-mode scientific controlled (final) Argo data are available for the 2006–07 time period, many real-time (preliminary) Argo data were used in both years. The real-time estimates of SSS made here could change after all the data have been subjected to careful scientific quality control.

SSS patterns are fairly well correlated with surface freshwater flux: the sum of evaporation, precipitation, and river runoff (e.g., Beránger et al. 1999) where advection processes are not dominant. In each ocean basin, subtropical salinity maxima centered between roughly 20° and 25° in latitude are signatures of the predominance of evaporation over precipitation. Conversely, in most regions where long-term climatological surface salinities are relatively fresh, precipitation generally dominates over evaporation. The 2007 anomalies from *WOA2001* (Fig. 3.11) reveal some large-scale patterns. In 2007 the regions around the climatological salinity maxima are mostly salty with respect to *WOA2001*, as they were in 2006 (Arguez et al. 2007) and 2005 (not shown). In many of the climatologically fresh regions, 2007 values appear fresher than *WOA2001*, including: most of the ACC near 50°S, the subpolar gyre of the North Pacific, much of the ITCZ over the Atlantic and Pacific Oceans, and the South Pacific convergence zone west of about 165°W.

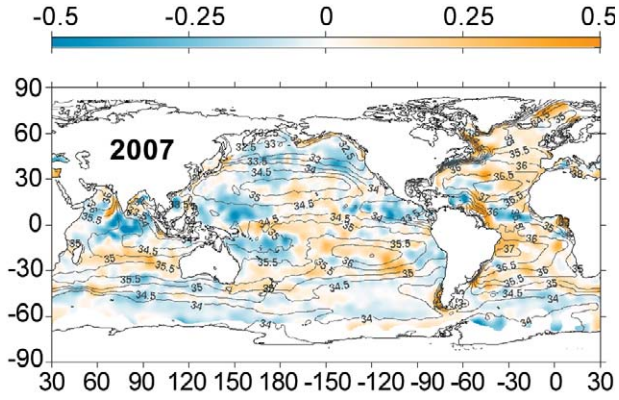

Fig. 3.11. Map of the 2007 annual surface salinity anomaly estimated from Argo data (colors in PSS-78) with respect to a climatological salinity field from *WOA2001* (gray contours at 0.5 PSS-78 intervals). White areas are either neutral with respect to salinity anomaly or are too data-poor to map. While salinity is often reported in psu, it is actually a dimensionless quantity reported on the PSS-78.

These patterns may suggest an increase in the hydrological cycle (i.e., more evaporation in drier locations and more precipitation in rainy areas), as suggested by recent increases in the global ocean average of latent heat flux (Fig. 3.8) and as seen in simulations of global warming. These simulations suggest this signal might be discernible over the last two decades of the twentieth century (Held and Soden 2006). Any increase in the hydrological cycle would certainly result in changes of local SSS values, but not necessarily alter the global average salinity by itself. Most of the anomaly patterns with respect to climatology observed in 2007 (Fig. 3.11) are not reflected in the 2007–2006 differences (Fig. 3.12). Hence, the anomalies observed in 2007 are similar to those observed in 2006 (Arguez et al. 2007) and 2005 (not shown), suggesting that these anomalies have evolved over longer time scales than interannual.

There may be alternate explanations. It is possible that the climatology, being based on relatively sparse data distributions in many parts of the oceans, may tend to underestimate regional extrema that the well-sampled Argo array can better resolve, or that the climatology contains regional biases on seasonal or longer time scales that are not present in the Argo data. Also, some of these patterns might be explained by interannual shifts in ocean features such as the ACC or atmospheric features such as the ITCZ. Indeed, the increase in salinity in the Pacific ITCZ between 2006 and 2007 (Fig. 3.12) is an obvious exception to any claim of long time-scale freshening in that region. Finally, since near-global coverage only commenced around 2005, it is difficult to determine variations on time scales beyond interannual.

Other interesting deviations from high-latitude fresh anomalies are obvious in the relatively salty subpolar North Atlantic and Nordic Seas in 2007 (Fig. 3.11), as well as in 2006 (Arguez et al. 2007), and 2005 (not shown). Year-to-year changes in these regions are relatively small, except in the high lateral gradient areas near the western boundary (Fig. 3.12). This salty subpolar anomaly is inconsistent with an increase in the strength of the hydrological cycle, because with such an increase, one might expect the fresh high latitudes to become fresher. However, the pattern may have less to do with local evaporation and precipitation fields and more with northward spread of saltier waters from the south. The salty anomaly in this region is consistent with a stronger influence of subtropical gyre waters in the northeastern North Atlantic in recent years and a reduced extent for the subpolar gyre (Hátún et al. 2005).

In the Indian Ocean, overall freshening north of about 10°S (Fig. 3.12) has enlarged and intensified the fresh anomaly located south of India around the equator in 2007 (Fig. 3.11) relative to its size and strength in 2006 (Arguez et al. 2007). This anomaly was not present in 2005 (not shown), suggesting an interannual time scale for this feature.

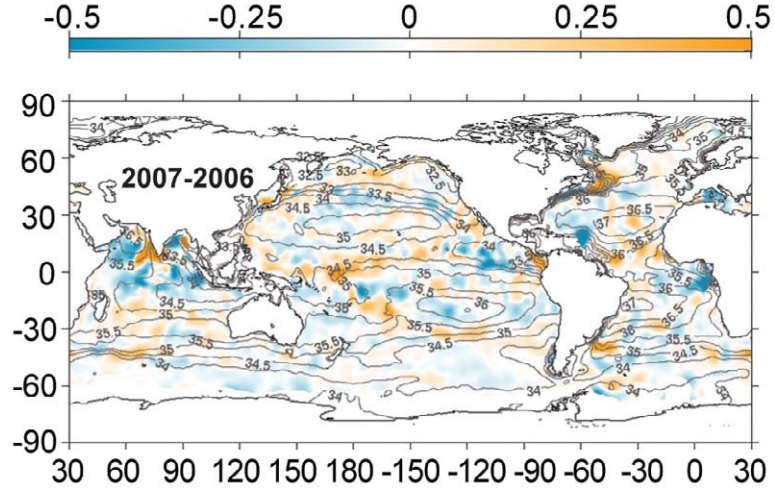

Fig. 3.12. The difference of 2007 and 2006 surface salinity maps estimated from Argo data (colors in PSS-78 yr^{-1} to allow direct comparison with Fig. 3.11). Other details follow Fig. 3.11.

One last feature of interest in the 2007 salinity field is the anomalously salty water located in the region of the fresh Amazon River plume (Fig. 3.11). The influence of this plume would normally be apparent in relatively fresh conditions to the north and west of the mouth of the Amazon River (the cluster of gray contours near 5°N, 40°W) that reach as far north as Puerto Rico. A salty anomaly observed in this region in 2006, but not 2005 (Arguez et al. 2007), intensified east of 60°W in 2007 (Figs. 3.11 and 3.12). This building salty anomaly may be partly explained by reduced freshwater flow from the Amazon into the ocean during a record drought in the Amazon River basin in 2005 (Shein et al. 2006) that continued, although somewhat moderated into 2006 (Arguez et al. 2007), when some time delay for hydrological and oceanic processes is included.

d. Circulation

1) Surface current observations—R. Lumpkin and G. J. Goni

Global analysis of surface currents indicate that westward current anomalies dominated the equatorial Pacific basin, reflecting the La Niña conditions that developed in the second half of 2007. Long-term trends in eddy kinetic energy reveal that major ocean currents such as the Gulf Stream, Kuroshio, Brazil, and Malvinas Currents are shifting in position and/or strength; these decadal-scale changes may reflect longer-term fluctuations or secular trends.

(i) Data and analysis

Near-surface currents are measured in situ by satellite-tracked drifting buoys and by current meters on ATLAS moorings.[1] During 2007, the drifter array ranged in size from a minimum of 1,180 to a maximum of 1,306, with a median size of 1,253 buoys. The moored array consisted of 41 buoys, all but two between 10°S and 21°N. The tropical moored array in the Indian Ocean was expanded considerably in 2007, with several buoys added along 90°E and a new site at 8°S, 67°E. In the Atlantic, the PIRATA array was expanded and now includes moored current meters at four sites along 23°W. The two nontropical moorings in the observing system are at the Kuroshio Extension Observatory (32°N, 145°E) and Ocean Station Papa (50°N, 145°W) sites.

The findings presented here are based on a combined evaluation of mooring, drifter, and satellite-based surface current measurements. Weekly maps of absolute surface currents and geostrophic current anomalies for 2007 were calculated from a synthesis of in situ observations, near-real-time AVISO gridded altimetry, and NCEP operational winds (Niiler et al. 2003). Anomalies are defined with respect to the January 1993–December 1998 mean. Global analyses using similar methodologies (Bonjean and Lagerloef 2002) and validation of surface currents (Johnson et al. 2007) can be found at www.oscar.noaa.gov and www.aoml.noaa.gov/phod/currents.

(ii) Global overview

In 2007, the most dramatic surface current anomalies were westward anomalies spanning the tropical Pacific basin (Fig. 3.13). Maximum annual averaged westward anomalies of 20–25 cm s^{-1} were observed at 120°–125°W on the equator, with annual-averaged values of 5–10 cm s^{-1} elsewhere. As discussed below, these anomalies were strongest during January–March, but were also sustained from mid-July through the end of 2007. These westward anomalies were associated with the La Niña that developed in the latter half of 2007. Anomalies elsewhere in the World Ocean were caused by energetic mesoscale (60–90 day period) variations or were associated with displacements of currents from their typical positions.

Longer-term trends in EKE were obtained from altimetry-derived sea height anomaly observations, to resolve changes in intensity and location of surface geostrophic currents. These trends were calculated for the observations binned in 1° boxes, calculated over the time period 1993–2007. The global observations indicate that large changes in EKE are occurring in all ocean basins, mainly in the most intense surface currents (Fig. 3.14).

(iii) Pacific Ocean

In January–February 2007, westward surface current anomalies developed and intensified across the central equatorial Pacific. During these months, the westward NEC was stronger by 10–30 cm s^{-1} across the basin, while the eastward NECC was barely present. The westward anomalies disappeared from the equatorial Pacific by the end of March 2007.

[1] Drifter data are distributed by NOAA/AOML (www.aoml.noaa.gov/phod/dac/gdp.html). Moored data are distributed by NOAA/PMEL (www.pmel.noaa.gov/tao). Altimetric time series of transports may be viewed online (www.aoml.noaa.gov/phod/satprod). NCEP data provided by the NOAA–CIRES Climate Diagnostics Center (www.cdc.noaa.gov/). AVISO altimetry produced by the CLS Space Oceanography Division as part of the Environmental and Climate EU ENACT project and with support of CNES.

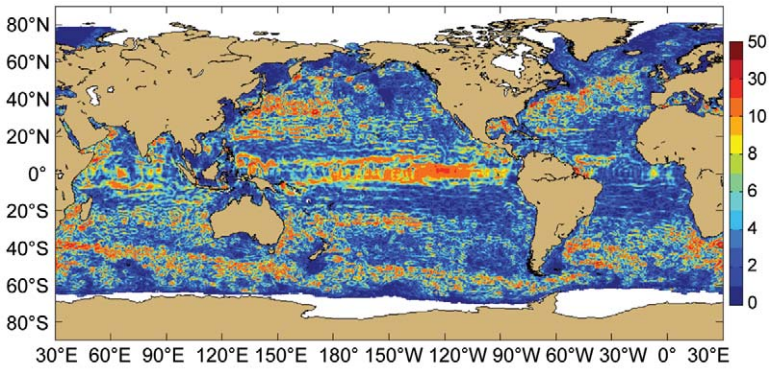

Fig. 3.13. Amplitude (cm s^{-1}) of 2007 annual averaged surface geostrophic current anomalies.

Weak eastward anomalies began developing during March, centered at around 130°W, intensified during April, and were very strong by early May at 110°–160°W. During May 2007, the center of the eastward anomalies shifted to 120°–150°W. Strong off-equatorial (3°–8°N) westward anomalies developed at 130°–180°W. The equatorial eastward anomalies weakened through June.

In July, strong westward anomalies developed in the eastern side of the equatorial Pacific basin (90°–140°W), a pattern that would grow through the remainder of the year to reflect the development of La Niña conditions. Also in July, eastward anomalies developed in the western side of the basin. These patterns created an anomalous confluence along the equator at 150°–160°W. During this period, cold SST anomalies that had previously been confined to the eastern side of the basin began to appear in the Niño-3.4 index region (120°–170°W) (see also, Figs. 3.2 and 3.20).

Through August, the eastward anomalies diminished, then disappeared. The westward anomalies persisted through this month, and intensified in September to expand and span the basin (Fig. 3.15). Also during this month, the Niño-4 index (150°W–160°E) exhibited a sharp drop in surface temperature partly attributable to westward advection of SST anomalies. The basin-scale pattern of westward equatorial anomalies weakened through October, but persisted in a weakened state through November and December 2007.

The long-term trends in EKE reveal large, positive values in the Kuroshio and Kuroshio Extension region (Fig. 3.14), extending to approximately 170°W, which may be related to the regional intensification of surface currents. Baroclinic instabilities of the Kuroshio are the main source of this EKE (cf. Niiler et al. 2003).

(iv) Indian Ocean

During January 2007, the equatorial Indian Ocean exhibited a band of anomalously eastward flow on the eastern half of the basin. Through February, westward anomalies developed in the western half of the basin, and persisted through early March. By April, and persisting through early May, eastward anomalies associated with the equatorial jet were well developed across the equatorial Indian Ocean Basin. This seasonal (monsoon driven) pattern disappeared in May, and in June through September there were no significant current anomalies. In October through November, strong eastward anomalies (the semiannual equatorial jet) developed and propagated across the basin; eastward anomalies persisted in the western third of the basin through December 2007.

The long-term EKE activity in the Agulhas Current region off South Africa (Fig. 3.14) may indicate increasing ring activity. The Agulhas becomes unstable as it separates off the southern tip of South Africa, shedding rings that transport Indian Ocean water into the South Atlantic. This exchange is a significant part of the upper limb of the global meridional overturning circulation, and a decadal-scale increase in this exchange rate may have profound climate implications if verified.

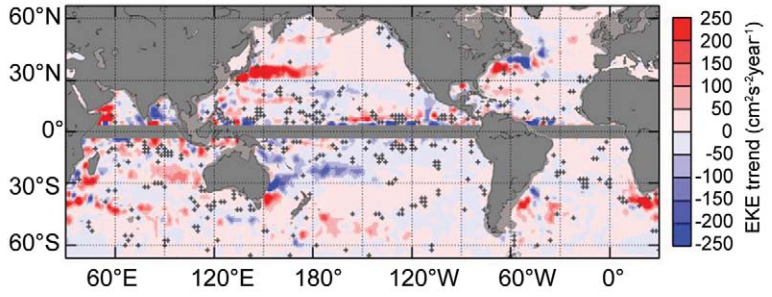

Fig. 3.14. EKE trend, 1993–2007. Crosses show regions where the confidence levels are <67%.

(v) Atlantic Ocean

The seasonal reversal of western tropical Atlantic Ocean currents (cf. Lumpkin and Garzoli 2005) was prominent in 2007. Anomalously strong eastward anomalies were seen on the equator in mid-March through

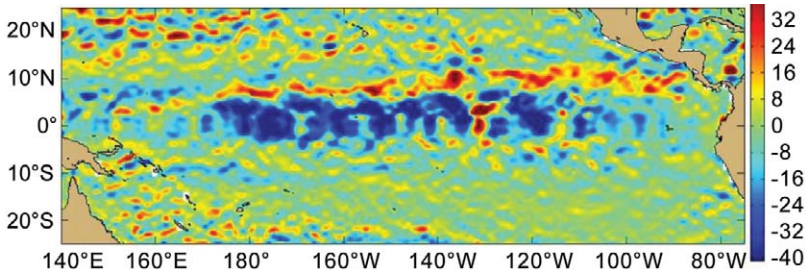

Fig. 3.15. Zonal geostrophic current anomalies (cm s^{-1}) in mid-Sep 2007 in the tropical Pacific, demonstrating the negative (westward) anomalies associated with the development of the 2007 La Niña.

early May. By late May, strong westward anomalies had developed at ~23°W on the equator. These were weak by mid-June, then reintensified in late June through early July, and diminished until they were gone by early August. In September, eastward anomalies were persistent across the central and eastern equatorial Atlantic. This pattern was confined to the Gulf of Guinea by mid-October, and gone entirely by mid-November. Currents in December 2007 were close to their climatological values.

The alternation of positive and negative values in the long-term EKE trend in the northwest North Atlantic and southwest South Atlantic (Fig. 3.14) are indicative of the variability in the subtropical gyres. This change in the South Atlantic is consistent with a shift to the south of the Brazil Current jet (Fig. 3.16). The Brazil Current runs south along the coast until it collides head-on with the northward Malvinas Current; both subsequently turn eastward. During the last 15 yr, the location where the Brazil Current separates from the continental shelf break has moved 2° to the south, possibly indicating an expansion of the South Atlantic wind-driven subtropical gyre (Goni et al. 2008).

2) The meridional overturning circulation—M. O. Baringer and C. S. Meinen

The global ocean–atmosphere system can be thought of as a massive heat engine, redistributing heat from the sun and in so doing causing both short-term weather systems and long-term changes in climate. In the ocean, the so-called MOC is largely responsible for the redistribution of heat, mass and freshwater within the global ocean system. Specifically, the MOC is defined here as the maximum of the zonal integral of mass transport of the large-scale, low-frequency, full-depth ocean circulation. The strengths of the overturning circulations in different basins are directly related to the strength of the heat transport (see Baringer and Meinen 2007 for more discussion). There are several available estimates of the steady-state global mass and heat transport based on inverse model calculations (Lumpkin and Speer 2007; Ganachaud and Wunsch 2003; Talley 2003). Recently, there have been only a few attempts to look at long-term changes in the MOC from direct observations. Bryden et al. (2005) postulate a 30% reduction in the MOC transport between the 1950s and the present day; however, that analysis is based on a very limited dataset (essentially five "snapshot" hydrographic sections). Other recent work using cross-basin hydrographic sections along 48°N in the Atlantic suggest conflicting conclusions relative to the state of the thermohaline circulation. In particular Koltermann et al. (1999) show large variability of the MOC that, they conclude, is related to the strength of Labrador Sea Water production, with larger (smaller) MOC transport corresponding to less (more) Labrador Sea Water export. More recently these data have been reanalyzed to formally test the hypothesis that the MOC circulation is steady. Lumpkin et al. (2008) find that a steady MOC over the same time period could not be ruled out based on the uncertainty in determining the barotropic circulation. It is also noteworthy that the Bryden et al. (2005) suggestion that the thermohaline circulation has declined by 30% over the past 50 yr represents a much higher rate of change than predicted in coupled climate model simulations (e.g., Schmittner

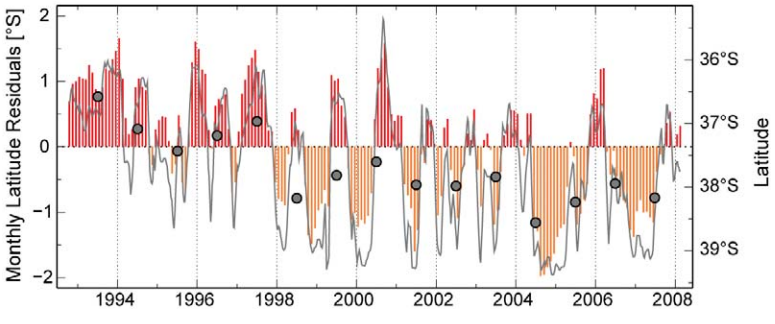

Fig. 3.16. Latitude of separation of the Brazil Current from the continental shelf (black line), monthly anomalies of the separation (vertical bars), and mean annual values (circles) calculated from AVISO altimetry, showing a mean shift to the south of approximately 2°. (From Goni et al. 2008.)

et al. 2005). Clearly, additional work needs to be done to understand the full range of time scales associated with MOC variability and the improvement of error estimates attached to these estimates.

Currently, observing systems capable of quantifying changes in the complete MOC are at fledgling stages that at best observe only one component (e.g., a specific current or ocean layer) of the MOC at discrete locations. At 27°N in the Atlantic the bulk of the warm upper limb of the MOC is thought to be carried in the Florida Current through the Straits of Florida, while the majority of the cold lower limb is believe to be carried to the south in the DWBC just east of the Bahamas. Since 1982, variations in the upper limb of the MOC have been monitored by measuring the Florida Current transport using a submarine cable across the Straits of Florida in combination with regular hydrographic sections. In 1984, monitoring was expanded to the deep limb of the MOC through regular hydrographic cruises (more than 30 to date) across the DWBC east of the Bahamas, and in 2004 the program commenced time series monitoring of the DWBC by adding moored inverted echo sounders and bottom pressure gauges east of Abaco Island in the Bahamas. In 2004 scientists at NOAA joined with collaborators from the University of Miami and the National Oceanography Centre, Southampton, to expand the MOC monitoring array to span the entire Atlantic basin at 26°N using a variety of measurement systems. Called the RAPID Climate Change Program by the U.K. contributors and the MOCHA by the U.S. contributors, this expanded project seeks to develop a cost-effective basinwide MOC monitoring system that will lead to a much greater degree of certainty in the magnitude of the variations in the integrated, basinwide MOC circulations and the time scales on which they vary. Results from the first year of this new MOC monitoring array appeared in *Science* in August (Kanzow et al. 2007; Cunningham et al. 2007). The results from the first year of this array indicate a surprising amount of variability in the MOC strength. In fact, all the MOC values estimated from Bryden et al. (2005) can be found within the first year of the time series (Fig. 3.17). These results cannot disprove the presence of a long-term trend in the strength of the MOC, but they do suggest that a careful error analysis be performed that includes the underlying variability of the MOC (the standard deviation of this first year was estimated as 3.1 Sv).[2]

More recent observations of the strength of the MOC array are available only with a delay in time as the moorings are recovered over 12- to 18-month intervals. However, as noted earlier, the Florida Current contains most of the upper limb of the MOC as it flows through the Straits of Florida in the North Atlantic at 26°N, with a smaller contribution being carried by the Antilles Current east of the Bahamas. Fluctuations in the Florida Current show a clear negative correlation with NAO during the 1982–98 time period (Baringer and Larsen 2001); however, while the NAO has been tending to decrease over the past 20 yr, the Florida Current transport shows no corresponding long-term trend through 2007. The annual mean Florida Current transport observed in 2007 (31.8 Sv) falls only slightly below the long-term mean of 32.1 Sv, and given the statistical standard error of the mean of 1 Sv for a year, 2007 cannot be termed as an unusual year in terms of the Florida Current transport. Compared to 2006 (annual mean of 31.3 Sv) the Florida Current appears to have increased only slightly. Note that 2007 shows similar variability to previous years and no anomalous events occurred during the year (Fig. 3.18).

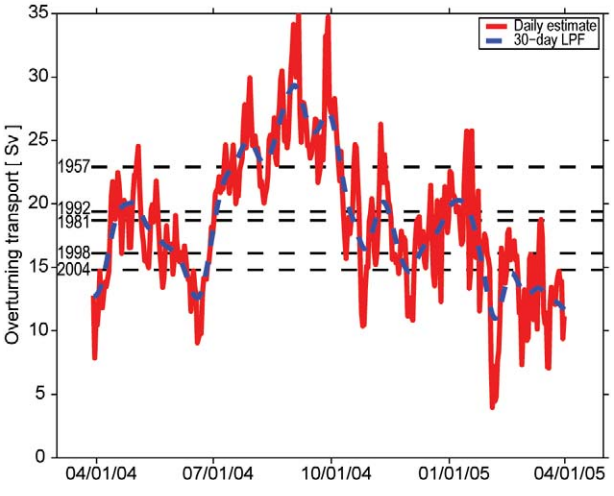

Fig. 3.17. Daily estimates of the strength of the meridional overturning circulation (red solid) as measured by the U.K. NERC Rapid Climate Change Program, the National Science Foundation's MOCHA, and the long-term NOAA Western Boundary Time Series Program. The MOC estimate is based on the upper-ocean transport from 29 Mar 2004 to 31 Mar 2005 based on the interior ocean transport array (adapted from Fig. 3 from Cunningham et al. 2007). The dashed blue line is the 30-day low-pass filtered version of the daily transport values. Dashed black horizontal lines are the Bryden et al. (2005) MOC values from the 1957, 1981, 1992, 1998, and 2004 trans-Atlantic hydrographic sections.

[2] Sverdrup is a unit commonly used for ocean volume transports and is defined as 1 Sv = 10^6 m^3 s^{-1}.

The programs in place since 2004 are an excellent first step toward the development of an integrated MOC measurement system, however, much work remains to fully monitor the Atlantic MOC and the global overturning circulation system. Recent work by Baehr et al. (2008) has shown that an array such as the one deployed at 26°N in the Atlantic may require up to 30 yr of data before a statistically meaningful change in the MOC can be detected.

e. *Sea level variations*—M. A. Merrifield, S. Gill, G. T. Mitchum, and P. L. Woodworth

Global sea level variability during 2007 is summarized using SLA data from the multimission, 1/4° gridded satellite altimeter Aviso product (www.aviso.oceanobs.com/), and RSL from tide gauges primarily from GLOSS (www.gloss-sealevel.org/). SLA and RSL are deviations from a 1993–99 baseline average. The inverse barometer correction has been applied to the SLA, but not to the RSL. We caution that quality controlled delayed-mode SLA data are available only for the first half of 2007 at this time and near-real-time data are used for the second half of the year.[3]

Annual mean SLA in 2007 was above the baseline average for over 80% of the sampled ocean surface (Fig. 3.19a). There is a strong correspondence between mean SLA and RSL patterns. The largest positive deviations occurred in the western equatorial Pacific, the western Indian Ocean, and the Baltic Sea. The region between 20° and 40°S in all oceans was generally above average in sea level. Areas of notable negative sea level deviation include the eastern equatorial Pacific and the northeast Pacific. Relative to 2006 (Fig. 3.19b), areas of increasing sea level include the zonal band just south of the equator in the western Indian Ocean, zonal bands in the general area of the Pacific tropical convergence zones, and the Baltic Sea. Areas of decreasing sea level include the equatorial Pacific cold tongue and the eastern Indian Ocean near 10°S.

The global mean SLA for 2007 was 1.1 mm higher than 2006, as compared to 2006 being 6 mm higher than 2005 (Merrifield et al. 2007). We note that the expected increase of 3 mm in a year has an uncertainty (1 sigma) of about 2 mm for a difference of annual mean values, which indicates that these values of 1 or 6 mm for the annual mean differences are not statistically unlikely. Recent studies have noted the significant increase of the 3.4 mm yr^{-1} trend determined from the 15 yr SLA record compared to the twentieth century consensus estimate of 1.7 mm yr^{-1} obtained using various analyses of the tide gauge dataset (see Bindoff et al. 2007 for a review). An area of active research is the impact of decadal and longer time-scale variations of sea level on global trend estimates. Over the overlap period of satellite altimeters and tide gauges, estimates of global sea level rise from both observing systems are similar (Church et al. 2004; Church and White 2006; Holgate 2007).

Maps of monthly SLA (Fig. 3.20) illustrate the evolving sea level variations that resulted in the annual mean patterns for 2007 (Fig. 3.19a). We begin in September 2006 to illustrate the transition from El Niño to La Niña conditions in the Pacific Ocean. A downwelling Kelvin wave (positive SLA) traveled eastward across the basin during October–December 2006. This was followed by the onset of La Niña conditions with a negative SLA starting in the central equatorial Pacific in January 2007 followed by negative SLA in the cold tongue region beginning in February 2007, and positive anomalies in the western equatorial Pacific and along zonal bands north and south of the equator. The La Niña pattern dominated

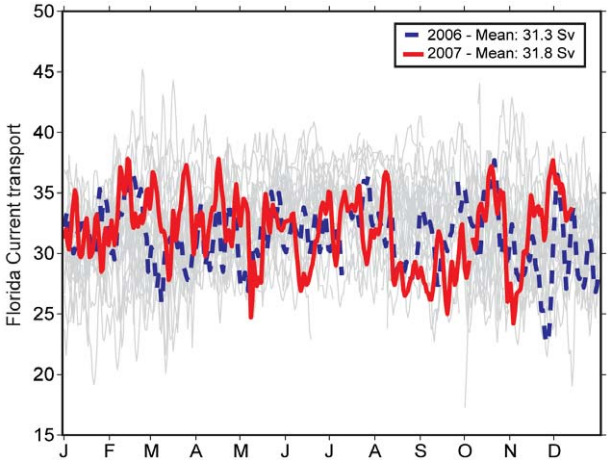

Fig. 3.18. Daily estimates of the transport of the Florida Current for 2007 (red solid line) compared to 2006 (dashed blue line). The daily values of the Florida Current transport since 1982 are shown in light gray. The transport in 2007 increased slightly relative to 2006, but remains slightly below the long-term mean for the Florida Current (32.1 Sv).

[3] The altimeter products were produced by Ssalto/Duacs and distributed by Aviso, with support from CNES (www.aviso.oceanobs.com). The Aviso dataset used is listed as the gridded sea level anomalies DT-MSLA "Ref," multimission product. Tide gauge data were obtained from the University of Hawaii Sea Level Center (http://uhslc.soest.hawaii.edu/). SLA is corrected for atmospheric pressure; the RSL time series are not.

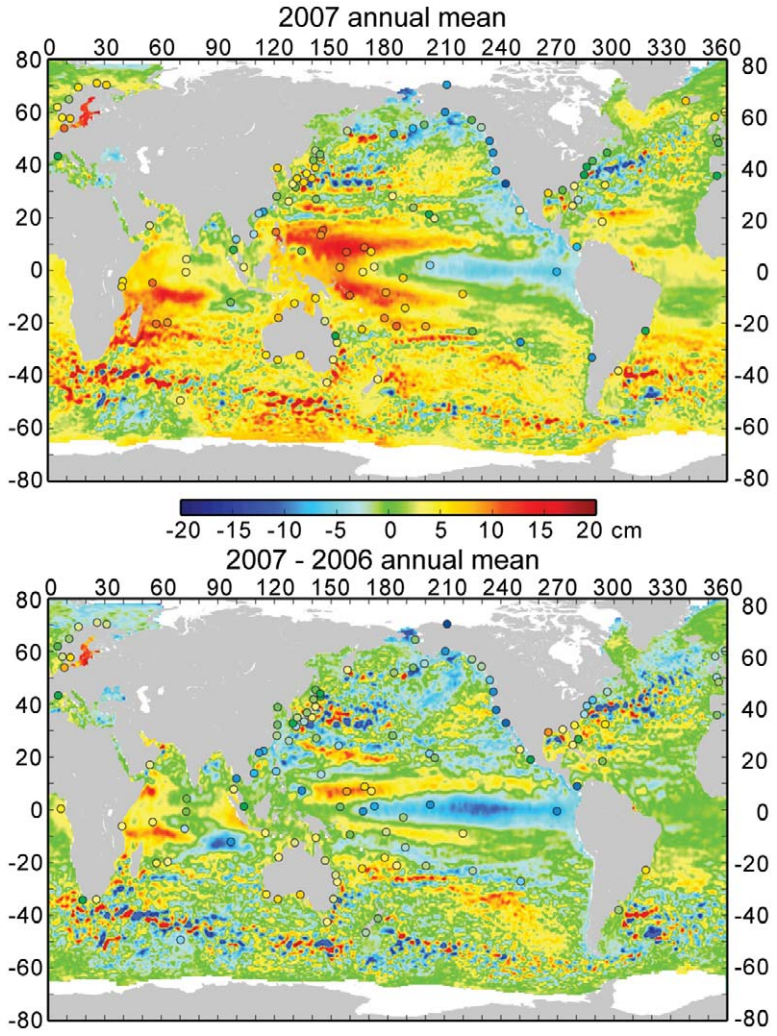

Fig. 3.19. (a) Annual mean (Jan–Dec 2007) SLA and RSL from tide gauges (circles) relative to the 1993–99 mean. (b) The difference in annual mean SLA and RSL for 2007 relative to 2006.

the monthly anomalies for the remainder of 2007 (see, also, Figs. 3.2 and 3.15).

In the Indian Ocean, a negative sea level anomaly occurred off the coasts of Sumatra and Java in September 2006, and a positive anomaly was present just west of this feature. Both high and low patterns grew in amplitude with the low extending northward into the Bay of Bengal and the high extending eastward to the African coast. By January 2007 a high/low pattern in the western/eastern basin resembled the positive mode of the IOD (Saji et al. 1999). The positive anomaly in the western Indian Ocean south of the equator peaked in amplitude during the first half of 2007 and diminished by September 2007. It was followed by a second positive SLA south of the equator that developed in the eastern Indian Ocean during the last quarter of 2007.

Extreme sea level events during 2007, associated with storms and other nontidal variability, are characterized by averaging the 5% highest daily average RSL values relative to the annual mean RSL at each station. The largest extremes generally occur at high-latitude stations due to winter storm activity, with sporadic high values at low-latitude stations (Fig. 3.21a). To determine how anomalous the extremes were at each station during 2007, the percentage of years with extreme values less than 2007 is depicted in Fig. 3.21b. Regions of higher than average extreme sea levels include northern Europe, much of North America, and southern Australia. Regions of lower than average anomalies include the western and central Pacific and the western and central Indian Ocean.

f. The global ocean carbon cycle—C. L. Sabine, R. A. Feely, R. Wanninkhof, and T. Takahashi

1) Air–sea carbon dioxide fluxes

The time and space scales of variability in the air–sea CO_2 flux make it challenging to assess global fluxes based on in situ surface observations. In 1990, Tans et al. (1990) combined 30 yr worth of shipboard pCO_2 observations in an attempt to develop the first global pCO_2 climatology. It excluded much of the Southern Ocean because of lack of data. The first true monthly global climatology was developed in 1997 (Takahashi et al. 1997) using a substantially larger dataset of approximately 250,000 measurements and then updated in 2002 (Takahashi et al. 2002) based on 940,000 measurements. Recently, Takahashi has submitted a revised climatology for publication that combines nearly 3 million measurements collected between 1970 and 2006 (Takahashi et al. 2008). In addition to the substantially larger database of observations, the revised climatology incorporates several other refinements in our understanding of CO_2 variability and fluxes. The annual mean contemporary CO_2 flux over the global oceans is estimated to be a net uptake of 1.4 ± 0.7 Pg-C yr^{-1}. Assuming the preindustrial steady-state ocean was a source of 0.4 ± 0.2 Pg-C yr^{-1} gives a net ocean anthropogenic CO_2 uptake of

1.8 ± 0.7 Pg-C yr^{-1} in 2000 (Takahashi et al. 2007). As with the previous climatologies the estimate is for a non–El Niño year. Since the efflux of CO_2 in the equatorial Pacific is depressed during El Niño periods (Feely et al. 2006), such conditions increase the net CO_2 flux into the ocean. Based on a time series of CO_2 fluxes in the equatorial Pacific (Feely et al. 2006) we estimate that the average CO_2 flux including El Niño years would be about 2.0 ± 0.7 Pg-C yr^{-1}. This value is well within the uncertainty of the ocean CO_2 uptake the estimate provided in Denman et al. (2007) of 2.2 ± 0.5 Pg-C yr^{-1} obtained by independent means.

Figure 3.22 shows a map of annual mean air–sea CO_2 flux climatology. Although the first-order patterns of CO_2 uptake and release have not changed, the revised flux map does vary from previous versions in the details. In general, both the sources and sinks are somewhat stronger in the latest climatology. The observed changes can be attributed not only to the improved database, but also to the revised formulations for calculating flux. Sweeney et al. (2007) have reassessed the bomb ^{14}C inventory and determined it to be about 20% less than the original estimate causing a corresponding 20% decrease in the wind speed dependence of the air–sea gas transfer. Examination of ocean CO_2 time series measurements has shown that, with a few small regional exceptions, global surface water pCO_2 values are increasing at about the same rate as the atmosphere (e.g., Takahashi et al. 2006). To create a climatology with a single nominal year of 2000, data collected prior to 2000 were adjusted to the climatology year by increasing the surface ocean CO_2 values at the same rate as the observed atmospheric CO_2 increase over the time interval. Based on historical pCO_2 observations, two regional exceptions for this adjustment were made in the Bering Sea and the winter high-latitude Southern Ocean. These are areas where vertical mixing is a stronger control on surface pCO_2 values than the atmospheric uptake so no time-dependent adjustment was made (Takahashi et al. 2007). It is important to note that the differences in flux in the different climatologies are not attributed to climate change or decadal variability but rather to improved methodology.

One region where new data has made a noticeable difference in the net flux is in the high-latitude South-

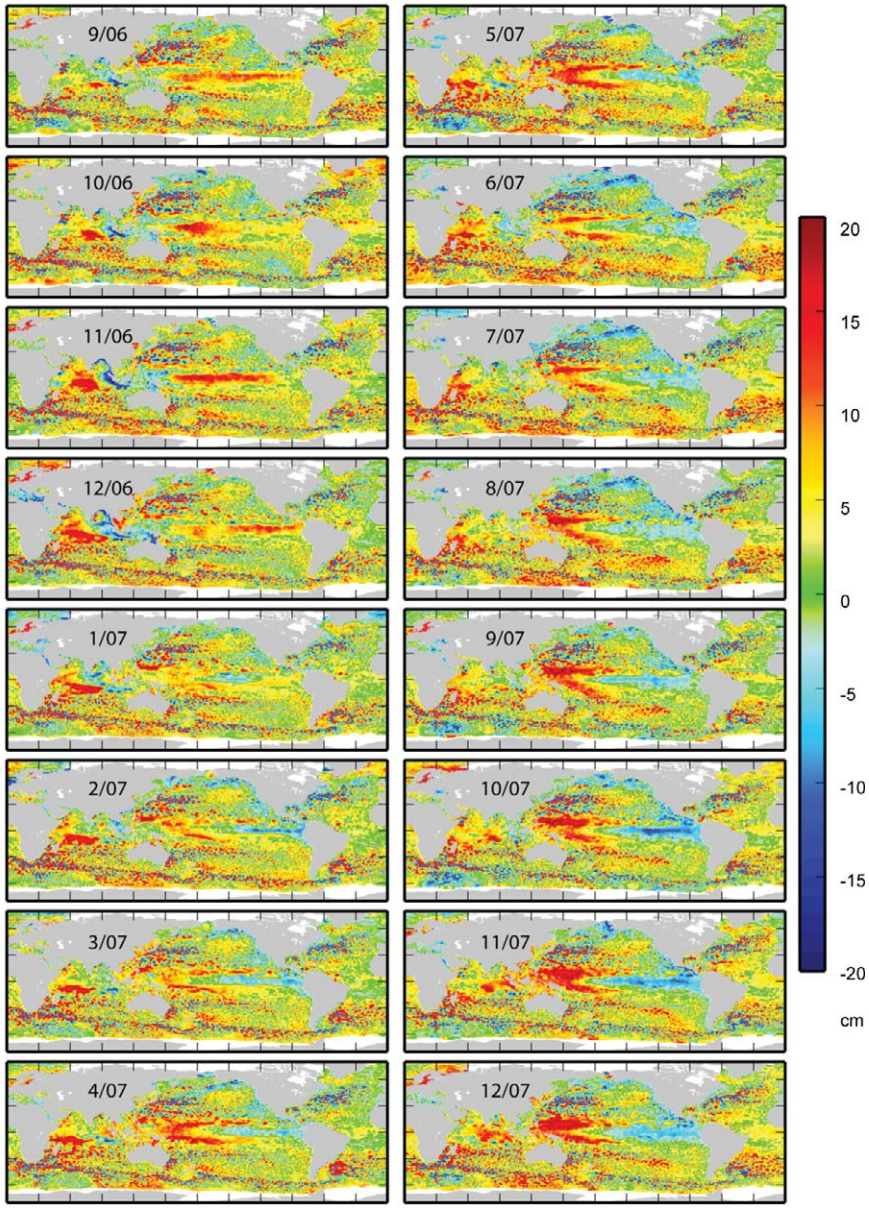

Fig. 3.20. Monthly mean SLA (1993–99 average for each month removed) for Sep 2006 through Dec 2007.

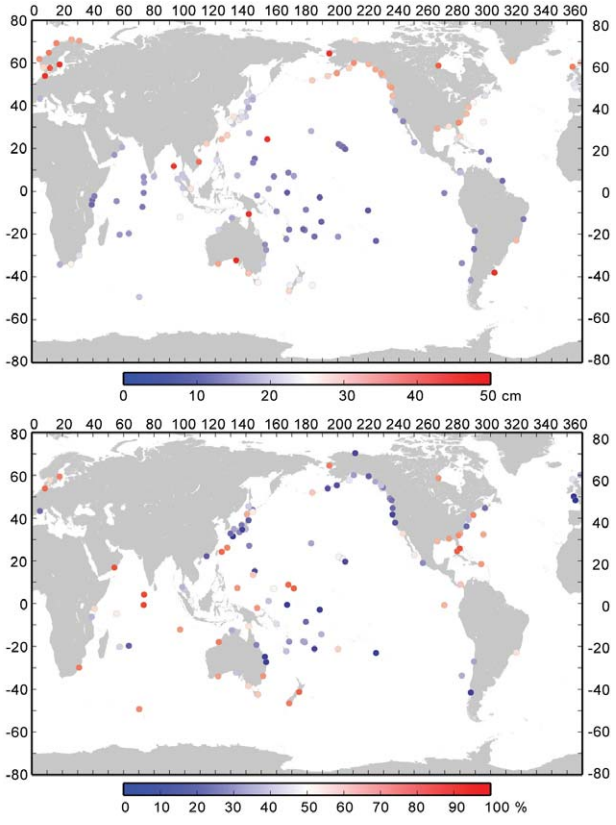

Fig. 3.21. (a) Extreme RSL values during 2007, defined as the average of the 5% largest daily averaged values relative to the annual mean at each station. (b) Percentage of years at each station with extreme RSL values less than in 2007.

ern Ocean between 50° and 62°S where the addition of new data and a new interpolation method utilizing SST significantly reduced the derived net ocean uptake. The lower Southern Ocean uptake is now more consistent with atmospheric inversion estimates of ocean uptake (e.g., Gurney et al. 2004; Jacobson et al. 2007) compared to the previous climatology. Although the new climatology still excludes coastal regions, it does include more regions in the Arctic Ocean where data are becoming available.

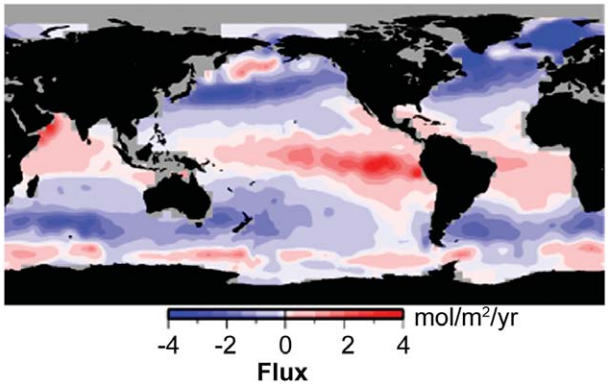

Fig. 3.22. Map of global climatological annual mean CO_2 flux for nominal year 2000 adapted from Takahashi et al. (2007). Negative fluxes represent uptake of CO_2 by the ocean.

Seasonal-to-annual estimates of net air–sea CO_2 fluxes are needed to properly evaluate the changing role of the ocean in the global carbon cycle. The global network of VOS and moored CO_2 systems has grown significantly over the past decade, but interpolation schemes are still needed to develop global flux maps on shorter time frames. We have taken the empirical approach of Lee et al. (1998) and Park et al. (2006) together with global monthly estimates of SST and a high-resolution wind speed assimilation product (available online at http://podaac-www.jpl.nasa.gov/products/product079.html) to develop monthly estimates of global air–sea CO_2 flux between 1995 and 2006. Linear least-squares fits of surface water pCO_2 versus SST are determined for each 4° × 5° pixel of the pCO_2 climatology for three periods: January–April, May–August, and September–December. These relationships are then used together with the interannual SST anomalies to determine pCO_2 anomalies relative to the climatology. Since the climatology specifically excluded data in the equatorial Pacific during El Niño periods, the derived fluxes are only representative of non–El Niño conditions. To better represent the interannual variations in the equatorial Pacific between 5°N and 10°S, CO_2 flux was calculated using surface water pCO_2 formulations of Cosca et al. (2003), including equations for both El Niño and non–El Niño conditions, atmospheric CO_2 from NOAA's Environmental Science and Research Laboratory (GLOBALVIEW-CO2 2007), and the wind speed gas exchange parameterization of Wanninkhof (1992).

The monthly flux map approach was first developed based on the climatology published in 2002, but here we calculate the anomalies relative to the new climatology (Takahashi et al. 2007). Figure 3.23 shows the interannual variability in the net annual air–sea CO_2 flux from 1995 to 2006. The red line shows the flux estimated using the empirical relationships determined by Park et al. (2006) based on the Takahashi et al. (2002) climatology. The blue line uses the same approach as Park et al. but a new set of empirical relationships was derived from the revised climatology. While the overall patterns are similar between the two lines, the revised relationships imply an interannual variability that is about 30% larger than suggested from the original fits. The majority of the interannual variability in the ocean is

typically attributed to ENSO variability in the equatorial Pacific. However, since both formulations use the Cosca et al. (2003) functions in this region, all of the 30% increase in interannual variability comes from the extratropical regions. We attribute this change to improved fits based on more actual observations rather than smoothed interpolated values in the original climatology.

There are significant uncertainties in the seasonal flux map calculations based on several factors, including the assumptions that go into the fits, the quality of the empirical fits, uncertainties in the reanalysis products, and uncertainties in the wind speed relationship for gas exchange. This approach does not account for the biological effects on surface water pCO_2 that are not correlated to temperature. Despite these shortcomings the interannual trends and magnitudes are similar to those obtained from numerical models. These estimates provide a useful observation-based tool for assessing the changing role of the ocean in global climate change. Extension of the global surface ocean CO_2 network will facilitate the development of improved regional algorithms that will lead to more accurate flux maps.

2) Subsurface carbon inventory

In the decade of the 1990s carbon samples were collected and analyzed from approximately 95 research cruises run as part of the international WOCE and the JGOFS. These data were carefully quality controlled and combined into a uniform dataset to make the first global assessment of DIC distributions with sufficient accuracy and coverage to evaluate the distribution of anthropogenic CO_2 in the ocean (Sabine et al. 2004; Key et al. 2004). Sabine et al. (2004) estimated that the total inventory of anthropogenic CO_2 in the ocean in the year 1994 was 118 ± 19 Pg C, accounting for 48% of the CO_2 released from fossil fuel burning between 1800 and 1994. This one-time global survey, however, could not provide information on how ocean carbon inventories have evolved over time or how the storage has varied geographically over different time periods.

In 2003, the United States CLIVAR/CO_2 Repeat Hydrography Program began reoccupying a subset of the WOCE/JGOFS lines in an effort to evaluate the decadal changes in ocean carbon inventories. The program has identified 19 hydrographic sections distributed around the global ocean that will be reoccupied approximately every 10 yr. This work is being conducted in collaboration with other nations that have similar repeat hydrography programs. In 2007 the U.S. CLIVAR/CO_2 Repeat Hydrography Program completed a meridional section nominally along 90°E in the Indian Ocean marking the half-way point of the U.S. portion of the decadal survey effort (Fig. 3.24).

Isolating the anthropogenic component of the DIC change is not simply a matter of subtracting the values measured on two cruises separated in time. Aliasing from mesoscale eddies and frontal oscillations that displace isopycnal surfaces (Haine and Gray 2001; Peacock et al. 2005) as well as variations in water mass properties associated with climate modes such as the ENSO (Feely et al. 2002, 2006) can complicate the signal when comparing two cruises separated in time. To correct for these variations, we use the multiple linear regression approach first introduced by Wallace (1995). The application of these corrections varies depending on data quality and the oceanographic conditions along the section, thus each section must be evaluated separately. A full global assessment of ocean DIC changes cannot be made until the resurvey of the oceans is completed in the next few years. However, each updated ocean section provides incremental insight into how carbon uptake rates are evolving spatially and temporally.

Table 3.1 summarizes the current best estimates of anthropogenic CO_2 accumulation along representative north–south cruise tracks in the Atlantic and Pacific

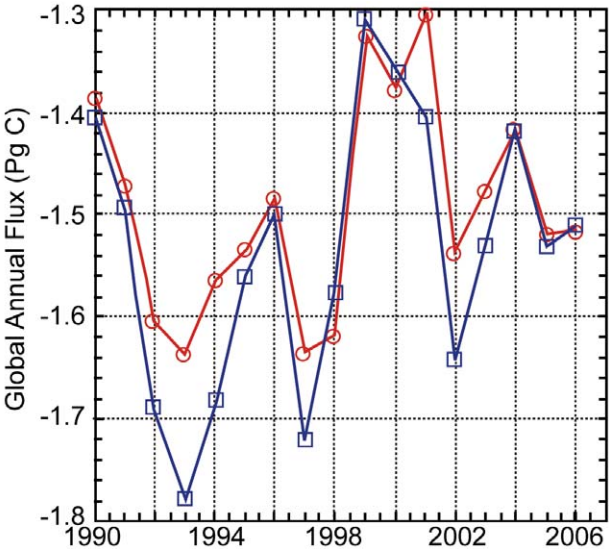

Fig. 3.23. Plots of global annual ocean CO_2 uptake using empirical functions described in the text. Red line is based on functions derived from Takahashi et al. (2002). Blue line is based on functions derived from Takahashi et al. (2007). The difference between the two lines gives a sense of the uncertainty in the estimates and how the improved data coverage in the 2007 climatology impacts the estimated interannual variability.

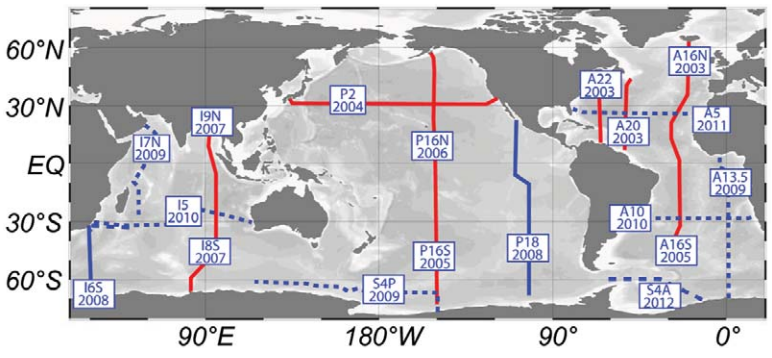

Fig. 3.24. Map of proposed and completed cruises for the U.S. CLIVAR/CO_2 Repeat Hydrography Program. Red lines show completed cruise, blue solid lines are 2008 cruises and the blue dashed lines show proposed cruises to complete the global survey.

Oceans over the last decade. The North Atlantic shows the largest increase, consistent with the long-term accumulation of Sabine et al. (2004), illustrating the importance of North Atlantic Deep Water formation as a mechanism for transporting anthropogenic CO_2 into the ocean interior. The formation of mode and intermediate waters in the Southern Hemisphere also contributes to the substantial DIC increases in the South Atlantic and South Pacific. The North Pacific shows a relatively modest increase because of the lack of deep-water formation and restricted intermediate water formation in that region.

Figure 3.25a shows the preliminary estimates of the accumulation of anthropogenic CO_2 in the Indian Ocean between the 1995 WOCE/JGOFS cruises and the 2007 repeat hydrography cruise. To a first order, the pattern of accumulation looks very similar to the anthropogenic CO_2 changes estimated by Sabine et al. (1999) between the 1978 GEOSECS cruise along 90°E and the 1995 WOCE/JGOFS cruise (Fig. 3.25b). Both sections show very little penetration of anthropogenic CO_2 into the high-latitude Southern Ocean with the deepest penetration, approximately 1,200–1,300 m, associated with the subtropical convergence zone at about 40°S. There is a suggestion of slightly deeper penetration of the 5 μmol kg^{-1} (minimum detection limit) contour and larger total inventory changes in the decade after WOCE/JGOFS compared to the decade before WOCE/JGOFS, but a full assessment of the uncertainties and patterns in these estimates is still underway.

These latest results show conclusively that anthropogenic CO_2 is continuing to accumulate in the Atlantic, Pacific, and Indian Oceans. Thus far, they agree with the long-term storage patterns of Sabine et al. (2004) that the largest inventories are associated with the regions where water masses are being formed and moving into the ocean interior. However, a single transect through an ocean basin is not sufficient for characterizing the full patterns of anthropogenic CO_2 storage. Results in both the Pacific and Atlantic Oceans have shown that circulation changes can have a significant impact on the net total change in carbon inventory on decadal time scales. In some cases these changes may enhance the storage of carbon and in other cases they may decrease the uptake resulting from rising atmospheric CO_2. Because circulation and biological changes can vary in cycles, it is critical to continue to monitor the changes in carbon inventories and how they interact with the secular increases in anthropogenic CO_2. As additional cruises are completed the full picture of the decadal storage will be developed.

g. Global ocean phytoplankton and productivity—M. J. Behrenfeld, D. A. Siegel, and R. T. O'Malley

Phytoplankton, the single-celled photosynthetic prokaryotic and eukaryotic organisms of the upper sunlit "photic" zone, are the base of ocean ecosystems and the primary conduit through which inorganic carbon is transferred into the organic carbon pool, driving the biological pump. This photosynthetic uptake of CO_2 by phytoplankton represents a key mechanism

Table 3.1. Estimates of ocean column inventory changes in anthropogenic carbon (mol C m^{-2} yr^{-1}) over the last decade.

	Atlantic Ocean (along 25°W)	Pacific Ocean (along 152°W)	Indian Ocean (along 90°E)
Northern Hemsphere	0.63	0.25	*
Southern Hemisphere	0.75	0.41	*

*Indian Ocean changes are still being evaluated.

through which ocean biology influences climate. Climate, in turn, plays a key role in regulating the growth and biomass of phytoplankton by controlling the distribution of nutrients and the availability of light during the growing season. The interaction between climate and phytoplankton is complex. The net effect of a shift in regional climate can be either an increase or decrease in phytoplankton abundance and productivity depending on how that climate shift impacts limiting resources (light, nutrients) for phytoplankton in the region. Nevertheless, in the broadest sense, ocean circulation–ecosystem models predict that future climate warming will result in a net reduction in mixed layer phytoplankton biomass and productivity in low-latitude, permanently stratified oceans due to an intensification in nutrient stress, while yielding a net increase at higher latitudes due largely to an increase in growing season and mixed layer light levels (via enhanced stratification) (Boyd and Doney 2002; Bopp et al. 2001; Le Quéré et al. 2003; Sarmiento et al. 2004).

Satellite observations of ocean color provide the best means for assessing interannual variability in phytoplankton abundance and productivity on a global basis. The only two U.S. sensors to provide global climate-quality ocean color data are the SeaWiFS (1997 to end of 2007) and the subsequent Aqua MODIS (2002 to present). Thus, 2007 was a milestone year marking the first full decade of climate-quality ocean color data. One of the primary products derived from satellite ocean color is surface-layer Chl_{sat}. Chlorophyll is not a robust measure of phytoplankton biomass, as it is strongly influenced by mixed layer growth conditions (light and nutrients), but it does provide an integrated index of phytoplankton abundance and physiology (Behrenfeld et al. 2005; Siegel et al. 2005a). ΣChl, a more relevant property for ocean biology and biogeochemistry, is roughly proportional to the square root of Chl_{sat} and can be reliably estimated using any one of a wide range of published expressions (e.g., Morel and Berthon 1989). From ΣChl, NPP can be derived provided additional information on incident light levels, attenuation coefficients, and physiology is available (Behrenfeld and Falkowski 1997; Carr et al. 2006).

Surface chlorophyll concentrations vary globally by three orders of magnitude (roughly 0.03 to >30 mg m^{-3}), with a first-order spatial distribution reflecting variations in light, nutrients, and grazing pressure (Fig. 3.27a). Global average Chl_{sat} for the 10-yr SeaWiFS record has a mean value of 0.342 mg m^{-3}, but exhibits strong seasonal cycles that peak during boreal summer at 0.381 mg m^{-3} (range: 0.360–0.400 mg m^{-3}) and are minimal in austral summer at 0.302 mg m^{-3} (range: 0.285–0.320 mg m^{-3}). This seasonal cycle largely reflects hemispheric differences in high-latitude summer blooms, with Southern Hemisphere blooms above 45° latitude generally diminished relative to the Northern Hemisphere due to the prevalence of iron-limiting conditions in the Southern Ocean. For 2007, global average Chl_{sat} was 0.349 mg m^{-3} (close to the climatological mean), with monthly values ranging from 0.297 to 0.400 mg m^{-3} (Fig. 3.27a).

Global photic zone chlorophyll varies by only 1.3 orders of magnitude, but exhibits a similar spatial distribution as Chl_{sat} (Fig. 3.27b). The global mean ΣChl value for 2007 was 14.2 mg m^{-2}, which is identical to the climatological mean for the SeaWiFS record. The spatial distribution of ΣChl during 2007 nevertheless exhibited some interesting deviations from the climatological pattern (Fig. 3.27c). In 2007,

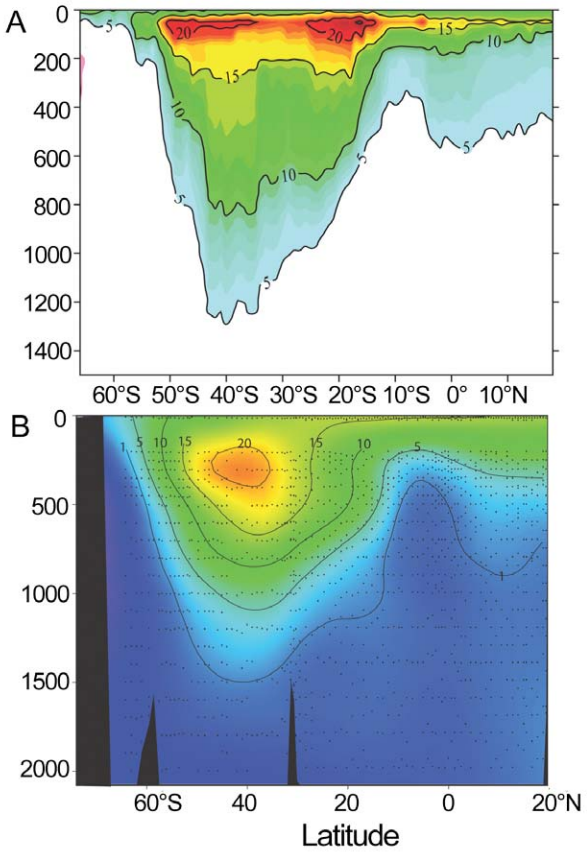

Fig. 3.25. Sections of change in anthropogenic CO_2 (μmol kg^{-1}) based on observations made in the Indian Ocean and Southern Ocean (along ~90°E) for the time period (a) 2007–1995 and (b) 1995–78. The black dots in (b) indicate the measurement locations used for the calculations.

Since the beginning of the industrial revolution the release of CO_2 from humankind's collective industrial and agricultural activities has resulted in atmospheric CO_2 concentrations that have risen from preindustrial levels of about 280 ppmv to nearly 385 ppmv. The atmospheric concentration of CO_2 is now higher than experienced on Earth for at least the last 800,000 yr and probably over 20 million yr, and is expected to continue to rise at an increasing rate. The oceans have absorbed approximately 525 billion tons of carbon dioxide from the atmosphere, or about one-third of the anthropogenic carbon emissions released. This absorption has proven beneficial in damping the rise of carbon dioxide concentrations in the atmosphere; however, the ocean's uptake of carbon dioxide is having negative impacts on the chemistry and biology of the oceans. Hydrographic surveys and modeling studies have revealed that the chemical changes in seawater resulting from the absorption of carbon dioxide are lowering seawater pH. For example, the time series data at Ocean Station Aloha shows an average pH decrease of approximate 0.02 units per decade in the northeast Pacific (Fig. 3.26; after Feely et al. 2008). The pH of ocean surface waters has already decreased by about 0.1 units from an average of about 8.21 to 8.10 since the beginning of the industrial revolution (Feely et al. 2004). Estimates of future atmospheric and oceanic carbon dioxide concentrations, based on the IPCC CO_2 emission scenarios and coupled ocean–atmosphere models, suggest that by the middle of this century atmospheric carbon dioxide levels could reach more than 500 ppm, and near the end of the century they could be over 800 ppm. This would result in an additional surface water pH decrease of approximately 0.3 pH units by 2100 (Feely et al. 2004; Orr et al. 2005). When CO_2 reacts with seawater, the reduction in seawater pH also reduces the availability of carbonate ions, which play an important role in shell formation for a number of marine organisms such as corals, marine plankton, and shellfish. This phenomenon, which is commonly called "ocean acidification," could have profound impacts on some of the most fundamental biological and geochemical processes of the sea in coming decades. Some of the smaller calcifying organisms are important food sources for higher marine organisms. Declining coral reefs, which are presumed to be due to increases in temperature and decreases in carbonate ion, have been observed in the oceans (Hoegh-Guldberg et al. 2007; Cooper et al. 2008). Further decline of the coral reefs would have negative impacts on tourism and fisheries. Abundance of commercially important shellfish species may also decline and negative impacts on finfish may occur. This rapidly emerging scientific issue and possible ecological impacts have raised serious concerns across the scientific and fisheries resource management communities.

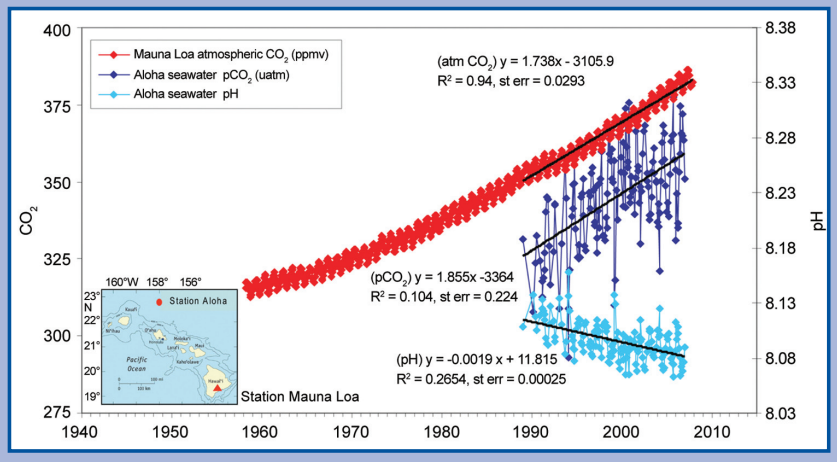

FIG. 3.26. Time series of atmospheric CO_2 at Mauna Loa (ppmv) and surface ocean pH and pCO_2 (µatm) at Ocean Station Aloha in the subtropical North Pacific Ocean. Note that the increase in oceanic CO_2 over the last 17 yr is consistent with the atmospheric increase within the statistical limits of the measurements. [Mauna Loa data: Dr. Pieter Tans, NOAA/ESRL, www.esrl.noaa.gov/gmd/ccgg/trends; HOTS/Aloha data: Dr. David Karl, University of Hawaii, http://hahana.soest.hawaii.edu.]

values of ΣChl were 10% or more above climatological average values in 11% of the global ocean area and 10% or more below climatological values in 13% of the ocean, with 46% of the gains and 58% of the losses occurring in the permanently stratified oceans (approximated by waters with annual average SST > 15°C). The patterns observed here are consistent with the recent satellite data analyses of Polovina et al. (2008).

Zonal average anomalies in ΣChl for 2007 relative to climatological values were inversely related to changes in SST equatorward of 45° latitude (Fig. 3.28). While this result at first appears consistent with earlier model expectations of decreased biological productivity from enhanced nutrient stress in the tropics and subtropics under warming conditions, Behrenfeld et al. (2008) show that physiological responses to changing mixed layer light conditions

(i.e., "photoacclimation") also play an important role. In contrast to the stratified oceans, a simple relationship between ΣChl and temperature changes at latitudes poleward of 45° is not observed in the annual zonal anomalies for 2007 (Fig. 3.28).

Global SST and chlorophyll values for 2007 were very close to climatological average values for the SeaWiFS period, making a relationship between these two properties difficult to decipher. A much clearer view of the ocean biology–climate link emerges when the 2007 data are viewed in the context of the entire 10-yr record (Fig. 3.29). Monthly anomalies in ΣChl for Northern Hemisphere high-latitude regions with annual average SST <15°C (roughly >45°N) exhibit an overall increase ($p < 0.001$) between 1997 and 2007, with a secondary oscillation peaking first in 2000–01 and again in 2006–07 (Fig. 3.29a). These changes in ΣChl exhibited a striking inverse correspondence with anomalies in SST (Fig. 3.29a). In the permanently stratified lower-latitude oceans, chlorophyll anomalies rose rapidly during the 1997 to 1999 El Niño–La Niña transition and then generally decreased thereafter (Fig. 3.29b). These chlorophyll changes also exhibit a strong inverse correlation with low-latitude SST anomalies (Fig. 3.29b). Finally, ΣChl anomalies at high southern latitudes indicate a slight but significant ($p < 0.001$) rise over the 1997 to 2007 period, which once again is inversely correlated with SST changes (Fig. 3.29c). In summary, all three zones show clear relationships between chlorophyll and climate fluctuations, but in each case either the sign of the relationship or the underlying physiology is inconsistent with model predictions.

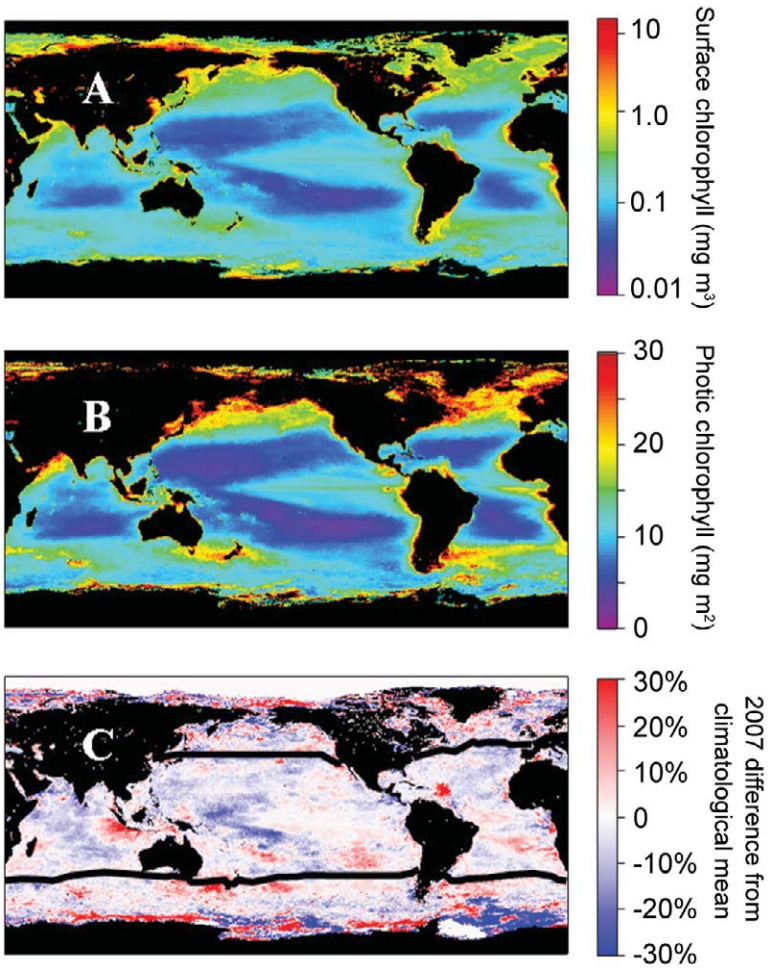

Fig. 3.27. (a) Average surface Chl_{sat} for 2007. (b) Average ΣChl for 2007. (c) Percentage difference between 2007 annual average ΣChl and climatological mean values for the SeaWiFS record. Heavy black lines demark low-latitude permanently stratified oceans (annual average SST >15°C) from higher-latitude regions (annual average SST <15°C).

The 2007 values and 10-yr chlorophyll record described above are based on the OC4v4 chlorophyll algorithm, the operational algorithm for SeaWiFS. The drawback of an empirical wavelength ratio algorithm, such as OC4v4, is its limited capacity to account for independent behavior in the multiple optically active in water constituents regulating the ocean color signal (IOCCG IOP report 2006). To assess the role of independent variations in ocean optical properties on our above results, we repeated the analysis using chlorophyll estimates from the alternative GSM semianalytical algorithm (Maritorena et al. 2002). The GSM inverts ocean color data to simultaneously solve for the independent contributions of chlorophyll absorption, particulate backscattering, and absorption by cDOM. The GSM algorithm yields monthly average chlorophyll values for the stratified oceans that are highly correlated with OC4v4 estimates ($r^2 = 0.84$), but are on average 34% lower. For the higher-latitude regions, GSM monthly Chl_{sat} values are more divergent from ($r^2 = 0.22$) and 43% lower than the OC4v4 estimates. These differences are due to the variable fraction of light absorption attributed to cDOM in GSM (Siegel et al. 2005b). For 2007, the GSM yields a global average Chl_{sat} of 0.216 mg m^{-3}, which is 38% lower than the global OC4v4 estimate above. When applied to

a simple NPP algorithm (Behrenfeld and Falkowski 1997), the GSM and OC4v4 chlorophyll values for 2007 yield productivity estimates of 46.6 and 55.1 Pg C yr^{-1}, respectively. However, although the two algorithms diverge significantly in chlorophyll and NPP estimates, their monthly anomalies in ΣChl for the full SeaWiFS record are in close agreement, indicating that the ocean biology–climate relationship illustrated in Fig. 3.29 is largely insensitive to choice of chlorophyll algorithm.

An added benefit of the semianalytical approach is that it provides estimates of particulate backscatter coefficients, which can be used to assess phytoplankton carbon biomass (Behrenfeld et al. 2005; Westberry et al. 2008). Behrenfeld et al. (2008) used this additional phytoplankton biomass information to resolve the underlying basis for interannual changes in Chl_{sat} observed over the SeaWiFS record. They found that changes in Chl_{sat} between September 1997 and December 2000 were largely due to changes in phytoplankton abundance. After 2000, however, phytoplankton biomass was relatively invariant and trends in Chl_{sat} were largely due to physiological changes in intracellular pigmentation. Between 2001 and 2006, these physiological adjustments could be primarily attributed to changes in global mixed layer light levels, but from 2006 through 2007 changes

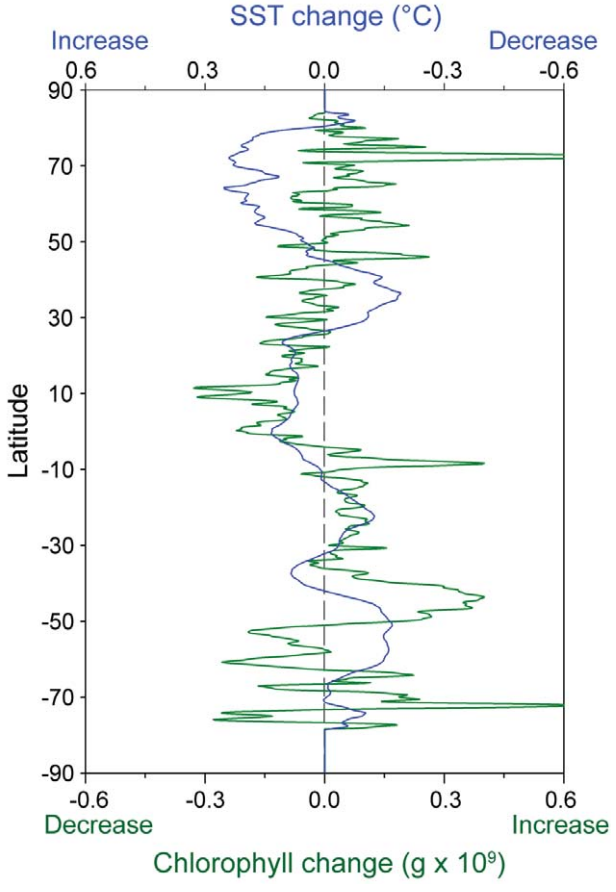

Fig. 3.28. Changes in ΣChl (green line, bottom axis) and SST (blue line, top axis) calculated as the difference between 2007 and climatological average values for the SeaWiFS period. Note that ΣChl changes show decreases on the left and increases on the right (bottom axis), while SST changes show increases on the left and decrease on the right (top axis). SST changes were calculated using only pixels where chlorophyll data were available.

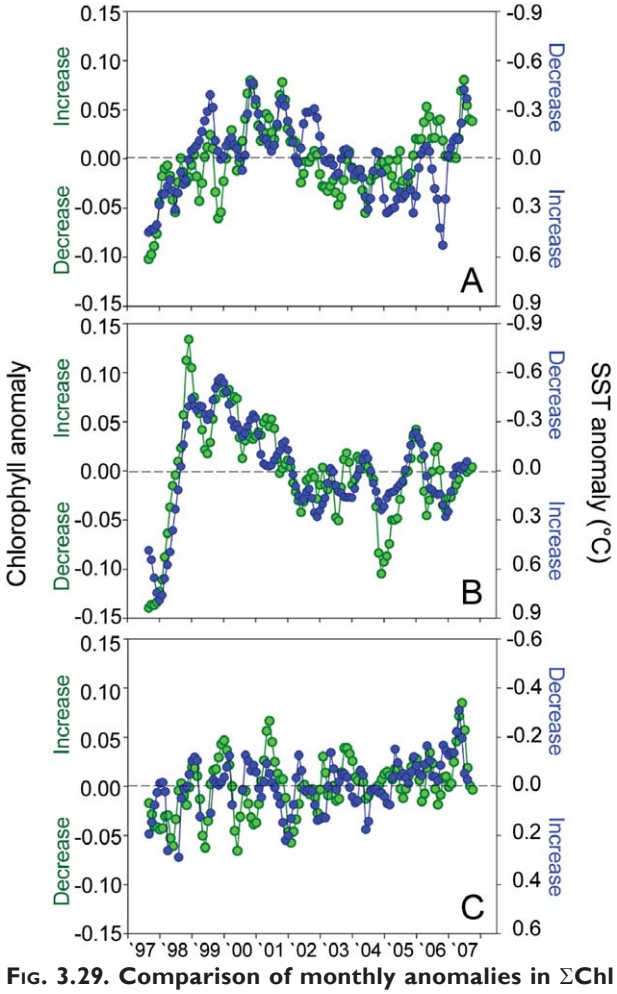

Fig. 3.29. Comparison of monthly anomalies in ΣChl (green symbols, left axis) and SST (blue symbols, right axis) for the 10-yr SeaWiFS record. (a) Northern waters with annual average SST <15°C. (b) Permanently stratified waters with annual average SST >15°C. (c) Southern waters with annual average SST <15°C. Horizontal dashed line indicates monthly climatological average values. Note, left axes increase from bottom to top, while right axes decrease from bottom to top. Also note that all left axes have the same range, while the right axis in (c) has a smaller range than in (a) and (b).

in global mixed layer nutrient levels appeared to be more important. Thus, although global Chl_{sat} values for 2007 are close to the climatological average for the SeaWiFS era, their ecological basis (i.e., combined influence of biomass and physiology) appears dissimilar from all years prior to 2006 (Behrenfeld et al. 2008).

A decade of global observations has demonstrated an exceptionally close pole-to-pole link between phytoplankton chlorophyll variability and coincident fluctuations in climate, with warming trends associated with decreases in chlorophyll and cooling trends associated with increases. Unfortunately, absence of plans to replace the aging MODIS and now dysfunctional SeaWiFS sensors, which are the only sources of climate-quality ocean color data records, jeopardizes further elucidation of this remarkable relationship between climate and ocean biology, observations of which contrast sharply with relationships predicted from ocean circulation–ecosystem models.

4. THE TROPICS—H. J. Diamond and G. D. Bell, Eds.

a. Overview—H. J. Diamond

This tropics section consists of five primary topics: 1) ENSO and the tropical Pacific; 2) the MJO; 3) TC activity for the 2007 season in seven basins: the North Atlantic, eastern North Pacific, northwest Pacific, north Indian and south Indian, South Pacific, and Australia; 4) ITCZ behavior in the Pacific and Atlantic basins; and 5) a new section on the Indian Ocean dipole.

The year was characterized by a transition to La Niña conditions that, while not developed until August, resulted in suppressed convection near the date line by early June. Therefore, La Niña–like impacts on the upper-tropospheric circulation were already evident during June–August across the subtropical South Pacific. At times, the patterns of tropical convection were strongly modulated by the MJO, which likely influenced the onset of La Niña.

The 2007 Atlantic hurricane season was near normal, and slightly more active than in 2006. In the North and south Indian Ocean Basins, the numbers and strength of the TCs were significantly above average and included a world record rainfall amount of 5,510 mm over a 3–8-day period associated with a TC in the south Indian Ocean Basin. A sidebar expanding on the extraordinary north Indian Ocean TC season, which featured two category 5 storms,[1] is included. In contrast, TC activity was significantly below average in the eastern North Pacific and northwest Pacific basins, and in the southwest Pacific and Australian regions.

A very strong positive phase of the Indian Ocean dipole was present during 2007, and its possible climate impacts are examined. This pattern likely contributed to the lack of a traditional La Niña signal in the Northern Hemisphere subtropics during the peak of the Atlantic hurricane season.

b. ENSO and the tropical Pacific—G. D. Bell and M. Halpert

ENSO is a coupled ocean–atmosphere phenomenon, and is the leading mode of interannual variability over the equatorial Pacific Ocean. Opposite phases of ENSO are called El Niño and La Niña. El Niño is a periodic warming of the central and east-central equatorial Pacific, which acts to strengthen convection in these regions and to suppress convection over Indonesia. Conversely, La Niña is a quasi-periodic cooling of the central and east-central equatorial Pacific, which acts to shut down convection in these regions and to enhance convection over Indonesia. These convection patterns extend more than half the distance around the globe, and are the main mechanism by which ENSO impacts the upper-tropospheric circulation.

NOAA defines El Niño and La Niña using the Niño-3.4 index, which measures area-averaged SST anomalies between 5°N–5°S, 170°–120°W. El Niño occurs when the 3-month running mean of the Niño-3.4 index (called the ONI) reaches +0.5°C, and La Niña occurs when the ONI reaches –0.5°C. Both phases of ENSO occurred during 2007. The Niño-3.4 index shows that a weak El Niño dissipated early in the year, and a moderate-strength La Niña developed late in the year (Fig. 4.1).

For the entire DJF 2006–07 season, the Niño-3.4 index averaged +0.8°C, which satisfied NOAA's definition for El Niño. Equatorial SSTs were generally +0.5° to +1.0°C above average between the date line and the west coast of South America during the period, with the largest departures (exceeding +1°C) centered near the date line and over portions of the eastern Pacific Ocean (Fig. 4.2a). Much of this anomalous warmth dissipated rapidly during January and February, with the weekly Niño-3.4 index returning to zero by mid-February.

During DJF the positive subsurface temperature anomalies were confined mainly to the region around the date line. These anomalies were weak (+1.0° to +2.0°C) and only extended to a depth of 100 m (Fig. 4.3a). Small negative anomalies were present across the equatorial Pacific Ocean at the thermocline depth, which is generally situated between 100 and 150 m as indicated by the depth of the 20°C isotherm (solid black line) in Fig. 4.3a. This pattern reflects a confinement of the anomalously warm water to the near-surface, and a shoaling of the thermocline in association with enhanced upwelling. These condi-

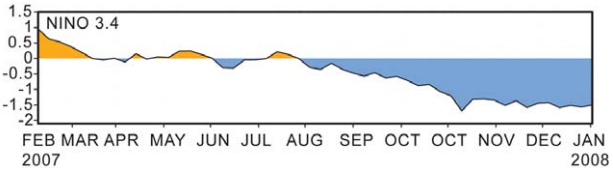

Fig. 4.1. Time series of SST anomalies (°C) in the Niño-3.4 region (5°N–5°S, 170°–120°W). Anomalies are departures from the 1971–2000 base period weekly means, and are obtained from the adjusted OI dataset (Smith and Reynolds 1998).

[1] Tropical cyclone categories are typically described using the Saffir–Simpson scale, and unless otherwise noted, category designations in this chapter will reflect Saffir–Simpson scale values (see www.nhc.noaa.gov/aboutsshs.shtml).

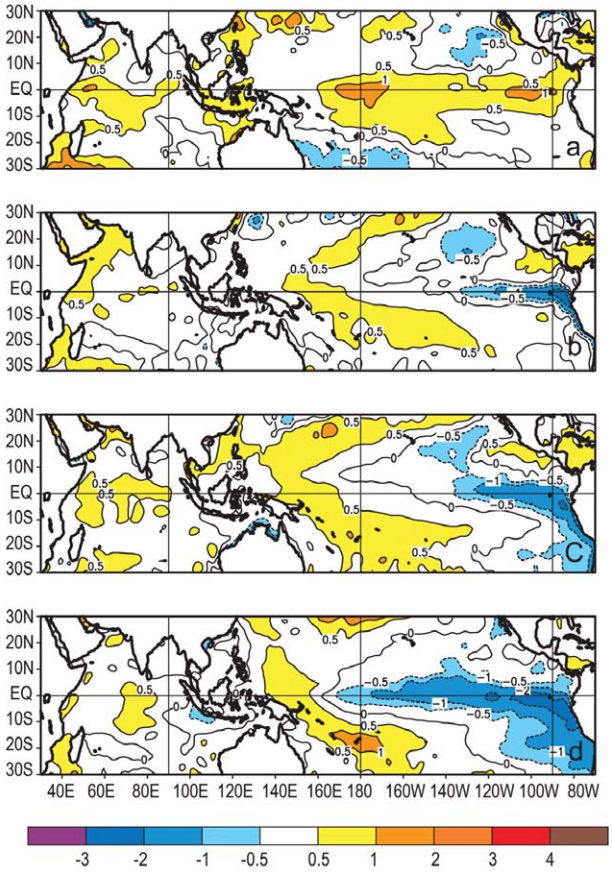

Fig. 4.2. SST anomalies (°C) during (a) Dec–Feb 2006–07, (b) Mar–May 2007, (c) Jun–Aug 2007, and (d) Sep–Nov 2007. Anomalies are departures from the 1971–2000 adjusted OI climatology (Smith and Reynolds 1998).

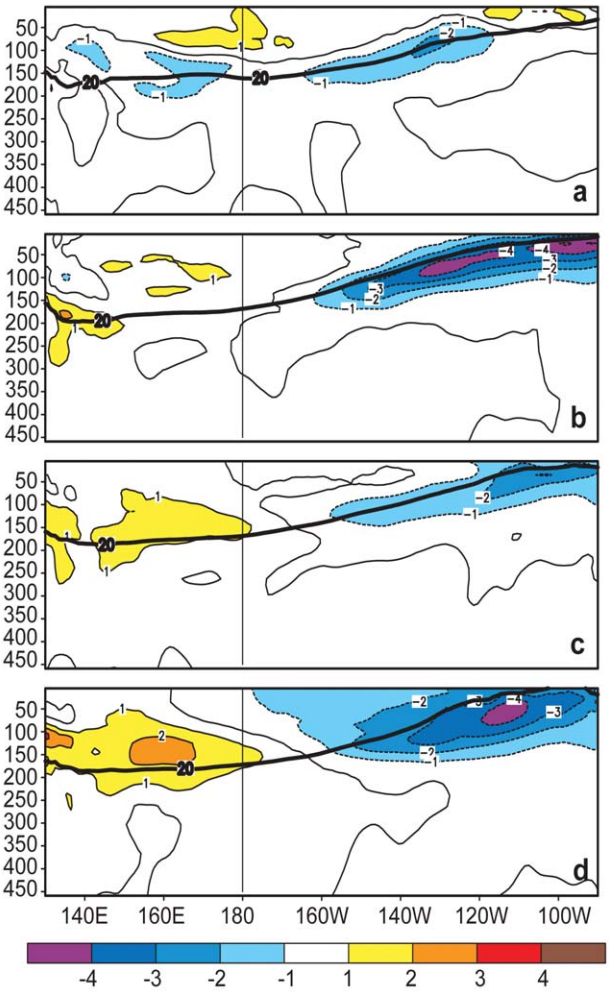

Fig. 4.3. Equatorial depth–longitude section of ocean temperature anomalies (°C) averaged between 5°N–5°S during (a) Dec–Feb 2006–07, (b) Mar–May 2007, (c) Jun–Aug 2007, and (d) Sep–Nov 2007. The 20°C isotherm (thick solid line) approximates the center of the oceanic thermocline. The data are derived from an analysis system that assimilates oceanic observations into an oceanic GCM (Behringer et al. 1998). Anomalies are departures from the 1971–2000 period monthly means.

tions were consistent with a weak and dissipating El Niño.

The patterns of anomalous tropical convection during DJF were also consistent with El Niño (shading, Fig. 4.4a). However, anomalous easterly winds at 850-hPa near the date line were not consistent with El Niño, and instead were associated with the increased oceanic upwelling. These easterly anomalies subsequently persisted throughout the year (Figs. 4.4b–d), and contributed to the drop in SST (Figs. 4.2b–d) and subsurface temperature (Figs. 4.3b–d) anomalies associated with the development of La Niña. By October–December, the value of the ONI had decreased to –1.2°C, indicating the strongest La Niña since 1999.

During key times of the year, the surface and subsurface temperature anomalies associated with ENSO were also strongly modulated by the MJO and its associated equatorial oceanic Kelvin wave activity (Figs. 4.7 and 4.8, section 4c). In December 2006, the upwelling phase of a strong Kelvin wave was triggered by an MJO and produced a sharp increase in upper-ocean heat content across the central and east-central equatorial Pacific. This was followed in January and early February by the upwelling phase of the wave, which contributed to El Niño's rapid demise (Fig. 4.8).

MJO activity also occurred during May–June, and the associated Kelvin wave activity may have delayed the onset of La Niña. For example, in June the downwelling phase of a Kelvin wave temporarily eliminated the negative heat content anomalies from

the entire eastern equatorial Pacific. The negative anomalies soon reappeared, but were interrupted by another Kelvin wave in early August. However, this impact was short-lived, and La Niña finally developed during August. During September–December, La Niña strengthened in association with a persistent pattern of suppressed convection and enhanced low-level easterly winds near the date line. Although the MJO and Kelvin wave activity were still present during this period, their impact on the oceanic heat content and SSTs was weaker, and mainly involved modulating the strength and westward extent of the negative anomalies associated with La Niña.

Although La Niña did not develop until late summer, suppressed convection was already established near the date line by early June (Fig. 4.5). Therefore, La Niña–like impacts on the upper-tropospheric (200 hPa) circulation were already evident during JJA across the subtropical South Pacific (Fig. 4.6a) (Kidson and Renwick 2002). These impacts included an extensive area of cyclonic anomalies across the subtropical South Pacific, and westerly wind anomalies (4–8 m s^{-1}) along the equator. Other impacts included easterly wind anomalies (4–12 m s^{-1}) across the eastern extratropical South Pacific, which reflected a marked westward retraction of the wintertime South Pacific jet stream and its associated jet exit region. As La Niña strengthened during SON, these anomalies became better defined and cyclonic anomalies also began to appear in the Northern Hemisphere subtropics near the date line (Figs. 4.6b).

By December, the La Niña signal was strongly influencing the upper-tropospheric circulation across the Pacific/North American sector. Impacts included a westward retraction of the wintertime East Asian jet stream. The downstream circulation features were also retracted westward, with a shift of the mean ridge from western North America to the central/eastern North Pacific, and a shift of the mean Hudson Bay trough to central and possibly western portions of North America. These conditions were associated with above average precipitation over much of the northern tier of the United States, and above-average temperatures in the southeast.

Regional La Niña impacts during 2007 included suppressed convection across the central and east-central equatorial Pacific, well above-average rainfall in South Africa during the first four months of

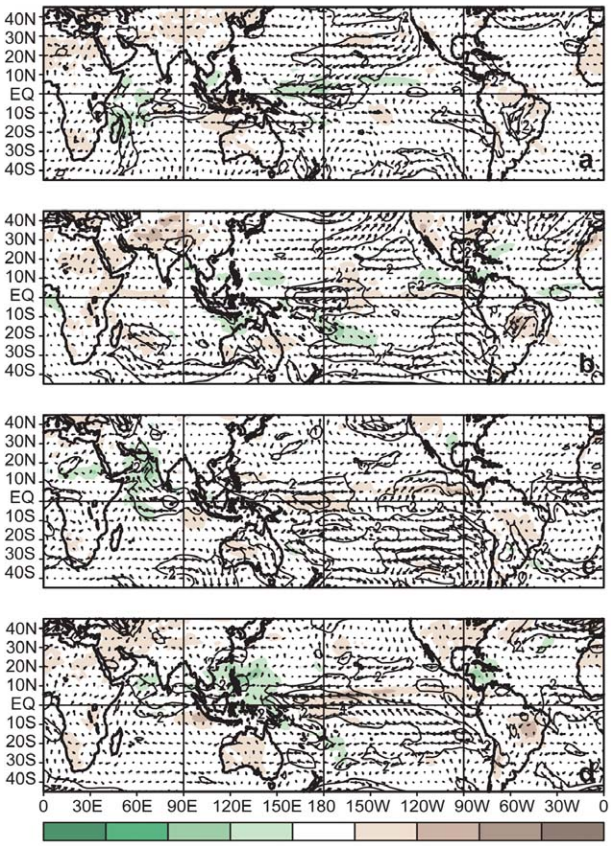

Fig. 4.4. Anomalous 850-hPa wind vector and speed (m s^{-1}) and anomalous outgoing longwave radiation (shaded, W m^{-2}) during (a) Dec–Feb 2006–07, (b) Mar–May 2007, (c) Jun–Aug 2007, and (d) Sep–Nov 2007. Anomalies are departures from the 1979–95 period monthly means.

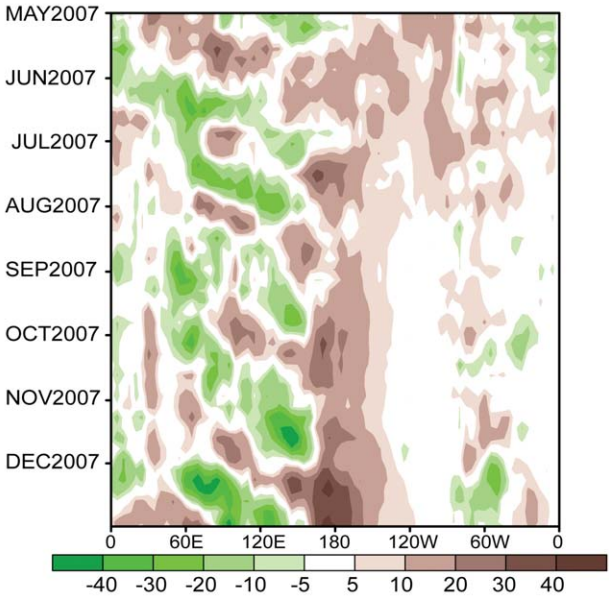

Fig. 4.5. OLR (W m^{-2}): (a) Time–longitude section of pentad anomalies between 5°N and 5°S. Green shading indicates enhanced convection, and brown shading indicates suppressed convection. Anomalies are departures from the 1979–2000 period means.

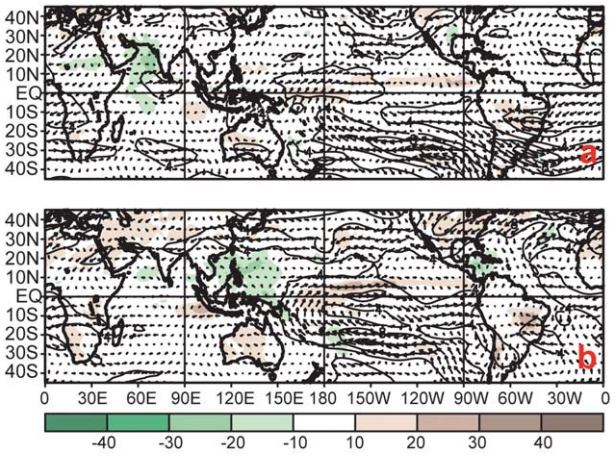

Fig. 4.6. Anomalous 200-hPa wind vector and speed (m s^{-1}) and anomalous OLR (shaded, W m^{-2}) during (a) Jun–Aug 2007, and (b) Sep–Nov 2007. Anomalies are departures from the 1979–95 period monthly means.

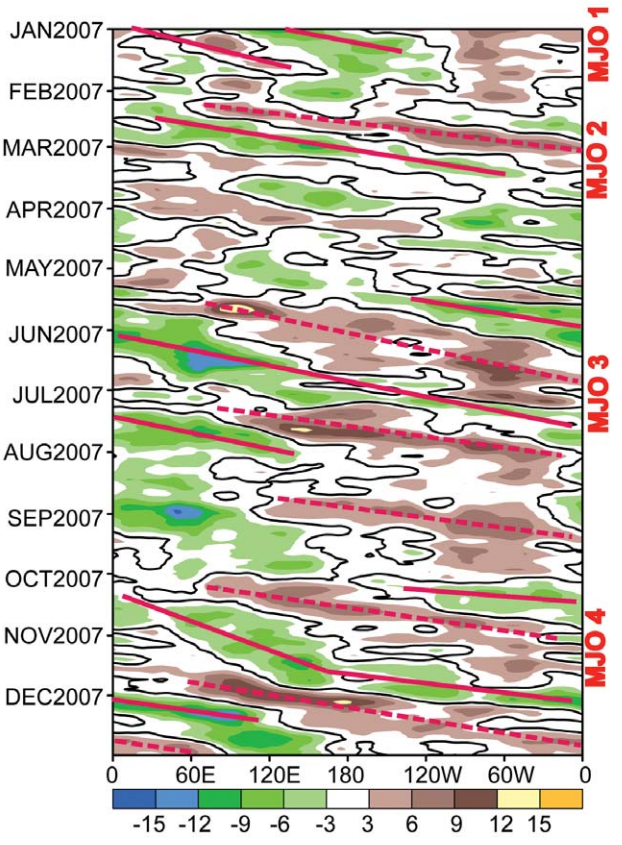

Fig. 4.7. Time–longitude section of 200-hPa velocity potential anomalies (5°N–5°S) for 2007. Green (brown) shading indicates anomalous divergence (convergence). Red lines highlight the MJO signal, and the four main periods of MJO activity are marked. Anomalies are departures from the 1971–2000 base period daily means.

the 2007–08 rainy season, increased storminess in the northwestern United States, and above-average temperatures across the southern tier of the United States. Another impact was the continuation of below average precipitation in the drought-stricken regions of northern Alabama, northern Georgia, and western North and South Carolina during the period from October to December. The SPCZ was displaced through ENSO activity, leading to regional rainfall anomalies over the southwest Pacific (see section 4d1).

c. The Madden–Julian Oscillation—J. Gottschalck and G. D. Bell

The MJO (Madden and Julian 1971, 1972, 1994) is a leading climate mode of tropical convective variability that occurs on intraseasonal time scales. The convective anomalies associated with the MJO often have the same spatial scale as ENSO, but differ in that they exhibit a distinct eastward propagation and generally traverse the globe in 30–60 days. The MJO can strongly affect the tropical and extratropical atmospheric circulation patterns, and sometimes produces ENSO-like anomalies (Mo and Kousky 1993; Kousky and Kayano 1994; Kayano and Kousky 1999). The MJO is often quite variable in a given year, with periods of moderate-to-strong activity sometimes followed by little or no activity. Overall, the MJO tends to be most active during neutral and weak ENSO periods, and is often absent during strong El Niño events (Zhang 2005; Zhang and Gottschalck 2002; Hendon et al. 1999).

The MJO is reflected in continuous propagation of 200-hPa velocity potential anomalies around the globe. A time–longitude section of this parameter shows four distinct periods during 2007 with at least moderate MJO activity (Fig. 4.7). These include 1) a strong event in January, 2) a short-lived event of moderate strength during late February and early March, 3) a long-lived event of moderate strength from May through early August, and 4) a strong event from late October through December.

The January event was a continuation of MJO activity that began in late 2006. That activity had previously triggered a strong equatorial oceanic Kelvin wave, whose upwelling phase and associated sharp drop in SSTs contributed to the rapid end of El Niño in early January. During January, enhanced equatorial convection associated with the MJO propagated eastward from Indonesia to the central Pacific Ocean, followed by an extended period of enhanced convection near the date line. These conditions were associated with anomalous easterly flow

and enhanced upwelling, which contributed to the drop in upper-ocean heat content in the east-central equatorial Pacific in February (Fig. 4.8).

The moderate-strength MJO activity during May through early August resulted in three distinct periods with below-average easterly winds near the date line. An oceanic Kelvin wave was triggered by the MJO during each of these periods (Fig. 4.8). Each wave was weaker than its predecessor, in part because of a gradual decrease in strength of the MJO. This Kelvin wave activity produced considerable intraseasonal variability in the SSTs and heat content across the central and east-central equatorial Pacific. In early June, the downwelling phase of a Kelvin wave eliminated the negative heat content anomalies in these regions. Significant cooling then ensued in late June as the upwelling phase of the wave propagated eastward. Another Kelvin wave produced a similar pattern of warming followed by cooling in late July and early August. This variability most likely delayed the onset of La Niña.

The strongest MJO event of the year began during October and lasted through December. This was the strongest and longest-lived event since March–June 2005. The 2007 event is somewhat unusual, in that MJO activity is typically reduced during La Niña. The resulting increased upwelling, which was linked to periods of enhanced easterly winds and the upwelling phases of oceanic Kelvin waves, acted to periodically reinforce the negative SST anomalies associated with La Niña. The MJO also periodically reinforced the La Niña–related pattern of tropical convection, as was seen in mid-December when exceptionally dry conditions spanned the central equatorial Pacific and exceptionally wet conditions covered Indonesia.

The MJO activity late in the year had two additional noteworthy impacts. It delayed the onset of the northwest Australia monsoon by 1–2 weeks in early December, and then strengthened that monsoon later in the month. The MJO also contributed to periods of intense storminess along the U.S. west coast during December and early January 2008, which produced heavy precipitation in central and Southern California that is not characteristically seen during La Niña.

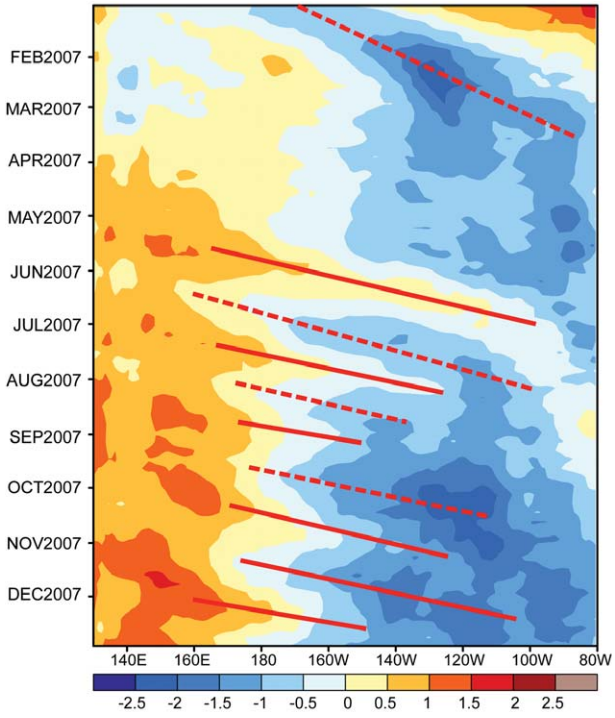

Fig. 4.8. Time–longitude section of anomalous upper ocean (0–300 m) heat content (5°N–5°S) during 2007. Blue (orange) shading indicates below (above) average heat content. The downwelling (solid) and upwelling (dashed) phases of oceanic Kelvin waves are indicated. Anomalies are departures from the 1982–2004 base period weekly means

d. Tropical cyclones

1) Overview—H. J. Diamond and D. H. Levinson

Averaged across all basins, the 2007 TC season (2006–07 in the Southern Hemisphere) saw a below normal (1981–2000 base) number of tropical or NS (≥34 kt) and HTC (≥64 kt), and significantly fewer major HTCs (≥96 kt) than average. Globally, 79 NSs developed during 2007 (18 below average), and 44 became HTCs (11 below average). Of these, only 18 (compared with 26 in 2006) attained major/intense status (average is 25.4). The global tallying of total storm numbers is always challenging, and involves more than simply adding up basin totals, as there are a number of storms that cross basin boundaries. Nonetheless, the overall numbers for the 2007 season were clearly below average.

The 2007 season was near normal in one basin (North Atlantic); significantly above average in two basins (NIO and SIO); and below average in the remaining basins (eastern North Pacific, northwest Pacific, southwest Pacific, and Australian). The SIO season saw twice the normal number of major TCs (6); while the NIO season featured two category 5 storms (Fig. 4.35), one of which was the strongest (and possibly first major TC) ever observed in the Arabian Sea. Both TCs caused considerable loss of life and extensive damage to the infrastructure of Oman, Iran, and Bangladesh (see sidebar article).

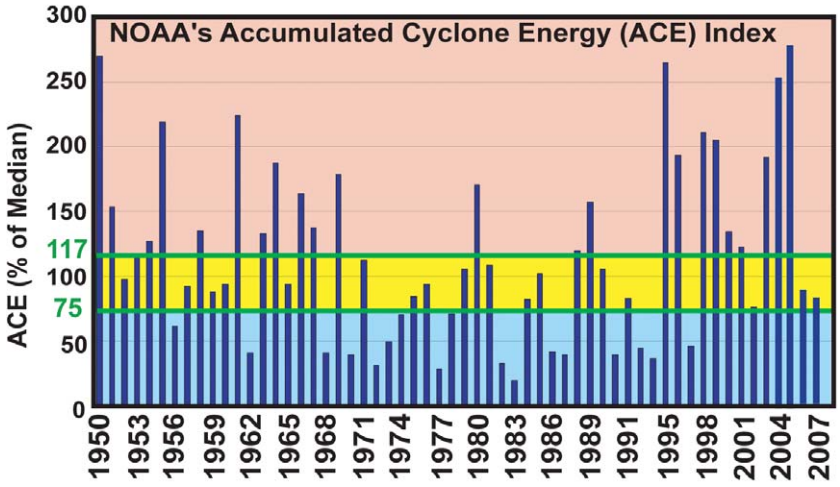

FIG. 4.9. NOAA's ACE index expressed as percent of the 1951–2000 median value (87.5×10^4 kt^2). ACE is a wind energy index that measures the combined strength and duration of the NSs. ACE is calculated by summing the squares of the 6-hourly maximum sustained wind speed in kts ($Vmax^2$) for all periods while the named storm has at least TS strength. Pink, yellow, and blue shadings indicate NOAA's classifications for above-, near-, and below-normal seasons, respectively.

2) ATLANTIC BASIN—G. D. Bell, E. Blake, C. W. Landsea, S. B. Goldenberg, R. Pasch, and T. Kimberlain

(i) Seasonal activity

The 2007 Atlantic hurricane season produced 15 NSs, 6 Hs and 2 MHs. The 1951–2000 averages are 11 NSs, 6 Hs, and 2 MHs. For 2007 the ACE index (Bell et al. 2000), a measure of the season's overall activity, was 84% of the 1950–2000 median (87.5×10^4 kt^2) (Fig. 4.9). This value is in the near-normal range (see www.cpc.noaa.gov/products/outlooks/background_information.shtml) and reflects fewer and generally shorter-lived hurricanes and MHs compared to recent years.

Two hurricanes made landfall in the Atlantic basin during 2007 with category 5 strength. MH Dean struck the Yucatan Peninsula near Costa Maya on 21 August with 150-kt sustained winds. MH Felix then made landfall near Punta Gorda, Nicaragua, on 2 September with 140-kt sustained winds. In addition, several other TSs and Hs struck the region around the Caribbean Sea. The United States was struck by one H, one NS, and three TD. This represented an increase in landfalling storms compared to 2006 (which had NS landfalls), even though both seasons had similar ACE index levels.

(ii) Atmospheric conditions

The peak months (ASO) of the season featured a persistent TUTT (also called the midoceanic trough) over the central North Atlantic and MDR [indicated by the green box spanning the tropical Atlantic and Caribbean Sea between 9.5°–21.5°N and 20.0°–80.0°W (Goldenberg and Shapiro 1996)] (Fig. 4.10). The period also featured a strong and persistent ridge over eastern North America.

During August and September, these conditions produced above-average vertical wind shear (Figs. 4.11a,c) and anomalous midlevel sinking motion (Figs. 4.11b,d) across the western half of the MDR, Gulf of Mexico, and the western and central subtropical North Atlantic. As a result, extensive areas were unfavorable for hurricane development and intensification.

These conditions include below-average vertical wind shear (the difference between the 200- and 850-hPa winds), above-average SSTs, and enhanced convection. However, the pressure pattern in the lower atmosphere was not particularly conducive to hurricane formation. The main area of low pressure was located over the northwestern Caribbean Sea and Central America, with much of the circulation located over land. The pronounced northward shift of this feature, which is normally situated over the southern Caribbean Sea, is likely to have suppressed TC formation in that region.

For the entire ASO period, the primary area of weak vertical wind shear (less than 8 m s^{-1}) was confined mainly to the extreme southern MDR and western Caribbean Sea (shaded regions, Fig. 4.12a).

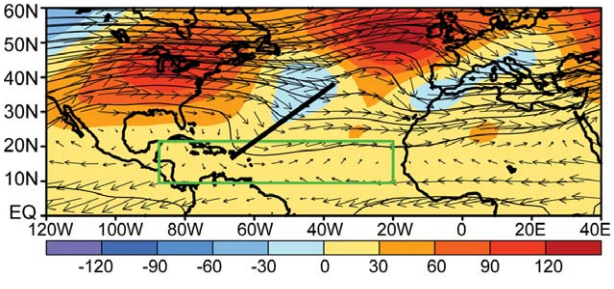

FIG. 4.10. Aug–Oct 2007: 200-hPa heights (contours, m), height anomalies (shaded), and vector winds (m s^{-1}). Thick solid line indicates the upper-level trough axis. Green box denotes the MDR. Anomalies are departures from the 1971–2000 period monthly means.

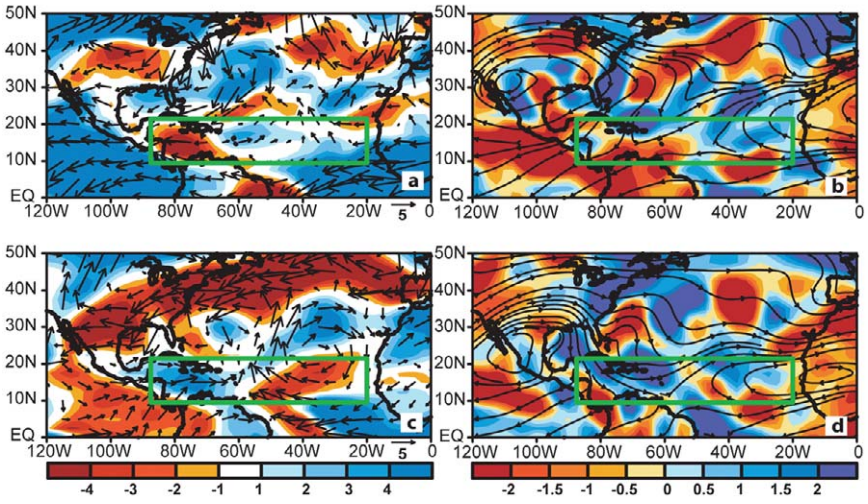

Fig. 4.11. (a),(c) The anomalous 200–850-hPa vertical wind shear strength (m s^{-1}) and vectors during (a) Aug and (c) Sep 2007. Red (blue) shading indicates below-average (above average) strength. (b),(d) The total 200-hPa streamlines and anomalous 500-hPa vertical motion (shaded) during (b) Aug and (d) Sep 2007. Red (blue) indicates anomalous ascent (descent). Green box denotes the MDR. Anomalies are departures from the 1971–2000 period monthly means.

This pattern was especially pronounced in August, when category 5 Hs Dean and Felix developed. Interestingly, the mean ASO vertical wind shear was below average across much of the MDR during ASO, which would normally suggest an above-normal season (Fig. 4.12b). However, for the eastern half of the MDR, most of the contribution to the negative anomalies came from October, a month when the total vertical shear is too strong to support TS formation.

It should be noted that improvements in tools such as QuikSCAT, and the AMSU, cyclone phase space, and the unique use of aircraft observations have likely led to more NSs and subtropical storms being identified now compared to a generation ago (Landsea 2007). For 2007, it is estimated that four NSs, Andrea, Chantal, Jerry, and Melissa, may not have been named a generation ago (Landsea 2007).

(iii) SSTs

SSTs in the MDR were above average (+0.27°C) during ASO 2007 (Fig. 4.13). This ongoing warmth since 1995 is associated with the warm phase of the AMO (Enfield and Mestas-Nuñez 1999) and the active Atlantic phase of the tropical multidecadal signal (Bell and Chelliah 2006). Some of the persistent warmth has also been linked to increasing global temperatures over the last 100 yr (Santer et al. 2006).

The above average SSTs during ASO 2007 were concentrated in the western half of the MDR, where departures averaged +0.47°C. The near-normal hurricane activity in these regions is not consistent with this ongoing warmth. Instead, it reflects the dominant role played by the atmospheric anomalies in controlling Atlantic hurricane activity (Shapiro and Goldenberg 1998). In the eastern MDR, SSTs cooled to near normal during ASO 2007. However, these cooler SSTs cannot account for the strong TUTT and upstream ridge in August and September or for the reduced Caribbean activity in October.

(iv) Prevailing global climate patterns

The occurrence of La Niña during an active hurricane era has been shown to significantly increase the probability of an above-normal Atlantic hurricane season,

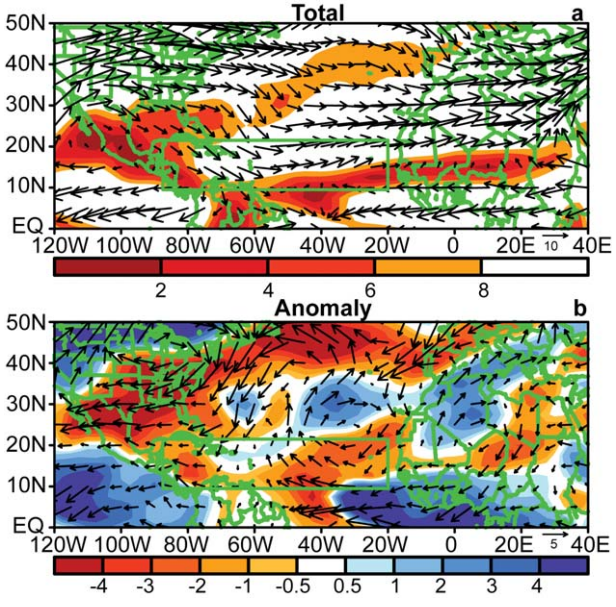

Fig. 4.12. Aug–Oct 2007: 200–850-hPa vertical wind shear magnitude (m s^{-1}) and vectors (a) total and (b) anomalies. In (a), shading indicates vertical wind shear below 8 m s^{-1}. In (b), red (blue) shading indicates below- (above) average magnitude of the vertical shear. Green box denotes the MDR. Vector scale is shown at bottom right of each panel. Anomalies are departures from the 1971–2000 period monthly means.

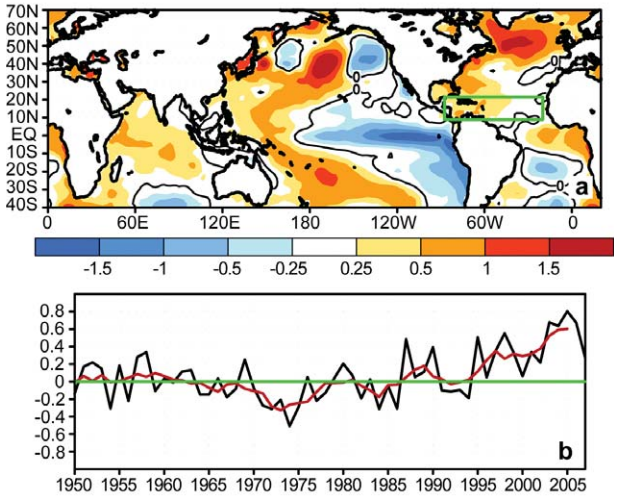

Fig. 4.13. (a) SST anomalies (°C) during Aug–Oct 2007. (b) Consecutive ASO values of SST anomalies in the MDR. Red line shows the corresponding 5-yr running mean. Green box in (a) denotes the MDR. Anomalies are departures from the 1971–2000 period monthly means.

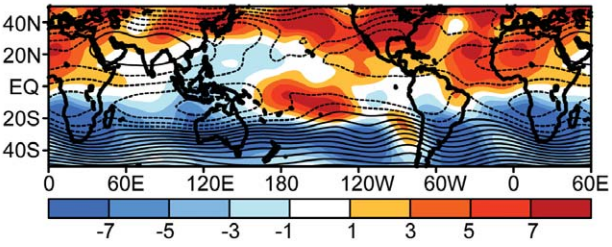

Fig. 4.14. Aug–Oct 2007: 200-hPa streamfunction (contours, interval is 10 x 106 m^2 s^{-1}) and anomalies (shaded). Anomalous ridges are indicated by positive values (red) in the NH and negative values (blue) in the SH. Anomalous troughs are indicated by negative values in the NH and positive values in the SH. Anomalies are departures from the 1971–2000 period monthly means.

in part because it typically produces a weaker TUTT and reduced vertical wind shear in the MDR (Gray 1984; Bell and Chelliah 2006). La Niña developed during August 2007, and subsequently reached moderate strength during September–November. Also, key atmospheric anomalies known to be associated with the current active hurricane period were in place as expected (section 2ivb).

(a) *La Niña*

Despite the strengthening La Niña during ASO 2007, its typical impacts on the upper-tropospheric circulation across the tropical North Pacific and MDR were notably absent (Fig. 4.14). Over the North Pacific, the 200-hPa streamfunction anomalies were weak, and the typical core of negative anomalies near the date line was absent. Also, there was a lack of persistent positive velocity potential anomalies near the date line, even though convection was suppressed throughout the region (Fig. 4.7). As a result, the downstream TUTT exhibited no connection to La Niña.

One suggested reason for this discrepancy is that convection over Indonesia and the eastern tropical Indian Ocean was also suppressed throughout the period (Fig. 4.15a). Negative streamfunction anomalies (indicating a weaker upper-level ridge) across the western subtropical North Pacific were consistent with this suppressed convection. These conditions are opposite to the typical La Niña signal, and indicate that the total La Niña forcing and resulting 200-hPa circulation anomalies were much weaker than would normally be expected for the observed Pacific cooling.

These conditions were associated with a record-strength pattern (Fig. 4.15b) that also included enhanced convection over the western equatorial Indian Ocean and enhanced convection across India and the Southeast Asian monsoon regions. This entire pattern is more typical of El Niño, as was seen in 2006. This climate signal may have overwhelmed the 200-hPa circulation anomalies normally associated with

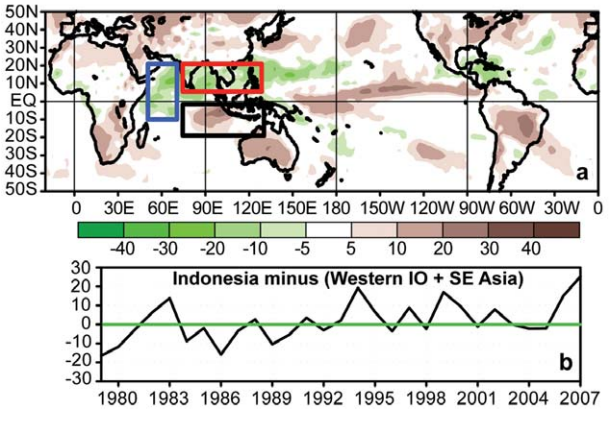

Fig. 4.15. Aug–Oct: (a) anomalous OLR (W m^{-2}), with green shading indicating enhanced convection, and brown shading indicating suppressed convection. (b) OLR time series based on boxed regions shown in (a). The time series is calculated as the area-averaged anomalies over Indonesia (black box) minus area-averaged anomalies over western IO (blue box) minus area-averaged anomalies over southeastern Asia (red box). Anomalies are departures from the 1979–2000 period monthly means.

La Niña, thus negating La Niña's normally enhancing influence on the 2007 Atlantic hurricane season. Conversely, this same pattern may have enhanced El Niño's suppressing influence on the 2006 Atlantic hurricane season (Bell et al. 2007).

(b) *Conditions associated with the ongoing active Atlantic hurricane era*

Although 2007 had about average activity, it was still more active than most seasons during the below-normal era 1971–94 (Fig. 4.9). A main contributing factor to the current active era is the tropical multidecadal signal, which reflects the leading modes of tropical convective rainfall variability occurring on multidecadal time scales (Bell and Chelliah 2006). A phase change in the tropical multidecadal signal corresponds with the dramatic transition in 1995 to the active era (Bell et al. 2007). Time series of key atmospheric wind parameters highlight the dramatic differences between these above-and below-normal hurricane eras (Fig. 4.16).

One key aspect of the current active hurricane era is an east–west oscillation in anomalous tropical convection between the West African monsoon region and the Amazon basin, signaling an enhanced West African monsoon system (Landsea and Gray 1992; Goldenberg and Shapiro 1996) and suppressed convection in the Amazon basin. A second aspect is ongoing above average SSTs in the North Atlantic, consistent with the warm phase of the Atlantic multidecadal mode (Goldenberg et al. 2001).

As shown by Bell and Chelliah (2006), these conditions are associated with an interrelated set of convectively driven atmospheric anomalies known to favor active hurricane seasons (Fig. 4.16). Most of these anomalies were again in place during 2007, including 1) enhanced ridging at 200 hPa in both hemispheres over the Atlantic Ocean (Fig. 4.14), 2) an enhanced tropical easterly jet and a westward expansion of the area of anomalous easterly winds at 200 hPa, 3) reduced tropical easterlies at 700-hPa across the central and eastern Atlantic (Fig. 4.16, middle), and 4) enhanced cyclonic relative vorticity along the equatorward flank of the African easterly jet (Fig. 4.16, bottom). In light of these ongoing conditions, there is no indication the current active hurricane era has ended.

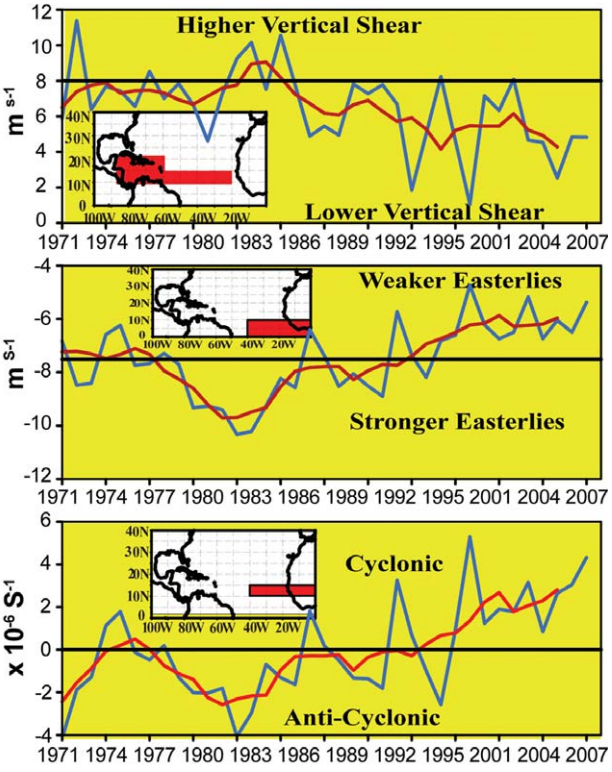

Fig. 4.16. Aug–Oct time series showing area-averaged values of (top) 200–850-hPa vertical shear of the zonal wind (m s^{-1}), (middle) 700-hPa zonal wind (m s^{-1}), and (bottom) 700-hPa relative vorticity (x 10^{-6} s^{-1}). Blue curve shows unsmoothed 3-month values, and red curve shows a 5-point running mean of the time series. Averaging regions are shown in the insets.

3) Eastern North Pacific basin—D. H. Levinson and J. Weyman

(i) Seasonal activity

The ENP basin includes two regions officially designated by NOAA's NWS for issuing NS and H warnings and advisories. The eastern Pacific warning area extends from the west coast of North America to 140°W and is the responsibility of NOAA's NHC in Miami, Florida, while the central Pacific warning area between 140°W and 180° is the responsibility of NOAA's CPHC in Honolulu, Hawaii. The 2007 TC activity in both these warning areas is covered using combined statistics, along with information summarizing activity and impacts in the central North Pacific region.

The ENP hurricane season officially lasts from 15 May to 30 November. The peak activity for the central (eastern) part of the region normally occurs in August (September). The 2007 ENP hurricane season produced 11 NSs, 4 Hs, and 1 MH (Fig. 4.17a). These values are well below the 1971–2005 averages, which are 16.2 NSs, 9.1 Hs, and 4.3 MHs. Four TDs also formed in the ENP during 2007 (03E, 04E, 05E, and 13E).

The 2007 season began quickly with two NSs in May (Alvin and Barbara), which has only happened twice before (1956 and 1984). However, the numbers of NSs and Hs were below normal in all subsequent

months. As a result, the seasonal ACE Index (Bell et al. 2000; Bell and Chelliah 2006) was only 52.7 $\times 10^4$ kt^2, which is less than half of the 1971–2005 mean (126.3 $\times 10^4$ kt^2), and the second lowest value (following 1977) since reliable records began in 1970 (Fig. 4.17b).

Only two systems (Cosme and Flossie) were observed in the central North Pacific region during 2007, which is also well below the 1971–2005 average of 4–5 TCs.[2] These storms both entered the region from the east.

(ii) Historical context of the 2007 ENP hurricane season

Since 1995, the numbers of NSs in the ENP basin has been near average, fluctuating around the long-term mean (Fig. 4.17a). However, the numbers of Hs and MHs have been generally below normal, with above normal H activity seen in only two seasons (2000 and 2006). NOAA has identified 8 of the 13 ENP seasons during 1995–2007 as being below normal, with only the 1997 and 2006 El Niño–influenced seasons producing above normal activity as measured by the ACE index. In contrast, higher activity seen during the preceding 1970–94 period, had 6 of 25 (24%) below normal seasons and 9 of 25 (36%) above normal seasons as measured by the ACE index.

These active and inactive ENP eras are opposite to those observed over the North Atlantic. Such east–west oscillations in activity reflect the large-scale atmospheric circulation anomalies that extend across both basins (Bell and Chelliah 2006). The spatial scale of these atmospheric anomalies is far larger than the area of warmer Atlantic SSTs (Lander and Guard 1998; Landsea et al. 1998, 1999; Goldenberg et al. 2001), suggesting this warmth alone is not a primary direct cause for the 1995 transition to generally below normal (above normal) ENP (Atlantic) hurricane seasons.

(iii) Environmental influences on the 2007 hurricane season

Seasonal TC activity (both frequency and intensity) in the ENP basin is influenced by several large-scale environmental factors, including SSTs, 200–850-hPa vertical wind shear, the phase of the ENSO in the equatorial Pacific region (Whitney and Hobgood 1997), and possibly the phase of the equatorial QBO in the tropical lower stratosphere. ENSO is known to strongly modulate both the SSTs and vertical wind shear on seasonal time scales (Whitney and Hobgood 1997). Multidecadal fluctuations in ENP activity are less well understood, but show a strong relationship to the phase of the tropical multidecadal signal (Bell and Chelliah 2006) and Atlantic hurricane activity.

El Niño typically favors an above-normal ENP season, while La Niña favors a below-normal season (NOAA 2007). These ENSO impacts are modulated by the multidecadal signal, with the combination of La Niña during an inactive hurricane era (as was seen during 2007) greatly increasing the probability of a below-normal season. During 2007, the development and subsequent strengthening of La Niña during ASO led to below average SSTs (–0.5° to 1.5°C below average) in the MDR[3] during the latter half of the season

[2] NOAA's CPHC includes TDs in their climatological statistics for the central North Pacific region.

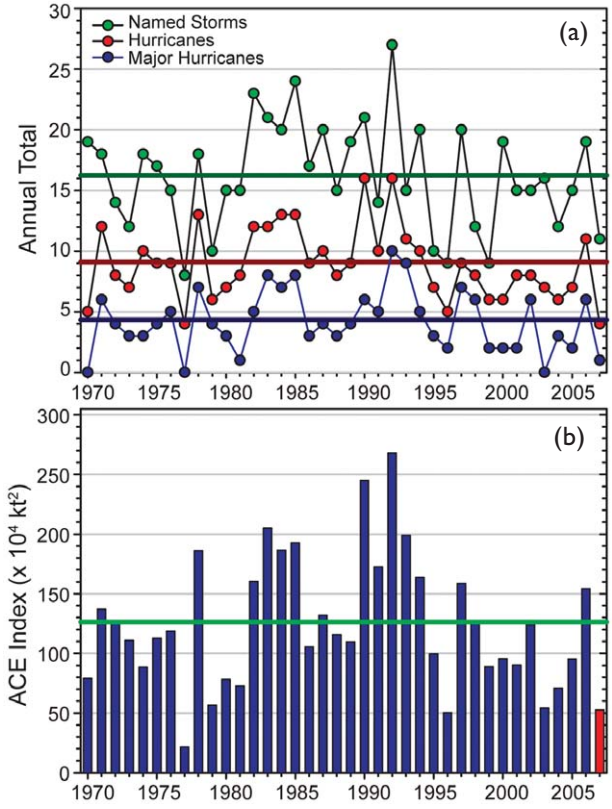

Fig. 4.17. Seasonal TC statistics for the east North Pacific Ocean during 1970–2007: (a) number of NS, H, and MH and (b) the ACE Index (x 10^4 kt^2) with the seasonal total for 2007 highlighted in red. Both time series include the 1971–2005 base period means.

[3] For the eastern North Pacific basin the MDR covers the area 10°–20°N and 90°–130°W (green boxes, Fig. 4.18).

(Figs. 4.2c,d). Another major contributing factor to the below-normal season was above-average vertical wind shear between 200–850 hPa in the MDR throughout the season. The largest shear anomalies (exceeding 9–12 m s^{-1}) were observed during JJA (Fig. 4.18, top), followed by anomalies of 3–6 m s^{-1} during SON (Fig. 4.18, bottom).

Previous studies have shown some statistically significant correlations between ENP hurricane activity and the phase of the QBO (Gray 1984; Shapiro 1989; Whitney and Hobgood 1997). In the ENP, TCs may attain a higher intensity when the QBO is in its westerly phase at 30 hPa, but there is also a corresponding decrease in the observed seasonal frequency (Whitney and Hobgood 1997).

During May, the phase of the QBO was in transition from westerly to easterly, as indicated by easterly winds at 30 hPa and westerly winds at 50 hPa. The winds were easterly at both levels in June, and subsequently strengthened over the remainder of the hurricane season (not shown). Therefore, the transition to the easterly phase of the QBO may have aided in inhibiting TC intensification in the ENP basin in 2007.

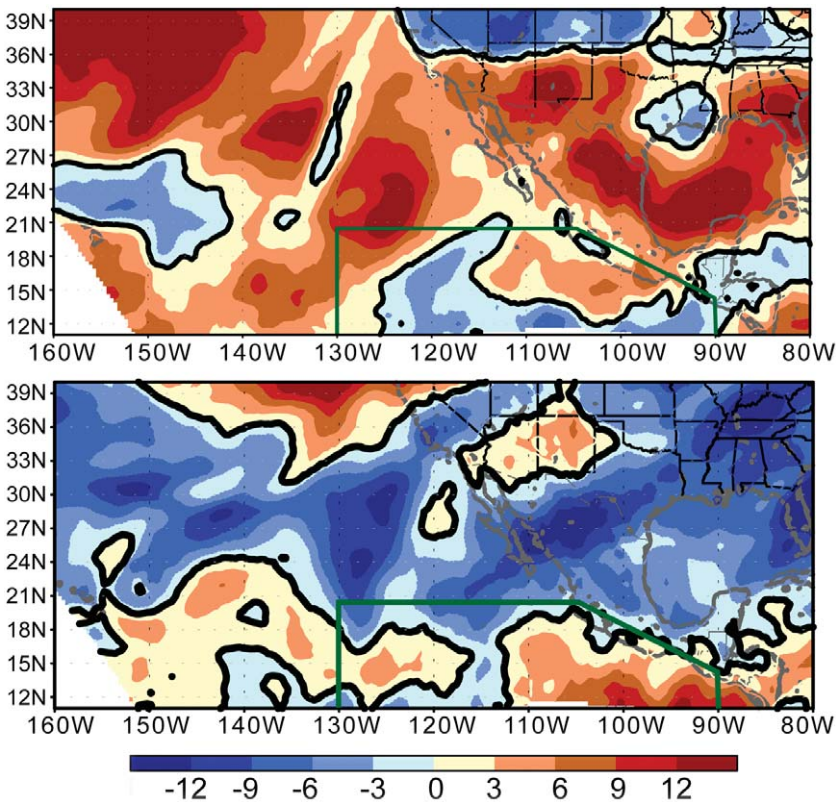

Fig. 4.18. The 200–850 hPa vertical wind shear anomaly (m s^{-1}) during (top) Jun–Aug and (bottom) Sep–Nov 2007. The green polygon shows the MDR for ENP hurricanes. Anomalies are departures from the 1979–2004 period means. [Source: NOAA NOMADS NARR dataset.]

(iv) TC Impacts in 2007

Two TCs made landfall along the Pacific coast of Mexico during 2007, one as a NS (Barbara) and one as a category 1 H (Henriette). These values are close to the 1951–2000 averages of 1.34 landfalling TS and 1.3 landfalling H (Jauregui 2003).

Tropical Storm Barbara made landfall along the Mexico–Guatemala border on 2 June with maximum sustained winds of 40 kt. Damages exceeding $50 million (U.S. dollars) resulted from agricultural crop loss, downed trees, a destroyed bridge, and roof damage.

Hurricane Henriette then made landfall east of Cabo San Lucas on 4 September with sustained winds of ~70 kt. Henriette then weakened to a tropical storm, moved over the Gulf of California on 5 September, and made a second landfall on the Mexican mainland with sustained winds of 60 kt. Henriette then weakened rapidly and dissipated over the mountains of northwest Mexico. Media reports attributed nine fatalities to Henriette, and estimated damages in the Mexican state of Sonora exceeded $275 million (U.S. dollars).

There were no direct landfalls or strikes associated with the two TCs in the central North Pacific. Cosme weakened to a TD just prior to crossing 140°W on 19 July, and moved almost directly westward before dissipating on 22 July. Showers and thunderstorms north of Cosme produced 100–180 mm of rain during 20–21 July in some areas along the east and southeast slopes of the Big Island of Hawaii.

Major Hurricane Flossie with maximum sustained winds of 110 to 120 kt crossed into the central North Pacific on 11 August. Fortunately, strong vertical wind shear weakened Flossie to a tropical storm on 14 August as it passed ~160 km (~100 miles) south of the Big Island. Tropical storm force winds were observed at South Point (the southern most point of Hawaii), but no heavy rainfall, significant damage, or injuries were reported. Flossie also generated large waves along the southeast facing shoreline, with the

largest waves estimated near ~6 m. Flossie eventually weakened to a TD on 15 August as it passed south of the islands of Oahu and Kauai.

4) Western North Pacific basin—S. J. Camargo

(i) Seasonal activity

Tropical cyclone data for the WNP basin is obtained from the JTWC best-track dataset for 1945–2006 (Chu 2002), and from the JTWC preliminary operational data for 2007. The 2007 season featured 26 TCs (includes TDs), with 23 becoming NSs, 15 becoming TY, and 4 reaching STY intensity (sustained winds ≥ 130 kt).[4]

The numbers of TCs were in the bottom quartile of the distribution (Fig. 4.19a), and well below the 1971–2000 median values of 30.5 TCs, and 26.5 NSs. The number of TYs and STYs were near median (16 and 3, respectively).

It is important to note that the RSMC in Tokyo—responsible for naming the TCs—identified 5 TCs that the JTWC did not issue any warnings or advisories on: 3 TDs in July and 2 NSs in October (Haiyan and Podul). Additionally, NS 06W was considered as having NS intensity by JTWC but no name was assigned by RSMC Tokyo (Padgett 2008; Chan 2008).

The cumulative distribution of NSs shows below-normal activity throughout the season (Fig. 4.19b), and also shows many months with NSs being at or below the 25th percentile of occurrences (Fig. 4.19c). Only November featured a considerably above normal number of NSs (4). The most suppressed period was April–June, which featured 1 TC in both April and May and no TCs in June. This activity is in lowest 10th percentile of occurrences, and reflected a very slow start to the season. Interestingly, for the first time since 1969, no NSs formed in June anywhere over the entire North Pacific (Padgett 2008).

The 2007 ACE Index for the western North Pacific (Bell et al. 2000) was below the 25th percentile (Fig. 4.20a), with most months having ACE values below the climatological median (Fig. 4.20b). This suppressed activity reflects fewer and shorter-lived TCs, which is typical of a La Niña year (Wang and Chan 2002; Camargo and Sobel 2005; Camargo et al. 2007a). For example, the median lifetime of a named storm during La Niña is 6.75 days, compared to 8.25 days for ENSO-neutral years, and 9.5 days for El Niño years.

During 2007, the median named storm duration was only 4.5 days. The duration of 14 TCs was in the bottom quartile of the distribution, and only 3 TCs had lifetimes above the median (8 days). As a result, the number of days with NS storms was only 97.5 (median is 144.23), which is the second lowest value in the historical record. Only 1950 featured fewer NS days (79.5). Also, there were only 87 typhoon days in

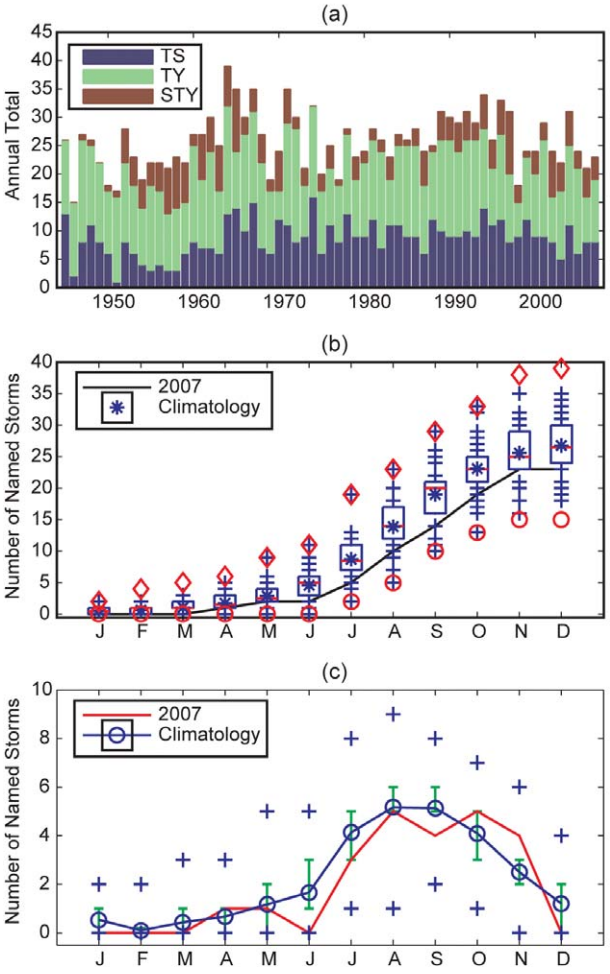

Fig. 4.19. WNP: (a) annual number of TSs, TYs, and STYs during 1945–2007. (b) Cumulative number of NSs with at least tropical storm intensity during 2007 (black line), and climatology (1971–2000). Boxes show the interquartile range, red line shows the median value, blue asterisks show the mean, blue crosses show values in the top or bottom quartile, and red diamonds (circles) show high (low) records in the 1945–2007 period. (c) Observed number of NS per month during 2007 (black curve) and climatology (blue curve). Blue "plus" signs denote the maximum and minimum monthly historical values, and green error bars show the interquartile range for each month. In the case of no error bars, the upper and/or lower percentiles coincide with the median. [Source: 1945–2006 JTWC best-track dataset, 2007 JTWC preliminary operational track data.]

[4] See http://metocph.nmci.navy.mil/jtwc/atcr/1989atcr/pdf/backmatter.pdf.

2007 (median is 120.4), which is in the lowest quartile of the distribution, and 15.5 STY days, which is also below the median (19.4 days).

During 2007, the mean genesis location (17.0°N, 135.5°E) and mean track position (21.3°N, 130.6°E) were shifted northwest of normal (12.9°N, 143.5°E and 19.0°N, 134.2°E, respectively), which is also consistent with La Niña (Chan 1985; Chia and Ropelewski 2002).

(ii) Landfalling WNP TCs

Fifteen WNP TCs made landfall during 2007, which equals the 1951–2000 median.[5] Four systems made landfall as a TD (median is 3), four made landfall as a NS (median is 6), five struck as a TY (median is 4), and two struck as a STY, which is well above the 75th percentile of occurrences. The landfalling STYs, Sepat (August) and Krosa (September), each struck Taiwan and then made a second landfall in China.

The TYs making the greatest impact were STY Sepat and Typhoon Lekima (October). STY Sepat first affected the Philippines, producing heavy rains and flooding in Manila. In Taiwan, Sepat's high winds and heavy rain caused mudslides and large agricultural losses, while in China they caused landslides in the Fujian Province. TY Lekima brought heavy rains and destruction to the Philippine Islands, followed by a second landfall in Vietnam where it destroyed approximately 100,000 homes. Lekima's rains also caused flooding and landslides in southern China.

(iii) Environmental conditions

Key environmental conditions during the peak of the WNP season (JASO) were consistent with La Niña. In particular, above average SSTs were confined to the western equatorial Pacific (Figs. 4.2c,d), the eastern portion of the monsoon trough was confined to a small region east of the Philippines (Fig. 4.21a), and anomalously high vertical wind shear was present along the equator near the date line (Fig. 4.21b). These conditions led to a northwest shift in the genesis and track activity, with most TCs also being shorter lived and weaker than normal (Wang and Chan 2002; Camargo and Sobel 2005; Camargo et al. 2007a).

The GPI (Emanuel and Nolan 2004) during 2007 was above normal in the western portion of the North Pacific and below-normal near the date line, which is also consistent with the presence of La Niña (Camargo et al. 2007b, their Fig. 6a). The decreased GPI near the date line is attributed mainly to the low-level vorticity, with some contribution from the vertical shear and midlevel relative humidity at 600 hPa. The increased GPI near the Asian continent is attributed mainly to an increase in relative humidity (Camargo et al. 2007b).

5) Indian Ocean Basins—K. L. Gleason

(i) North Indian Ocean

The NIO TC season typically extends from April to December, with two peaks in activity during May–June and November when the monsoon trough is positioned over tropical waters in the basin. Tropical cyclones in the NIO basin normally develop over the Arabian Sea and Bay of Bengal between latitudes 8° and 15°N. These systems are usually short lived and relatively weak, and often quickly move into the Indian subcontinent. However, strong and "severe cyclonic storms"[6] can develop with winds exceeding 130 kt (Neumann et al. 1993).

[5] Here we consider only one landfall per TC. If a TC makes more than one landfall, the landfall event with the highest wind speed is considered.

[6] The Bangladesh supercyclone of 1970 produced perhaps the greatest human death toll (300,000 persons) on record, primarily from storm surge flooding of low-lying deltas (Holland 1993).

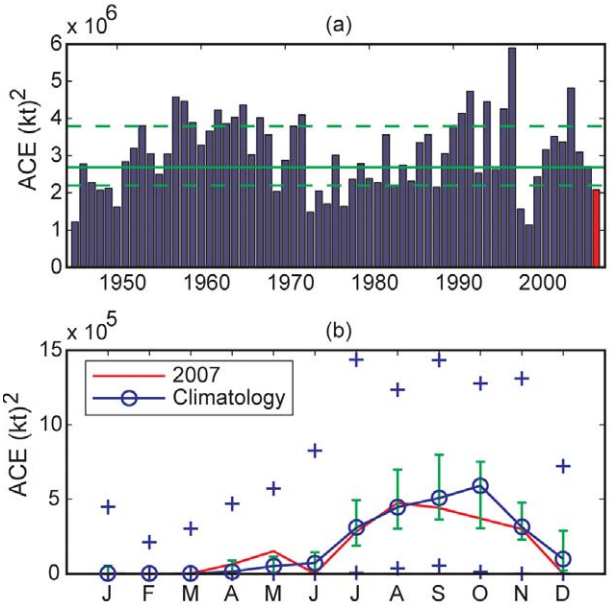

Fig. 4.20. (a) Annual ACE index for the western North Pacific. The solid green line indicates the 1971–2000 median value, and dashed green lines show the 25th and 75th percentiles. (b) Monthly ACE index during 2007 (red line), with the median (blue line) and 25th and 75th percentiles (green lines) also shown. In the case of no error bars, the upper and/or lower percentiles coincide with the median. The blue "plus" signs denote the maximum and minimum values during 1945–2007. [Source: 1945–2006 JTWC best-track dataset, 2007 JTWC preliminary operational track data.]

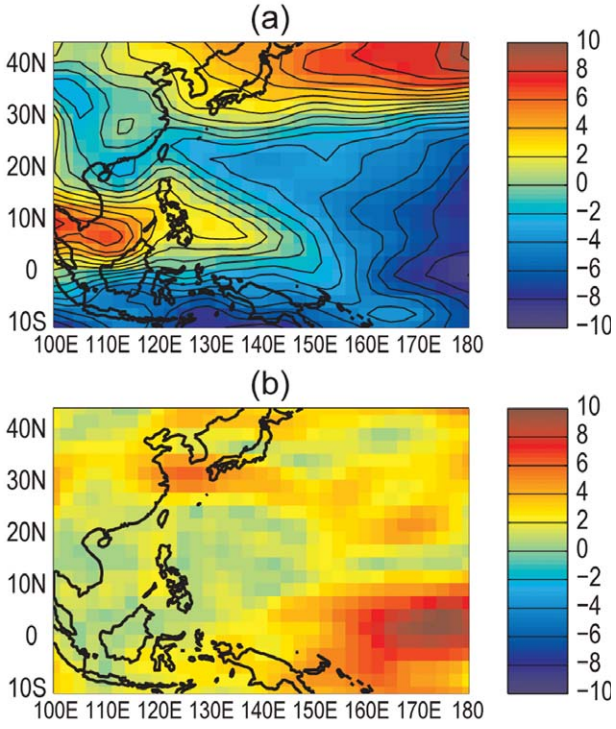

Fig. 4.21. (a) Zonal 850-hPa winds (m s^{-1}) during JASO 2007. The contour interval is 1 m s^{-1}. (b) Anomalous magnitude of the vertical wind shear (200–850 hPa) during JASO 2007. Anomalies are departures from the 1971–2007 climatological means. [Source: NCEP Reanalysis data, Kalnay et al. (1996).]

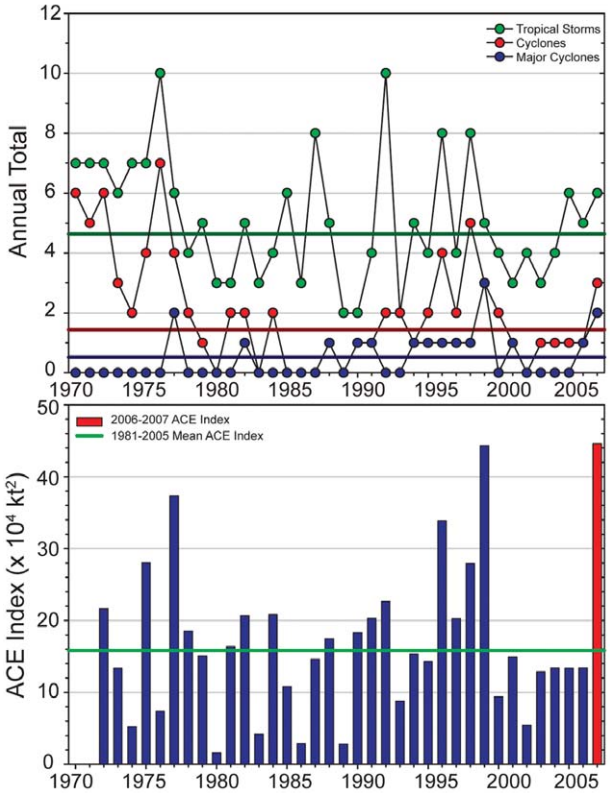

Fig. 4.22. Annual TC statistics for the NIO: (a) number of TSs, CYCs, and MCYCs, and (b) estimated annual ACE index (x 10^4 kt^2) for all TCs during which they were at least tropical storm or greater intensities (Bell et al. 2000). The 1981–2005 base period means are also shown. The ACE Index is estimated due to the lack of consistent 6-h sustained winds for every storm.

The 2007 TC season produced six NSs, three CYCs, and two MCYCs (Fig. 4.22a). These values are above the 1981–2005 averages of 4.6 NSs, 1.4 CYCs, and 0.5 MCYCs. The season also produced a record high ACE index value (44×10^4 kt^2), eclipsing the previous high ACE set in 1999 when a record three MCYCs formed (Fig. 4.22b). The 2007 ACE is almost 3 times the 1981–2005 mean (16×10^4 kt^2), and breaks a string of seven consecutive years with near- or below-average ACE.

The 2007 season was most noted for MCYCs Gonu and Sidr (see sidebar). Another storm of interest was CYC Akash, which made landfall near the Bangladesh–Myanmar border on 15 May with maximum sustained winds of 65 kt. This storm triggered a 1.2-m (4 ft) storm surge that impacted coastal areas, destroyed crops, and damaged hundreds of homes. Akash was responsible for at least three deaths and many missing persons.

(ii) South Indian Ocean

The SIO basin extends south of the equator from the African coastline to 105°E, with most CYCs developing south of 10°S. The SIO TC season extends from July to June encompassing equal portions of two calendar years (e.g., the 2007 season is composed of storms from July to December 2006 and January to June 2007). The peak activity occurs during December–April when the ITCZ is located in the Southern Hemisphere and is migrating equatorward. Historically, the vast majority of the landfalling CYCs in the SIO impact Madagascar, Mozambique, and the Mascarene Islands, including Mauritius and Réunion.

The historical SIO TC data are probably the least reliable of all the TC basins (Atkinson 1971; Neumann et al. 1993), primarily due to a lack of historical record keeping by individual countries and centralized monitoring agency; however, the historical dataset for the region has been updated (Neumann 1999). The historical data are especially deficient before reliable satellite data in the region beginning about 1983.

The 2006–07 season produced 10 NSs and well above-average numbers of CYCs (8) and MCYCs (6) (Fig. 4.23a). The 1981–2005 averages are 11.8 NSs, 6.4 CYCs, and 3 MCYCs. However, the 2006–07 ACE index (109×10^4 kt^2) was near the 1981–2005 average (Fig. 4.23b). Over the last 10 yr, only the 2001–02 season had above average ACE. Previous to that, the most recent period with above average ACE occurred during the period from 1994 to 1997.

One significant landfalling storm during the 2006–07 season was MCYC Bondo, which reached peak strength of 120 kt on 19 December, and then weakened somewhat before brushing the northern tip of Madagascar on 23 December. Most of the damage and casualties associated with Bondo occurred on Farquhar Atoll and the island of Agalega while the storm was northeast of Madagascar. Bondo then paralleled the Madagascar coastline as it continued to weaken, and made landfall near Mahajanga on 25 December as a strong NS.

The strongest storm of the season was Favio, which produced heavy rains and displaced over 25,000 people in Madagascar. Favio then intensified to a peak intensity of 125 kt after moving west of Madagascar's southern tip on 19 February. MCYC Favio then struck Mozambique's Inhambane province near Vilanculos on the 22 February with maximum sustained winds near 110 kt. At least four deaths and 70 injuries were reported.

A third significant storm of the season was MCYC Gamede, which reached a peak strength of 100 kt. Gamede did not make landfall, but did produce a record 5,510 mm (217 in.) of rain during the period from 21 to 28 February at Cratére Commerson on Réunion Island. This amount broke all world records for rainfall for a "3–8 day" period. Most of the previous records were set during TC Hyacinthe in January 1980 (Chaggar 1984).

MCYC Indlala, another significant landfalling storm, reached peak intensity of 115 kt on 14 March. MCYC Indlala struck near Antalaha, Madagascar, on 15 March with maximum winds near 105 kt. The storm resulted in more than 80 fatalities and left over 100,000 people homeless. Indlala was the fourth CYC in as many months to affect Madagascar.

6) Southwest Pacific basin—M. J. Salinger and S. M. Burgess

The TC season in the southwest Pacific normally runs from November through April.

The southwest Pacific (east of 150°E) experienced seven TCs during the 2006–07 season, two less than the long-term average (Fig. 4.24). They were evenly distributed across the basin, with four TCs west of the date line and three east of the date line. Four of these systems became NSs and one became a major TC (Fig. 4.25).

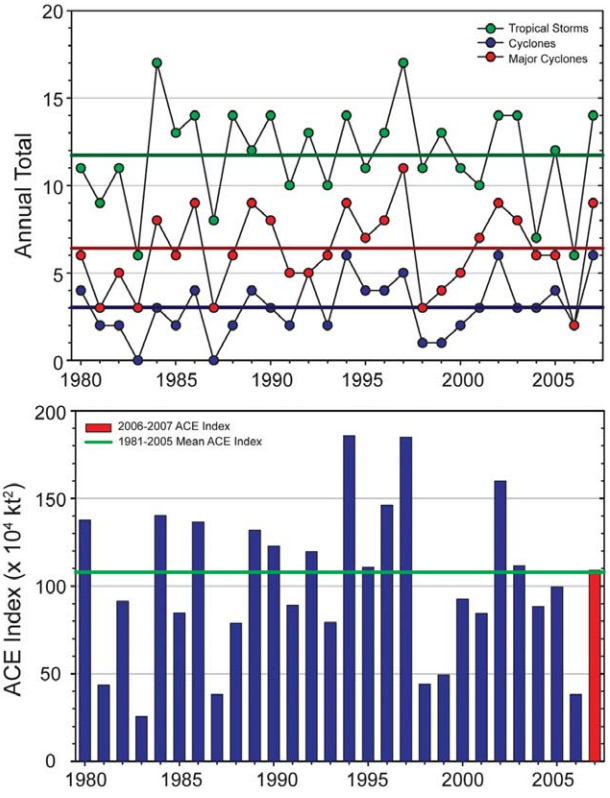

Fig. 4.23. Same as in Fig. 4.22 but for TCs in the SIO.

The first TC of the season (Xavier) occurred on 22 October, making this the earliest start to the TC season since that of 1997, in addition Xavier reached MCYC status with sustained winds of 115 kt. Such an early start is consistent with El Niño conditions. However, the El Niño dissipated earlier than expected in January, having a dampening effect on the total number of TCs over the remainder of the season. The last TC of the season (Pierre) occurred unusually late in May. Rather than the normal February–March peak, there was a fairly even distribution of TCs throughout the season; February was unusually quiet, with no occurrences.

Significant landfalling storms included Zita and Arthur, the first TCs of the 2006–07 season, which had maximum sustained winds of 50 and 65 kt, respectively. These storms produced wind damage and coastal flooding in parts of southern French Polynesia during 23–26 January.

Tropical Cyclone Becky developed in the Coral Sea south of the Solomon Islands on 26 March and

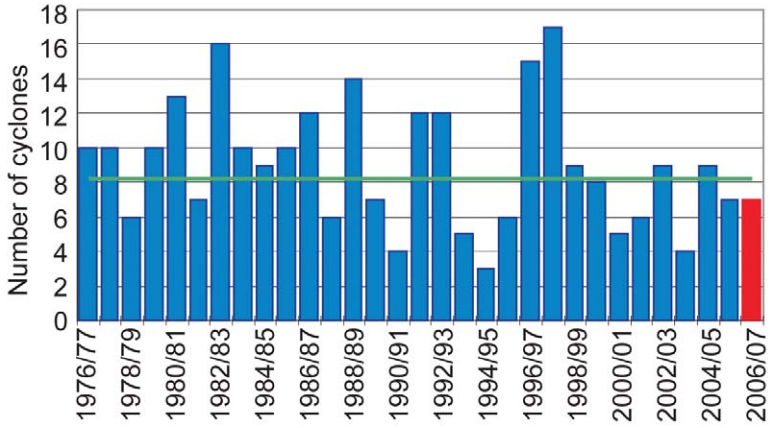

Fig 4.24. Tropical cyclones frequencies in the southwest Pacific from 1976 to 2007.

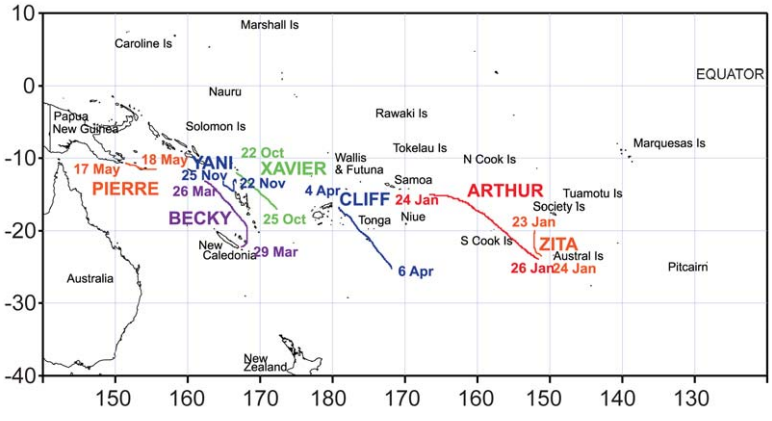

Fig. 4.25. Tropical cyclone tracks in the southwest Pacific during 2007.

reached maximum sustained winds of 70 kt. Becky tracked toward Vanuatu and then veered south toward New Caledonia. Fortunately, Becky dissipated on approach to New Caledonia, the highest wind gust reaching nearly 50 kt there. In Vanuatu, there were fallen trees and damage to crops in Espiritu and Malakula.

Tropical Cyclone Cliff occurred over the east of Fiji and Southern Tonga during 4–6 April, with maximum sustained winds of 55 kt. Some eastern parts of Fiji suffered minor wind damage and minor-to-moderate flooding. Tropical Cyclone Pierre was the last system of the 2007 season, occurring over the southeast of Papua New Guinea and the sea area south of the Solomon Islands during 17–18 May.

7) Australian basin—B. Trewin and A. B. Watkins

(i) Seasonal activity

The 2006–07 TC season was notably below normal in the broader Australian basin (areas south of the equator and between 90° and 160°E,[7] which include Australian, Papua New Guinea, and Indonesian areas of responsibility). The season produced five TCs, which is well below the long-term average of 10. This activity is the equal lowest since at least 1943–44. Historically, TC activity in the Australasian region, especially the Pacific region, is most suppressed during El Niño. There were only two TCs in the eastern sector[8] of the Australian region during 2007 and three TCs in the western sector. The inactive season coincided with a late monsoon onset over northern Australia, which was delayed by two weeks until mid-January, and also with long periods of below-average tropical convection over Indonesia and northern Australia (Fig. 4.5).

(ii) Landfalling TCs

MCYC George was the most significant system of the season, forming on 3 March off the west coast of the top end of the Northern Territory, and ultimately made landfall on 8 March as an Australian category 5 (see www.bom.gov.au/weather/cyclone/faq/index.shtml for a definition of Australian TC categories) storm 50 km ENE of Port Hedland. George weakened slowly after landfall (Fig. 4.26), and was still an Australian category 2 system late on 9 March. The remnant low finally dissipated on 12 March between Giles and Laverton in the western Australian interior.

George caused widespread minor-to-moderate damage in Port Hedland, with the most severe damage and three deaths occurring in mining camps south and east of town. Bedout Island recorded a 10-min mean wind of 105 kt (equivalent to wind gusts of approximately 150 kt). It was the most significant impact in the town since 1975. Fortunately, there was

[7] The Australian Bureau of Meteorology's warning area overlaps both the SIO and SWP.

[8] The western sector covers areas between 90° and 125°E. The eastern sector covers areas east of the eastern Australian coast to 160°E, as well as the eastern half of the Gulf of Carpentaria. The northern sector covers areas from 125°E east to the western half of the Gulf of Carpentaria.

no significant storm surge on the populated coastline, and no substantial flood damage in western Australia. However, heavy rains from the precursor low pressure system in late February and early March caused significant flooding in the Northern Territory.

Another landfalling storm was TC Nelson, which caused some flooding north of Karumba on the east coast of the Gulf of Carpentaria on 6 February. Tropical Cyclones Jacob and Kara were important in that they both caused major disruption to offshore oil and gas operations as platforms were evacuated in advance of the approaching systems. The remnants of TC Jacob crossed the coast on 12 March in almost exactly the same location that MCYC George had struck four days earlier.

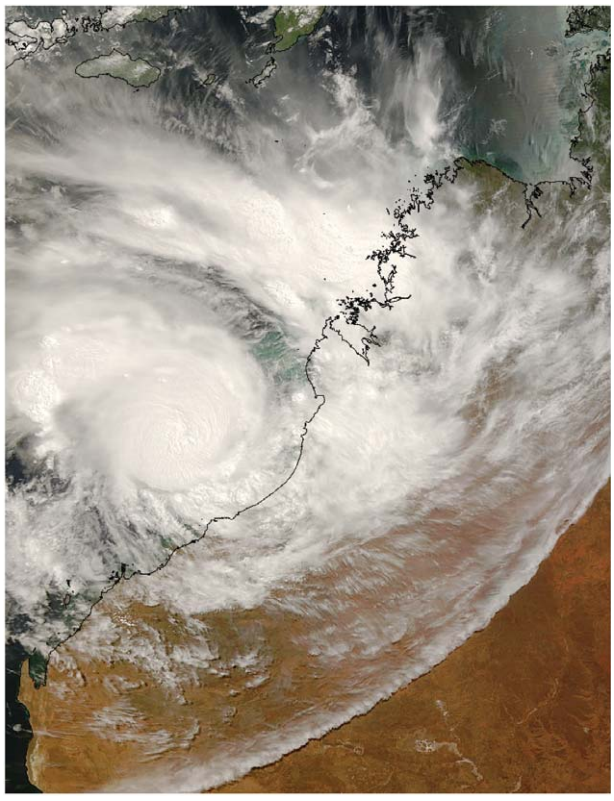

Fig. 4.26 Tropical Cyclone George approaching the coast of western Australia at 0155 UTC, 8 Mar 2007. [Courtesy of MODIS Rapid Response Project at NASA's Goddard Space Flight Center.]

e. *Intertropical convergence zones*

1) Pacific ITCZ—A. B. Mullan

There are two prominent convergence zones in the Pacific: the ITCZ in the Northern Hemisphere between 5° and 10°N, and the SPCZ that extends southeastward from near the Solomon Islands (10°S, 160°E) to near 30°S, 140°W. The Southern Hemisphere counterpart to the ITCZ also occurs near 5°S, but is seen mainly during February through April and east of the date line. This feature is suppressed or absent during El Niño years when warmer waters near the equator disrupt the seasonal convergence patterns. During 2007, the Pacific convergence zones reflected the transition from weak El Niño conditions early in the year to a moderate La Niña by the end of the year (section 4b).

The ITCZ appears as a fairly broad feature in the annual mean pattern of tropical rainfall due to its normal meridional movement throughout the year (Fig. 4.27, top). However, in 2007 the ITCZ was closer to the equator than normal at the beginning of the year in association with El Niño, and farther poleward than normal later in the year due to La Niña (Fig. 4.28). A double ITCZ was present from the second half of February through April and, although it appears weak in the annual mean, was nearly as intense as the northern branch during March 2007. West of the date line where the ITCZ and SPCZ tend to merge, the annual rainfall totals were comparable to the 1998–2006 TRMM climatology.

The SPCZ was shifted equatorward and eastward of normal in January consistent with El Niño, and produced enhanced convection from north of the Solomon Islands to central French Polynesia (Fig. 4.27, bottom). Penrhyn, in the northern Cook Islands, recorded its second highest January rainfall on record (262% of normal). At the same time, the Caroline Islands of northern Micronesia experienced dry conditions through March 2007 (Fig. 4.28). The SPCZ was particularly active in March between 180°–150°W, producing record rainfall in Niue, Tonga, and some of the northern Cook Islands.

Although the National Aeronautics and Space Administration's ENSO Precipitation Index (Curtis and Adler 2000) was persistently negative and consistent with La Niña from March–December 2007, the convergence zones did not stray from their climatological positions until July. The northward displacement of the ITCZ first occurred in the far eastern equatorial Pacific (120°–90°W) in July and then extended to the central Pacific during September (Fig. 4.29).

2) Atlantic ITCZ—A. B. Pezza and C. A. S. Coelho

The Atlantic ITCZ is a well-organized convective band that oscillates between 5° and 12°N during July–November, and between 5°N and 5°S during January–May (Waliser and Gautier 1993). The Atlantic ITCZ is active throughout the year, demarcating the transition from the southeasterly to the northeasterly Atlantic trade winds. Its positioning

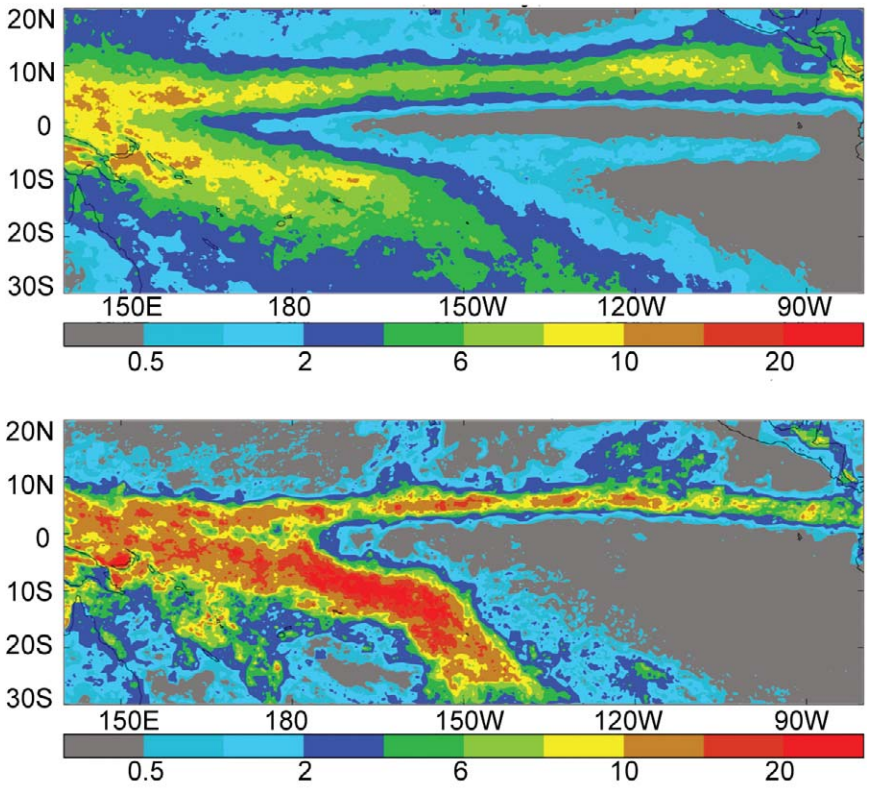

Fig. 4.27. Average rainfall rate (mm day^{-1}) during (top) 2007 and (bottom) Jan 2007. Note the uneven contour intervals (0.5, 1, 2, 4, 6, 8, 10, 15, and 20 mm day^{-1}). Data are NASA TRMM estimates (3B-43 product) provided on a 0.25° lat–lon grid.

by land–sea temperature contrasts, low-level winds, moisture convergence, and the meridional SST gradient between the North and South Atlantic (Nobre and Shukla 1996). Large-scale dynamics associated with equatorial atmospheric Kelvin waves can also influence the interannual variability of the ITCZ, while ENSO can influence its seasonal variability (Münnich and Neelin 2005).

During 2007 the Atlantic ITCZ reached its southernmost position (2.5°S) in early May (Fig. 4.31b), which is slightly later than the climatological period of March/April (Waliser and Gautier 1993). This delay may partly be a lagged response to the demise of the 2006 El Niño event (Münnich and Neelin 2005). The ITCZ also displayed some erratic southerly bursts during the year. A major event in February (Fig. 4.31a) produced enhanced rainfall across northeastern Brazil, with the

modulates the rainy seasons of northern and northeastern South America and northwestern Africa. In northeastern Brazil where annual rainfall is low, an occasional southward burst can produce widespread heavy rains (Fig. 4.30).

The seasonal migration and zonally asymmetric structure of the Atlantic ITCZ are primarily driven

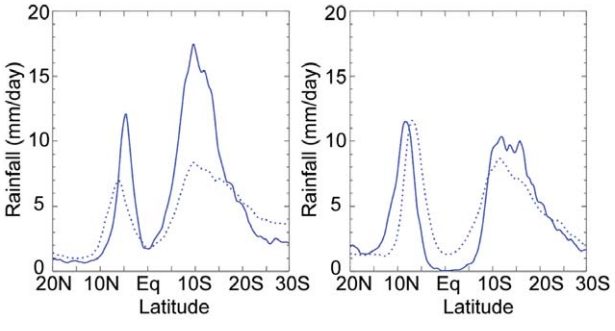

Fig. 4.28. Latitudinal cross sections of TRMM rainfall (mm day^{-1}) averaged between 180° and 150°W during (a) Jan and (b) Dec 2007. Solid (dotted) lines indicate the profiles for 2007 (1998–2006 average).

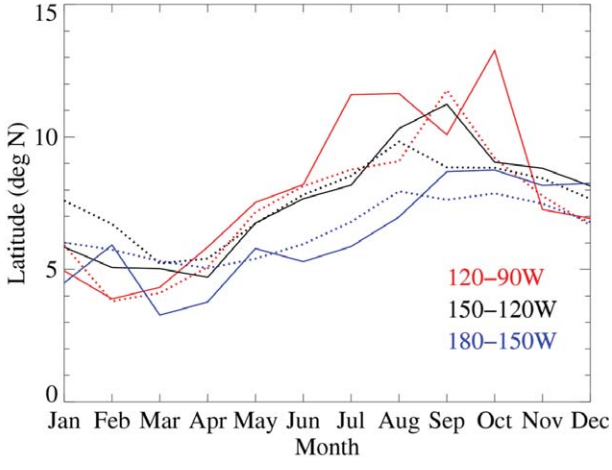

Fig. 4.29. Monthly variation in latitude of peak ITCZ rainfall over three longitude sectors: 180°–150°W (blue), 150°–120°W (black), and 120°–90°W (red). Solid (dotted) lines show annual cycle variations during 2007 (1998–2006 average).

largest surpluses exceeding 300 mm (Fig. 4.30). Enhanced precipitation during this period also extended well to the south due to interactions with cold fronts.

For the remainder of the year the Atlantic ITCZ either oscillated around its mean latitudinal position or stayed anomalously to the north. Its northernmost position occurred along the eastern flank in July and August, which produced strong convection over the western tip of Africa between 10° and 15°N (Fig. 4.31c). As a result, a large area of the tropical South Atlantic recorded less rainfall in 2007 than the 1998–2006 annual mean (Fig. 4.32), similar to what was observed in 2006.

f. Indian Ocean dipole—J. J. Luo and G. D. Bell

The IOD is an El Niño–like air–sea coupled ocean–atmosphere climate phenomenon in the tropical IO (Saji et al. 1999; Webster et al. 1999). It usually develops during JJA, peaks during SON, and decays during December and January, undergoing a strong phase-locking with the East Asian–Australian monsoon winds. The IOD signal can intensify quickly through air–sea interactions, and its intrinsic period is approximately two years. The duration is mainly controlled by a delayed negative feedback transmitted in the IO subsurface temperature (Behera et al. 2006).

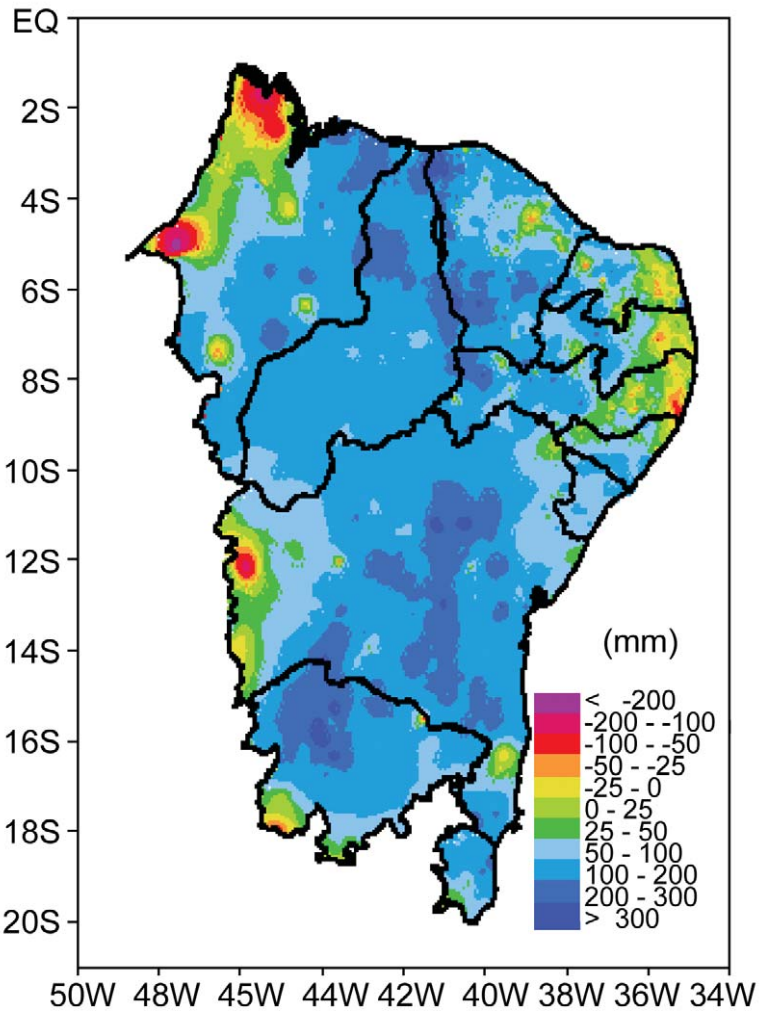

Fig. 4.30. Northeastern Brazil precipitation anomalies (mm) during Feb 2007. Anomalies are departures from the 1961–90 base period monthly means. [Data source: federal and regional networks (CMCD/INPE, INMET, SUDENE, ANEEL, FUNCEME/CE, LMRS/PB, EMPARN/RN, ITEP/LAMEPE/PE, CMRH/SE, SEAAB/PI, SRH/BA, CEMIG/SIMGE/MG, SEAG/ES).]

The pIOD features anomalously cool SSTs and a shallower than normal oceanic thermocline along the west coast of Sumatra, and anomalously warm SSTs and a deeper than normal thermocline in the western IO. Despite the fact that the IOD signal is usually weak compared to El Niño, its related SST anomalies in the warm IO may cause large climate anomalies, particularly in the Eastern Hemisphere. For instance, the strong pIOD event in 2006 boreal fall, which was coincident with a weak El Niño, caused considerable impacts in Australia, East Asia, Indonesia, and East Africa (Luo et al. 2008).

During 2007, a pIOD signal began during August in association with anomalous low-level southeasterly winds extending from west of Sumatra to the central equatorial IO (Fig. 4.33a). The initial SST cooling occurred along the Java Coast, followed by stronger negative anomalies (–1°C) in September near the Sumatra–Java coast (Fig. 4.33b). The cold signal then dissipated in mid-November, making it a relatively short-lived event. This early decay was partly linked to the downwelling phase of an oceanic Kelvin wave that was triggered in the west-central equatorial IO by westerly wind anomalies associated with the MJO.

The 2007 IOD probably contributed to drought in the eastern IO, Indonesia, and southeastern Australia, and floods in the western IO, South India, and East Africa. Drought damage estimates in Victoria, Australia alone were estimated at $2 billion (Australian

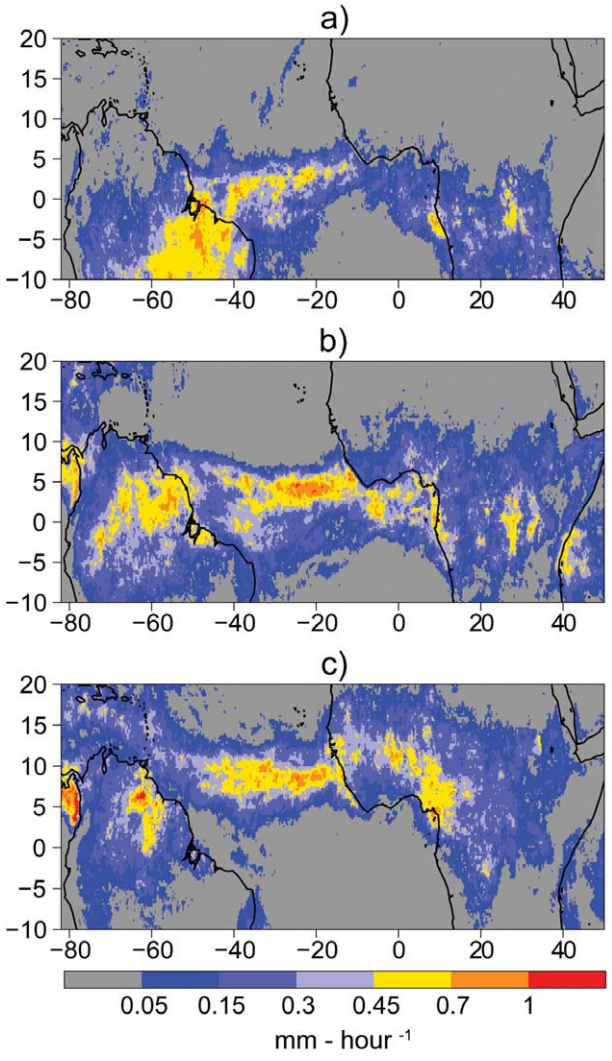

Fig. 4.31. Average rainfall rate (mm h^{-1}) during (a) Feb, (b) May, and (c) Aug 2007. Data are TRMM estimates calculated from a 0.25° lat–lon grid.

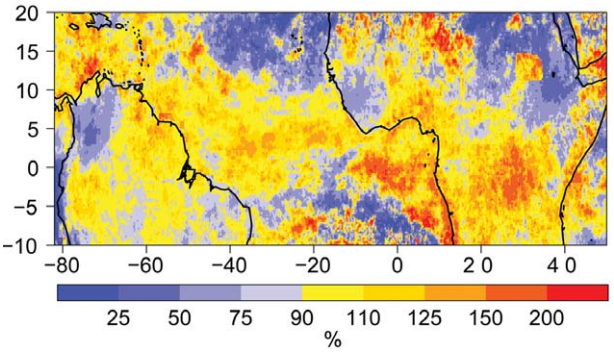

Fig. 4.32. Percentage of the 1998–2006 mean annual rainfall during 2007. Data are TRMM estimates calculated from a 0.25° lat–lon grid.

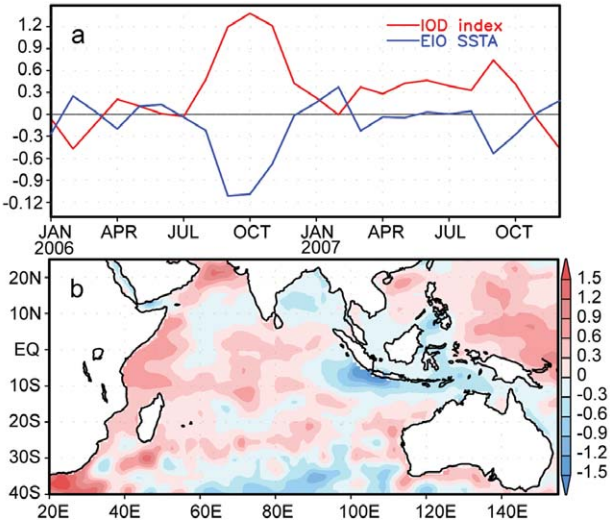

Fig. 4.33. (a) Monthly SST indices (°C) for the IOD and for the eastern IO (EIO) (10°S–0°, 90°–110°E). The IOD index is defined as the difference in SST anomalies between the western IO (10°S–10°N, 50°–70°E) and the EIO (Saji et al. 1999). (b) Anomalous SSTs (°C) in Sep 2007. Analysis is based on the NCEP optimum interpolation SST (Reynolds et al. 2002). Anomalies are departures from the 1982–2006 period monthly means.

dollars) (source: Australian Bureau of Meteorology). A pIOD was also present in 2006, and it is unprecedented to have consecutive positive events. Using only SSTA as a guide, the 2007 event was approximately one-half as strong as the 2006 event, which occurred during El Niño and likely contributed to the observed El Niño–related pattern of suppressed convection over Indonesia and the western tropical Pacific. That combination of conditions was associated with the climate and societal impacts described earlier (Luo et al. 2008).

The 2007 IOD event occurred during La Niña, suggesting an independence from ENSO that was also noted by Saji et al. (1999) and Saji and Yamagata (2003). As discussed in section 4diva (Fig. 4.15), the 2007 IOD was part of a much-larger, record-strength pattern of tropical convection spanning the IO, Indonesia, and southeastern Asia (Fig. 4.15b). This pattern is more typical of El Niño, meaning that the total La Niña forcing onto the upper-level atmospheric winds was weaker than would normally be expected for the observed equatorial Pacific SST anomalies.

Embedded within this pattern, the outgoing longwave radiation anomalies in the IOD region were comparable to the strongest in the record (Fig. 4.34a). The north–south dipole of anomalies between the Indian/Southeast Asian monsoon regions and the

eastern IO/Indonesian region was the strongest in the record, surpassing the previous record set in 2006 (Fig. 4.34b). The underlying mechanisms for the 2006 and 2007 pIOD events are found to differ. The 2006 event is consistent with the large-scale IOD dynamics, and was predictable at long leads due to the oceanic subsurface memory (Luo et al. 2007, 2008). However, the 2007 event was apparently triggered by active intraseasonal easterly wind anomalies during May–July in the central equatorial IO. As a consequence, that event had less predictability (Luo et al. 2008).

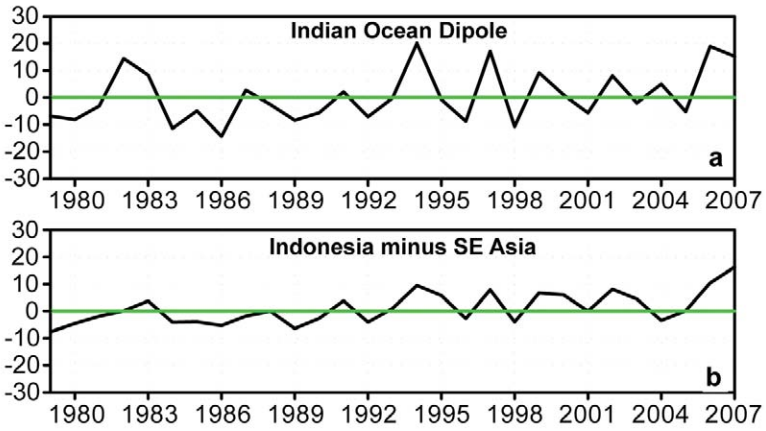

Fig. 4.34. Aug–Oct time series of OLR (W m^{-2}) anomalies based on the boxed regions in Fig. 4.15a; (a) the IOD (Indonesia minus western IO); and (b) Indonesia minus southeastern Asia. Anomalies are departures from the 1979–2000 period monthly means.

A RECORD NORTH INDIAN OCEAN TC SEASON—K. L. GLEASON AND H. J. DIAMOND

The 2007 TC season in the NIO basin featured MCYC Gonu, the strongest documented storm in the Arabian Sea, and the second strongest documented storm in the NIO. It also produced MCYC Sidr, which was perhaps the worst storm to strike Bangladesh since 1991. These two systems produced major impacts across the region (Fig. 4.35).

Tropical Cyclone Gonu developed in early June within the eastern Arabian Sea. Within three days, Gonu had strengthened to a MCYC with peak winds near 140 kt (category 5) on 4 June. The storm then weakened within an environment of cooler water and dry air prior to making landfall on 5 June along the eastern tip of Oman. Gonu struck with 80-kt sustained winds, and was the strongest CYC on record to hit the Arabian Peninsula. Gonu then entered the Gulf of Oman and made a subsequent landfall in Iran with sustained winds of 108 kt.

During a 24-h period from 6–7 June, rainfall totals were approximately 70 mm in the capital city of Muscat, Oman and surrounding stations (source: WMO Severe Weather Information Centre at http://severe.worldweather.wmo.int/). These amounts are especially significant, considering the average June rainfall in Oman is only 0.6 mm, and the mean annual rainfall is 100 mm (source: WMO World Weather Information Service). This widespread, heavy rain produced floods and landslides across coastal portions of Oman, resulting in over 50 fatalities and damages estimated at over $1 billion (U.S. dollars).

MCYC Sidr then formed near the Andaman Islands in the Bay of Bengal during mid-November. Sidr was named on 12 November, and reached maximum intensity of 135 kt on 15 November. Sidr then made landfall later that day in the Sundarbans forest area of Bangladesh as a strong category 4 storm with 130-kt winds. The storm produced heavy rains, high surf, and widespread flooding, and affected nearly 3 million people. More than 2,400 fatalities were reported, mostly attributable to collapsed buildings and flying debris.

MCYC Sidr was a category 5 storm that developed in the Bay of Bengal and became perhaps the most intense storm ever recorded in the NIO, achieving a minimum central pressure of 898 hPa with maximum sustained winds of 140 kt . It was also one of the deadliest recorded storms with over 140,000 confirmed fatalities in Bangladesh, many resulting from the 6-m storm surge in the Chittagong district.

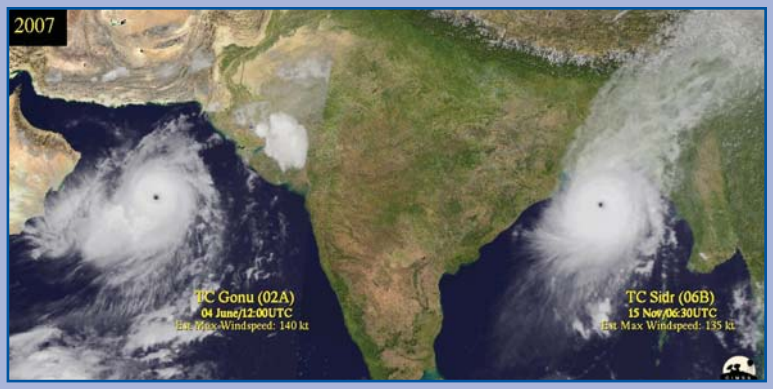

Fig. 4.35. Satellite montage of two category 5 TCs over the NIO. [Courtesy: C. Velden, University of Wisconsin—Madison, CIMSS.]

5. THE POLES—F. Fetterer, Ed.

a. Arctic—J. Richter-Menge, Ed.

1) Overview—J. Richter-Menge

The permanent presence of sea ice, ice sheets, and continuous permafrost are unique features of the polar regions. The Arctic is further distinguished because it sustains a human population in a harsh environment. These characteristics amplify the impact of global climate change on both the regional physical and societal systems. These impacts reach beyond the Arctic region. For instance, studies are underway to determine the extent to which the loss of sea ice cover and the conversion of tundra to larger shrubs and wetlands, observed to have occurred over the last two decades, have impacted multiyear persistence in the surface temperature fields, especially in the Pacific sector. In this chapter observations collected in 2007, combined with historical records, provide insights into continuing trends in the state of physical components of the Arctic system, including the atmosphere, ocean, sea ice cover, and land.

In 2007 there continued to be widespread evidence of the impact of a general warming trend in the Arctic region, where surface air temperatures reached their highest level on record. One of the most dramatic signals was the significant reduction in the extent of the summer sea ice cover and in the relative amount of older, thicker ice, both showing signs of an increase in the relative rate of reduction. Accompanying the reduction in sea ice cover was an increase in the temperature and a decrease in the salinity of the surface ocean layer. Water temperatures in deeper ocean layers also increased due to the influx of warmer waters into the Arctic Basin. On land, there was a general greening of tundra and browning of forested areas. Permafrost temperatures tended to increase and snow extent tended to decrease. Measurements of the mass balance of glaciers and ice caps indicate that in most of the world, glaciers are shrinking in mass. The largest of these, Greenland, experienced records in both the duration and extent of the summer surface melt.

2) Atmosphere—J. Overland, J. Walsh, and M. Wang

The year 2007 was the warmest on record for the Arctic, continuing a general, Arctic-wide warming trend that began in the mid-1960s (Fig. 5.1). The AO circulation regime, widely considered the main source of Arctic climate variability during the twentieth century, returned to a strongly positive wintertime index value for the first time in more than a decade, but was still lower than the large positive values of the early 1990s (Fig. 5.2). A positive AO is associated

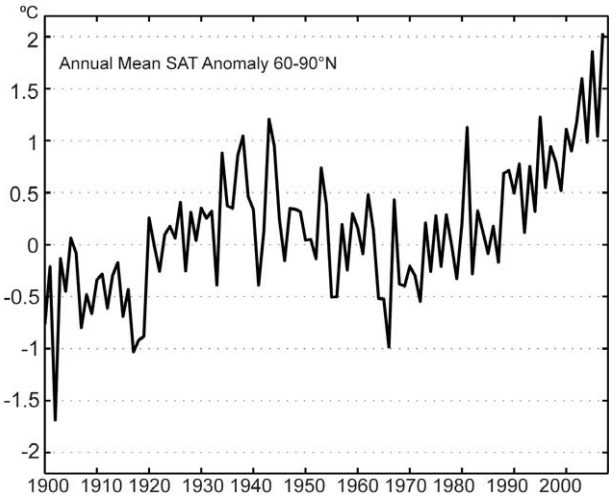

Fig. 5.1. Arctic-wide annual averaged surface air temperature anomalies (60°–90°N) based on land stations north of 60°N relative to the 1961–90 mean. From the CRUTEM3v dataset, (available online at www.cru.uea.ac.uk/cru/data/temperature/).

with lower pressure over Arctic regions and higher pressure at midlatitudes. The SLP anomaly field for winter–spring (December–May) 2007 shows low anomalies over most of the Arctic with a minimum over northern Europe (Fig. 5.3, left). This pattern contrasts with that of the canonical positive AO, where the lowest anomalies are centered over Iceland and the central Arctic. The geostrophic wind pattern associated with the 2007 SLP anomaly field brought air flow from western Russia toward the North Pole, with a positive (warmer) SAT anomaly maximum over the northern Barents Sea (Fig. 5.4, left). During the previous years of weak and variable AO (1996–2006), the geostrophic wind flow anomaly was generally from the Pacific toward the North Pole with positive SAT

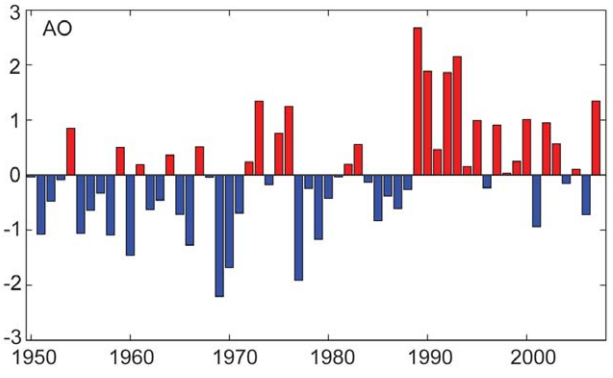

Fig. 5.2. The extended winter (DJFM) Arctic Oscillation index, 1950 to 2007 (based on data available online at www.cpc.ncep.noaa.gov).

anomalies north of eastern Siberia. It is difficult to say whether the strong positive AO will be sustained. There are historical examples of both single strong AO years and years where the anomaly is the beginning of a multiyear event.

A similarity of 2007 with the early years of the twenty-first century is the nearly Arctic-wide extent of positive SAT anomalies in winter, spring, and fall. These years contrast with the twentieth century in which positive and negative SAT anomalies were more evenly distributed. This Arctic-wide background SAT anomaly of greater than +1°C is consistent with projections from IPCC climate models (Chapman and Walsh 2007a). The exceptions are the Bering Sea and western Alaska, which were experiencing a third consecutive cold or average winter as 2007 came to a close.

The Arctic-wide negative SLP anomaly pattern of winter and spring was followed in summer by an unusually strong high pressure region in the Beaufort Sea and low SLP over central Russia (Fig. 5.3, right) that set up sustained geostrophic winds blowing from the North Pacific across the North Pole. These winds contributed to sea ice advection toward the Atlantic sector and the advection of warm moist air into the central Arctic, and to a record minimum Arctic sea ice cover in September (see section 5a4). The summers of 2005 through 2007 all ended with extensive areas of open water. As a result, freeze-up occurred later than usual, and surface air temperature remained high into the following autumn, with warm SAT anomalies above +6°C during October and November across the central Arctic. Such autumn SAT anomalies are also consistent with sea ice extent projections from IPCC climate model simulations performed with increasing greenhouse gas concentrations.

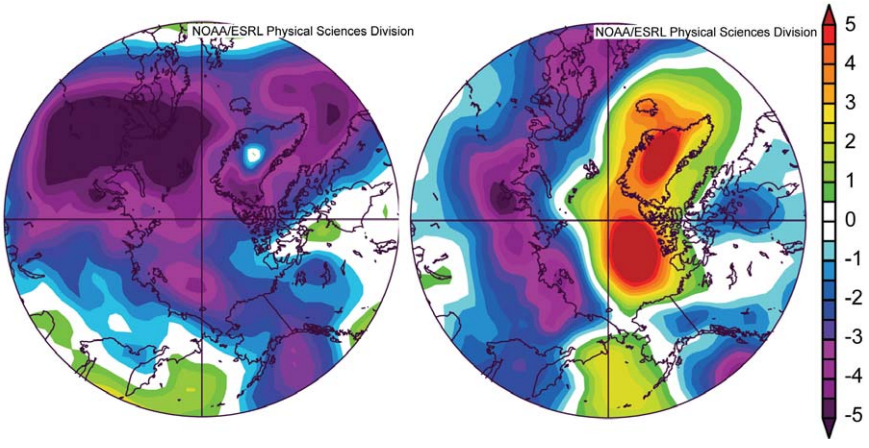

Fig. 5.3. SLP anomaly pattern for (left) Dec 2006–May 2007 and (right) Jun–Aug 2007. Note the extensive Arctic-wide areas of low SLP in winter and spring, which project onto a positive AO index. Data are from the NCEP–NCAR reanalysis through the NOAA/Earth Systems Research Laboratory, generated online at www.cdc.noaa.gov. Anomalies are relative to a 1968–96 climatological period.

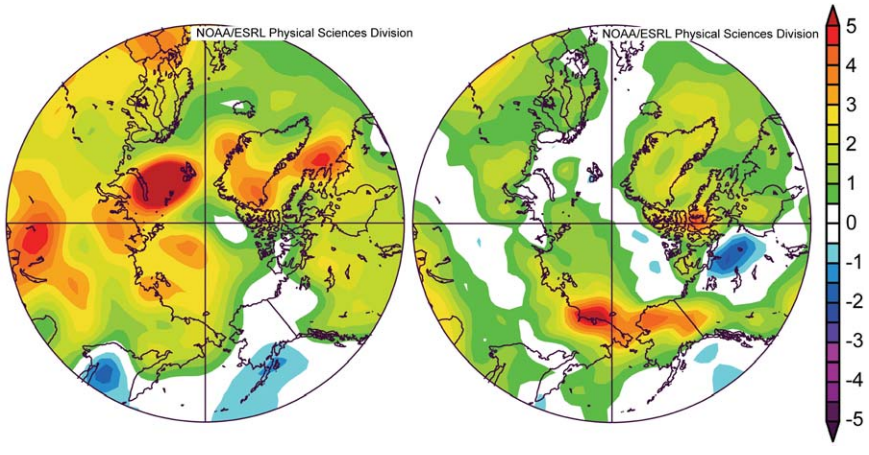

Fig. 5.4. Similar to Fig. 5.3, but for surface air temperature anomalies in °C for (left) Dec 2006–May 2007 and (right) Jun–Aug 2007. Note the nearly Arctic-wide positive values in winter and spring. In summer, melting ice keeps air temperature near the surface close to zero. After fall freeze-up, air temperature anomalies exceeded 6°C over much of the Arctic Ocean (not shown). Anomalies are relative to a 1968–96 climatological period.

3) Ocean—A. Proshutinsky, J. Morison, I. Ashik, E. Carmack, I. Frolov, J. C. Gascard, M. Itoh, R. Krishfield, F. McLaughlin, I. Polyakov, B. Rudels, U. Schauer, K. Shimada, V. Sokolov, M. Steele, M.-L. Timmermans, and J. Toole

(i) Circulation

In 2007, the ocean surface circulation regime in the Beaufort Sea was strongly anticyclonic (clockwise) in winter and summer (Fig. 5.5).

In winter the major flow stream removed sea ice from the Kara and Laptev Seas, while in the summer sea ice from the Canada Basin was transported out quickly by strong winds. Data from satellites and drifting buoys indicate that the entire period of 1997–2007 was characterized by an anticyclonic ocean surface circulation regime in the Beaufort region. This circulation pattern was the result of a higher sea level atmospheric pressure over the Beaufort Gyre, relative to the 1948–2007 mean, and the prevalence of anticyclonic winds.

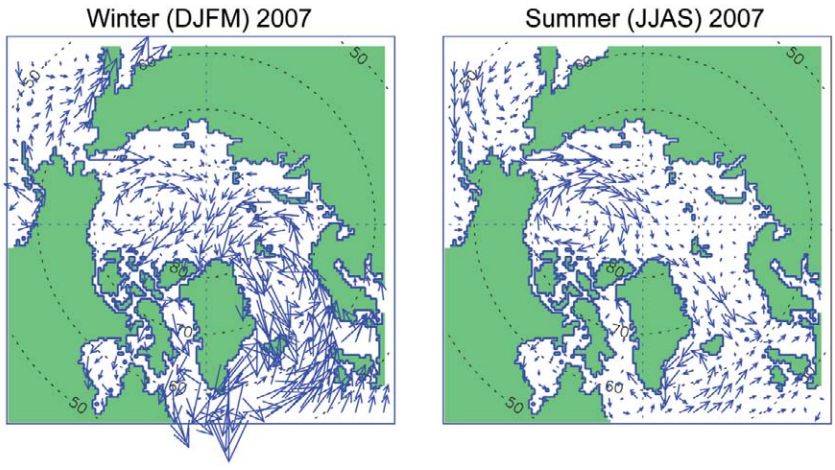

Fig. 5.5. Circulation patterns of the simulated upper-ocean wind-driven circulation in (left) winter and (right) summer of 2007. Updated following Proshutinsky and Johnson (1997).

(ii) Water temperature and salinity

(a) *Marginal Seas*

SST trends over the past 100 yr in the Arctic marginal seas (White, Kara, Laptev, East Siberian, Chukchi, and Beaufort) were analyzed by Steele et al. (2008). They found that many areas cooled up to ~0.5°C decade^{-1} during 1930–65 as the AO index generally fell (see Fig. 5.2), while these areas warmed during 1965–95 as the AO index generally rose. Warming is particularly pronounced since 1995, and especially since 2000 when the AO index exhibited relatively low and fluctuating values. Summer 2007 satellite-derived data indicate that SST anomalies were up to 5°C in ice-free regions (Fig. 5.6).

Long-term (1930–95) salinity trends (Steele and Ermold 2004) show that since 1930, the White Sea has gained freshwater while the East Siberian Sea has lost it, consistent with river discharge trends over this period. Over the past 20 yr, increases in both river discharge and direct precipitation can explain ob-

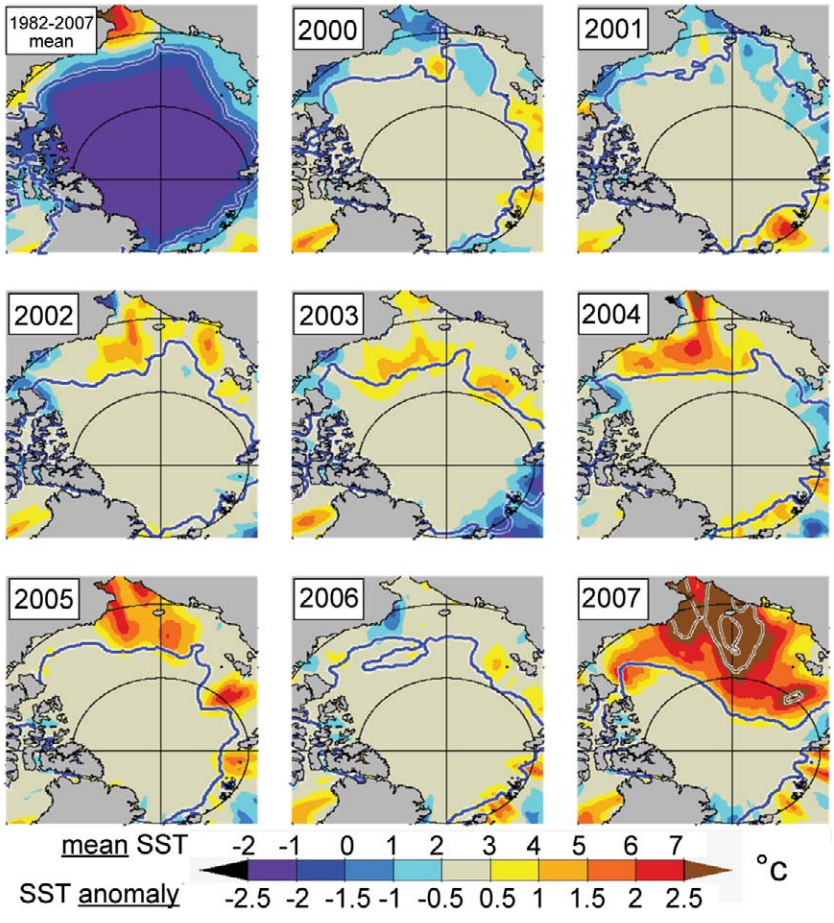

Fig. 5.6. (top left) Mean satellite-derived summer (Jul–Aug) SST (Reynolds et al. 2002) and anomalies from this mean over 2000–07. Latitudes 70° and 80°N and longitudes 0°/180° and 90°E/270°E are shown. For 2007, extra contours for 3° and 4°C are provided. Also shown is the Sep mean ice edge (blue contour) for each year (from Steele et al. 2008).

served salinity decreases in the White Sea, but not in the Kara Sea. Salinity trends in the Laptev Sea and East Siberian Sea indicate that ocean circulation plays a dominate role in these areas, where in recent years freshwater has been diverted eastward along the coast, rather than northward toward the deep ocean. Polyakov et al. (2008) confirmed these results and extended the data analysis up to 2003. The result shows that the freshwater content trend in the Siberian Seas (upper 50-m layer) for the period 1920–2003 is 29 ± 50 km^3 $decade^{-1}$. In 2007, all expeditions working in the marginal seas (I. Polyakov et al. 2007, personal communication) indicated an unusual freshening of the surface layer due to an extreme rate of sea ice melt.

(b) *Central Arctic (Nansen, Amundsen, and Makarov basins)*

In spring 2007 near surface salinities at the NP were increased by about 1 unit and the AW core temperature was increased by 0.5°C, respectively, above pre-1990s climatology. Data collected since 2000 at the NPEO (http://psc.apl.washington.edu/northpole/) indicate that in 2000 and 2001 the spring salinities in the upper 150 m near the pole and in the northern Makarov Basin were elevated 1–2 units above climatology and temperatures in the Atlantic Water core along the Lomonosov Ridge were elevated 1°–2°C. These conditions were nearly the same as observed in 1993 (Morison et al. 2000). In spring of 2004 and 2005, NP region hydrographic conditions largely returned to climatology (Morison et al. 2006). In spring of 2006, temperature and salinity anomalies near the NP region began to move away from climatological norms, again, repeating their behavior in spring of early 2000–03. The 2007 International Polar Year expansion of NPEO airborne surveys, combined with observations of the Switchyard project (W. Smethie 2007, personal communication), yielded a springtime section across 90°W–90°E. Results from this survey were consistent with the NP data, a further indication that in 2007 upper-ocean salinity structure and Atlantic Water temperatures in the central Arctic Ocean moved away from climatological norms, with increased salinity and temperature.

Atlantic Water enters the Arctic Ocean through the Barents Sea and Fram Strait, where it transitions from surface water to water of intermediate depth. The Atlantic Water temperature increase can be partially explained by other observed changes in the AW layer circulation. The first evidence of strong warming within the AW layer was found in the Nansen Basin in 1990 (Quadfasel et al. 1991). Positive AW anomalies of up to 1°C were carried along the continental margins into the Arctic Ocean interior (Woodgate et al. 2001; Schauer et al. 2002). Schauer et al. (2004) and Polyakov et al. (2005) have also shown that since the late 1990s, AW temperature has increased. Polyakov et al. (2007) and Dmitrenko et al. (2008) found that the 2000–05 Atlantic Water warming along the Siberian continental slope has propagated as a series of several AW warm impulses that penetrated into the Arctic Ocean through Fram Strait in 1999–2000 with a mean speed of 2.5 cm s^{-1}. The 2007 results suggest one of these pulses has reached the central Arctic Ocean. Preliminary reports from the summer hydrographic surveys in the central Arctic (U. Shauer et al. 2007, personal communication) indicate that, relative to 2004–05, in the Nansen and Amundsen Basins the temperature of the Atlantic Water core increased by approximately 0.5°C, and the thickness of this layer increased by 100–150 m mostly due to the propagation of a warming signal into the deeper ocean layers. In the Makarov Basin, no changes in the parameters of the Atlantic Water layer were detected. In contrast to the NPEO springtime results, in all basins the summer surface salinity was 1–2 units less than in 2003–05. It is speculated that the decrease in salinity in these regions is related to the extent of the massive sea ice melt in 2007 (see section 5a4).

(c) *Canada Basin and Beaufort Gyre*

The 2007 Canada Basin and the Beaufort Gyre summer conditions exhibited very strong freshening relative to 2006 and previous years of observations (Richter-Menge et al. 2006). Data collected as part of the BGOS (www.whoi.edu/beaufortgyre/index.html) show that in 2000–07, the total freshwater content in the Beaufort Gyre has not changed dramatically relative to climatology (although the absolute maximum was observed in 2007), but there was a significant change in the freshwater distribution (Fig. 5.7c,d). The center of the freshwater maximum shifted toward Canada and significantly intensified relative to climatology. This region of the Beaufort Gyre is much fresher than 30 yr ago.

Significant changes were observed in the heat content of the Beaufort Gyre (Fig. 5.7a,b). It has increased relative to the climatology, primarily because of an approximately twofold increase of the Atlantic layer water temperature (Shimada et al. 2004). In the late 1990s, Atlantic Water with temperatures as much as 0.5°C warmer than previous records was observed in the eastern Canada Basin (McLaughlin et al. 2004). These observations signaled that warm-anomaly

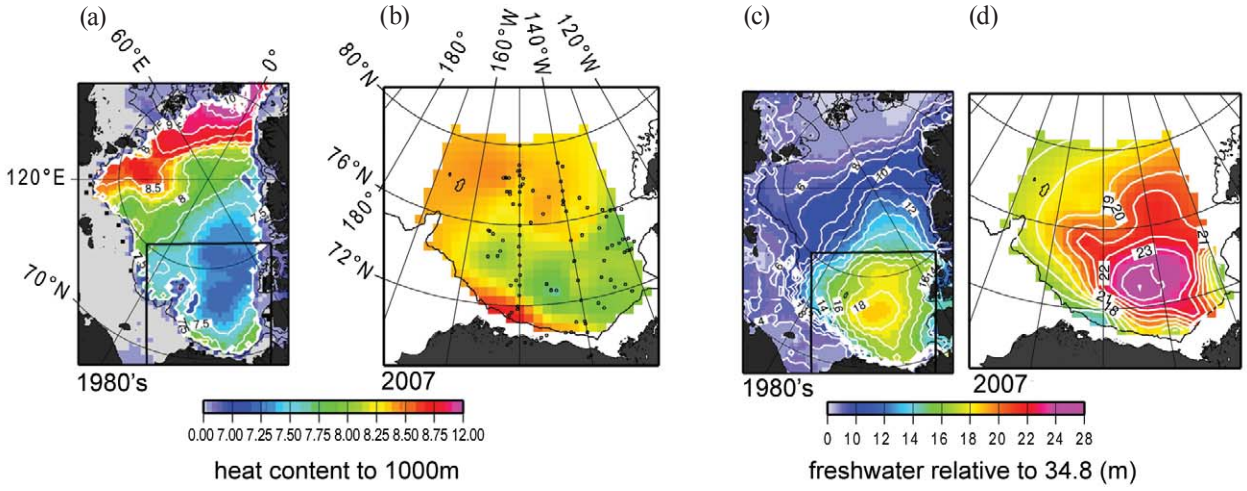

Fig. 5.7. (left) Summer heat (1 x 10^{10} J m^{-2}) and (right) freshwater (m) content. (a),(c) Heat and freshwater content in the Arctic Ocean based on 1980s climatology (Timokhov and Tanis 1997). (b),(d) Heat and freshwater content in the Beaufort Gyre in 2007 based on hydrographic survey (black dots depict locations of hydrographic stations). For reference, this region is outlined in black in panels a and c. The heat content is calculated relatively to water temperature freezing point in the upper 1,000-m ocean layer. The freshwater content is calculated relative to a reference salinity of 34.8.

Fram Strait waters, first observed upstream in the Nansen Basin in 1990, had arrived in the Canada Basin, and confirm the cyclonic circulation scheme. The 2007 observations manifested that these processes are still in progress and the AW layer warming signal propagated farther east.

The surface layer water in the Beaufort Gyre also accumulated a significant amount of heat in 2007, due to the significant retreat of the ice cover causing its exposure to the direct solar heating. This was similar to the conditions observed in the regions free of ice in the Amundsen, Nansen, and Makarov Basins.

(iii) Sea Level

Figure 5.8 contains SL time series from nine coastal stations having representative records for the period of 1954–2007 in the Siberian Seas (from the Arctic and Antarctic Research Institute data archives). There is a positive SL trend along Arctic coastlines, which, for 1954–89, after correction for GIA, was 1.94 ± 0.47 mm yr^{-1}. This compares to an estimated rate of 1.85 ± 0.43 mm yr^{-1} along the Arctic coastlines over the same period, based on 40 Arctic coastal stations available at the time (Proshutinsky et al. 2004). The addition of 1990–2007 data increases the estimated rate of SL rise for the nine stations in the Siberian Seas, beginning in 1954, to 2.61 ± 0.45 mm yr^{-1} (after correction for GIA).

From the beginning of the record until 1996, SL correlates relatively well with the time series of the AO index and SLP at the North Pole (Fig. 5.8). In contrast, from 1997–2007 SL generally increased despite the relatively stable behavior of AO and SLP, indirectly indicating that after 1996 something other than the inverted barometric effect dominated sea level rise in the region. Among possible candidates are ocean expansion due to heating, freshening, and wind-driven effects.

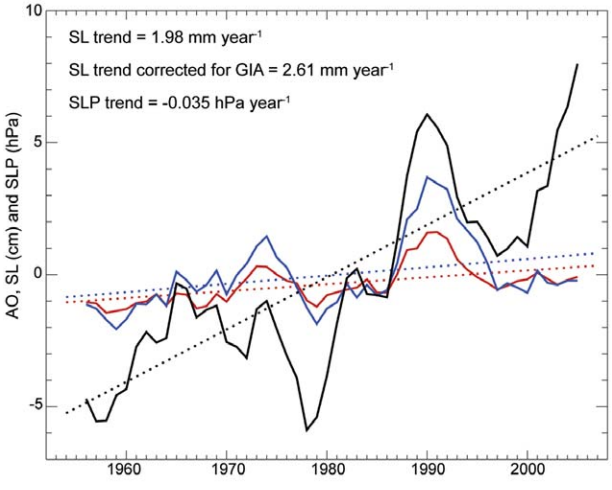

Fig. 5.8. Five-year running mean time series: annual mean sea level at nine tide gauge stations located along the Kara, Laptev, East Siberian, and Chukchi Sea coastlines (black line). The red line is annual mean AO index anomaly multiplied by 3. The blue line is the SLP at the North Pole (from NCAR–NCEP reanalysis data) multiplied by –1.

4) Sea Ice Cover—J. Richter-Menge, J. Comiso, W. Meier, S. Nghiem, and D. Perovich

(i) Extent and thickness

Satellite-based passive microwave images of sea ice cover have provided a reliable tool for continuously monitoring changes in the extent of Arctic ice cover since 1979. During 2007, the summer minimum ice extent, observed in September, reached 4.3 million km^2 (Fig. 5.9, right panel). This marked a new record minimum, with a dramatic reduction in area of coverage relative to the previous record of 5.6 million km^2, set just two years ago in 2005. At the end of the 2007 melt season, the sea ice cover was 23% smaller than it was in 2005 and 39% below the long-term average from 1979 to 2000. An extended time series of sea ice extent, derived primarily from operational sea ice charts produced by national ice centers, suggests that the 2007 September ice extent was 50% lower than conditions in the 1950s to the 1970s (Stroeve et al. 2008). The 2007 summer retreat of the ice cover was particularly pronounced in the East Siberian and Laptev Seas, the Beaufort Sea, and the Canadian Archipelago.

The annual maximum sea ice extent occurs each March. In March 2007, the maximum ice extent was 14.7 million km^2 (Fig. 5.9, left panel). This marked a slight recovery from the record minimum of 14.4 million km^2 for the period 1979–2007, which was observed in 2006. Consistent with 2006, the March 2007 ice extent fell within the mean contour at almost every location.

For comparison, the mean monthly ice extent for March and September, for the period 1979–2007, is 15.6 and 6.7 million km^2, respectively.

The annual variation of the extent of the Arctic sea ice cover in 2007, relative to past years, is shown in Fig. 5.10. As explained in Comiso et al. (2008), the 2007 Arctic ice cover was comparable to the 2005 and 2006 ice covers through mid-June but then began a more precipitous decline. Five-year averages from 1980 through 2004 show a general decrease in the Northern Hemisphere sea ice extent throughout the seasonal cycle, with this pattern being especially strong in the late summer and early fall. The 2007 ice extent rebounded with a rapid early autumn growth, albeit with an exceptionally slow recovery in the Chukchi and Barents Seas. By early November 2007, the ice extent conditions were comparable to those observed in recent years, while remaining well below the long-term (1979–2007) average.

Figure 5.11 shows the time series of the anomaly in ice extent in March and September for the period 1979–2007. Both winter and summer have a negative trend in extent: –2.8% decade^{-1} for March and –11.3% decade^{-1} for September. The seasonality of the observed ice retreat is consistent with model projections.

Ice thickness is intrinsically more difficult to monitor. With satellite-based techniques (Laxon et al. 2003; Kwok et al. 2004) only recently introduced, observations have been spatially and temporally limited. Data from submarine-based observations indicate that the ice cover at the end of the melt season thinned by an average of 1.3 m during the period 1956–78 and from 3.1 to 1.8 m in the 1990s (Rothrock et al. 1999). New measurements from ICESat and estimates of thickness using ice age as a proxy indicate the ice has thinned significantly over the last decade (Stroeve et al. 2008; Maslanik et al. 2007).

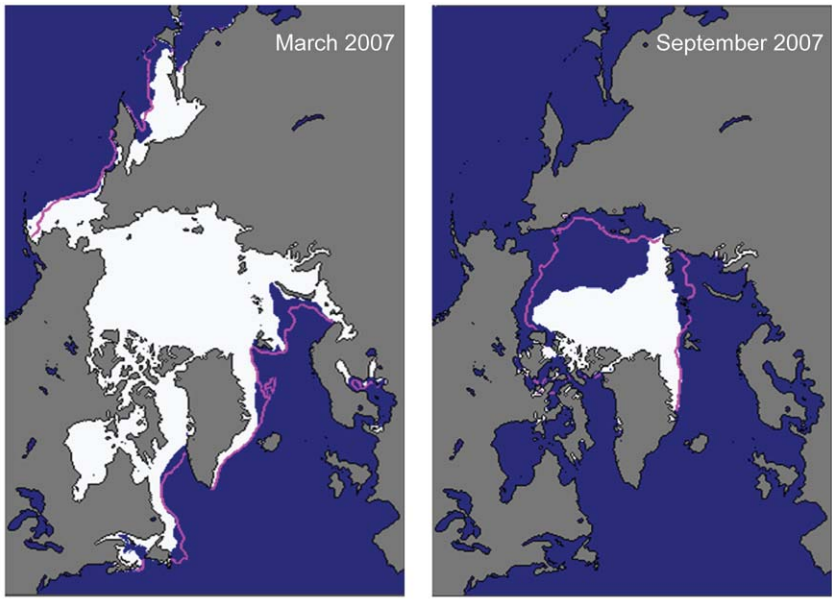

Fig. 5.9. Sea ice extent in (left) Mar and (right) Sep 2007, when the ice cover was at or near its maximum and minimum extent, respectively. The magenta line indicates the median maximum and minimum extent of the ice cover, for the period 1979–2000. The Sep 2007 minimum extent marked a record minimum for the period 1979–2007. [Figures from the National Snow and Ice Data Center Sea Ice Index: nsidc.org/data/seaice_index.]

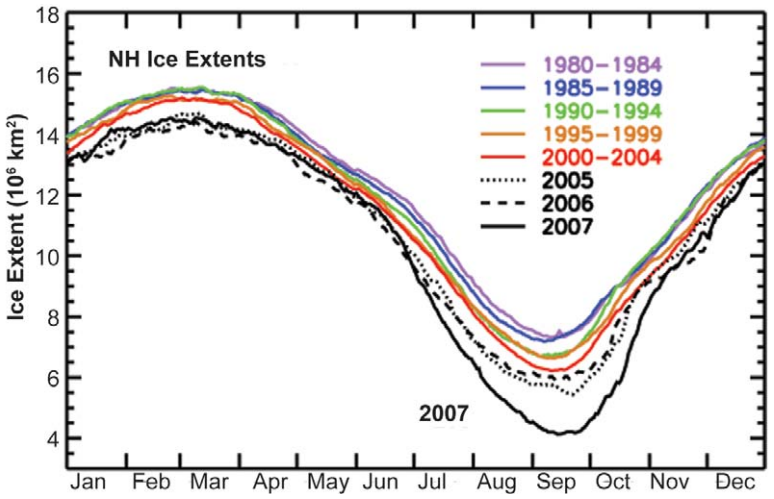

Fig. 5.10. Daily ice extents 2005, 2006, and 2007, and averaged over the 5-yr periods 1980–84 through 2000–04. Values are derived from satellite passive microwave data from NASA's SMMR and the Department of Defense's SSM/I. (Adapted from Comiso et al. 2008.)

Measurements of the seasonal and coastal ice cover do not indicate any statistically significant change in thickness in recent decades (Melling et al. 2005; Haas 2004; Polyakov et al. 2003).

(ii) Seasonal versus perennial ice

The Arctic sea ice cover is composed of perennial ice (the ice that survives year-round) and seasonal ice (the ice that melts during the summer). Consistent with the diminishing trends in the extent and thickness of the cover is a significant loss of the older, thicker perennial ice in the Arctic (Fig. 5.12). Data from the NASA QSCAT launched in 1999 and the buoy-based DM developed in earlier work by Rigor and Wallace (2004) and Nghiem et al. (2007) indicate that the amount of perennial ice in the March ice cover has decreased from approximately 5.5 to 3.0 million km^2 over the period 1958–2007. While there is considerable interannual variability, an overall downward trend in the amount of perennial ice began in the early 1970s. This trend appears to coincide with a general increase in the Arctic-wide, annually averaged surface air temperature, which also begins around 1970 (see Fig. 5.1). In recent years, the rate of reduction in the amount of older, thicker perennial ice has been increasing, and now very little ice older than 5 yr remains (Maslanik et al. 2007).

The QSCAT and DM techniques are consistent in their indication that the older, thicker ice is concentrated in the western Arctic Basin. This result reflects the recent prevailing ice circulation patterns in the Arctic (see Fig. 5.5). Ice residence times are typically longer in the western Arctic in the region of the Beaufort Gyre. The eastern Arctic is dominated by the Transpolar Drift, which carries sea ice out of the Arctic Basin via the Fram Strait.

Many authors have recently acknowledged that a relatively younger, thinner ice cover is more susceptible to the effects of atmospheric and oceanic forcing (e.g., Gascard et al. 2008; Stroeve et al. 2008; Kwok 2007; Ogi and Wallace 2007; Maslanik et al. 2007; Serreze et al. 2007; Shimada et al. 2006). Warming temperatures (Christensen et al. 2007), atmospheric and oceanic circulation patterns that advect ice out of the Arctic, and the amplification of these effects through the ice albedo feedback mechanism (Perovich et al. 2007) are combining to reduce the area covered by perennial ice.

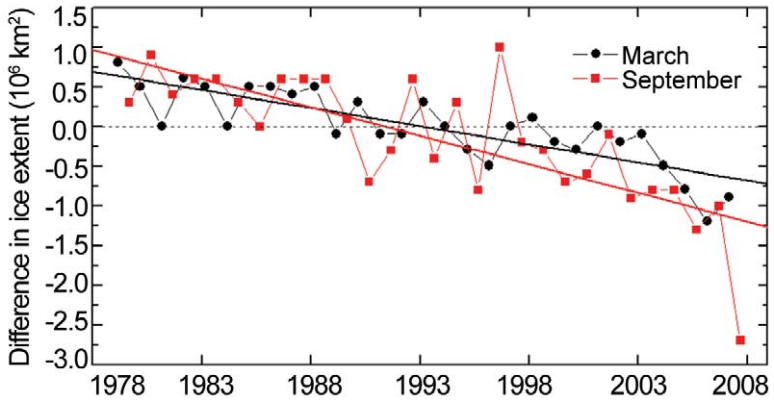

Fig. 5.11. Time series of the difference in ice extent in Mar (the month of ice extent maximum) and Sep (the month of ice extent minimum) from the mean values for the time period 1979–2007. Based on a least squares linear regression, the rate of decrease for the Mar and Sep ice extents was –2.8% and –11.3% per decade, respectively.

5) Land—V. Romanovsky, R. Armstrong, A. Shiklomanov, D. Walker, and G. Jia

(i) Vegetation

Evidence of widespread changes in vegetation in northern latitudes comes from trends in terrestrial greenness

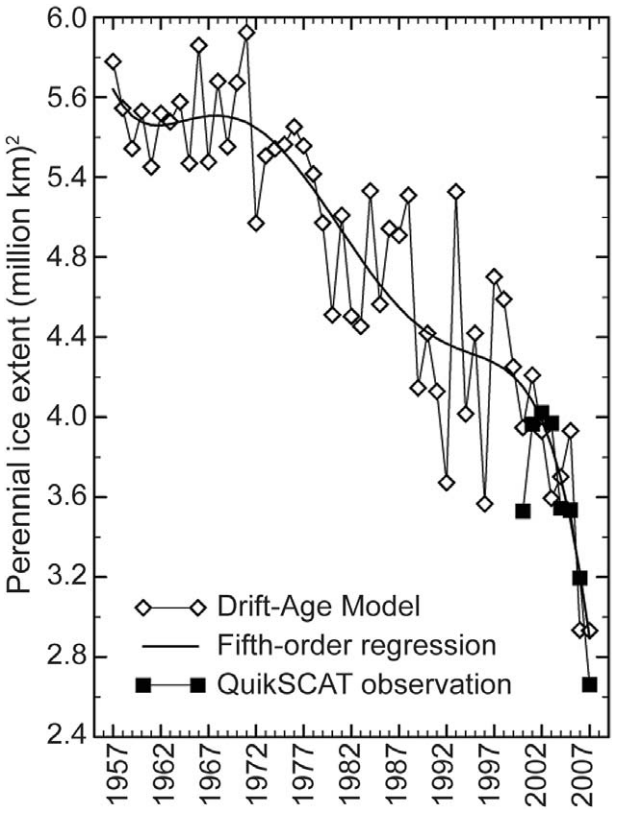

Fig. 5.12. Time series of area of perennial sea ice extent in Mar of each year estimated by the Drift-Age Model (with a fifth-order regression) and observed by QuikSCAT satellite scatterometer within the model domain. In each year, the model result was an average over Mar, and the satellite observation was on the spring equinox (21 Mar). (Adapted from Nghiem et al. 2007.)

as detected by the NDVI derived from the NOAA AVHRR satellites (Myneni et al. 1997; Zhou et al. 2001; Lucht et al. 2002; Jia et al. 2003; Goetz et al. 2005; Bunn et al. 2007). During the 1981–2005 period of observation, about 6% of the circumpolar tundra area experienced an increase in NDVI and about 1% experienced a decrease (Fig. 5.13; Bunn et al. 2007). The positive trends in NDVI in tundra areas have been strongest in North America. For example, in the tundra region south of 70°N (the region of the Arctic with a consistent AVHRR record from 1982 to 2005) the rate of change in NDVI is +0.58% yr^{-1} over the North American Arctic compared to +0.34% yr^{-1} over the Eurasian Arctic (Jia et al. 2007). Forested areas experienced a slight decline over the same period: NDVI declined in 6% of the forested area versus an increase in 4% of the area.

Vegetation responds relatively quickly to warming temperatures by growing more vigorously and densely. Over a longer time span, changing climate alters vegetation type. Land cover on much of the Alaska North Slope, for example, is transitioning from tundra to shrubs (Wang and Overland 2004). Changes in land cover, vegetation density, and other factors are reflected in NDVI. Overall, increasing NDVI is consistent with warming soil and air temperatures, earlier snow melt, and the expansion of shrubs and tree line to the north.

(ii) Permafrost

Observations show a general increase in permafrost temperatures during the last several decades in Alaska (Osterkamp and Romanovsky 1999; Romanovsky et al. 2002; Osterkamp 2003; Romanovsky et al. 2007a), northwest Canada (Couture et al. 2003; Smith et al. 2005), Siberia (Pavlov 1994; Oberman and Mazhitova 2001; Romanovsky et al. 2007b; Pavlov and Moskalenko 2002), and northern Europe (Isaksen et al. 2000; Harris and Haeberli 2003).

Permafrost temperature records uninterrupted for more than 25 yr have been obtained by the University of Alaska Fairbanks along the International Geosphere-Biosphere Programme Alaskan transect, which spans the entire continuous permafrost zone in the Alaskan Arctic. All of the observatories show a substantial warming during the last 20 yr (Fig. 5.14). The detailed characteristic of the warming varies

Fig. 5.13. Spatial distribution of trends in May to Aug photosynthetic activity across the northern high latitudes from 1981 through 2005. Significant positive trends in photosynthetic activity are shown in green, and negative trends are shown in rust. (From Bunn et al. 2007.)

between locations, but is typically from 0.5° to 2°C at the depth of zero seasonal temperature variations in permafrost (Osterkamp 2005). These data also indicate that the increase in permafrost temperatures is not monotonic. During the observational period, relative cooling has occurred in the mid-1980s, in the early 1990s, and then again in the early 2000s. As a result, permafrost temperatures at 20-m depth experienced stabilization and even a slight cooling during these periods. Permafrost temperature was relatively stable on the North Slope of Alaska during 2000–06. However, 2007 data show a noticeable increase in the temperature at 20-m depth by 0.2°C at the two northernmost sites of Deadhorse and West Dock. Permafrost temperature did not change significantly at the other North Slope sites. This may indicate a new wave of permafrost warming similar to the warming that started in 1994 (Fig. 5.14), which also started at the Deadhorse and West Dock sites and only later appeared at the interior sites.

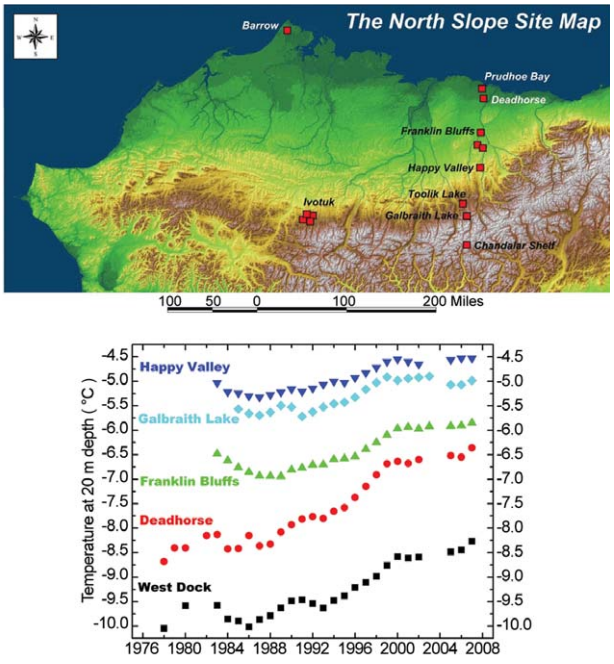

Fig. 5.14. (top) Location of the long-term University of Alaska permafrost observatories in northern Alaska. West Dock is at Prudhoe Bay. (bottom) Changes in permafrost temperatures at 20-m depth during the last 25 to 30 yr (updated from Osterkamp 2003).

(iii) Snow extent

Northern Hemisphere snow cover extent has a mean maximum of approximately 47 million km^2, typically occurring in February. The minimum usually occurs in August and is less than about 1 million km^2, most of which is snow on glaciers and perennial snow fields. As a result, snow cover is the land surface characteristic responsible for the largest annual and interannual differences in land surface albedo. Snow covers a much smaller area in the Southern Hemisphere, approximately 2% of the global total, and plays a relatively small role in global climate.

Time series of snow extent in the Northern Hemisphere, beginning in 1978 and derived from two sources, consistently show a decreasing trend in snow cover in the months of April through October, with the strongest seasonal signal occurring between April and August (Fig. 5.15). Data derived from NOAA snow charts (Robinson and Frei 2000; Frei and Robinson 1999; Ramsay 1998; NOAA/NESDIS/OSDPD/SSD 2006) indicate a statistically significant decreasing trend of –2.1% decade^{-1} (Brodzik et al. 2006). Snow cover data derived from passive microwave imagery (Armstrong and Brodzik 2001; Armstrong et al. 2005a,b) show a decreasing trend of –0.7% decade^{-1}, although it is not significant at the 90% level. Both time series show similar inter-annual variability and consistently indicate Northern Hemisphere maximum extents exceeding 40 million km^2. The western United States is among the regions with the strongest decreasing trends, supporting Groisman et al. (2004) and Mote et al. (2005) results using in situ observations. Shallow snow cover at low elevations in temperate regions is the most sensitive to temperature fluctuations and hence most likely to decline with increasing temperatures (Lemke et al. 2007, 343–346).

For the Northern Hemisphere winter of 2006–07, the microwave data indicate negative departures from the long-term mean (1978–2007) for every month except October and February, with an average negative departure for the winter months (November through April) of approximately 0.7 million km^2. For the calendar year of 2007, the NOAA data indicate an average snow cover extent of 24.0 million km^2, which is 1.5 million km^2 less than the 38-yr average and represents the third least extensive snow extent for the period of record (see section 2c2 for additional information on 2007 Northern Hemisphere snow extent).

(iv) Glaciers

Glaciers and ice caps, excluding those adjacent to the large ice sheets of Greenland and Antarctica, can be found on all continents except Australia and have an estimated total area between 512 and 540 $\times 10^3$ km^2. The complicated and uncertain processes that control how fast glaciers move make it difficult

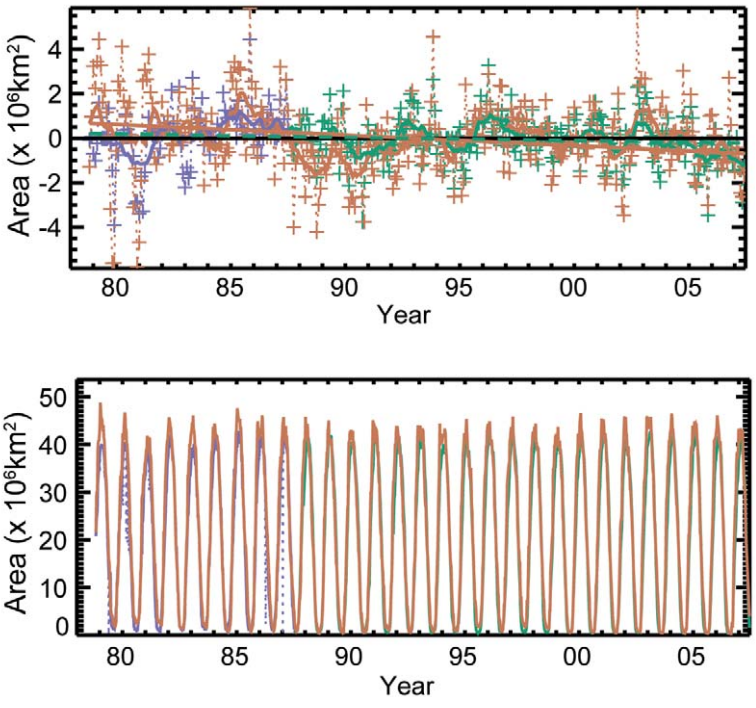

Fig. 5.15. (top) Time series of Northern Hemisphere SCA derived from passive microwave (purple/green) and NOAA snow charts (orange), and (bottom) SCA departures from monthly means, 1978–2007.

to use changes in the areal extent of glaciers as a straightforward indicator of changes in climatic conditions. Mass balance measurements, or the difference between the accumulation and ablation, are a more direct method to determine the year-to-year "health" of a glacier. Changes in mass balance correspond to changes in glacier volume. These measurements are typically obtained from less than about 0.2% of the world's glaciers. Researchers have measured mass balance on more than 300 glaciers since 1946, with a continuous record for about 40 glaciers since the early 1960s (e.g, Cogley 2005; Kaser et al. 2006).

These results indicate that in most regions of the world, glaciers are shrinking in mass. From 1961 to 2005, the thickness of "small" glaciers decreased approximately 12 m, or the equivalent of more than 9,000 km^3 of ice (Dyurgerov and Meier 2005; online at http://nsidc.org/sotc/glacier_balance.html). Recent mass loss of glaciers, ice caps, and ice sheets is estimated to be 0.58 mm SLE per year between 1961 and 2005 and 0.98 mm SLE per year between 1993 and 2005 (Dyurgerov and Meier 2005; online at http://nsidc.org/sotc/sea_level.html). In contrast to the two major ice sheets, Greenland and Antarctica, the network of small glaciers and ice caps, although making up only about 4% of the total land ice area or about 760,000 km^3, may have provided as much as 60% of the total glacier contribution to sea level change since the 1990s. This acceleration of glacier melt may cause 0.1 to 0.25 m of additional sea level rise by 2100 (Meier et al. 2007). The greatest mass losses per unit area are found in Patagonia, Alaska, and northwest United States/southwest Canada. However, because of the corresponding large areas, the biggest contributions in total to sea level rise come from Alaska, the Arctic, and the Asian high mountains.

(v) River discharge

Overall, the twenty-first century to date is characterized by an increased level of river discharge to the Arctic Ocean (www.R-ArcticNet.sr.unh.edu). The mean 2000–06 discharge from six of the largest Eurasian rivers (North Dvina, Pechora, Ob, Yenisei, Lena, and Kolyma) was 127 km^3 (7%) higher than long-term mean over the period 1936–99 (Fig. 5.16). The largest Siberian rivers, Yenisey and Lena, provided more than 70% of this increase. Preliminary 2007 estimates of annual discharge to the Arctic Ocean from the Russian rivers have been made using near-real-time data (http://RIMS.unh.edu). These estimates indicate a relatively high annual discharge for the six largest Eurasian rivers, possibly achieving a new historical maximum in 2007 for total discharge to the Arctic Ocean over the 1936–2007 observational period.

The mean annual discharge to the ocean over 2000–06 from the five largest North American rivers was about 6% (30 km^3) greater than the long-term mean over 1973–99. The historical annual maximum was observed for the summary discharge in 2005 (Fig. 5.16). However, the relatively short discharge time series for North America (37 yr) and the significant unmonitored land area does not support conclusions with the same reliability as for Eurasia.

6) Greenland—J. Box, J. Cappelen, D. Bromwich, L.-S. Bai, T. Mote, B. Veenhuis, N. Mikkelsen, and A. Weidick

(i) Synopsis

Greenland experienced regional warming in 2007, with statistically significant positive (warm) annual temperature anomalies in the 1.3° to 2.7°C range for coastal stations and 1.3°C for the inland ice sheet

with respect to the 1971–2000 averages. Seasonal temperature anomalies were largest in winter but not positive in every season. Upper air temperatures indicate lower- to midtropospheric warm anomalies in all seasons above sounding stations surrounding Greenland. Noteworthy are western and southern locations where midtropospheric anomalies exceed those observed at the surface. Ice sheet surface melt duration anomalies were up to 53 days longer than the 1973–2000 average, based on passive microwave remote sensing. MODIS-derived surface albedo anomalies in 2007 versus the 2000–07 period were persistently negative, consistent with extensive surface melting. Greenland's largest glacier continued its recession, with ice flushing out from an embayment thought to have been ice filled since at least the onset of the Little Ice Age. The overall ice sheet mass budget was likely in mass deficit by at least 100 km^3 yr^{-1}.

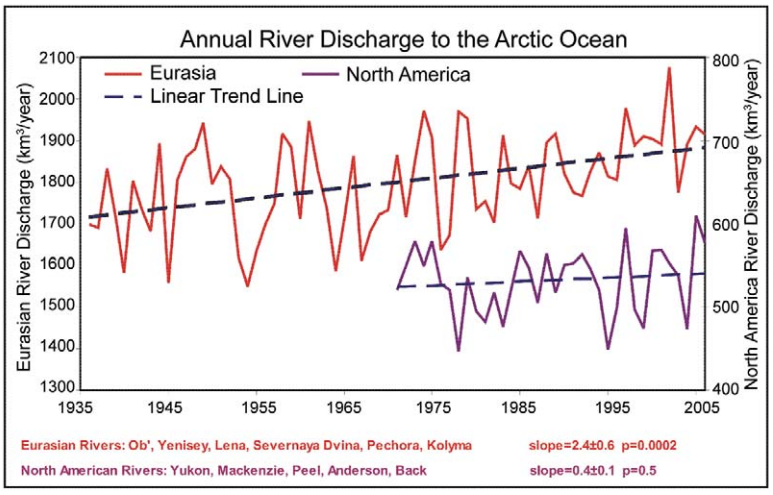

Fig. 5.16. Total annual discharge to the Arctic Ocean from the six largest rivers in the Eurasian pan-Arctic for the observational period 1936–2006 (updated from Peterson et al. 2002) (red line) and from the five largest North American pan-Arctic rivers over 1973–2006 (purple line). The least squares linear trend lines are shown as dashed blue.

(ii) Coastal surface air temperatures

Warm (positive) anomalies predominated in 2007, relative to the last 50-yr period (1958–2007), when con-

Table 5.1. Greenland station surface air temperature anomalies by season, 2007 vs 1971–2000. Anomalies are in K. Bold values indicate values that meet or exceed 1 *Z*-score.

Station (Region), latitude N, longitude W, time range	Winter	Spring	Summer	Autumn	Annual
Pituffik/Thule AFB (NW), 76.5°N, 68.8°W, 1961–2007	**–2.9**	1.4	**1.2**	0.4	0.1
Upernavik (NW), 72.8°N, 56.2°W, 1958–2007	5.3	9.0	–1.8	2.8	1.9
Ilulissat (W), 69.2°N, 51.1°W, 1958–2007	**5.4**	1.6	**1.4**	0.0	**2.1**
Aasiaat (W), 68.7°N, 52.8°W, 1958–2007	**5.5**	2.9	**1.9**	0.3	**2.7**
Nuuk (SW), 64.2°N, 51.8°W, 1958–2007	1.4	2.8	**–3.1**	–0.4	–0.1
Prins Christian Sund (S), 60.0°N, 43.2°W, 1958–2007	1.5	0.4	**1.8**	**1.2**	**1.3**
Tasiilaq (SE), 65.6°N, 22°W, 1958–2007	2.0	1.6	1.6	1.2	1.6
Danmarkshavn (NE), 76.8°N, 18.8°W, 1958–2007	1.0	0.5	0.4	1.7	0.9

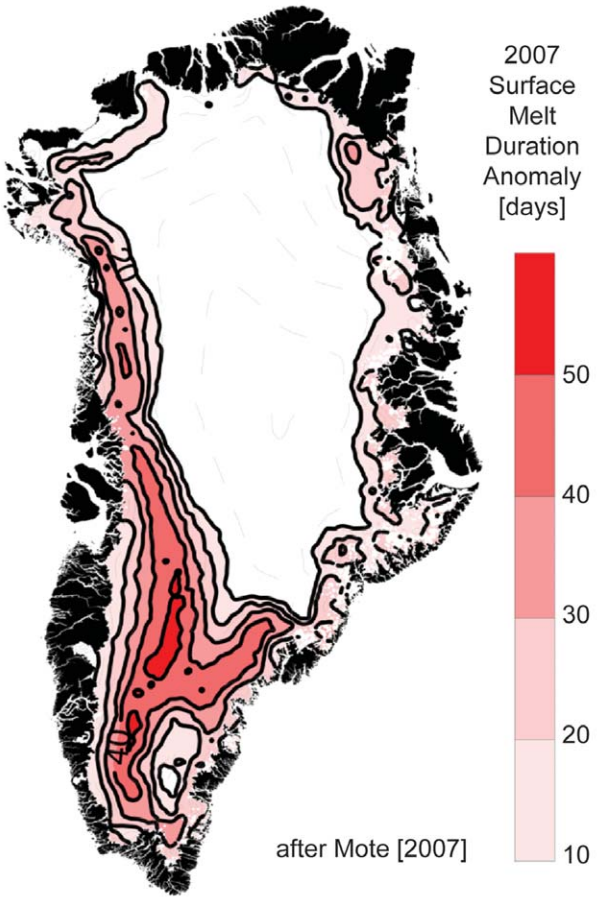

Fig. 5.17. Surface melt duration departure from average for summer (Jun–Aug) 2007 from SSM/I; units are days. The average is based on the summers from 1973 to 2000 (excluding 1975, 1977, and 1978). Only departures >10 days are included. (Figure after Box et al. 2006 and Mote 2007.)

tinuous surface air temperature records are available from a collection of stations around the island (Cappelen et al. 2007, 2008). Exceptions included an anomalously cold winter at Pittufik (northwest), an unusually cold summer and autumn at Nuuk (southwest), and an anomalously cold summer at Upernavik. The *Z*-scores exceeding ±1.0 or ±2.0 indicate anomalies exceeding the most common 66% or 95% of the observed cases, respectively (Table 5.1). At Upernavik (northwest) the spring temperature was the warmest in the past 50 yr, and at Nuuk (southwest) the summer temperature was the coldest in the past 50 yr. The only anomalies that were significant annually, that is, with *Z*-scores ≥1.0, were warm anomalies for 2007 annual means.

(iii) Upper air temperatures

Upper air sounding data available from the Integrated Global Radiosonde Archive (Durre et al. 2006) indicate for Greenland in 2007 a continued pattern of lower- to midtropospheric warming and lower-stratospheric cooling, consistent with trends since 1964 (Box and Cohen 2006). In the lower troposphere at the 850-hPa level (1.1–1.5-km altitude), for example, annual temperature anomalies were between +0.6° and +1.5°C at sites surrounding the island, relative to the 1971–2000 average. Seasonal anomalies were largest in winter with +8.1°C at 1,000 hPa at the Aasiaat/Egedesminde sounding site, with smaller positive anomalies elsewhere in almost all seasons. At the upper limit of mandatory observational levels, (20 hPa, in the lower–mid stratosphere), –11.6°C anomalies are evident. Large lower-stratospheric temperature anomalies are not necessarily abnormal given the relatively large observed temperature variability due in part to much lower atmospheric mass (e.g., Christy and Drouilhet 1994). Summer anomalies above southern Greenland balloon launching sites at the 850 and 600-hPa levels were between 0.2° and 1.3°C.

(iv) Greenland ice sheet melt extent

Passive microwave observations indicate summer 2007 (June–August) SMD was greater than any other observed summer since records began in 1973 (Mote 2007). The ice sheet area undergoing surface melt was 60% greater in 2007 than the next highest year (1998). Summer 2007 had 20 days more melt than average (1973–2000) across nearly all of the regions that exhibit melting. Up to 53 more days of melting than average was observed for elevations in the 2,000- to 2,400-m above sea level range between the north and south domes of the ice sheet (Fig. 5.17).

(v) Ice sheet precipitation, evaporation, and meltwater runoff

Polar MM5 climate data assimilation model runs spanning 50 yr (1958–2007), calibrated by independent in situ ice core observations (Bales et al. 2001; Mosley-Thompson et al. 2001; Hanna et al. 2006) and ablation stakes (van de Wal et al. 2006), indicate that year 2007 precipitation and accumulation was not abnormal despite a +10 km^3 $decade^{-1}$ positive total precipitation trend over the 1958–2007 period. Surface water vapor fluxes were within an insignificant inter-annual range. In accordance with a +1.3°C year 2007 annual mean temperature anomaly, the fraction of precipitation that fell as rain instead of snow, surface meltwater production, and meltwater runoff were well above the 1971–2000 mean (Table 5.2). Due to abnormally large mass loss by meltwater runoff despite normal snow accumulation,

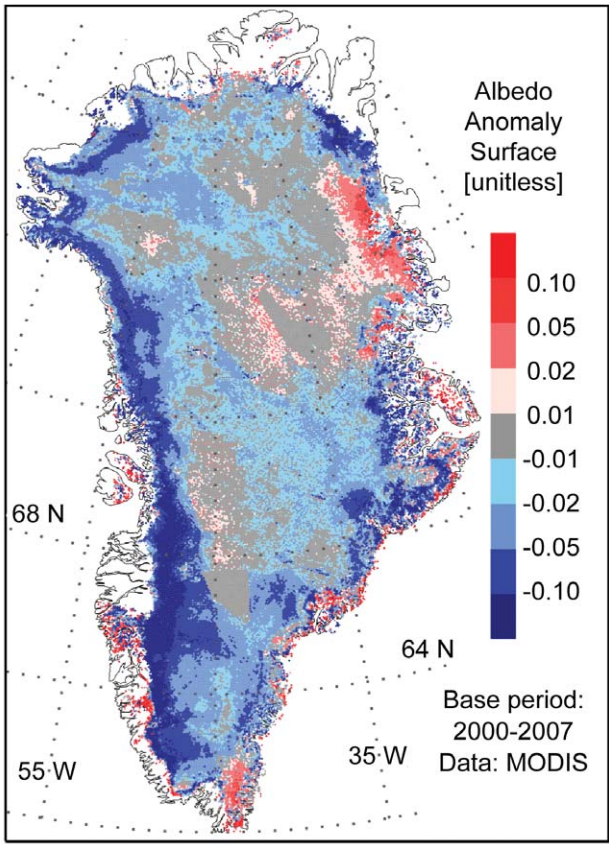

Fig. 5.18. Albedo anomaly (unitless) for 8–23 Aug (days 220–235) 2007 vs the 2000–07 average (from algorithm based on Liang et al. 2005).

the net surface mass budget was 46% below normal, corresponding with a –156 km^3 yr^{-1} anomaly. The 2007 surface mass budget anomaly was a significant fraction of the accumulation rate of 613 km^3 yr^{-1} for the 1971–2000 period.

(vi) Ice sheet albedo

Surface solar radiation reflectance, referred to as albedo, decreases in response to surface melting. Melt season surface albedo anomalies were calculated using the Liang et al. (2005) algorithm for the 2000–2007 period in 15-day intervals that provided sufficient cloud-free viewing of the surface. Negative surface albedo anomalies were widespread beginning in early June, when melting normally begins, through late August when abnormal melt and more frequent rainfall darkened the snow and ice surface (Fig. 5.18).

(vii) Glacier changes

The terminus of Greenland's largest glacier, the Jakobshavn's Isbrae near Ilulissat, moved 0 to 500 m in 2007 (Fig. 5.19), continuing a retreat that began in 2001 with a dramatic 11-km floating ice collapse (Weidick and Bennike 2007). The large ice lagoon called Tissarissoq at the south side of the fjord was flushed of ice by the end of the summer, ice-free probably for the first time since at least the onset of the Little Ice Age (ca. 0.4–0.1 ky BP). It is possible that Tissarissoq was ice-free before that time during the medieval warm period (ca. 1.1–0.5 ky BP).

b. Antarctic

1) Overview—T. A. Scambos

The Antarctic climate system is distinctly different from the Arctic, governed more strongly by the high degree of symmetry of both land and ocean surrounding the pole. The continent's high plateau anchors a strong polar vortex of westerly winds, and is the source of a near-constant katabatic airflow from a frequent inversion layer near the ice sheet surface. Along its coastline, a narrow zone of easterly flow occurs south of the girdling westerlies. (Captain James Cook noted in 1796 that if he were to try to approach the continent again, he might take advantage of this high-latitude shift in the prevailing winds.) Variations in this westerly flow, and in the relative air pressure between the vortex interior and the encircling regions is the primary oscillation of the far southern climate system, the so-called SAM (Marshall 2003). Another recognized pattern is zonal wave 3 (Raphael

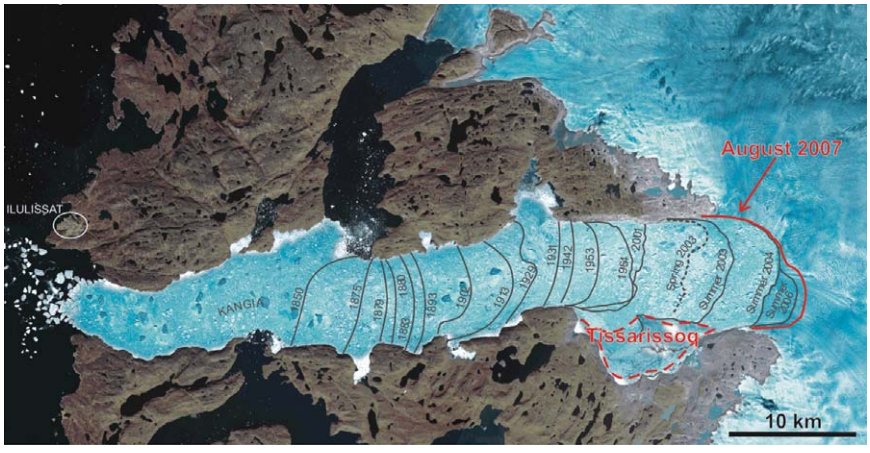

Fig. 5.19. Front position of the Ilulissat (Jakobshavn Isbrae) glacier in 2007 and earlier years, based on Weidick and Bennike (2007). The image mosaic is from Jun 2003 Landsat and ASTER images.

Table 5.2. Greenland ice sheet surface mass balance parameters: 2007 departures from 1971–2000 average (adapted from Box et al. 2006).

Total	2007 as % of average	2007 minus average ($km^3\ yr^{-1}$)
Total precipitation	97%	–18.9
Liquid precipitation	140%	8.3
Evaporation	97%	–2.1
Blowing snow sublimation	106%	2.1
Snow accumulation	97%	–18.9
Meltwater production	153%	154.9
Meltwater runoff	177%	137.3
Surface mass balance	64%	–156.4
Mean temperature	—	1.3
Accumulation area ratio	93%	–0.064 (%)

and Holland 2006; Raphael 2004), describing the tendency for a trio of fixed high pressure cells, and adjacent low pressure cells, to dominate circulation patterns about the continent.

Several studies have noted the apparent slight cooling trend in near-surface temperature records of Antarctic continental stations over the past several decades (e.g., Chapman and Walsh 2007b). Coupled with this cooling pattern is the warming trend observed in the Antarctic Peninsula, among the fastest-warming regions on Earth. Continental Antarctica is the largest remaining region on our planet with unchanged or cooling climate, and this has occasionally been pointed out by non-scientists as a basis for skepticism about GHG-induced "global" climate warming. Yet the Antarctic system is indeed showing a response over recent decades, in the form of an increasing tendency toward a positive SAM mode, that is, increased westerly wind flow. This pattern is consistent with both GHG forcing of climate (Arblaster and Meehl 2006), and with seasonal ozone reduction in the stratosphere (Thompson and Solomon 2002). This increased tendency toward stronger westerlies tends to isolate the cold continental plateau more, leading to cooling, and drives northwesterly flow over the peninsula, resulting in warming. But, importantly, the stronger westerly flow may be influencing ocean currents as well, moving coastal surface water northeastward via Ekman flow, and as a result drawing a return flow of warmer Antarctic Circumpolar Deep Water onto the continental shelf at depth, thus accelerating basal melt rates of thicker ice masses (e.g., Pine Island glacier; Rignot 2008).

The year 2007 was somewhat anomalous relative to

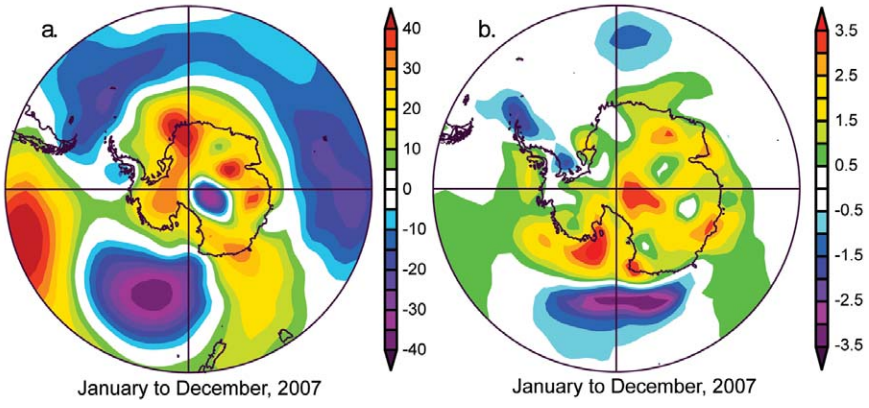

Fig. 5.20. Annual anomaly of (a) 850-hPa geopotential height and (b) surface temperature for 2007 relative to the 1979–2006 period, from NCEP–NCAR reanalysis data. The 850-hPa value is inferred for high-altitude regions of the continent; however, this level best illustrates the near-surface and middle troposphere patterns. These graphs, and climate diagrams shown in Fig. 5.22 (section 5b2), are from the NOAA/ESRL Physical Sciences Division (generated online at www.cdc.noaa.gov). Note that station data for a station near 85°S, 120°E is suspect, particularly for geopotential height, in all NCEP data here.

recent preceding years, with an extended period of negative SAM index, but a sharp rise to strongly positive SAM in December (that persisted into January 2008). The end of the year was likely influenced by the moderate La Niña pattern in the Pacific ENSO circulation. The continent as a whole was warmer than average for the year (underscoring the influence of SAM and the temperature trends in the main continent), and the Antarctic Peninsula was considerably cooler than the period of record (1979 to 2006; see Fig. 5.20b). This resulted in extensive fast ice accumulation on the eastern peninsula coast by the end of the calendar year, and an unusually late start to the summer melt season there. The high degree of variability in the climate pattern led to highly variable sea ice extent anomalies, with monthly mean record highs and record lows being set again this year, as in 2006. Springtime ozone levels were above the record lows of last year, and near the average of the past 15 yr, due to a warmer springtime stratosphere.

2) Atmospheric circulation—R. L. Fogt, T. A. Scambos, and S. Barreira

Antarctic circulation anomalies (here, area-averaged 60°–90°S) were near normal for the first half of the year. During austral fall, however, a weaker than normal SAM pattern (Figs. 5.21 and 5.22) allowed for multiple penetrations of warmer maritime air, and generated significant (beyond +2 standard deviations) mid- to lower-tropospheric warming in late fall/early winter (Marshall 2007) while the stratosphere was anomalously cool (< –2 standard deviations). The surface warming in winter, in conjunction with increased planetary wave activity, propagated anomalous heat flux throughout the depth of the troposphere into the stratosphere, leading to marked (>2 standard deviations) geopotential height increases (Fig. 5.21a), reduction of the previously cold stratosphere (Fig. 5.21b), and weakening of the circumpolar vortex (Fig. 5.21c) in July. Near the end of the year, La Niña's effect on the Antarctic circulation was apparent, with anomalies (low temperatures and geopotential heights, stronger westerly winds) first starting in the stratosphere in November, and then propagating downward to the surface in December. These La Niña–related anomalies were more than 1 standard deviation from the 1979–2006 mean, and the fact that they began earlier in the stratosphere suggests the stratosphere may play a role in coupling the ENSO and the SAM, as seen in earlier austral summers (e.g., L'Heureux and Thompson 2006; Fogt and Bromwich 2006).

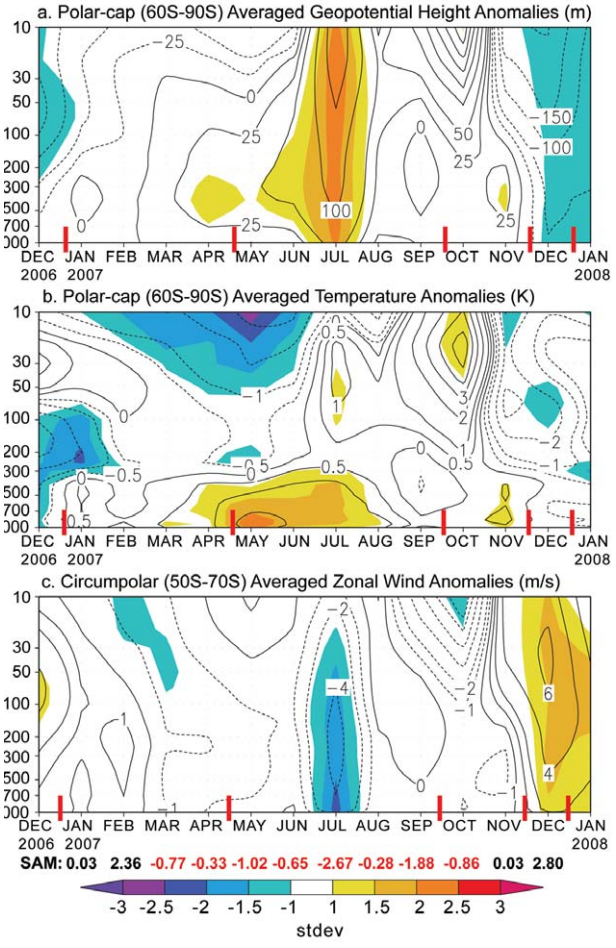

Fig. 5.21. Zonally averaged climate parameter anomalies for the southern polar region in 2007 relative to the 1979–2006 period: (a) Polar cap averaged geopotential height anomalies (m); (b) averaged temperature anomalies (K); (c) averaged wind anomalies (m s^{-1}). Absolute anomaly values are contoured, and the panels are tinted according to the standard deviation of the anomaly (color bar at bottom for scale). Red vertical bars indicate the four separate periods shown as spatial climate anomalies for 2007 in Fig. 5.22 (section 5b2). Primary contour interval is 50 m in (a), 1 K in (b), and 2 m s^{-1} in (c), with selected additional contours at ±25 m, ±0.5 K, and ±1 m s^{-1} in (a), (b), and (c), respectively. Values for the SAM index are shown along the bottom in black and red (SAM values are from www.nerc-bas.ac.uk/icd/gjma/sam.html).

Although many uncertainties exist regarding the mechanisms of climate pattern changes in each polar region, a few factors appear to play dominant roles in the circulation response to external forcing. Important among these is the contrast in orography in the Arctic and Antarctic, leading to very different patterns of Rossby wave propagation (including the stability of tropical teleconnections). Meridional

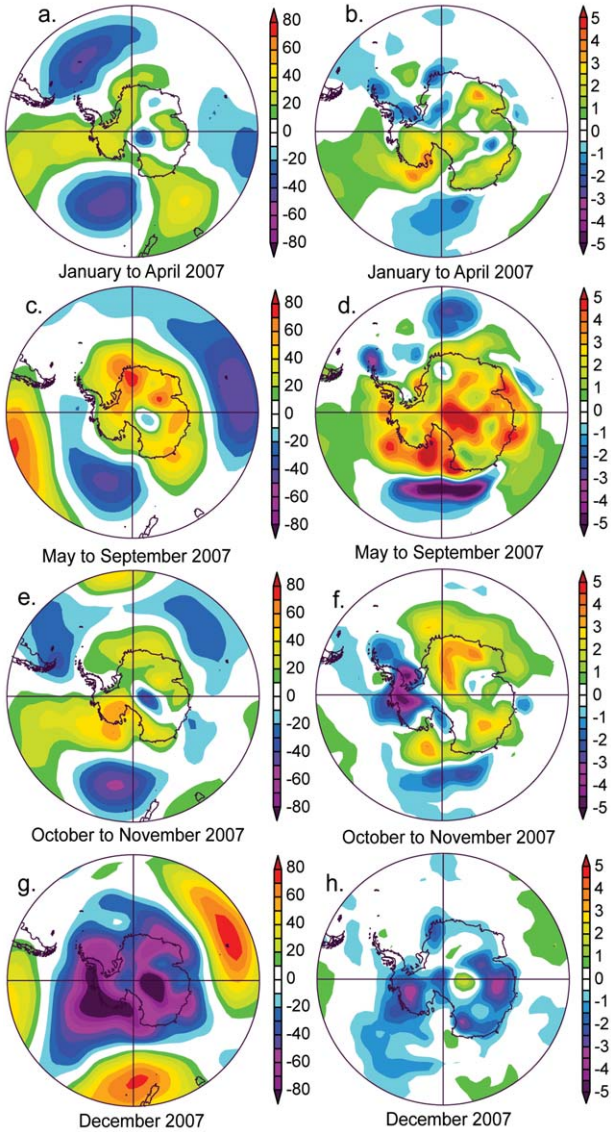

Fig. 5.22. (left) The 850-hPa geopotential height anomaly and (right) surface temperature anomaly relative to 1979–2006 climatology for four distinctive periods in 2007. Note that station data for a station near 85°S, 120°E are suspect, particularly for its geopotential height observation, in all NCEP data here.

mountain ranges and the distribution of land and oceans in the Northern Hemisphere generate strong standing wave patterns, while the Southern Ocean and nearly zonally symmetric Antarctic continent allow for generally stronger zonal flow and annular patterns. Further, stratospheric ozone depletion is playing a more crucial role in the Antarctic circulation (i.e., Thompson and Solomon 2002; Keeley et al. 2007) than in the Northern Hemisphere, and could be amplifying the changes expected from greenhouse gas forcing in some seasons (Turner et al. 2007).

3) Surface station observations—S. Colwell, J. Turner, and S. Barreira

Surface observations from six representative stations across the continent (Fig. 5.23) provide a localized look at the broader atmospheric circulation patterns. The cool tendency year-round for the northern peninsula region is reflected in the negative temperature anomaly at Base Marambio (64°S, 56°W); however, on the western peninsula farther to the south, the climate was several degrees warmer than the mean through this same period (Base San Martin: 68°S, 67°W). These trends indicate a divide in mean airflow during the winter period, with generally southerly winds for the northeastern peninsula (a large deviation in direction from the norm) and northwesterly flow for the southwestern peninsula. Halley V Station (75°S, 26°W) showed a significant pressure anomaly through the winter months, which in turn is part of the pattern that drove the southerly and southeasterly flow across Marambio. Atmospheric pressure at McMurdo Station (77°S, 166°E) was unusually high in July, a trend seen across much of the continent (e.g., Halley, Mawson 67°S, 62°E, and Casey, 66°S, 110°E, as well). This was indicative of the very low SAM index, slower circumpolar westerly flow, and warm conditions seen (Fig. 5.22d).

Two extreme events of 2007 are worth noting, as an indication of how climate trends can set up strong weather anomalies. On 9 July, for the first time in 90 yr, snow was recorded in Buenos Aires, Argentina, and from that city south across Patagonia, temperatures were as much as 15°C below normal. The event was driven by a large high-pressure region just west of southern South America, flanked by two deep lows in the South Pacific and South Atlantic. The resulting winds drove warm air far to the south and into the central West Antarctic, and brought air rapidly northward from that region to the eastern flank of the Antarctic Peninsula and the southern Andes (mountain topography may have played a role in directing this flow). During the period of snowfall and cold weather in Buenos Aires, temperatures near Byrd Station AWS (near 80°S, 120°W) were as much as 16°C above normal.

Troll Station (72.02°S, 2.53°E) was the site of an extreme, and unusually long-lived, storm event during the first week of November. Surface air pressure and temperature anomalies for this period reveal that the storm was augmented by an extensive area of low pressure offshore, and high pressure to the east and south. The boundary region between these two centers sent an intense northeasterly to easterly

flow toward the station as the storm proceeded. It was likely that, again, mountain topography near the station augmented the regional flow pattern. Winds remained above 100 km h^{-1} for five consecutive days. Peak gusts reached 200 km h^{-1}, leading to significant damage at the station, including a 3,500-kg ship container that was blown several *kilometers* away from the base during the storm. The period during the latter part of the storm and just afterward was characterized by much warmer-than-average temperatures, as much as 16°C above the mean.

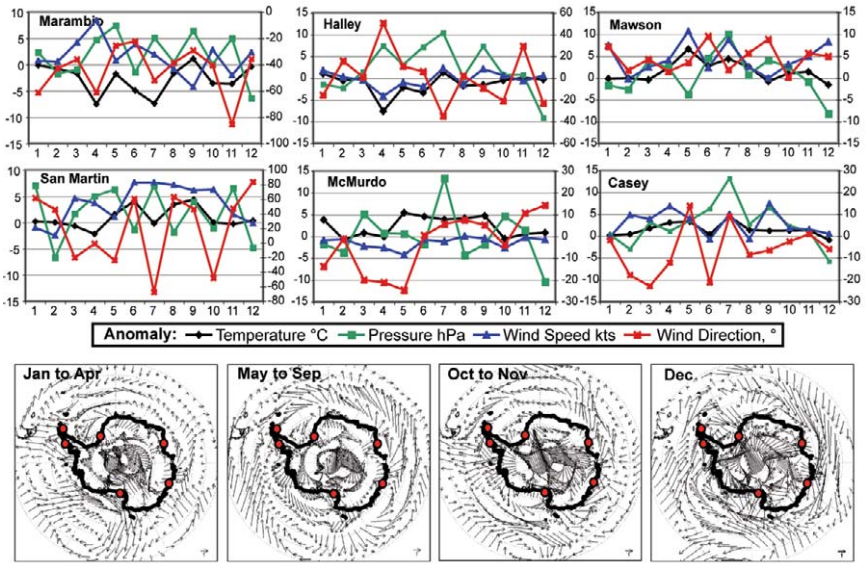

Fig. 5.23. (top) Antarctic station data and surface wind anomalies for 2007. Monthly mean anomalies for air temperature, sea level pressure, wind speed, and wind direction are shown for six representative stations. Wind direction anomaly is given in degrees clockwise (+) or anticlockwise (–) along the right-side y axis for the plots. (bottom) Mean wind direction and intensity anomaly (vector difference from mean) for the four climatological periods identified in Fig. 5.22 (section 5b2). Red dots indicate the six station locations. Reference vector is 1 km h^{-1} (=~1.85 kt). The base period used for all plots is 1991–2000.

4) Surface mass balance—A. Monaghan and D. Bromwich

Snowfall accumulation is the mass input to the Antarctic ice sheets, and is the net result of precipitation, sublimation/vapor deposition, drifting snow processes, and melt (Bromwich 1988). Of these, precipitation is the dominant term of the Antarctic surface mass balance at regional and larger scales (Genthon 2004). To date, atmospheric models have been the most widely used means of assessing the temporal variability of the Antarctic snowfall for periods longer than a decade (e.g., Bromwich et al. 2004). The most recent modeling studies indicate there has been no trend in snowfall since about 1980 (Van de Berg et al. 2005; Monaghan et al. 2006).

Precipitation fields from the NCEP/DOE Reanalysis II (NN2) were employed to assess Antarctic snowfall for 2007. The snowfall in NN2 has been found to have an anomalously upward trend from 1979 onward compared to other model-based records and measurements from snow-stake farms and ice core records (Bromwich et al. 2004); however, the inter-annual variability of the snowfall is in very good agreement with other models (Monaghan et al. 2006). Therefore, if detrended, the NN2 record roughly approximates the "flat" trends that more accurate models predict, and the 2007 snowfall can be compared to the average for 1979–2007 to give a proxy of whether the snowfall for the year was above or below the mean.

Figure 5.24 shows the 2007 detrended annual precipitation anomalies from the 1979–2007 mean. In general, the anomalies over the continent were negative, consistent with above average annual 850-hPa geopotential height anomalies (which indicate lower-than-normal synoptic activity) over nearly the entire continent (Fig. 5.20a). Conversely, precipitation anomalies over the Antarctic Peninsula and near the front of the Ross Ice Shelf and Marie Byrd Land (~135°W) were positive, consistent with lower-than-normal geopotential height anomalies nearby. Overall the pattern was very similar to 2006.

The 2007 detrended monthly precipitation anomalies from the 1979–2007 mean, averaged over the grounded Antarctic ice sheets, were also derived (not shown). None of the anomalies exceeded two standard deviations, but the anomalies in February, November, and the annual anomaly varied from the mean by more than one standard deviation. Continent-wide precipitation was below average during winter and spring 2007. This may have been due to below-normal synoptic activity during these months as indicated by positive 850-hPa geopotential height

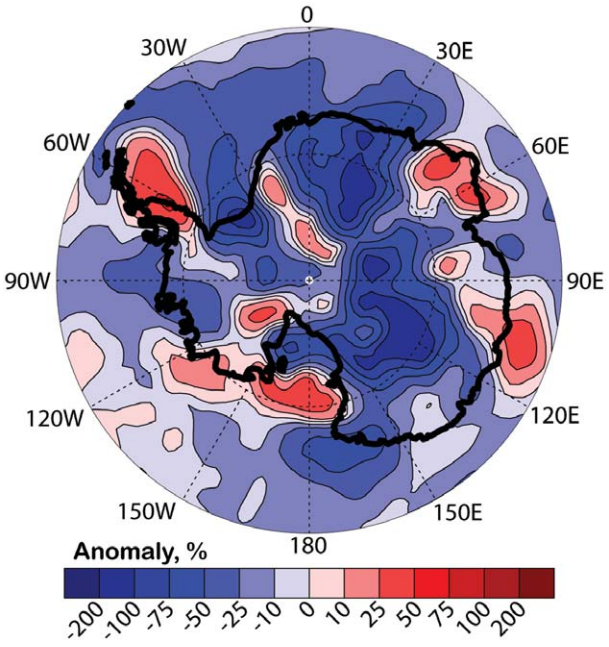

Fig. 5.24. Detrended precipitation anomalies (% yr^{-1}) from the NCEP–DOE Reanalysis II for 2007 compared with the 1979–2007 mean.

anomalies across the continent and near the coastal margins (Fig. 5.22c), which projected strongly onto the annual mean. Overall, the 2007 annual precipitation was about 7% below normal. This downward fluctuation had a positive contribution to sea level of approximately 0.35 mm.

The 2006 annual precipitation anomaly at the continental scale was similarly below normal, by 6% (Arguez et al. 2007). However, the causality of the similar annual precipitation between the two years appears to have been due to different reasons, as the 850-hPa annual and seasonal anomalies were quite different. For example, precipitation was above normal during April/May 2007, while it was below normal during the same period in 2006; weaker SAM conditions during austral autumn 2007 led to enhanced penetration of maritime air at that time.

5) Seasonal melt extent and duration—H. Liu, L. Wang, and K. Jezek

Using a wavelet transform–based edge detection method (Liu et al. 2005), the extent, onset date, end date, and duration of snow melt on the Antarctic ice sheet during the 2006–07 austral summer were derived. The 19-GHz horizontal polarization channel of satellite passive microwave data (SSM/I, a sensor flown on several U.S. defense meteorological satellites) is utilized for the melt information extraction. Melt onset date, duration, and extent are shown in Fig. 5.25. The total melt extent during the austral year 2006–07 was 900,625 km^2, covering only 6.6% of the continent. This was determined by summing all pixels with at least one day of surface melting. The melt index during 2006–07 (sum of total melt extent for each day in the melt season; Liu et al. 2006) was 28,011,250 day km^2. As shown in Fig. 5.25c, there has been a decreasing trend in melt extent the past five years, and for the overall record (1978–2007). The austral year 2006–07 melt extent, and intensity (melt index) rank the second lowest since 1978.

The surface melt during 2006–07 mainly occurred on the Antarctic Peninsula, Abbot Ice Shelf, West Ice Shelf, Shackleton Ice Shelf, and Amery Ice Shelf. A brief but extensive surface melting was detected over the Ronne–Filchner Ice Shelf during January 2007. Amery Ice Shelf, Queen Maud Land, Wilkes Land, and Ross Ice Shelf have an extremely low melt

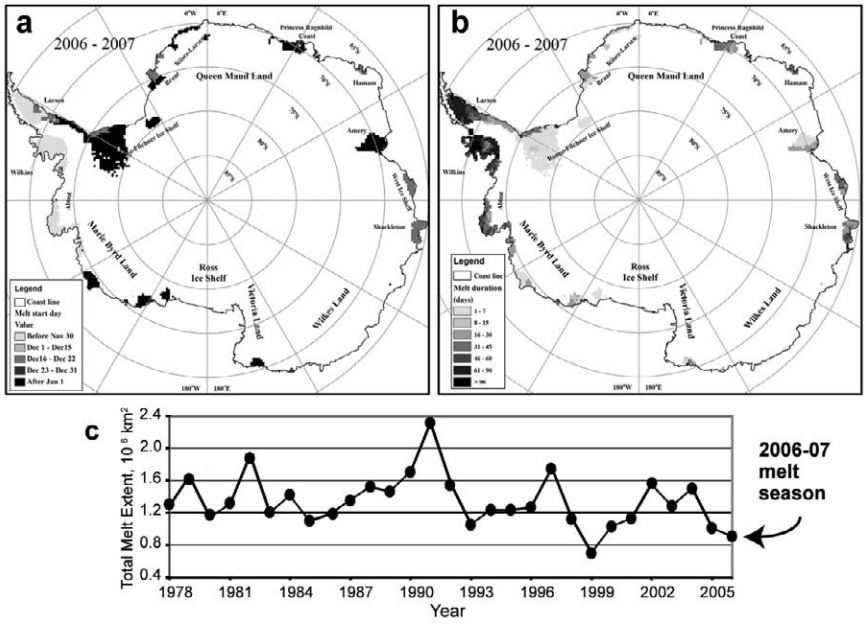

Fig. 5.25. (a) Melt onset date and (b) melt season duration in days, for the 2006–07 melt season. The sum of the regions indicated in both plots indicates total melt extent for the year as shown in the (c) graph of total melt extent.

extent and melt intensity. Surface melt primarily took place in December, January, and February, and the extent peaked on 21 January 2007.

6) Sea ice extent and concentration—R. A. Massom, P. Reid, S. Barreira, and S. Stammerjohn

Antarctic sea ice in 2007 was characterized by considerable temporal and spatial variability, with ice extent anomalies ranging from a record low in May of –12% or -1.2×10^6 km^2 (equal to 1980) to a record high in December of +14% or $+1.7 \times 10^6$ km^2 for the satellite time series (1978–present; Fig. 5.26). The analysis is based on monthly mean SSM/I-derived sea ice concentration data produced by the NSIDC Sea Ice Index project (Fetterer et al. 2002, updated monthly).

With the exception of May, sea ice extent overall was generally close to or only slightly lower than the long-term mean for January through August. There was, however, considerable regional variability, largely in response to the strong circulation and temperature patterns described earlier. This resulted in sea ice extent and concentration anomalies that were both greater and zonally asymmetric (Fig. 5.26).

A strong feature of the 2007 austral minimum ice extent period (January–March) was the persistence of zones of high concentration ice in the east Weddell Sea, the Ross Sea, around the BI, and along the Indian Ocean coastal sector (Fig. 5.26a). Conversely, significantly less

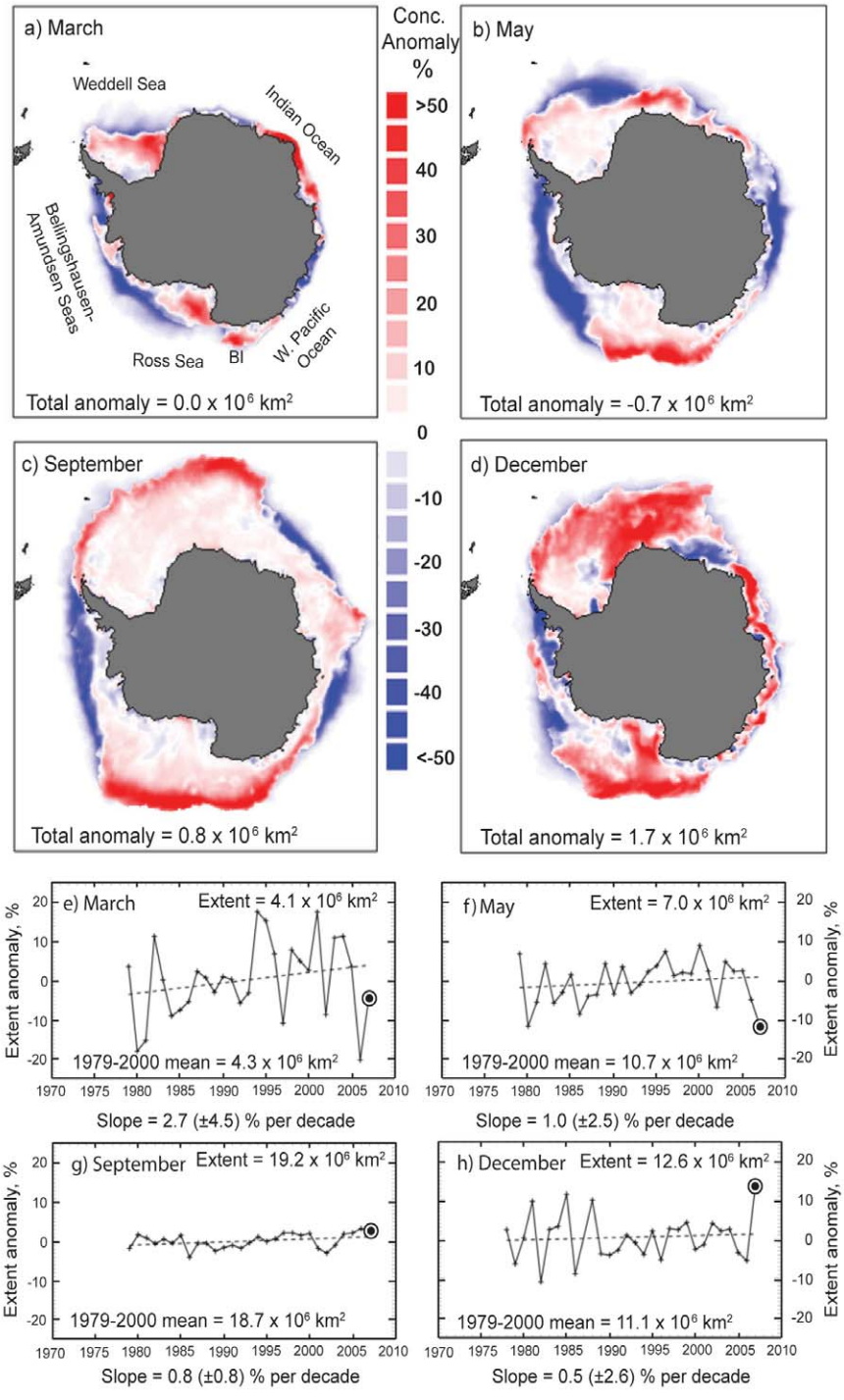

Fig. 5.26. Antarctic sea ice concentration anomalies in 2007 relative to the 1979–2000 mean for the month for (a) Mar, (b) May, (c) Sep, and (d) Dec, and (e)–(h) trends in sea ice extent for the same months. "BI" in (a) indicates the Balleny Islands area. Sea ice concentration is the area covered by ice per unit area. Concentration is derived for 25-km grid cells; the color mapped monthly concentration anomalies are the difference between the 2007 value and the 1979–2000 mean value for those grid cells. The total concentration anomaly is the sum of anomalies over all grid cells. Ice extent is the total area covered by ice at any concentration. From the Sea Ice Index (http://nsidc.org/data/seaice_index/).

ice occurred in the Amundsen Sea and west Pacific Ocean sectors at this time compared to the mean.

The distinctive zonal asymmetry in ice extent and concentration anomalies was particularly well developed in May (Fig. 5.26b). The record negative extent anomaly at this time, which represents a strong departure from the upward trend for ice extent in this month (Fig. 5.26f), resulted from lower-than-average autumnal advance over broad zones across the Weddell Sea, the sector 70°–110°E, and the Bellingshausen–Amundsen Seas. The latter was associated with a persistent, deep low pressure circulation centered on approximately 70°S, 135°W—the "Amundsen Sea Low." This created a persistent and dominant west-northwesterly airflow that led to compaction of the sea ice against the West Antarctic Peninsula and Amundsen Sea coasts, preventing normal autumnal ice edge advance (see Massom et al. 2008). Conversely, cold air outflow to the west from continental Antarctica resulted in an ice edge advance and a positive ice concentration anomaly across the Ross Sea sector.

The remainder of the year (September–December) was characterized by similar regional patterns in negative and positive ice extent, area, and concentration anomalies (Figs. 5.26c,d), but with overall extent anomalies becoming positive (Figs. 5.26g,h). At 19.2 $\times 10^6$ km^2, ice extent in September was 3% above the 1979–2000 September mean; this was the second highest extent on record (just behind 2006 at 19.35 $\times 10^6$ km^2), but the highest in terms of areal coverage, that is, the product of ice extent and concentration (at 15.2 $\times 10^6$ km^2 versus 15.1 $\times 10^6$ km^2 for September 2006). As was the case in May, a major determinant of the wide zone of negative extent and concentration anomalies across the Bellingshausen–Amundsen Seas sector was wind-driven compaction associated with a deep Amundsen Sea low air pressure anomaly, this time coupled with a blocking high-pressure anomaly in the South Atlantic.

Spatially, the August through October sea ice extent showed, in most areas, a continuation of the long-term trend in Southern Hemisphere sea ice extent for those months. For example, sea ice extent to the north of the Ross Sea continued to expand during these months, while farther to the east there was a contraction of ice extent. Both anomalies were primarily a result of deepening low pressure in the Amundsen Sea. Interestingly, in the far southwest of the Indian Ocean, sea ice extent was anomalously low, in contrast to the long-term trend in that area. This was primarily due to the central low pressure system being farther to the west than normal in that region. Both January and December 2007 had a continuation of the trend in lowering sea ice concentration around Davis Station (68° 35′S, 77° 58′E) and an increase in sea ice concentration around Mawson (67° 36′S, 62° 52′E).

As noted above, the December 2007 value of +14% (+1.7 $\times 10^6$ km^2) is the highest on record. Notable also is the SAM index value for December, which was +2.80, among the highest ever, based on observational records dating back to 1957 (www.nerc-bas.ac.uk/icd/gjma/sam.html; see also Marshall 2003). The 2007 La Niña also reached its maximum late in the year, with an SOI value[1] of 14.4 in December and the Niño-3 region reaching a minimum sea surface temperature in November. The persistence of unusually compact sea ice into the summer melt period of 2007–08 in the Weddell Sea, East Antarctic coastal, and Ross Sea sectors led to reported difficulties in ship navigation during the critical shipping (base resupply) season.

7) Ozone depletion—P. A. Newman

The Antarctic ozone hole was less deep in 2007 than the severely depleted 2006 ozone hole, and was near average in comparison to the last 15 yr. The areal extent of the hole was slightly smaller than average. South Pole ozonesondes showed higher than average ozone in comparison to the last 20 yr, and the OMI measurement of the Antarctic minimum ozone value was also slightly higher than average. This slightly improved Antarctic ozone situation resulted from warmer-than-average stratospheric temperatures during the ozone loss period in September–October (Fig. 5.21b).

The ozone hole is primarily caused by human-produced compounds that release chlorine and bromine gases in the stratosphere. Observations by the *Aura* satellite's MLS showed extremely high levels of ClO chemicals in the lower stratosphere (465 K, ~20 km) during August and September. These high levels of ClO covered almost the entire Antarctic region but had been largely converted to other nonozone destroying forms by early October. Coincident with the high ClO were extremely low values of ozone.

A fundamental process behind the formation of the ozone hole is the conversion of chlorine molecules from the nonreactive forms (HCl and ClONO2) into reactive forms on the surfaces of PSCs. This reactive chlorine leads to rapid ozone destruction. The CALIPSO satellite provides an extremely high-resolution estimate of PSC structure over Antarctica

[1] The December SOI value of 14.4 is based on nonstandardized data.

using lidar technology. Using this instrument, it is estimated that the volume of PSCs was smaller in 2007 than 2006 by about two-thirds. In addition, the presence of PSCs over Antarctica ended at a slightly earlier date at altitudes near 20 km. The smaller volume of PSCs resulted in less conversion to reactive chlorine, and hence a smaller ozone hole in 2007 than 2006.

Over the last 15 yr, the ozone hole has reached an average yearly maximum size of about 23–24 million km^2. On 13 September 2007 the Antarctic ozone hole reached an areal extent of 25.1 million km^2. For the period 21–30 September, the area of the ozone hole was almost in the average range at 22.8 million km^2. The minimum values of ozone inside the ozone hole were also higher than the last few years (the record low value occurred in 2006, at 85 Dobson units on 8 October). In 2007 the lowest value observed by OMI was 106 Dobson units on 30 September. The spatial extent of the hole on this day is shown in Fig. 5.27.[2]

Balloon-borne ozonesonde observations from NOAA/ESRL at the South Pole showed a low ozone value of 125 Dobson Units on 8 October 2007. The layer between 14 and 21 km had a typical 95% loss of ozone. This contrasts with a value of 93 Dobson units on 9 October 2006 and essentially complete destruction in the 14–21-km layer. These balloon measurements also showed that temperatures in the critical layer of 20–24 km were below average in early September, but warmed to above average values in mid-September.

The severity of the ozone hole varies from year to year with the temperature of the Antarctic stratosphere. Colder than average temperatures result in larger and deeper ozone holes, while warmer temperatures lead to smaller size and less ozone destruction. NOAA satellite temperatures and balloon temperatures during the late-September 2007 period indicated that the lower-stratospheric temperatures at the rim of Antarctica (65°–75°S, 20 km) were almost equal to the long-term temperature average of 198 K.

As a result of regulations, the concentrations of ozone depleting substances in the lower atmosphere (troposphere) peaked in about 1995 and are now decreasing in both the troposphere and stratosphere. It is estimated that these gases reached peak levels in the Antarctic stratosphere in 2001 and are now slowly decreasing. However, these ozone depleting substances typically have very long lifetimes in the atmosphere (>40 yr). The chlorine and bromine gases are now slowly decreasing from peak levels by about 0.7% yr^{-1} (down only 3.1% from the 2001 peak). As a result of this slow decline of ozone depleting substances, the ozone hole is estimated to be very slowly decreasing in area by about 0.2% yr^{-1}. This slow decrease is masked by the large year-to-year variations caused by the Antarctic stratospheric weather fluctuations (Newman et al. 2006).

The Antarctic stratosphere is warmed by the return of sunlight at the end of the polar winter and by large-scale weather systems (planetary-scale waves) that form in the troposphere and move upward into the stratosphere. During the 2007 Antarctic winter and spring, these planetary-scale wave systems were stronger than normal (10%–15% above average for the August–September period). Because the wave levels were above average in 2007, the Antarctic stratospheric temperature was also slightly above average.

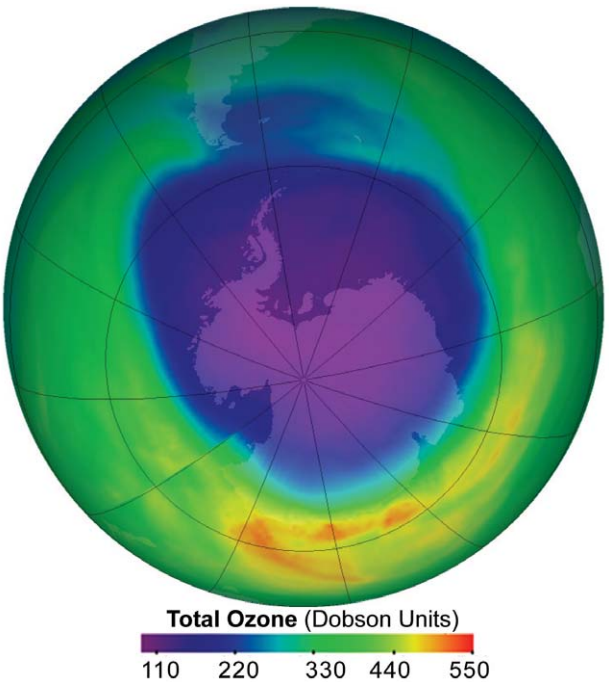

Fig. 5.27. Total ozone (in DU) measured on 30 Sep 2007. Purple blue coloring indicates the low values of the Antarctic ozone hole. The minimum value observed on this day was 106 DU. The image is based on total ozone observations from the OMI aboard the NASA Aura satellite. From Ozone Hole Watch (http://ozonewatch.gsfc.nasa.gov/).

[2] The analysis was based upon data from the NASA *Aura* satellites, in particular, the KNMI OMI and the JPL MLS. PSC information was obtained from the NASA LaRC CALIPSO instrument. NOAA/NCEP provided analyses of satellite and balloon stratospheric temperature observations. NOAA/ESRL regularly launches ozone- and temperature-measuring balloon instruments from the South Pole.

6. REGIONAL CLIMATES

a. Overview—A. Arguez

This section provides a localized perspective of global climates in 2007, offering analyses of individual continents, nations, and subregions. Consistent with the remainder of the report, the year 2007 is described and placed in a historical context to the extent possible. The vast majority of contributions to this section are authored by scientists that hail from the respective region for which they cover. The remainder of this section is divided into seven parts: Africa, North America, Central America and the Caribbean, South America, Asia, Europe, and Oceania. These regions are further divided into pragmatic subdivisions. Naming conventions in this section do not reflect any particular sympathies, political or otherwise. Please note that varying reference periods are utilized in the computation of climate anomalies. Please also note that seasonal averages (boreal winter or austral summer) sometimes include data from December 2006, and in some cases annual anomalies are defined for December 2006 to November 2007, due to lags in acquiring data. Where omitted, the source of data used in analyses is typically the agency that the section's lead author is affiliated with.

b. Africa

1) Eastern Africa—C. Oludhe, L. Ogallo, L. Njau, M. Kadi, and S. Tinni

The GHA subregion can be divided into three sectors (southern, equatorial, and northern) based on periods of rainfall onsets and withdrawals associated with the movement of the ITCZ. The southern sector, consisting of central and southern Tanzania, experiences a unimodal rainfall regime, with rainfall occurring from December to April. The equatorial sector is made up of northern Tanzania, Rwanda, Burundi, Uganda, Kenya, southern and extreme eastern Ethiopia, southern Sudan, and the southern half of Somalia; it exhibits a bimodal rainfall regime, with the "long rains" season occurring in March–May and the "short rains" being experienced in October–December. In the northern sector, composed of central and northern Ethiopia, Eritrea, Djibouti, and the northern half of Sudan, the major rainy season is June–September, but a few areas receive a secondary peak from March to May.

Most of the southern and equatorial sectors as well as much of Ethiopia received rainfall amounts ranging from 75% to 125% of their LTM in 2007 during the usually dry months of January–March. Rainfall in north-central Tanzania was over 25% greater than normal. The remaining parts of the region received less than 75% of their LTM rainfall. March marks the beginning of the long rains over the equatorial sector, and March 2007 was marked with reduced rainfall activity and poor distribution over most parts of the GHA. Specifically, much of the northern half of the GHA received less than 100 mm of rainfall while most of the southern sector received more than 100 mm of rainfall during March .

The period JJA marks the summer rainfall season over many parts of the northern sector, and is also important for the western and coastal parts of the equatorial sector. In 2007, the season was marked by very wet conditions with rainfall totals that were 25% to over 75% greater than the LTM, with extremely wet conditions in northeast Sudan, Somalia, northern Kenya, and western Tanzania. Severe floods ravaged the GHA during the 2007 rainy season. The Mpeketoni and Witu divisions of Kenya were hit by floods in early June. In late July, Sudan's Humanitarian Aid Commission reported that the level of the Blue Nile at Khartoum, the capital, was "far above" the record levels seen at this time of year in 1988. August brought flooding to western Kenya's Budalangi region and the Teso subregion of Uganda. A major flood event also affected Rwanda on 12 September.

Climatologically, the various stages of the life cycle of the short rains are associated with specific months by sector. September marks the withdrawal of rainfall over the northern sector. October marks the onset of the seasonal rainfall over the equatorial sector. November marks the peak of the rainfall season over the equatorial sector. December marks the cessation of the rainfall season over the equatorial sector. During 2007, rainfall in September was mainly concentrated over the southern and central parts of the northern sector. In October, a delayed onset of the seasonal rainfall over most parts of the equatorial sector was observed, while rainfall activity was confined to the central and western equatorial sector. In November, rainfall activity was depressed over most parts of the northern and southern sectors and above average over the equatorial sector.

2) Northern Africa

(i) Northwest Africa—K. Kabidi and A. Sayouri

Most of northwest Africa's rainfall occurs during the period of October–May as the result of extratropical weather system incursions from the Atlantic Ocean and Europe, bringing cold air and cloudiness. The typical rainfall distribution is characterized by a positive gradient from south to north and the topographic influence exerted by the Atlas Mountains. The dry season extends from June to

Table 6.1. Daily minimum temperature records for March.

Station	Record value (°C) and date	Previous record (°C) and date	Record period
Rabat Sale Lat: 34°3′N Lon: 6°46′W	1°C on 23 Mar 2007	1.9°C on 6 Mar 1967	1957–2007
Sidi Slimane Lat: 34°14′N Lon: 6°3′W	–0.5°C on 23 Mar 2007	0.4°C on Mar 2004	1980–2007
Chefchaouen Lat: 35°5′N Lon: 5°18′W	–3.5°C on 23 Mar 2007	–1°C on 6 Mar 2005	1995–2007
Tanger Aero Lat: 35°43′N Lon: 5°53′W	1°C on 23 Mar 2007	1.4°C on 6 Mar 2005	1931–2007

early September, influenced by hot, dry air originating from the Sahara. Nevertheless, some convective clouds develop occasionally during the dry season when subtropical maritime air masses converge in the region. Summer is generally dry and hot; daily maximum temperatures exceeding 40°C is a common feature of the continental areas.

The year 2007 was characterized by several extreme weather events including heavy rainfall, heat waves, cold spells, and strong winds.[1] Several records were broken and the annual mean temperature continued to rise. northwest Africa experienced windy conditions across the region during February and March, with wind speeds exceeding 31 m s^{-1} in some areas. The maximum wind speed was recorded at Khouribga, Morocco (~36 m s^{-1}). On 23 March, very low temperatures were recorded in several locations (Table 6.1). The daily temperature anomalies are plotted in Fig. 6.1.

At the beginning of spring, there was significant rainfall activity over northwest Africa. In April, many stations in Morocco, Algeria, and Tunisia reported rainfall exceeding 100 mm. A total of 73.6 mm of rainfall fell on 21 April in Nador in northern Morocco. These extreme rainfall events caused damage to property and infrastructure and claimed numerous lives, mainly because of the resulting springtime flooding in Algeria.

Several heat wave events occurred in the summer of 2007, contributing to forest fires in the Rif Mountains of northern Morocco in July. Tunisia and Algeria withstood a severe heat wave during June and July, where the daily maximum temperature exceeded 47°C (117°F), breaking all-time high temperature records in some locations (Fig. 6.2).

During autumn, northwest Africa experienced a succession of weather systems. Region wide the mean rainfall exceeded 100% of the normal for the season, and daily rainfall records for November were broken. For example, 94 mm of rain fell at Tetouan City in the extreme north of Morocco on 24 November, breaking the previous daily record of 90 mm on 19 November 1969. Flooding in parts of Algeria occurred throughout the fall, causing additional damage and loss of life.

[1] Based on observations from the Direction de la Météorologie Nationale in Morocco.

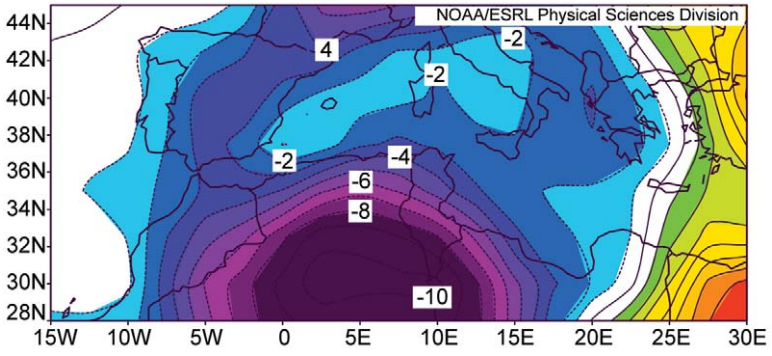

Fig. 6.1. Daily temperature anomalies (°C; 1968–96 base period) over northwest Africa on 23 Mar 2007. [Source: NOAA/ESRL.]

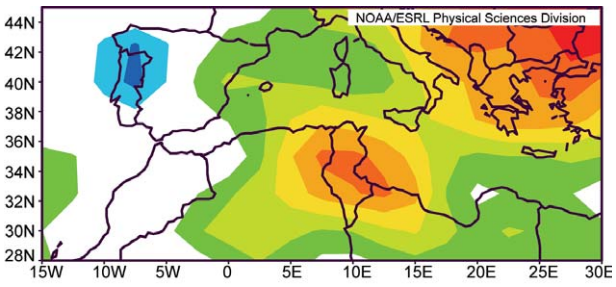

Fig. 6.2. Monthly temperature anomalies (°C; 1968–96 base period) for Jun 2007 over northwest Africa. [Source: NOAA/ESRL.]

(ii) Egypt—S. M. Attaher and M. A. Medany

Egypt is located in the northeast corner of the African continent, with 3,500 km of coastline facing the Mediterranean in the north and the Red Sea in the east. Egypt is divided into four major geographic zones: 1) the Nile Valley and Delta, 2) the Western Desert, 3) the Eastern Desert, and 4) the Sinai Peninsula. Egypt is composed of two climatic zones, the Mediterranean zone and the arid zone of the North Africa region. In general, Egypt's climate is semiarid to arid, characterized by hot dry summers, moderate winters, and very little rainfall. Temperatures average between 27° and 32°C in summer and 13° and 21°C in winter, and most rainfall occurs in the winter months. Snow periodically falls on Sinai's mountains, and on rare occasions in the northern coastal cities. Several prominent wind regimes affect Egypt, including the Khamaseen, which is a seasonal southeasterly wind that blows every spring. The Khamaseen advects sand and dust, and can be associated with temperatures that exceed 38°C.

The average annual surface temperature in 2007 was 0.9°C above the 1961–90 average (Fig. 6.3). For the year, all stations indicated an increase in minimum temperature in the range of 1.0°–2.1°C, with an increase in average temperature of 0.5°–1.3°C. Approximately six cold waves occurred in winter, during which the temperature decreased by 3°–7°C below normal, with each event lasting 3–6 days. Several heat waves with daily temperature anomalies exceeding +2°–6°C were observed during January, February, March, and December, with each heat wave lasting about 2–7 days. From May–November, temperatures were near normal or above the average by 2°–6°C, with an increased frequency of heat waves. Although the number of the rainy days was near the annual average, the total precipitation in 2007 was below the normal by about 8%–17%.

Strong winds and dust and sand storms typically occur in February–April in Egypt. During February and March 2007, there were a limited number of these events, with an average wind speed less than 6 m s^{-1}, whereas the recorded average horizontal visibility was 4–6 km. On 17 April, a strong sand storm associated with the Khamaseen hit Egypt with wind speeds reaching 17 m s^{-1} coupled with temperatures reaching 36°C (~8°C above normal). This sand storm decreased the horizontal visibility to less than 100 m, effectively shutting down all transportation activities for a day and a half. The National Meteorological Authority declared that this sand storm was the strongest in 30 yr.

3) Southern Africa—W. M. Thiaw, A. C. Kruger, D. M. Patricio, L. Njau, M. Kadi, and S. Tinni

(i) Precipitation

During the 2006–07 rainfall season, the climatologically wet region of southern Africa (the eastern half of the region) registered amounts that ranged between 300 mm in central South Africa to over 1200 mm in northern Madagascar and parts of northern Zambia (Fig. 6.4a). In the climatologically dry zone (the western part from Namibia and Botswana southward into western South Africa) rainfall totals ranged between less than 100 mm along coastal Namibia and South Africa to 400 mm in the northern areas of Namibia and Botswana. The rainfall season featured a north–south dipole structure with enhanced rainfall in the northeastern part of the region from central Mozambique and eastern Zimbabwe northward into eastern Zambia (Fig. 6.4b). Rainfall was particularly enhanced over central Mozambique, where anomalies exceeded 200 mm in some localities. The area of suppression was in the southern part of the region, and mainly over South Africa, Botswana, and Namibia, where rainfall anomalies averaged 50–200 mm below the mean.

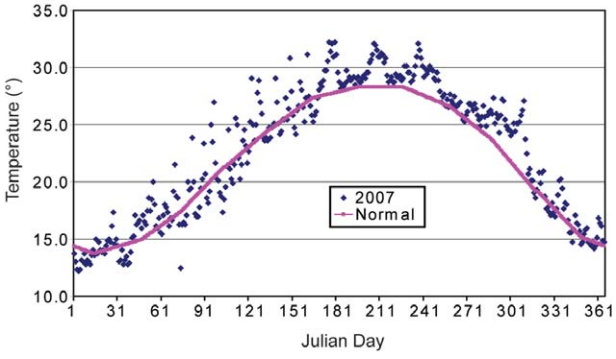

Fig. 6.3. Average annual surface temperature (°C) of 2007 for Egypt (blue diamonds) compared with the average normals for 1961–90 (pink line).

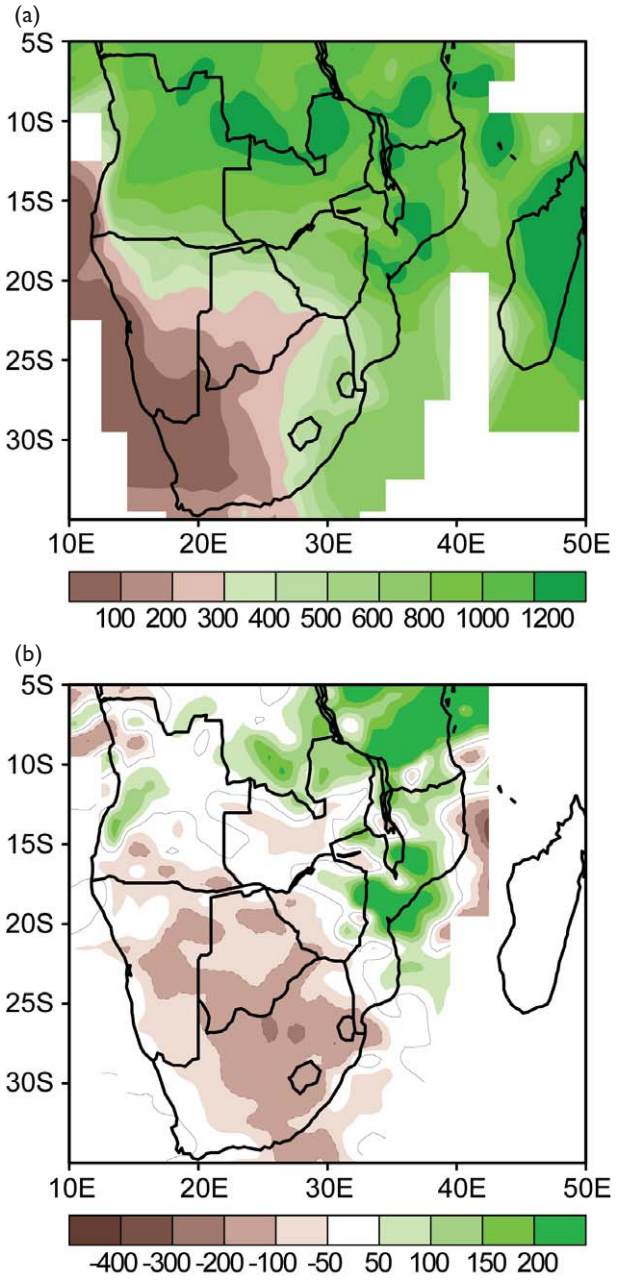

Fig. 6.4. (a) Total precipitation (mm) and (b) anomalies (mm; 1971–2000 base period) for Nov–Apr 2006/07 over southern Africa.

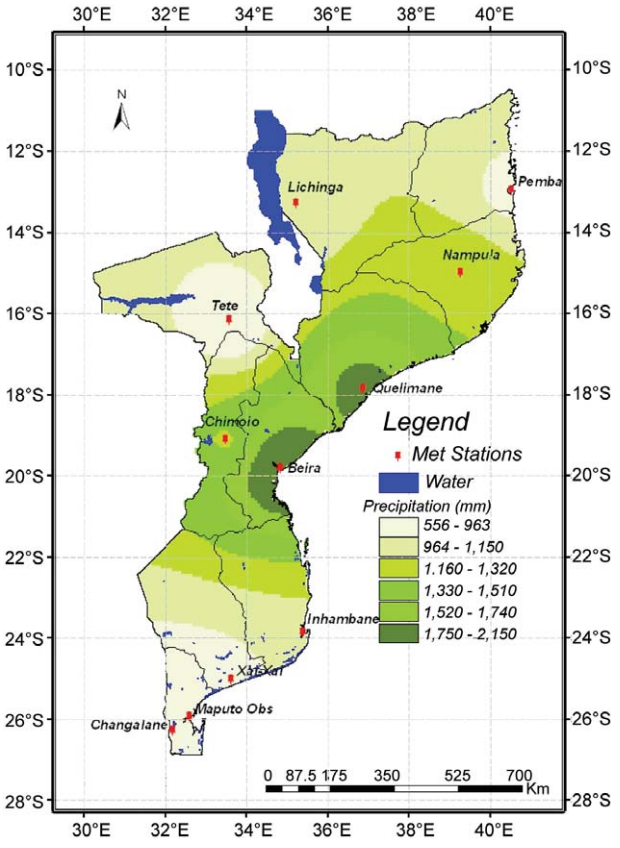

Fig. 6.5. Annual total rainfall (mm) for 2007 over Mozambique.

The rainfall season was once again marked by sharp intraseasonal variability. In the area of enhancement, rainfall was off to a quick start early in November, and the months of December and January ranked above the 90th percentiles based on the 1971–2000 mean. In response to a warm Indian Ocean, and especially to the Agulhas Current, strong tropical cyclones brought extremely heavy rainfall to central Mozambique and caused flooding along many river basins, including the Save River. In contrast, in the area of suppression (Fig. 6.4b), while the rainfall was near average in November, and December ranked in the 70th percentile, the period from January to March 2007 was extremely dry, with both January and February ranking only in the 10th percentile and March in the 30th percentile.

Annual rainfall in 2007 over southern Africa was highly variable. The most noteworthy deviations from normal were dry conditions over the central and eastern parts of South Africa, the southeastern coast of Madagascar, and southern parts of the Democratic Republic of the Congo. Very high rainfall was received along the coasts and adjacent interiors of Angola into northern Namibia, central Mozambique into eastern Zimbabwe, and along the west coast of Madagascar, mostly during the latter part of the year from October to December. South Africa suffered from drought and wildfires in July, ravaging swaths of KwaZulu-Natal, Mpumalanga, and Swaziland.

Rainfall over Mozambique, in particular, was significantly above average in 2007. In southern Mozambique, rainfall was 31.5% above normal. In

December, 333 mm fell in Inhambane. In central Mozambique, 2007 rainfall was 26% above normal, with 640 mm of rain falling in January in Quelimane and 2,153 mm falling for the year in Beira (Fig. 6.5). Northern Mozambique was near normal for 2007, but heavy rainfall (430 mm) fell in Pemba in February.

(ii) Temperature

Annual mean temperatures[2] over southern Africa were generally very close to the 1971–2000 mean. However, areas in northern South Africa, northern Madagascar, and a wide area in southern Angola and in northwestern Zambia were 1°–2°C above normal. The near-normal temperature conditions in the southern parts is reflected by the mean temperature anomalies of 28 South African climate stations, which show that temperatures in South Africa in general were about 0.44°C above the 1961–90 mean, making 2007 approximately the 11th warmest year since 1961.

(iii) Atmospheric circulation

Consistent with warming in the equatorial Pacific and in the midlatitudes of the South Atlantic and south Indian Oceans, the low-level atmospheric circulation associated with the 2006–07 rainy season featured weaker-than-normal westerlies south of about 35°–40°S. As a result, midlatitude frontal systems from the southwest were less active, setting up unfavorable conditions for rainband disturbances to develop and move across southern Africa. These socalled tropical temperate troughs result from the coupling between midlatitude systems and tropical lows and account for much of the synoptic rainfall in southeastern Africa. In addition, the 500-hPa geopotential height pattern (Fig. 6.6) revealed the presence of a persistent anomalous high pressure system of 70–210 m above average, mostly located over southern Africa for much of the peak of the Southern Hemisphere summer. In contrast, on the equatorward flank of the Mascarene high pressure system, an easterly wind anomaly indicated by magnitudes of 2–8 m s^{-1} converged over the Mozambique Channel north of Madagascar with a northeasterly flow that originated from the Congo. These conditions, in addition to an active south Indian Ocean tropical cyclone season, contributed to enhanced rainfall in the northeastern sector of southern Africa.

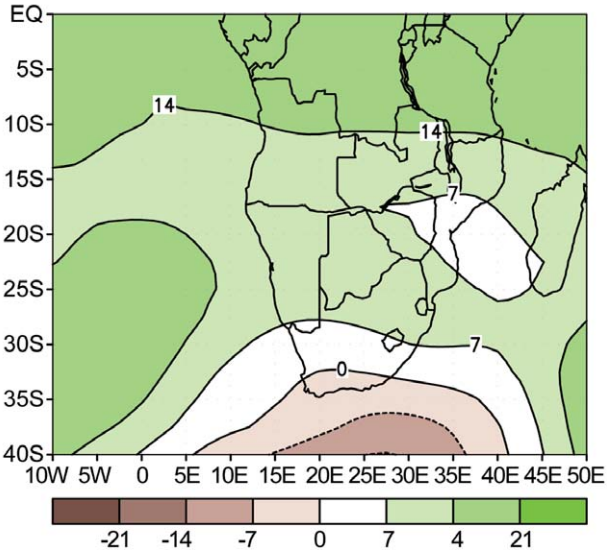

Fig. 6.6. Geopotential height anomalies (tens of meters) at 500 hPa for Dec–Feb 2006–07. Green (brown) shades indicate areas of anomalous anticyclonic (cyclonic) flow.

4) West Africa—W. M. Thiaw, L. Njau, M. Kadi, and S. Tinni

(i) Precipitation

Rainfall totals (from numerous rain gauges) during the period July–September 2007 ranged between less than 100 mm in the northern part of the Sahel to over 900 mm in the areas of maximum precipitation, including the western Guinean coast, and the southern boundary between Nigeria and Cameroon (Fig. 6.7a). The 300-mm isoline stretched from northern Senegal to eastern Chad almost continuously along 15°N. The position of this isoline is critical in determining the strength of the monsoon system.

The 2007 rainy season once again featured above-average rainfall across most areas in the Sahel and portions of the Gulf of Guinea region. Rainfall totals exceeded 100 mm above average across southern Mauritania, Senegal, western Mali, Burkina Faso, most areas in southern Niger, and central Chad (Fig. 6.7b). Anomalies of over 200 mm above the mean exacerbated flooding in many areas from Niger to Senegal. Overall, the 2007 rainy season was the second wettest since 1968, but as in 2006, the rainfall season was marked by a late onset in June. As of July, rainfall was significant enough to offset the delayed onset of the monsoon, and flooding occurred in many areas, especially in Mali. This change in the rainfall pattern was associated with an abrupt northward shift of the position of the ITCZ. As of August, positive rainfall anomalies extended well north of 20°N to encompass areas including central Mauritania and the northern areas of Mali and western Niger. These

[2] Some of the temperature data used in the southern Africa section are from the forthcoming climate data bank of the South African Weather Service.

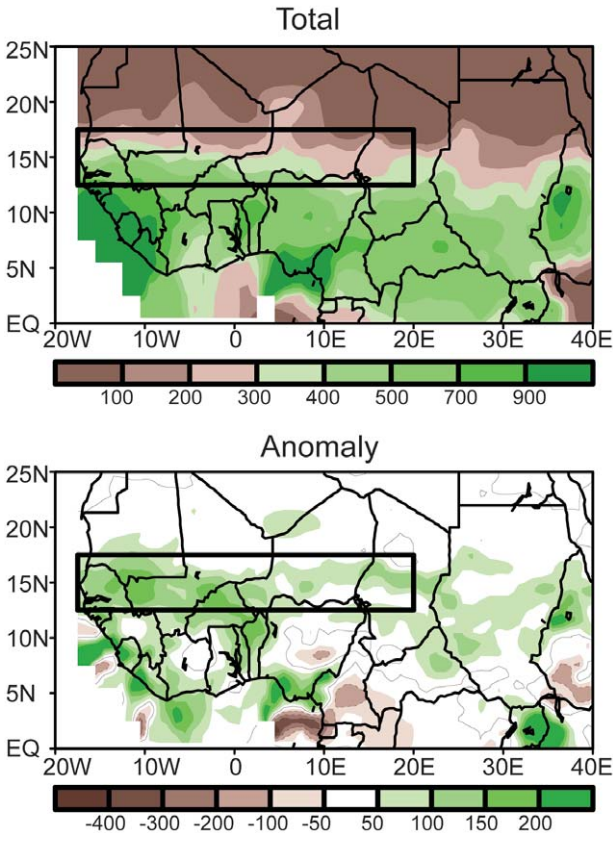

Fig. 6.7. (a) Total precipitation (mm) and (b) anomalies (mm; 1971–2000 base period) for Jul–Sep 2007. The boxed region denotes the approximate boundaries of the Sahel region.

positive rainfall anomalies persisted through September 2007. In contrast to the 2006 rainfall season, and despite sporadic dry spells in various parts of the region, including central Cote d'Ivoire, Ghana, and the southern portions of Togo and Benin, the Gulf of Guinea region also received near- to above-average rainfall for the period July–September 2007. The largest anomalies exceeded 150 mm and were observed over southern Nigeria, northern Benin, and along the western Guinean coastline.

Severe flooding events occurred across the region. In Burkina Faso, two-thirds of all houses in the village of Banh were washed away by flood waters in early August. Concurrently, flood events occurred in many parts of Nigeria, Niger, and Chad.

(ii) Atmospheric circulation

The Sahel and the Gulf of Guinea regions' rainfall is controlled by the depth and northward penetration of the West African monsoon, which in turn is related to the position of the mid- and upper-level jets, the AEJ and the TEJ, respectively. These larger-scale circulation features are fairly sensitive to changes in the global monsoon circulation on both the interannual and interdecadal time scales. The above-average 2007 rainfall resulted from an enhanced global monsoon circulation with a direct impact on West Africa. In fact, the composite map of the 200-hPa velocity potential anomaly overlaid with divergent wind (Fig. 6.8) during August–September 2007 revealed a wavenumber 1 pattern featuring divergence across Africa and Indonesia, and subsidence from the central Atlantic to the western Pacific. Consistent with this pattern, strong southwesterly winds at 925 hPa averaging 3–6 m s^{-1} extended well northward into the Sahel region. This enhanced monsoonal inflow was also evident at 850 hPa, with cross Atlantic westerly wind anomalies exceeding 3 m s^{-1} contributing to a deep penetration of moist, unstable air well into the Sahel region. The enhanced monsoon was also associated with an anomalous enhanced cyclonic shear along the equatorward flank of the AEJ.

c. *North America*

1) Canada—R. Whitewood and D. Phillips

In Canada, 2007 was a warmer- and wetter-than-normal year (relative to the 1951–80 base period). The summer was especially hot and humid on the prairies and warm and dry across southern Ontario. Also of interest was the record low of Arctic sea ice during the summer, possibly a result of many warmer-than-normal years across the north. Meanwhile, BC dealt with springtime flooding.

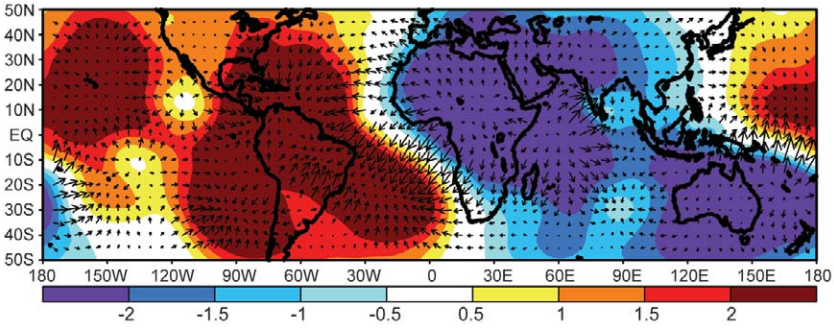

Fig. 6.8. The 200-hPa velocity potential anomaly overlaid with divergent winds at the same level for Aug–Sep 2007. Blue (red) shades indicate areas of upper-level divergence (convergence) and enhanced (suppressed) surface rainfall.

(i) Temperature

Canada, as a whole, experienced its 13th warmest year in 2007, 0.9°C above normal. The year 1998 remains as the warmest year, with 2.5°C above normal, since reliable nationwide records began in 1948. In 2007, temperatures were at least 1°C above normal north of 60°N, with the extreme northern regions experiencing temperatures more than 2°C above normal. Elsewhere in Canada, temperatures were generally 0.5°C warmer than normal. A notable exception was the Atlantic Canada region where temperatures were within half a degree of normal over the year. 2007 marked the 11th straight year of above normal temperatures, with six of the warmest 10 years occurring in the last decade.

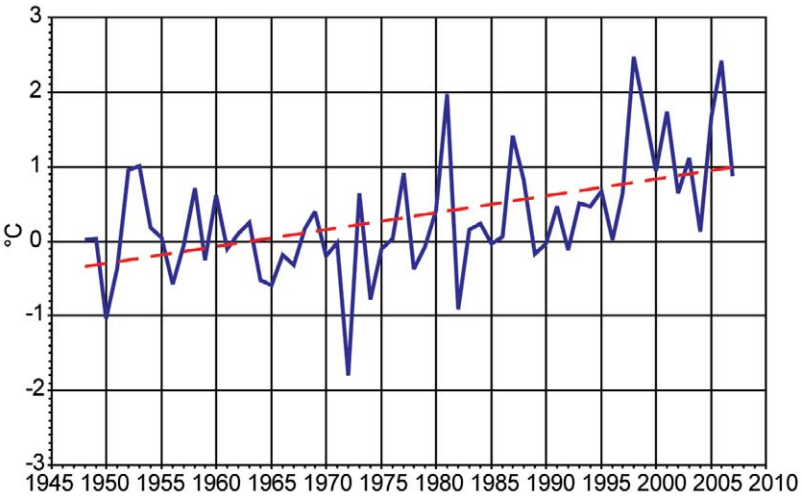

Fig. 6.9. Annual mean temperature anomalies 1948–2007 (°C; blue; 1951–80 base period) with a linear trend of +1.4°C (red) for Canada. [Source: Environment Canada.]

Regionally, annual temperatures were generally reflective of the nation's temperature, with anomalies that were 0.5°–1.0°C above normal. The easternmost part of the Arctic Islands was exceptionally warm, with 2007 ranking among the 10 warmest years (sixth warmest, 1.6°C above normal). The east coast (26th warmest, 0.1°C above normal) and the west coast (27th warmest, 0.3°C above normal) experienced temperature anomalies that were below the 0.5°–1.0°C range. The national temperature trend over the period of record (1948–2007) is +1.4°C (Fig. 6.9). The northern regions, specifically the Yukon and the Northwest Territories, have seen the largest trend of +2.1°C, whereas the Atlantic Canada region had the least temperature trend of +0.2°C.

(ii) Precipitation

As a whole, Canada experienced its 15th wettest year in 2007, 3.3% above normal. The wettest region (>20% wetter than normal) included southwestern and northern BC, southeastern Yukon, southern Northwest Territories, western Nunavut, most of Saskatchewan, southern Manitoba, and northern Quebec (Fig. 6.10). This was partially offset by areas that were at least 20% drier than normal, which included northwestern Northwest Territories, eastern BC, large parts of Alberta, and the eastern Arctic Islands.

Two of Canada's climate regions experienced wetter-than-normal conditions, causing 2007 to rank among the 10 wettest years in the 60-yr record. Most of Nunavut had its eighth wettest year (16.7% above normal), and the northern half of the prairie provinces, had its ninth wettest year (7.8% above normal). The regions with the driest conditions were southern Ontario and Quebec, which had its 13th driest year

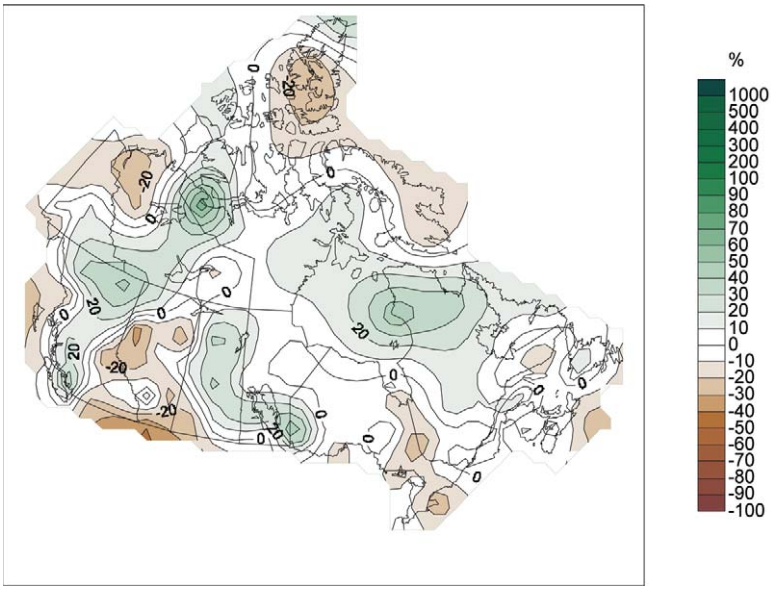

Fig. 6.10. Canadian 2007 annual total precipitation anomalies (percent of the 1951–80 normal). [Source: Environment Canada.]

(6.6% below normal). Southern BC experienced its 14th driest year, 9% below normal.

(iii) Notable events

Winter 2007 over the west coast of British Columbia was exceptionally good for the ski industry; however, record snowpacks created ongoing concern for flood managers and residents near rivers. A cooler-than-normal April contributed to the slow melting of the large mountain snowpack. In May, a 5-day warm spell started a rapid snow melt. River basins in west-central British Columbia were drenched with some of the worst flooding ever, swamping several communities including Terrace, Price Rupert, and Smithers.

July was hot across the prairies, with many locations experiencing near-record heat. Calgary experienced its warmest July since 1936, and Regina had its warmest July since 1937. Prolonged record high humidity exacerbated the situation across the normally semiarid prairies. Remarkably, on 30 July, Carman, Manitoba, recorded a humidex rating of 53. Humidex is a metric of felt air temperature based on temperature and dewpoint, analogous to the "heat index." The reading of 53 is a record for Canada, surpassing the previous record of 52.1 set in Windsor, Ontario, back in 1953.

During the summer, southern Ontario experienced 30–40 "hot days" (days where the temperature exceeded 30°C), 2 to 3 times the normal number . Accompanying the heat were very dry conditions. From July to September, Toronto received only 45% of its normal amount of rain. The drought in southern Ontario extended from the beginning of the year through October. Toronto experienced its second driest January–October period on record. The hot and dry conditions helped reduce river flows and Great Lake levels to near-record lows throughout the region.

Canada witnessed its first F5 tornado (EF5 using the Enhanced Fujita Scale) on record, according to the Fujita intensity scale. The tornado was spotted near Elie, Manitoba (about 40 km west of Winnipeg), on 22 June. Winds near Elie were likely in excess of 116 m s^{-1}.

2) UNITED STATES—R. R. Heim Jr., K. L. Gleason, M. C. Kruk, D. H. Levinson, A. M. Sánchez-Lugo, R. Fritsch, R. Thoman, J. Papineau, and S. Lindsey

(i) Overview

Reliable monthly, seasonal, and annual weather records for the United States exist from 1895 to the present, enabling the climate of 2007 to be placed in a 113-yr context for the contiguous United States. Based on preliminary data available at the end of the year, 2007 tied with 2005 as the ninth warmest year on record with a nationally averaged temperature of 12.4°C (54.3°F). Considerable variability in temperatures and precipitation occurred throughout the year for the nation as a whole and regionally, with record warmth occurring in March and record cold following in April. Unseasonably warm temperatures dominated in the western United States and cold in the east under a strong upper-level ridge/trough pattern during July. A heat wave in August broke numerous record high temperatures, stressing residential energy systems.

The year was characterized by dry conditions in the West and a historic drought in the Southeast, with unusually wet conditions in the plains, especially during the first nine months of the year. Texas and Oklahoma had the wettest June–August on record, while Georgia and Mississippi experienced the driest March–May and Tennessee had the driest January–August. Drought persisted for much of the year in the western Great Lakes. Nationally, seven months were drier than average, with 2007 ranking as the 47th driest year on record. Moderate-to-extreme drought, as defined by the U.S. Drought Monitor (Svoboda et al. 2002), expanded from a fourth of the contiguous United States at the beginning of the year to nearly half by the end of summer before decreasing to a third of the country by year's end. Above-normal temperatures and below-normal precipitation during the spring contributed to a below-normal snowpack in the West. The persistently dry conditions, coupled with excessive summer heat, contributed to a near-record wildfire year.

(ii) Temperature

For the contiguous United States, 2007 ranked as the ninth warmest year on record and marked the 10th consecutive year with temperatures much warmer than the long-term average (Fig. 6.11). The past 10 yr have all been among the 25 warmest years on record, a feat which is unparalleled in the historical record. The annual average temperature in 2007 was 0.8°C (1.5°F) warmer than the twentieth century mean, yet was 0.4°C (0.7°F) cooler than 2006 (third warmest). The long-term warming trend for annual temperatures is approximately 0.56°C (1.0°F) per century. Temperature ranks for the contiguous United States were second warmest on record in March and third warmest in August. Large regions of below-average temperatures were present during January, February, April, and July.

Collectively, the 2006–07 winter (December–February) temperatures were near average across most of the nation. December 2006 was marked by above-average to record warm temperatures across a large portion of the Northeast. January was cold across most of the western and southern states and above average in the eastern United States. A persistent trough positioned over the eastern United States in February was responsible for cold temperatures from the Great Plains to the Atlantic coast. The central region ranked ninth coldest on record and was near the center of the coldest anomalies with departures from average less than –3.9°C (–7°F) for the month. The Northeast region was more than 3.1°C (5.5°F) below average and ranked 14th coldest.

After a relatively cool beginning to the year, March rebounded and ranked second warmest for the contiguous United States. Temperatures were much above average across 22 states from the West Coast to the Ohio Valley. Oklahoma had its warmest March on record during 2007. In fact, March statewide-averaged temperatures in Oklahoma had not been within 1.1°C (2°F) of the 2007 average since the late-1930s. The prolonged warm spell during March led to a premature leaf and bloom for many plants and trees across the central, southern, and southeastern United States. In early April, temperatures plummeted as Arctic air brought record-breaking cold temperatures and a cold freeze event to much of the central plains, the South, and parts of the East. Over 1,200 daily minimum temperature records were broken across the contiguous United States during this event. Nonetheless, the spring season (March–May) temperatures ranked eighth warmest nationally, reflecting the dominance of the March warmth during the season.

The summer (June–August) months were characterized by a near-record to record warm July across portions of the West, and below to much below-average temperatures across much of the remainder of the contiguous United States. In addition, widespread warmth blanketing a majority of the contiguous United States resulted in a rank of third warmest August on record for the nation. A severe and persistent heat wave moved across the country from the Intermountain West to the Southeast and Ohio Valley during August 2007. More than 50 deaths were attributed to the excessive heat. Over 70 all-time record highs were set in August, along with scores of new daily high temperatures. Average temperatures during the warmest periods from the 7th–11th, and again from the 15th–17th, were more than 5.6°C (10°F) warmer than average in many parts of the country. Seven states (Utah, Kentucky, Tennessee, Alabama, Georgia, South Carolina, and Florida) had a record warm August and an additional 17 states had temperatures that ranked much above average for the month (Fig. 6.12a). For the season, the summer of 2007 was sixth warmest across the nation despite the colder-than-average anomalies present over Texas and Oklahoma, which resulted from persistent cloud cover and rainfall during much of June and July. Both July and August were exceedingly warm across Utah and ranked second warmest and warmest, respectively, giving the state a record warmest ranking for the summer season.

Autumn (September–November) was marked by persistent near- to above-average temperatures. October ranked fifth warmest for the contiguous United States, with much above-average temperatures observed across most of the eastern third of the nation. Record warmth during October occurred in New Jersey, Maryland, and Delaware. For the season as a whole, national temperatures ranked sixth warmest.

For the year, the only state where temperatures ranked below average was Maine. Thirteen states had temperatures that ranked much above average, and the remaining states were near or above average (Fig. 6.12b).

The annual temperature for Alaska in 2007 ranked as the 15th warmest in the 1918–2007 record, representing a return to warm anomalies after near-normal conditions in 2006. Only 10 of the last 31 yr had annual temperatures near to or below the long-term mean for the state. Winter temperatures in 2007 were above average for the eighth consecutive year, although a severe Arctic outbreak affected southeast Alaska in late February to early March. For the greater Fairbanks area, 15 February–15 March was the coldest ever on record during that time of year.

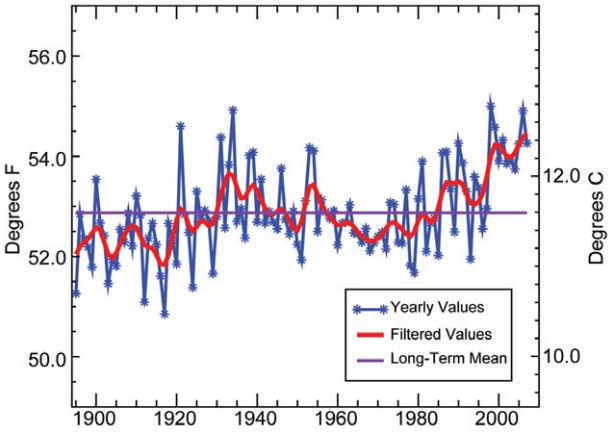

Fig. 6.11. Annual temperature for the contiguous United States over the period 1895–2007. [Source: NOAA/NCDC.]

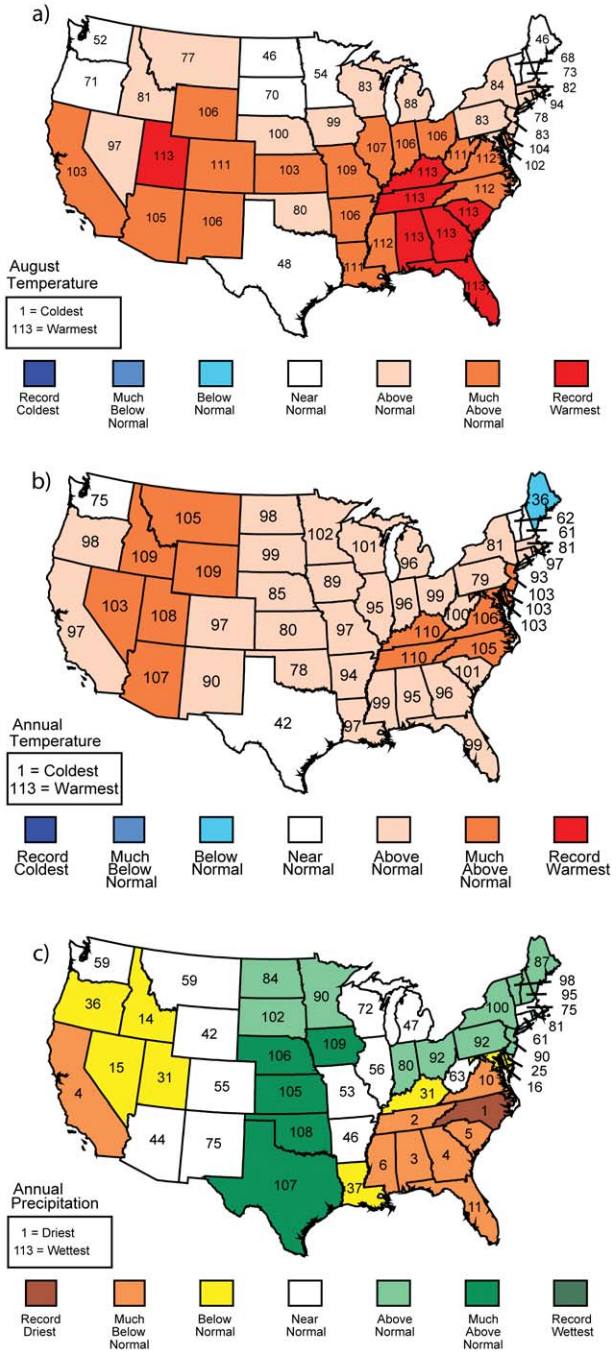

Fig. 6.12. Statewide ranks of (a) Aug 2007 temperatures, (b) annual 2007 temperatures, and (c) annual 2007 Precipitation. A rank of 113 represents the warmest/wettest year since 1895. Much above-normal temperature/precipitation is defined as occurring in the top 10% of recorded years, which corresponds to a rank of 103–112. Above-normal temperature/precipitation is defined as occurring in the warmest/wettest third of recorded years (ranks 76–102). Much below-normal temperature/precipitation is likewise the bottom 10% of coolest/driest years since 1895, and below normal is defined as the remaining coolest/driest third of the distribution. [Source: NOAA/NCDC.]

The average high was –19.9°C and the average low was –33.5°C. Spring was slightly below average, summer was warmer than average, and fall was significantly warmer than the 1918–2000 average.

(iii) Precipitation and drought

Precipitation in the United States during 2007, although variable, was characterized by periods of excessive rainfall across the central third of the United States, and persistent and developing drought in the southeastern quarter of the country and the far western states. This pattern dominated during the winter and spring months, with the Southeast and West regions having the driest and sixth driest spring, respectively, while the west-north central region of the northern plains ranked third wettest. A series of severe storms caused flooding, extensive damage, and loss of life from Texas to Kansas and Missouri in June and July. This was followed by the remnants of Tropical Storm Erin, which produced heavy rainfall in the same area in August, giving the South region (composed of Mississippi, Louisiana, Texas, Arkansas, Oklahoma, and Kansas; see Karl and Koss 1984) its wettest summer on record. Precipitation during fall was below normal for much of the nation, although widespread extreme anomalies were absent.

Severe to exceptional drought affected the Southeast and western United States throughout much of the year. After a slight contraction during 2005–06, the drought area in the West expanded this year, covering half or more of the region beginning in late spring. The persistent dryness in the Southeast started in December 2006 and resulted in an expanding drought area with time, with more than two-thirds of the region in drought from midsummer 2007 through the end of the year. Unusually warm temperatures and scarce rainfall exacerbated conditions. Drought also affected large parts of the upper Midwest for much of the year. Several short-lived dry episodes occurred in other regions throughout the year, notably in the Ohio Valley and Northeast in May and the northern plains in July.

The cumulative effects of the drought resulted in the driest year in the 113-yr record for North Carolina, second driest for Tennessee, third driest for Alabama, and fourth driest for Georgia and California (Fig. 6.12c). Note the sharp gradient between the severe drought in the Southeast, above normal to much above normal precipitation in the country's midsection and Northeast, and the intervening regions from Louisiana north to Missouri and east to the Potomac, where conditions were near normal. Conditions in the southern plains went from extremely wet to extremely

dry during September, with Texas having the wettest January–September on record, followed by the 11th driest October–December. Water conservation measures and drought disasters, or states of emergency, were declared by governors in five southeastern states, along with California, Oregon, Maryland, Connecticut, and Delaware at some point during the year. Unusually dry conditions during May–October of this year and for the last several years resulted in a record low level for Lake Superior, impacting shipping and recreational activities. Also noteworthy is that, in contrast to the severe drought in the Southeast, heavy precipitation was noted from the Ohio Valley and Great Lakes into the Northeast for the year.

(iv) Snowpack

The 2006–07 snow season was variable in many areas across the United States. Parts of the Northern Cascades, Big Horn Mountains in Wyoming, and the Colorado Front Range had generally near- to above-average snowfall, while the Sierra Nevada, Wasatch, and the mountains of Arizona experienced below-average snow accumulations. The snow cover extent was slightly above average for the North American continent as a whole over the winter season, but well below average during the spring, consistent with a trend over the last 40 yr toward reduced spring snow cover for North America (Fig. 6.13). The below-average snowpack during the spring can be associated with the anomalous warmth that engulfed most of the contiguous United States during March (when monthly mean temperatures were more than 3°C above average in many places) and May.

Notable snow storms that affected the contiguous United States in 2007 include the deadly ice storm that occurred 11–16 January, affecting areas from the Rio Grande Valley to New England and southeastern Canada. Two subsequent storms affected the southern United States and later the southern plains and mid-Atlantic states. During mid-February, a major snow storm deposited 10–50 cm of snow across much of the central United States, while parts of eastern New York and northern Vermont received up to 76 cm. The Northeast Snowfall Impact Scale (Kocin and Uccellini 2004; Squires and Lawrimore 2006) classified this as a category 3 (major) storm and ranked it as the 14th most intense on record for the Northeast. This event was preceded by a 10-day lake effect storm that produced over 254 cm of snow on New York's Tug Hill Plateau, with a total of 358 cm reported at Redfield in Oswego County. In southeast Alaska, all stations saw well above-normal snowfall in March, with many locations breaking March snowfall records.

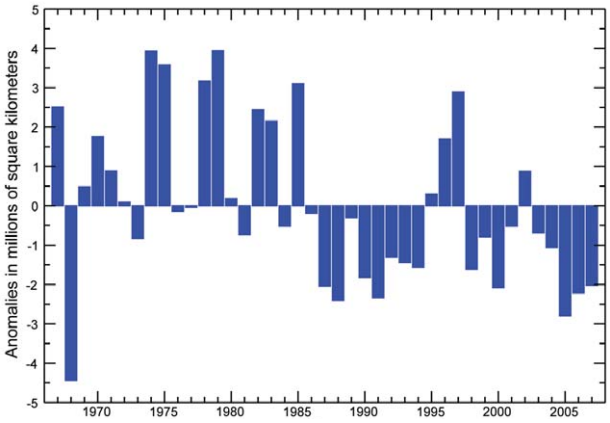

Fig. 6.13. North America snow cover extent anomalies for spring (Mar–May), 1967–2007, as derived from visible satellite observations.

Near the end of spring, few areas in the contiguous United States had above-average snowpack, while snowpack water content less than 50% of average was widespread from Oregon to the Southwest.

The beginning of the 2007–08 snow season was above average across parts of the Southwest, with well below-normal amounts in the Sierra Nevada, Cascades, the Bear River, and Salt River Ranges. A severe winter storm in the second week of December covered Missouri and Oklahoma in a thick layer of ice. Several back-to-back midlatitude cyclones brought significant snowfall from the Great Plains through New England in mid- and late December.

(v) Wildfires

The 2007 fire season continued a string of record or near-record wildfire seasons across the United States. Long-term precipitation deficits played a critical role in the severity of the 2007 wildfire season, especially in the Southeast and West, where drought conditions persisted or worsened during the year.

According to preliminary data from the NIFC, the 2007 fire season had the second most acres burned in the historical record, with more than 9.3 million acres (~3.8 million hectares) for the United States as a whole, about 500,000 acres (~200,000 hectares) less than was reported in 2006 (the record year). Based on annual statistics that extend back to 1960 (source: NIFC in Boise, Idaho, www.nifc.com/fire_info/fire_stats.htm), the number of fires reported each year has shown a steady decline since the early 1980s for the entire United States, and since the early 1990s for Alaska. However, the total number of acres burned each year has increased steadily since about 1995 (Fig. 6.14). As a result, there has been an increasing

trend in the size of wildfires (Westerling et al. 2006), with 6 of the 10 worst seasons in terms of acres burned having occurred since 2000.

Wildfire activity started earlier than usual in 2007, as wildfires affected portions of the Tennessee Valley and the Southeast in March, eventually spreading to northern Minnesota in April and southern Florida in May. In the West, the fire season started slowly in June, except in central California, where numerous blazes affected the Lake Tahoe area. Fire activity increased dramatically in July, as large portions of the Intermountain West were affected by wildfires. The most severe fire activity during the summer occurred in the northern Rockies, where numerous large fires burned in July and August. Fire activity persisted into September across Idaho and Montana, but eventually shifted southward into

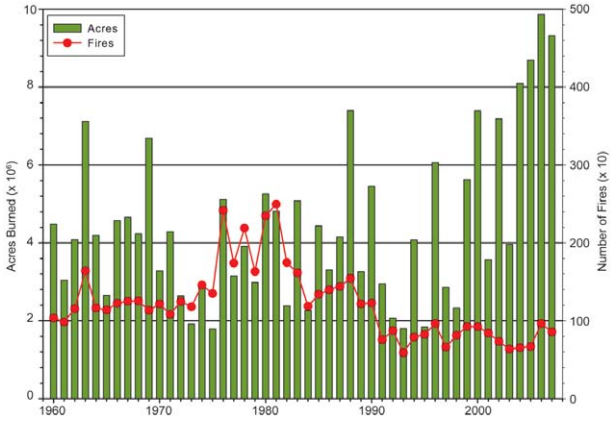

FIG. 6.14. The annual number of wildland fires (curve, right axis) and acres burned (bars, left axis) for the contiguous United States for 1960–2007.

DIAGNOSIS OF CAUSE(S) FOR 2007 U.S. PRECIPITATION EXTREMES—
M. P. HOERLING IN CONJUNCTION WITH THE NOAA CSI TEAM

For the contiguous United States, large precipitation deficits occurred in the Southwest and Southeast regions during all seasons in 2007, with annual departures exceeding –30% of the 1971–2000 climatologies (Fig. 6.15, top). The concurrent oceanic conditions consisted of a lingering El Niño during winter/early spring 2007 followed by a La Niña event in late summer and fall of 2007. Three different atmospheric climate models were used to assess whether such dryness was related to global SST conditions. The models (NCEP GFS, NCAR CCM3, and GFDL AM2.1, with nominal resolution of ~200 km) were forced with the monthly varying global 2007 SSTs. For these so-called GOGA runs, 50 separate realizations were conducted for each model. The multimodel ensemble mean precipitation anomaly (percent of climatology), computed relative to control simulations that had used climatological global SSTs of 1971–2000, consists of a dry signal over much of the southern United States (Fig. 6.15, middle).

In a further suite of runs, SSTs were specified over the region 20°N–20°S, 160°E to the South American coast only (i.e. the ENSO domain), while climatological SSTs were specified elsewhere over the world's oceans. For these so-called EPOGA runs, 50 separate realizations were again conducted for each model. A strong wet signal occurs over the Southwest (Fig. 6.15, bottom left), opposite of the observed drought conditions. The simulated wet signal is especially strong during winter/spring 2007 when El Niño conditions prevailed, and is also consistent with historical observations that reveal ENSO impacts to be largest during that time of year (Kiladis and Diaz 1989). It is evident, however, that the expected wet signal failed to emerge during 2007; both the empirically derived wet signal expected from historical ENSO impacts, and the simulated signal from these EPOGA simulations are opposite to the observed drought conditions. It thus appears that ENSO was not a critical factor with respect to the droughts of 2007.

The principal anomalies in global SSTs during 2007, outside the ENSO region, were characterized by warmth in the tropical Indian and Atlantic Oceans, and warmth across much of the extratropical North Pacific and North Atlantic Oceans (see section 3). The effect of the "non-ENSO region" SST forcing was estimated by constructing the differences "GOGA-EPOGA" (subsequently referred to as global/non-ENSO). To the extent that the U.S. response can be viewed as the simple linear superposition of various ocean-forced signals, this analysis is one estimate for the SST-forced signal from the ocean conditions outside of the tropical eastern Pacific. The global/non-ENSO results (Fig. 6.15, bottom right) reveal a strong U.S. precipitation sensitivity to this non-ENSO region forcing. In particular, a dry signal occurs along the entire southern tier of states, having a maximum percentage reduction in precipitation over the Southwest akin to the observed anomalies. Over the United States as a whole, this dry signal overwhelms the east Pacific induced wet signal. Thus, the modest U.S. drying emerging in response to the full global SST conditions of 2007 (Fig. 6.15, middle) reflects the cancellation between two mutually exclusive SST influences—a wet ENSO effect and a stronger drying effect due to non-ENSO SST conditions.

The preliminary diagnosis presented above provides some attribution of key features of the observed 2007 U.S. climate conditions. The text uses subjective language to interpret the likelihood that certain conditions were caused by certain forcings, but at this point that should be viewed as a *qualitative*, expert assessment. Regarding the anomalously low precipitation within

California later in the month. The most destructive fires of the year occurred in Southern California during the fall, as severe-to-exceptional drought and strong Santa Ana winds exacerbated brush and forest fires, destroying homes across the region in October and November.

The 2007 fire season was not an especially severe one in Alaska, which had just over half a million acres (~202,000 hectares) burned during the year. However, in September the Anaktuvuk River wildfire, which was caused by lightning, burned over 250,000 acres (~100,000 hectares) and set a record for the largest fire on Alaska's North Slope.

(vi) Severe extratropical storms

Several severe extratropical cyclones affected the United States in 2007. The first major system moved across parts of the Midwest and the Northeast on 13–15 February. The intense storm produced significant accumulations of ice and snow in these areas, with some locales in Illinois receiving more than 30 cm of snow. In upstate New York more than 100 cm of snow was reported. During 15–17 April, a nor'easter moved up the eastern seaboard, bringing strong winds, high seas, and heavy rains from South Carolina to Maine. Some locations across the Northeast received over 190 mm of rain in a single day, producing widespread flooding, while on the cold side of the storm, more than 40 cm of snow fell across Vermont and New Hampshire.

During the normal spring peak in severe weather, several tornado outbreaks occurred across the plains, producing over 400 tornadoes during April and May combined. The worst of these outbreaks occurred

the two drought regions, this diagnosis suggests the following main conclusion:

The droughts were inconsistent with east tropical Pacific SST variability during 2007, and thus were unlikely caused by the ENSO cycle occurring during January–December 2007. We estimate less than a 5% probability that the observed droughts were consistent with climate conditions driven from the tropical east Pacific in 2007.

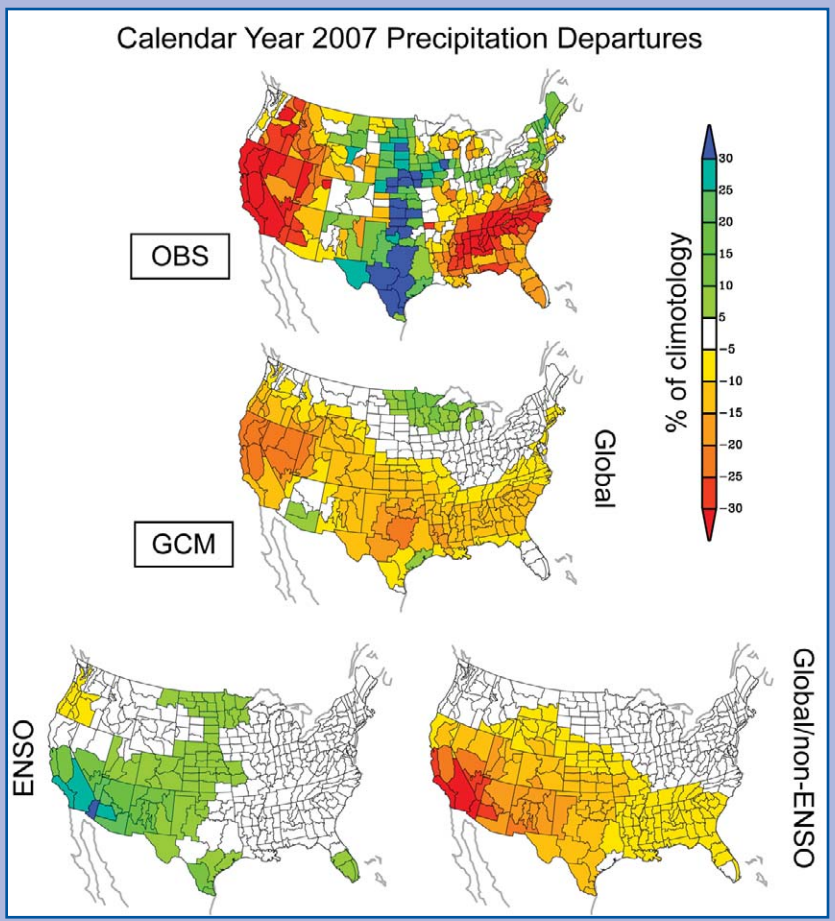

Fig. 6.15. The U.S. 2007 annually averaged (Jan–Dec) precipitation departures expressed as a percentage of the 1971–2000 climatologies for (top) observations (OBS), for (middle) simulations based on global SST forcing (contour interval half as for OBS), (bottom left) for simulations based on tropical east Pacific SST forcing (same contour interval as for OBS), and (bottom right) for simulations based on global SST forcing excluding the tropical east Pacific (global/non-ENSO; same contour interval as for OBS). [Source: NOAA CSI Team.]

on 4–5 May, when an EF5[3] tornado devastated the town of Greensburg, Kansas, killing 10 people and destroying nearly 95% of the town. This was the first category 5 tornado since the Oklahoma City, Oklahoma, tornado in May 1999. According to preliminary statistics compiled by NOAA's Storm Prediction Center, there were 1,074 tornadoes reported in 2007, with May having the most of any month (251). The most severe day was 3 April, when 594 reports of severe weather (tornadoes, wind, and hail combined) were documented.

Although the summer and much of the fall were relatively quiet for much of the United States, there were two major extratropical storms of note to end the year. The first was a strong Kona Low which brought heavy rains greater than 25 cm and flooding to Maui and the Big Island of Hawaii during the first week of December. The second was a storm system that battered the coasts of Washington and Oregon from 1 to 3 December. Several locations along the northern Oregon coast received more than 250 mm of rain for the period, along with peak wind gusts exceeding 45 m s^{-1}.

3) Mexico—V. Davydova-Belitskaya and F. Romero-Cruz

Mexico was on average 5.3% wetter than normal in 2007, with much warmer-than-normal temperatures. Mexico's SMN reported a national precipitation average of 812.2 mm, compared with a historical average of 771 mm (1941–2000). The nationwide annual mean temperature was 21.8°C, 1.1°C above the long-term climate average. Tabasco suffered heavy rain and flooding in January, experienced severe drought conditions and wildfires through the summer, and ended the year with some of the most powerful storms and flooding ever to hit the state.

(i) Precipitation

The rainfall distribution was inhomogeneous spatially and temporally. The year 2007 began wetter than normal, but the March–July period was considerably below average. A partial recovery of precipitation totals, particularly in southern and southeastern Mexico, began in August. The total annual precipitation reported by the Mexican SMN was 53% above normal. However, many states reported rainfall deficits. These include Baja California (48% below the long-term mean), Oaxaca (23.7% below), Zacatecas (19.4% below), Sinaloa (17% below), Durango (14.1% below), Quintana Roo (13.3% below), Morelos (12.5% below), Yucatan (8.9% below), Baja California Sur (6.4% below), and Tlaxcala (4.5% below). Considering the May–October rainy season, precipitation deficits abounded across the country (Fig. 6.16a). Only the northeast region of the country reported above-normal precipitation.

(ii) Temperature

Mexico experienced its second warmest year, 1.1°C above normal (Fig. 6.16b), with 2006 being the warmest (1.2°C above normal), since reliable records began nearly three decades ago. Most of Mexico had temperatures at least 1°C above normal. The warmest states were San Luis Potosí (3.2°C above the long-term mean), Oaxaca (3.1°C above), Distrito Federal (2.1°C above), Nayarit (1.9°C above), Chihuahua (1.7°C above), and Morelos (1.5°C above). Only three states had near or below normal temperatures. These were Durango (0°C), Estado de México (–0.7°C below) and Michoacan (–1.9°C below).

(iii) Extreme events

Despite the very warm annual mean temperature, a notable cold outbreak occurred across northern Mexico on 4 January when La Rosilla, Durango, recorded a minimum temperature of –16.5°C; Guachochi, Chihuahua, recorded –10.3°C; and Yecora recorded –10°C. An exceptionally early winter cold outbreak occurred in the northwest on 30 October with temperatures in La Rosilla plummeting to –12.5°C and Santa Barbara, Durango, to –12°C.

Events of extreme precipitation were recorded due to the landfalling Hurricanes Dean (13–23 August) and Lorenzo (25–28 September), which formed in the Atlantic Ocean, and Henriette (30 August–6 September), which formed in the Pacific Ocean. Precipitation reached record levels in the states of Veracruz, Tamaulipas, Puebla, San Luis Potosí, Tlaxcala, Baja California Sur, and some regions of Sonora. Heavy precipitation caused severe flooding in the Rio Panuco basin, where areas remained inundated from 23 August (the passing of Dean) through the first week of October, when the passing of Lorenzo reinforced the flooding. By the end of October, the passing of the fourth cold front over Mexico and its interaction with Tropical Storm Noel (28 October–2 November) caused heavy precipitation in Chiapas and Tabasco. This resulted in record accumulated values (700–1000 mm in the period from 28 to 31 October) and Tabasco's worst flooding in history, with 80% of

[3] The National Weather Service switched to the Enhanced Fujita Scale from the Fujita Scale on 1 February 2007. (for more information on the EF Scale, please see www.spc.noaa.gov/efscale/).

the territory inundated until the end of the year.

(iv) Wildfires

During 2007, more than 80,000 wildfires were reported in Mexico. Most of them were recorded during March–June. May accounted for almost 45% of the total fires. Wildfires mainly affected the west, northwest, along the Gulf of Mexico, the southeast, and the Yucatan Peninsula. Due to severe drought conditions in the area of Campeche and Tabasco, these fires continued unabated until the passing of Hurricane Dean in late August. In the northwestern and western parts of Mexico, the development of the North American monsoon helped extinguish these fires during the 2007 rainy season.

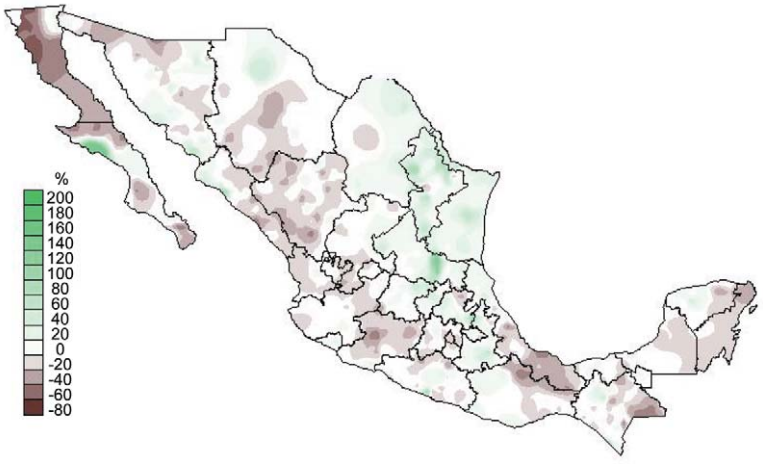

Fig. 6.16a. Mexican seasonal rainfall anomalies (May–Oct) in 2007.

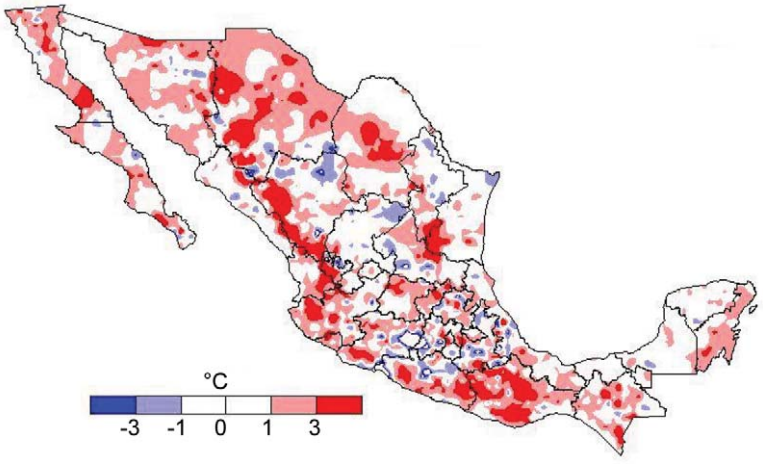

Fig. 6.16b. Mexican annual mean temperature anomalies in 2007 (°C; 1981–2005 base).

d. Central America and the Caribbean

1) Central America—P. Ramírez

(i) Temperature

Annual mean surface temperatures in 2007 were slightly above normal across Central America, with anomalies between 0.1° and 0.4°C. Monthly temperatures slightly above normal predominated during winter. April temperatures were near normal, although positive anomalies were found in the southern part of the isthmus, and summer months were also above average. The highest temperature anomalies were observed in the northern part (Guatemala and Honduras) in July and September. Fall was also warmer than normal, except for October when near-normal temperatures were observed across the region.

(ii) Precipitation

In Central America, 2007 was influenced by two primary features: the La Niña event that developed in the central Pacific in the middle of the year and the persistence of above-normal SSTs in the Caribbean. This situation created an SST dipole that enhanced the flow of humid air from the Pacific to the Caribbean, which generally increased humidity, particularly over southern Central America.

Monthly distributions of accumulated rain, however, varied over the region. Dry anomalies affected the Caribbean basin from Honduras to Panamá in January and February. From March to May an above-normal rainfall pattern prevailed over the southern part of the region with the highest anomalies over Costa Rica and Panamá. A late season cold front that reached the northern part of the region brought above-normal springtime rains to the Caribbean plains of Honduras and to northern and central Guatemala. A precipitation deficit occurred in June over the Pacific basin, especially over the "Dry Corridor" (El Salvador, western and southern Honduras, western Nicaragua, and northwestern Costa Rica). The region had above-normal rainfall during October. In November, as the transition to the dry season was evolving in the Pacific basin, above-normal rainfall was observed on the Caribbean side from Honduras to Panamá as the first cold fronts of the winter moved into the Caribbean. In the southern part of the isthmus, the rainy season ended later than normal.

(iii) Notable events

Hurricane Dean brought heavy rains to Nicaragua and El Salvador in August. However, the total accumulation of rainfall was limited due to the rapid propagation of the system. In early September, Hurricane Felix struck Nicaragua, causing more than 100 deaths and damages to infrastructure exceeding $30 million (U.S. dollars). Also in September, a low pressure system near the Yucatan Peninsula induced another low off the Pacific coast of the isthmus; the combination of both systems generated a period of continued and heavy rains known as "temporal." During the second half of October a persistent disturbance over southern Central America and northern South America produced several days of very heavy rainfall and storms. Impacts from this event were also felt in Costa Rica, where floods and landslides affected many parts of the country, causing extensive damage to houses and roads.

2) Belize—R. Frutos and A. Gordon

Frontal activity during the winter 2006–07 was above normal.[4] A total of 14 cold fronts reached Belize, with the first one crossing the country around mid-October, and the last one making its entry in early May 2007. Two strong cold air incursions were experienced during the winter period 2006–07. The first was in mid-December 2006, which lasted about five days, while the second cold episode occurred in late January 2007 and lasted about four days.

The dry season in 2007 began in February, with signs of an early onset during the first week of the month. The dry period intensified in late March through mid-May, generating widespread bush fires that burned hundreds of acres in the coastal savannah and inland areas. About three major forest fires burned in the Mountain Pine Ridge Forest Reserve.

The weather was warmer than normal across Belize in 2007. Figure 6.17 depicts 2007 monthly maximum and minimum temperatures compared to the 1961–90 averages. The annual maximum (minimum) temperature for 2007 was 30.8°C (23.7°C), 0.8°C (1.2°C) higher than normal and tied for the second highest on record with 1997 (2002). For the year, all months were warmer than normal except November (and March for minimum temperature).

The 2007 rainy season began during the period of 15–23 May, about a week earlier than usual. A combination of a late-season frontal incursion and a trough in the easterlies moving through the western Caribbean generated rainfall across Belize during 17–23 May 2007. After the initial onset of the rains, showers continued intermittently during the rest of May through June. Nonetheless, rainfall at most places during June was well below normal (Fig. 6.18), as well as in July, September, October, and December. However, intense rainfall occurred along the central coast of Belize during the period of 28–30 August, when 299.7 mm of rain fell, which made August 2007 the wettest in the historical record. The rainfall total for August 2007 was 550.7 mm, approximately 200% above normal. In addition, January was 74% above normal. The main airport in Belize City recorded a total of 83 days with rain during the 2007 rainy season, compared to a normal of 103 days.

[4] The data used in the Belize section are the property of the National Meteorological Service of Belize from its national meteorological and hydrological surface network.

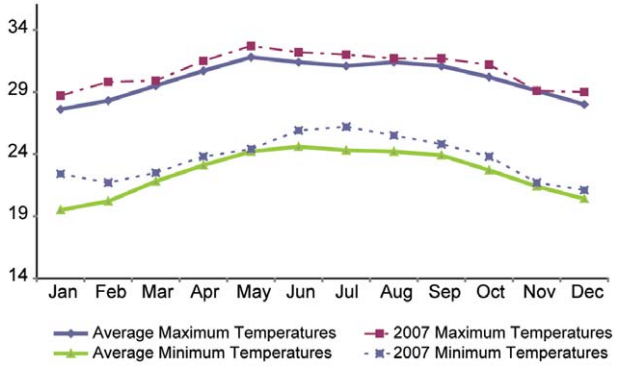

Fig. 6.17. Average maximum and minimum temperatures (°C) in 2007 and the 1961–90 base period normals for Belize.

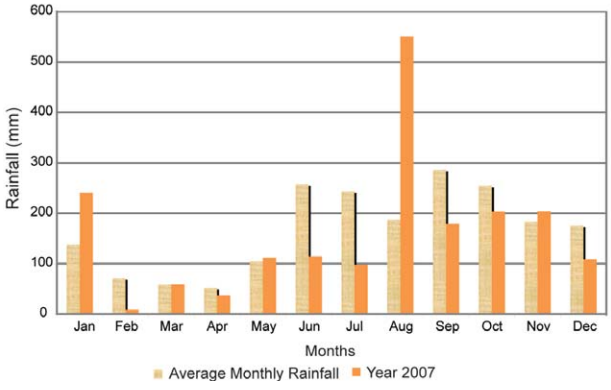

Fig. 6.18. Average rainfall (mm) in 2007 vs the 1961–90 normals for Belize.

3) Cuba—C. Fonseca Rivera, B. Lapinel Pedroso, V. Cutié Cansino, D. Boudet-Roco, A. M. Carrión Romero, and R. Pérez Suárez (translated by A. Arguez)

Consistent with observed trends, Cuban temperatures in 2007 were warm, ranking as the eighth warmest year since 1951. The annual mean temperature was 26.0°C, about 0.5°C above normal. January and February were much warmer than normal over the island. January, climatologically the coldest month, was 1.6°C above normal while February was the 10th warmest since 1951 with an anomaly of 1.1°C. The period from March to November was near normal as a whole, although most months exhibited positive anomalies, including anomalies of about 0.5°C in August and October. In December, typically the second coldest month in Cuba, the temperature anomaly was 1.1°C.

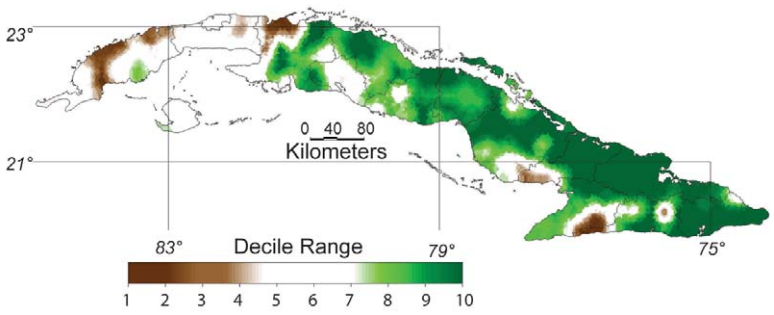

Fig. 6.19. Annual rainfall expressed as a decile ranking, based on the 1971–90 reference period (preliminary analysis).

Precipitation totals for the year were either above normal or near normal for the vast majority of the island (Fig. 6.19). Most of the eastern two-thirds of the country received rainfall amounts exceeding the 80th percentile. A few regions experienced below-normal precipitation: northern and central Pinal del Río, northern Matanzas, the southern coast of Las Tunas, as well as the border between Granma and Santiago de Cuba. Cuba was impacted by Tropical Storm Noel in October, bringing torrential rains and flooding to eastern Cuba.

4) Jamaica—J. M. Spence and M. A. Taylor

Jamaican rainfall in 2007 reflected the influence of warm anomalies in the tropical North Atlantic through June and cold anomalies in the equatorial Pacific through December. Respectively, the temperature anomalies contributed to wetter-than-normal conditions in both May (the early rainfall peak; Fig. 6.20) and between August and November (the primary rainfall period). For both periods, most parishes equaled or exceeded the 30-yr mean, with some (Trelawny in the north; St. Catherine and Clarendon in the south) in excess of twice the normal rainfall during October–November. Intense and persistent island-wide rainfall during the latter half of March contributed to the wettest March on record, which is climatologically the driest month. Frontal systems stayed well north of Jamaica during December, resulting in most parishes falling below their 30-yr mean. The impact was most severe for southern regions, which constitute the main agricultural belt. The December rainfall deficits were consistent with the north (dry)–south (wet) gradient in Caribbean rainfall associated with La Niña conditions.

Prevailing warm Caribbean ocean temperatures resulted in positive air temperature anomalies of up to 1°C for most stations for the first five months of the year. Thereafter, the traditionally warmer months saw negative anomalies, especially over southern parishes, likely because of the long periods of persistent cloudiness and rain. By the end of the year, positive temperature anomalies were again reported by some stations while others tended to be near normal. The aforementioned lack of frontal systems in the vicinity of the islands precluded the reduction in temperature that normally accompanies them.

The island was affected by the passage of category 4 Hurricane Dean on 19 August 2007. Its passage just south of the island resulted in extensive wind and flood damage over the southern parishes. Hurricane Felix in September generated swells on the south coast, and in December tropical storm Olga impacted Ja-

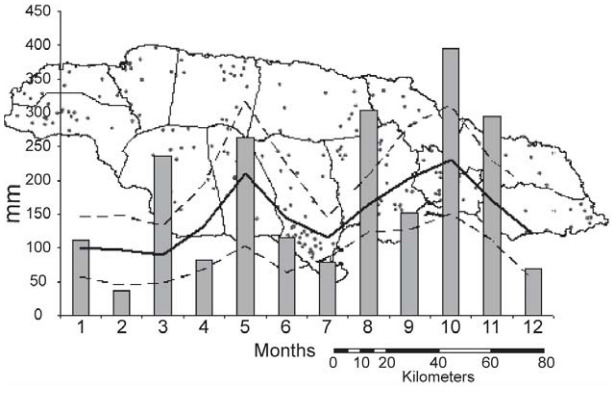

Fig. 6.20. Monthly Jamaican rainfall for 2007 (bars). Data are for a composite index derived from station data. Also shown are the climatology (black) and one standard deviation from climatology (dashed). Baseline period: 1971–2000. Map background shows Jamaica and location of stations used in analysis.

maica. Also noteworthy were the prolonged periods of rainfall, which affected the island during October and November, as flash flood warnings and watches were issued for 18 days in October and 13 days in November. Wet conditions in 2007 continued the trend of above-average rainfall, which began in the late 1990s.

5) Puerto Rico—J. P. Cupo and E. Morales

The Puerto Rican climate in 2007 was affected by the neutral ENSO to moderate La Niña conditions that were observed for much of the year. Both precipitation and temperature measurements were generally slightly above normal island-wide, with few exceptions. When distributed by month, temperature readings were found to be slightly to moderately above normal every month of the year. The annual mean temperature at the San Juan International Airport was 26.7°C, whereas the overall average temperature was 27.3°C for 2007.

Precipitation was slightly above normal for the year, with the exception of the eastern interior and the southern slopes of Puerto Rico. At the end of 2006, the eastern interior and southern slopes were already experiencing below-normal precipitation. Since the Puerto Rican dry season normally occurs between the latter half of January through April, these areas experienced drier-than-normal soil conditions as a result. The dry season extended through most of the Puerto Rican rainy season as well. The National Drought Mitigation Center classified this event as a D1. Tropical Storm Noel ended the dry spell over these regions when it produced 12–17 in. of rain across the eastern half of Puerto Rico at the end of October. Meanwhile, normal to above-normal rainfall conditions were reported for the rest of the island, with convection and other local effects the main source of the precipitation.

Rainfall across the eastern portions of Puerto Rico is normally generated by tropical waves that typically move across the area every 3–5 days. A normal number of tropical waves were noted for 2007, but rainfall associated with these systems was below normal. The eastern portions of Puerto Rico experienced dry conditions similar to that of other smaller Caribbean islands that also depend on showers generated by these tropical waves. The observed precipitation across Puerto Rico for 2007 was near normal.

Puerto Rico was affected by three tropical cyclones during the year. Tropical Cyclone Dean brushed the southern coast of the island as it developed into a category 5 hurricane in mid-August. Impacts included torrential rains across the southern and western coastline. In October, Tropical Storm Noel moved very slowly as it traversed the local waters of the Caribbean along the periphery of the island, generating very heavy rainfall across the southeastern portions of the island. Rainfall in excess of 17 in. (432 mm) was reported at the Lago Carite near Cayey. Finally, subtropical storm Olga, which eventually transitioned into a tropical storm, impacted the island in mid-December. Due to its development outside of the normal tropical cyclone season, it ended up shattering the normally drier month's records for precipitation at numerous stations across the island. One such record was at the San Juan International Airport, where 2.26 in. of rain fell, breaking the old record of 1.29 in. in 1965. Despite these three tropical cyclones, the 2007 hurricane season was relatively quiet for Puerto Rico, considering the above-average activity over the past decade.

e. *South America*

1) Overview—P. López Carmona and M. Rusticucci

The data used in this section were acquired from 300 meteorological stations by the National Meteorological and Hydrological Services of Argentina, Bolivia, Brazil, Chile, Colombia, Ecuador, Guyana, Paraguay, Perú, Surinam, Uruguay, and Venezuela. The data were compiled by CIIFEN.

In general terms, climate conditions over South America during 2007 were drier than normal in the southern and eastern parts of the continent, very dry over the west, and near normal to wetter than normal in the region north of the equator and parts of the Amazon basin (Fig. 6.21). With regard to temperatures, an unusually cold winter was reported over the southern portion of the continent, while warmer-than-normal conditions prevailed in the Amazonian region. This marked meridional contrast in temperature, between the anomalously warm conditions in the tropics and the lower-than-normal temperature over the southern half of the continent, was observed for 2007 as a whole in terms of mean, maximum, and minimum temperatures (Fig. 6.22).

The weak El Niño conditions in January quickly dissipated in early February, shifting to La Niña conditions by April. The negative SST anomalies in the equatorial Pacific strengthened in the following months until reaching the mature stage by the end of the year. Modulation by the MJO and upper-level conditions were also factors in 2007, as were dynamic changes in the SWJ. The SWJ was anomalously intense and displaced northward over the continent during January, resulting in the strengthening of the SACZ and the development of intense convec-

tive activity and enhanced rainfall in west-central Brazil, southern Amazonia, and eastern Bolivia. The impacts were particularly severe in Bolivia, where flooding events and associated damages were similar in magnitude to those associated with the 1997–98 El Niño event. The rainfall anomaly pattern along the west coast of South America was generally coherent with typical cold episodes in the equatorial Pacific, particularly the above-normal precipitation in Colombia and the dry conditions in central Chile (Fig. 6.21). In Ecuador, precipitation during the rainy season (February–March) was the lowest in the last 50 yr. The deficient rainy season in northeastern Brazil was linked to an anomalous displacement of the ITCZ toward the north from March to June, with generally a rainfall surplus in Colombia, Venezuela, Guyana, and Surinam. The southern half of South America experienced mostly below-average annual rainfall, excluding Uruguay, southern Brazil, and large areas of the northern half of Argentina.

Regarding extreme precipitation events, very intense rainfall episodes occurred in Bolivia and southern Brazil in early 2007. A flood event between 4 and 6 May in Uruguay dropped over 300 mm of rainfall, the most intense rainfall event since April 1959. The interaction between the ITCZ and the anomalously warm North Atlantic conditions were associated with intense rainfall in Colombia from March to May and during the second half of the year. La Niña conditions that developed during 2007 partially explain some of the rainfall anomalies across the continent during this year, particularly the relatively wet conditions in Colombia and the below-average precipitation in central Chile.

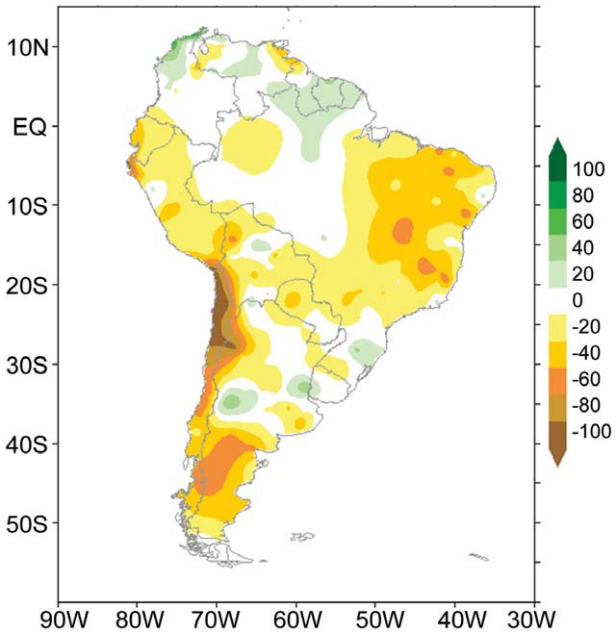

Fig. 6.21. Annual precipitation anomalies during 2007 (percent of 1961–90 normal) in South America. [Source: National Meteorological Services of Argentina, Brazil, Bolivia, Chile, Colombia, Ecuador, Guyana, Surinam, Uruguay, Paraguay, Peru, and Venezuela. Data compilation and processing: CIIFEN.]

Other very unusual weather episodes were observed during 2007. A snowfall episode in Buenos Aires and the surrounding areas on 9 July was the first one since 1928. The first snowfall event in a decade affected the rich agricultural region of central Chile on 9 August, exacerbating the damage caused by numerous freezing days during an anomalously

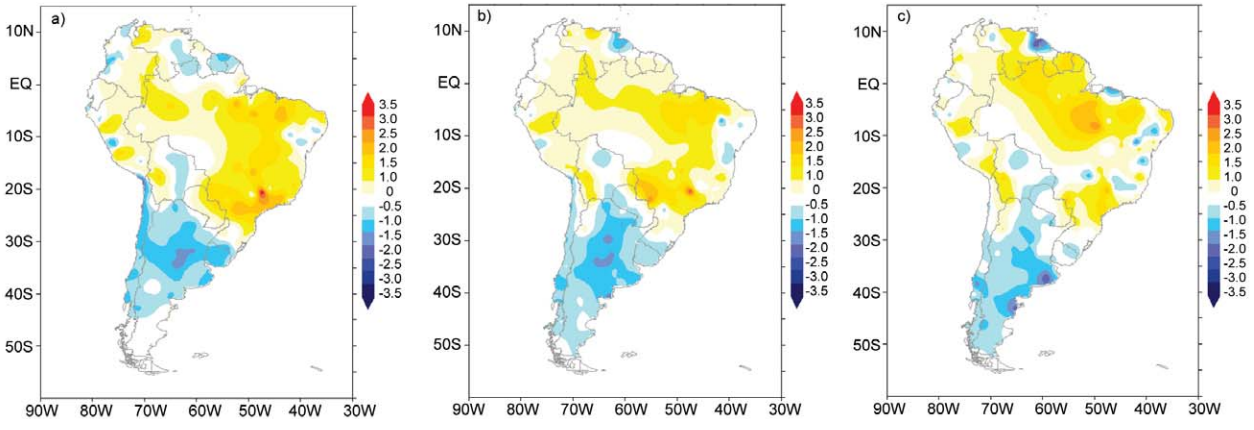

Fig. 6.22. Annual (a) mean, (b) maximum, and (c) minimum temperature anomalies for 2007 (°C; base period is 1961–90) over South America. [Source: National Meteorological Services of Argentina, Brazil, Bolivia, Chile, Colombia, Ecuador, Guyana, Surinam, Uruguay, Paraguay, Peru, and Venezuela. Data compilation and processing: CIIFEN.]

cold winter. A couple of waterspouts were observed during August in Venezuela near Margarita Island and in Lake Valencia. Last, an extremely intense 1-h long hail storm hit Bogotá, Colombia, on 3 November, producing severe damage and effectively bringing the city to a halt.

2) Northern South America and the Tropical Andes—R. Martínez Güingla, A. Quintero Mercardo, G. Hurtado, and E. Jaimes Espinoza

(i) Guyana, Surinam, and Venezuela

Monthly precipitation anomalies for January–February in Venezuela, Guyana, and Surinam were slightly below normal for a large portion of this region. Over Guyana and Surinam, rainfall was 20–40 mm below normal. Following the intensification of the ITCZ during March, a slight increase in rainfall was observed across the region, particularly in southern Venezuela, Guyana, and Surinam. The agricultural region in central and western Llanos—the grassland east of the Andes in northwestern South America—registered anomalies near –40 mm. The drier-than-normal conditions were also evident in northern Guyana. In Venezuela, a 140-mm deficit was observed in the state of Guárico and affected the farming communities in Bolívar, Anzoátegui, and Maturín.

During the third quarter of 2007, positive precipitation anomalies were observed in Surinam and central and southern parts of Guyana. In Venezuela, positive precipitation anomalies (up to 200 mm) were registered in August over Guarico and Anzoategui states and over the northern part of the country, while anomalies from 60 to 180 mm were observed in the south. However, for the entire season the precipitation anomalies in the western, central, and eastern regions were below average.

During August, two exceptional occurrences of waterspouts were observed in Venezuela, one on 6 August near the airport on Margarita Island (11°N, 64°W), and the second one on 8 August in Lake Valencia (Caraboo state), specifically in the small barren island of Chambergo.

The tropical cyclone season in the Caribbean Sea was less active than usual, and the cyclones that were observed did not affect the Caribbean sector of northern South America. Only tropical easterly waves over the Caribbean Sea influenced the weather of the Caribbean sector. A total of 50 tropical easterly waves moved from the Caribbean Sea to the north of Venezuela, interacting with the ITCZ and generating cloudiness and precipitation, as is typical during the rainy season.

Precipitation during the last quarter of 2007 was above the average in Venezuela, Guyana, and Surinam, with the exception of northern Guyana, where a 60 mm deficit was observed in November. Nevertheless, for December, positive precipitation anomalies reached near 100 mm in the region.

An analysis of precipitation records for different stations in Venezuela during recent years, including 2007, reveals a general negative trend in the frequency of rainy days. The development of large convective systems was common during 2007 in different regions, especially in central Llanos and southern Venezuela. These systems, characterized by the development of multiple convective cells, produced intense rainfall, storms, and showers.

Regarding temperature, an anomaly of +0.5°C was observed in the annual mean value of maximum daily temperature over northern Venezuela, where most of the populated cities are located, and +1.0°C over the northwest. The average minimum daily temperature was above normal in most of the territory in Venezuela, with an anomaly of +1.0°C over the northern portion of the country. Over Guyana, negative temperature anomalies on the order of –1.0°C were observed in the northern part of the country, in contrast with positive anomalies of +1.0°C in the southern region; this was also the case in Surinam. With respect to annual mean temperatures, anomalies of +1.0°C were observed in northern Venezuela and +0.5°C in the rest of the country, Guyana, and Surinam.

(ii) Colombia

During January and February, the displacement of warm waters toward the Colombian coast (from Kelvin waves) in response to the 2006–07 El Niño, combined with an anomalous northward displacement of the frontal systems over the Caribbean Sea, favored below-normal precipitation over most of the country and temperature anomalies around +2.0°C over isolated areas in eastern Colombia. Furthermore, during the first week of February, most of the highland regions located above 2500 m experienced very low minimum temperatures, with freezing conditions generated by extremely intense and rare nocturnal radiative cooling. From March to May, the ITCZ interacted with frontal systems that originated over the North Atlantic and produced favorable conditions for dense cloud generation and above-normal precipitation amounts in most of Colombia. Beginning in June, widespread above-normal rainfall was observed over the Andes, Caribbean, and Pacific regions. Rainfall was below average over the eastern part of Colombia in the second half of 2007.

(iii) Ecuador

The observed climate pattern over Ecuador during January showed limited influence from the 2006–07 El Niño event, as rainfall was slightly below normal along the northern coast and central highlands. In February, as the El Niño dissipated, the whole country experienced the most significant precipitation deficit of the last 50 yr, which was mostly associated with atypical circulation patterns in the upper troposphere over Amazonia and the Caribbean. During March, the rainy season became more intense, with above-normal precipitation in most of the highlands and along the central and northern coast. In April and May, the rainy season was characterized by significant rainfall episodes primarily along the northern coast, while precipitation deficits were observed in the rest of the country.

The second half of 2007 was characterized by dry conditions in most of the country. However, above-normal precipitation was recorded in highland areas and the Amazon region from August to October. The ITCZ exhibited weak-to-moderate convective activity and very limited influence over the continent between 2°N and 1°S. This behavior was due to the blocking of cold air advection from the Caribbean, among other factors, in the upper troposphere over Colombia and northern Ecuador. This inhibited the development of convection over the ITCZ, mainly in the coastal region.

The temperature was above normal during January and February over the Ecuadorean territory. From March to May and October to December, temperature was below normal. During the first quarter, although negative SLP anomalies were present in the equatorial Pacific, the above-average SLP offshore of the Peruvian coast favored fair weather conditions. The SPA was displaced slightly to the south and exhibited anomalies up to +3.0 hPa.

(iv) Perú

The first four months of 2007 were characterized by enhanced humidity convergence over the Amazonian portion of the Peruvian territory, sustained by a persistent transport of water vapor from the northeast. This process, combined with upper-level divergence, favored the development of intense deep convection and associated intense precipitation over Amazonia and the highlands. Humidity transport led to the development of rainfall events along the central coast and northern Perú. Migratory high pressure systems routinely formed over the continent, shifting quickly toward the South Atlantic and displacing the frontal systems to southeast Brazil. A ridge located near northeast Brazil favored the advection of warm and wet air masses from the north.

During the first 10 days of February, a change in the regional atmospheric circulation pattern favored the advection of humidity toward the eastern slopes of the Andes, producing moderate-to-intense rainfall over the Amazon region in Perú. During the second week of February, an intense episode of the LLJ, with winds up to 22 m s^{-1}, produced some light damage in the Department of San Martin. Furthermore, advection of warm and moist air from the north favored the development of intense convection over the jungle, while over the highlands westerly winds generated convection and intense hail storms that caused extensive agricultural damage.

At the beginning of May, the southeast Pacific subtropical anticyclone was anomalously intense (anomalies up to +10 hPa) and displaced southward from its mean position. A ridge over El Chaco, which is characteristic of this season, inhibited precipitation. However, the presence of easterly winds over tropical South America aided the development of convection and rainfall over the Peruvian jungle and the eastern slopes of the Andes. In contrast, several episodes of cold air advection were associated with the passage of migratory high pressure systems.

During July–September, an episode of intense winds occurred along the Peruvian coastal strip (called Paracas winds) that was associated with the intensification of the zonal pressure gradient and the southern configuration of the SPA. The strong winds lifted dust and sand from Ica to the north, and generated persistent drizzle along the coast, including in Lima. At low levels (950 hPa) offshore of the central coast of Perú, winds surpassed 25 m s^{-1}.

During the first part of October, an upper-level anticyclone predominated over southern Perú. The associated divergence over the central and northern part of the Peruvian Amazon supported the development of several episodes of moderate-to-strong convection and precipitation, as was observed over Loreto (northeast Perú) on 4 October when 140 mm of rainfall was recorded.

During December, subsidence was predominant over the Peruvian territory, and convection was restricted to isolated episodes over the eastern slope of the Peruvian Andes. Rainfall events that occurred mainly in the central and southern part of the Amazon region of Perú, during the second week of the month, were forced by advection of warm and moist air associated with an intense LLJ episode. Southerly winds over Argentina, Paraguay and Bolivia, associated with migratory highs, generated intense

convergence over northern Bolivia, leading to strong convection and rainfall.

3) Tropical South America, east of the Andes—J. A. Marengo and J. Báez

(i) Regional precipitation

In general, the most important features of summer rainfall in the region were the intense rainfall and flooding episodes in January–February in Bolivia, eastern Perú, central Chaco and eastern Paraguay, and western and southeastern Brazil. In Bolivia, floods affected nearly 200,000 people and 70,000 hectares of cropland. According to SENAMHI (www.senamhi.gov.bo), during January and February 2007 rainfall in the lowlands was 57% above normal in January and 23% above normal in February. However, during the whole year, the lowlands of Bolivia east of the Andes, from Pando to Santa Cruz, experienced moderate drought conditions while the Andean region experienced intense drought from La Paz to Potosi. In Paraguay, from April until the first half of October, rainfall deficits predominated over the country. In cities such as San Pedro, San Estanislao, Concepción, and others in the north, rainfall was absent for 40 consecutive days, prompting the most prolonged and extensive forest fires ever recorded in the country. In the upper Amazon region of Perú, floods in San Ramón affected 90% of the city, while intense rains over the Huallaga Valley produced floods that affected crops and left hundreds homeless. In Brazil, large areas in the southeastern and west-central regions were affected by abundant rainfall that produced landslides; rainfall was almost 80% above normal in many cities in those regions during January 2007. northeast Brazil's prerainy season was below normal, similar to most of the Amazon and southern Brazil regions. This was due to the configuration of the SACZ and a lack of cold fronts. January 2007 was among the five wettest over the past 46 yr. The upper-level circulation in January was characterized by a subtropical westerly jet stronger than normal and displaced anomalously northward over South America. The upper-tropospheric Bolivian anticyclone was very intense and positioned over southeastern Bolivia; its presence led to the amplification of convective activity over its diffluent region, bringing moisture and favoring rainfall over eastern Bolivia, central Chaco in Paraguay, and west-central Brazil and the southern Amazon, with intense rainfall events over these regions. In the Amazon region, rainfall in January was 100 mm above normal in northern and southwestern zones, while in the rest of the region rainfall was below normal.

As in January, most of the summer and autumn months were characterized by episodes of intense rainfall. In some cities of the Amazon and northeast Brazil regions in March, the accumulated rain in 2–3 days was larger than the long-term means by at least 100 mm. However, in the same month a dry air mass was stationary over large regions of southeastern and southern Brazil, and the relative humidity reached values of about 30% or less. For instance, in Resende-Rio de Janeiro, Curitiba-Parana, and the Sao Paulo International Airport, relative humidity reached 20% on 4 March. In the austral winter (June–August), the dry season in most of tropical and subtropical Brazil was interrupted by intense rainfall events due to the presence of cold fronts and extratropical cyclones that produced storms and hail in southern Brazil. During spring (September–November), rainfall was above

DRY CONDITIONS IN BOLIVIA IN 2007: BLAME IT ON EL NIÑO?—J. A. MARENGO

The brief El Niño event of late 2006 quickly dissipated in January 2007, and La Niña conditions became well established across the central and eastern equatorial Pacific in the latter half of 2007. According to Bolivian Government sources, early 2007 dryness in Bolivia was attributable to the 2006–07 El Niño. The warming of the tropical Pacific was considerably weaker than in other El Niño events, as in 1982–83 and 1997–98. Compared to the 1997–98 El Niño, when 34% of the country was affected, conditions linked to the 2006–07 El Niño affected almost 60% of the country. Total losses in this year were about $405 million (U.S. dollars), compared to $570 million (U.S. dollars) during the 1997–98 El Niño.

Ronchail et al. (2002) have suggested that drought conditions in the regions that experienced rainfall deficits in early 2007 in Bolivia have occurred in the past not only in El Niño years, but also in years that experienced anomalous warming in both the tropical North and South Atlantic, and also in La Niña years accompanied by anomalously warm surface waters in the tropical North Atlantic. They argue that El Niño–induced droughts typically affect the provinces of Pando and Beni, as well as Potosi and Tarija, while above-normal rainfall may be detected from La Paz to Santa Cruz. The rainfall anomaly pattern observed in 2007 over Bolivia compares more favorably with the pattern characterized by warming in the tropical Atlantic than that of a typical El Niño. Therefore, it is likely that the 2006–07 El Niño was not the main cause of dry conditions in Bolivia in 2007.

normal along the eastern coast of Brazil, while in the interior a dry air mass persisted, with lower values of relative humidity (13% in Goiânia-Goias). Rainfall was above normal in the Amazon and southern Brazil regions, associated with the presence of the SACZ. Consequently, rainfall was above normal in some cities of southeastern Brazil, including in Ubatuba-São Paulo, where it rained 235 mm during 22–26 October, 13 mm above the climatological average for all of October.

The rainy season March–May in northeast Brazil in 2007 was deficient, about 200 mm lower than normal, in contrast to 2005 and 2006, both of which had rainfall surpluses (Fig. 6.23). The region most affected by drought was the semiarid region, as well as the northern region of northeast Brazil. The 2006–07 El Niño event was weak during the austral summer and had dissipated during autumn, so the most important dynamic cause of dry conditions in northeast Brazil in 2007 was the behavior of the tropical Atlantic. The tropical Atlantic oscillated between normal and relatively warm north of the equator; therefore, the ITCZ was located northward of its climatological position during summer and autumn. Even though the whole season was considered as rainfall deficient, some intense rainfall events were reported.

(ii) Regional temperatures

Most of tropical South America east of the Andes experienced a warm 2007, with temperatures about 2°–3°C warmer than normal in January–February. In the Amazon and northeast Brazil regions, temperature anomalies were above 3°C in January. Unusually warm temperatures approximately 3°–6°C above average were also observed during September–October in Paraguay, extending into west-central and southeastern Brazil and into northern Argentina, southern Brazil, and Uruguay.

South America experienced an unusually cold winter (June–August), bringing winds, blizzards and rare snowfall to various provinces with temperatures falling to –22°C in Argentina and –18°C in Chile in early July. May 2007 was unusually cold, and in southern Brazil the temperatures reached values as low as –5°C on 29 May in São Joaquim-Santa Catarina. In the Amazon region, temperatures fell as low as 13.5°C on 9 May and 9°C on 10 May in Vilhena-Rondonia, where the average temperatures are greater than 20°C. The penetration of a polar air mass associated with a cold front affected the Amazon region in late June, when minimum temperatures reached 14.9°C on 26 June, with a drop in temperature of 7.6°C from the previous day. In southern Brazil, minimum temperatures reached –5°C in the highlands. Monthly temperature anomalies were 2°–3°C below normal in southern Brazil, Paraguay and northeast Argentina during July and August, while tropical Brazil experienced temperatures about 1°–3°C warmer than normal from April to August.

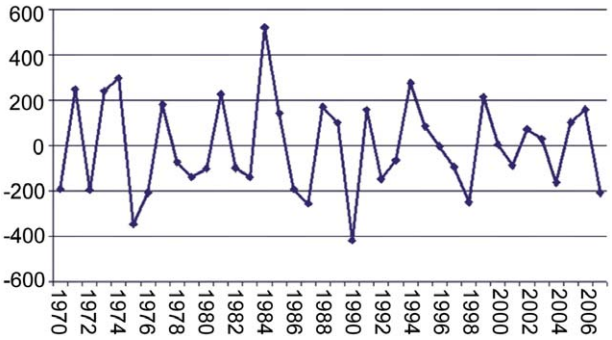

Fig. 6.23. Rainfall anomalies (mm; base period in 1970–2000) during the peak season Mar–May in northeast Brazil during 1970–2007. [Source: CPTEC/INPE and INMET.]

4) Southern South America: Argentina, Chile, Paraguay, and Uruguay—M. Bidegain, M. Skansi, P. Aceituno, and J. M. Quintana

(i) Regional temperatures

Temperature anomalies were negative during 2007 throughout a great portion of SSA, and anomalously low along the extratropical west coast of the continent. Annual temperatures between 0.5° and 1.0°C below normal were observed in Argentina, Chile, Paraguay, and Uruguay.

The beginning of 2007 was relatively hot in Chile, Paraguay, Uruguay, and Argentina (north of 40°S), where mean temperature was above normal (0.2°–0.5°C). Below-normal temperatures (anomalies from +0.2° to –1.0°C) were observed over Uruguay and the eastern portion of Argentina during the austral autumn. The winter was extremely cold over the entire region with temperatures 0.5°–4.0°C below normal. July was exceptionally cold, and record minimum temperatures were broken at many stations in northeastern Argentina, southern Paraguay, and northern Uruguay, where monthly anomalies of up to –5°C were observed. A strong cold spell after the passage of a cold front that affected the region from 6 to 12 July produced extremely low minimum and maximum temperatures and covered a large part of Chile and Argentina with snow, including Buenos Aires, where a rare snowfall episode was observed on 9 July, the first one since 1928. The winter's end was abrupt, and September was anomalously hot, particularly over

WINTER IN ARGENTINA—M. SKANSI

The winter of 2007 was extremely cold in almost all of Argentina, breaking a recent pattern of very warm winters. Mean temperature anomalies in the center and north of the country were below –1.0°, while those in the Pampas (30°–45°S) reached –2°C to –3.5°C (Fig. 6.24). Many locations recorded their lowest mean temperatures in the last 45 yr. The negative anomalies for the daily minimum temperatures were even more significant. The only exception was the southernmost region of Tierra del Fuego, where temperatures were above normal. In the Pampean region, anomalies ranged from –2° to below –4°C in the southern portion of Buenos Aires province. Mean daily maximum temperatures were on the order of 1°–2°C below normal in the central and northern portions of the country, while the southern part of Patagonia recorded anomalies that were slightly positive.

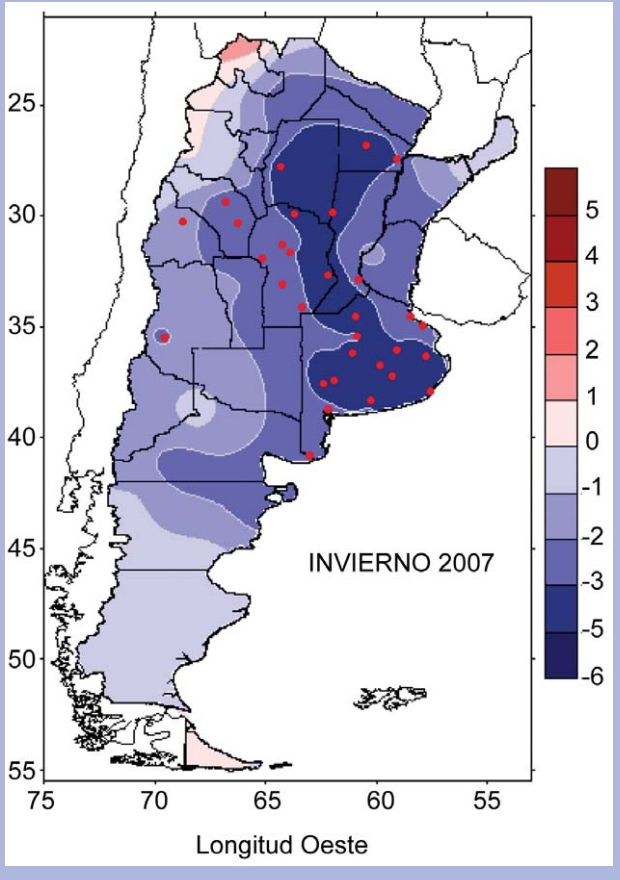

Fig. 6.24. Average minimum temperature anomalies (°C; 1961–90 base period) over Argentina in winter (Jun–Aug) 2007. Red dots depict stations that reported record cold minimum temperatures (since 1961) averaged over winter in 2007.

eastern Argentina and Uruguay (>2°C), where the hottest conditions of the last 45 yr were observed in some sectors. The spring showed positive temperature anomalies from 0.5° to 1.0°C above the mean.

As elsewhere in SSA, anomalously cold conditions characterized the austral winter and spring in central Chile, as shown in Fig. 6.25, which shows the evolution of daily minimum temperature in Santiago (33.5°S). The large frequency of freezing days during June–August produced considerable damage to agriculture along the central valley in the region from 30° to 40°S. In fact, the mean daily minimum temperature of 2.6°C in Santiago during August was the lowest since 1914, and the snowfall episode observed in central Chile during the night of 9 August was the first one in a decade.

(ii) Regional precipitation

Beginning in February 2007, heavy rainfall and storms caused severe flooding in SSA, affecting mainly the Argentine provinces of Entre Ríos and Santa Fe, located on the lower basin of the Paraná River. During the last week of March, 500 mm of rain was registered over this region, almost 4 times the climatological average for the entire month. It was estimated that more than 80,000 people were affected by the flooding.

The year 2007 was characterized by below-normal rainfall along the extratropical west coast of the continent. The deficit in annual rainfall in Chile, associated with an intensified SE Pacific subtropical anticyclone during the development of a La Niña event in the tropical Pacific, was 60% below average in the semiarid territory between 25° and 30°S and was of the order of 40% below average in the rich agricultural region between 33° and 37°S (Fig. 6.26).

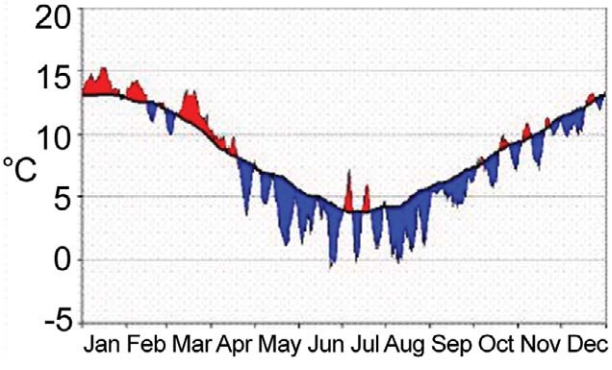

Fig. 6.25. Evolution of 5-day moving average of daily minimum temperature at Santiago (33.5°S) during 2007. The black line indicates the 1961–90 climatological mean.

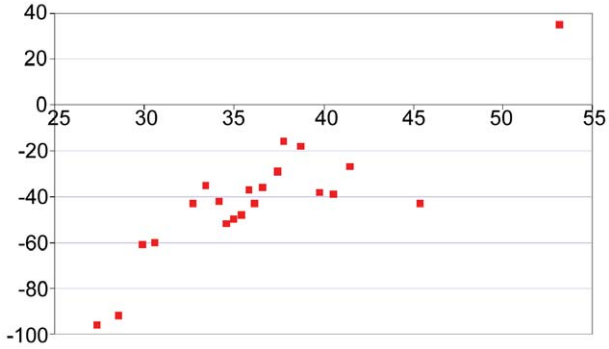

Fig. 6.26. Annual rainfall anomalies (percent of 1961–90 normal) for various Chilean stations. The *x* axis depicts latitude (28°–53°S).

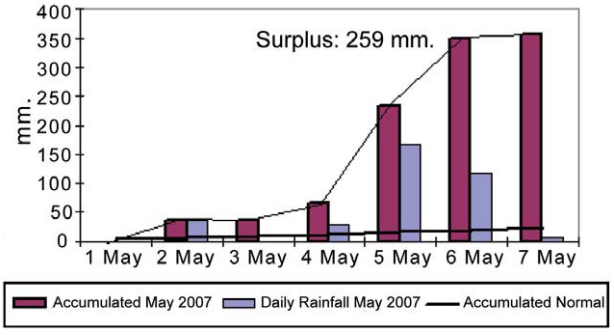

Fig. 6.27. Daily rainfall (mm) during 1–7 May in Treinta y Tres, Uruguay. The solid line represents the cumulative rainfall during this period in 2007, while the solid line depicts normal conditions.

In Uruguay, a heavy rainfall event during 4–6 May 2007 caused severe floods in the central part of the country (Fig. 6.27). It was the most intense rainfall episode (>300 mm) since April 1959. More than 110,000 people were affected in the cities of Treinta y Tres, Durazno, and Mercedes. Consistent with the mature phase of the La Niña episode at the end of 2007, rainfall deficits were observed in the southeastern portion of the continent during November and December, including southern Brazil, Uruguay, and eastern Argentina.

f. Asia

1) Russia—O. N. Bulygina, N. N. Korshunova, and V. N. Razuvaev

The year 2007 was the warmest on record in Russia, where regular meteorological observations date back to 1891. The mean annual air temperature anomaly averaged over the Russian territory was +2.0°C (1961–90 base period). Winter (December 2006–February 2007) and summer (June–August) were the warmest on record, registering anomalies of +3.2° and +1.8°C, respectively. In spring (March–May) and fall (September–November), mean seasonal air temperature anomalies were second-warmest on record, with anomalies of +2.2° and +1.8°C, respectively.

January 2007 proved to be abnormally warm over most of Russia. The vast territory of Russia, from its western boundaries to the Lena River, had not experienced such high temperatures in the entire instrumental record. Severe Atlantic storms moved eastward and brought warm and wet air masses, effectively weakening the Siberian anticyclone and displacing it to the northeast. The largest mean monthly air temperature anomalies (Fig. 6.28) were recorded in the northern Krasnoyarsk Territory (>14°C) and in the southwest of the Yakutia-Sakha Republic (>12°C). In European Russia, the positive mean monthly air temperature anomalies in the Volga Region and the Southern Urals exceeded +10°C. In the center of European Russia, the first half of January was particularly warm. Many meteorological stations, including those in Moscow, reported air temperatures that exceeded their maximum daily records. Over most of European Russia, February brought very cold weather, with mean monthly air temperatures of 8°–10°C below normal.

Spring air temperatures over the Russian territory were higher than the long-term average. In March (especially the second half), many meteorological stations in central European Russia exceeded their maximum daily record air temperatures. For most stations, March was the warmest in the entire period of record. In the southern Far East, cool and humid weather was generated by unusually deep cyclones that, while moving from the south, brought heavy snowfall and strong winds. The Maritime Territory (extreme southeast Russian territory whose principal city is Vladivostok), which experiences heavy snow nearly every year, received record snowfall in March when the all-time daily precipitation maximum was exceeded at 24 meteorological stations (Fig. 6.29). For March, the Maritime Territory received 300%–400% of the monthly precipitation norms, the southern Khabarovsk Territory received 200%–300%, and Sakhalin received 200%. Okhotsk, in the southern Khabarovsk Territory, received 62 mm of precipitation, 5 times the average amount. April was warm over most of the country, especially over the Asian territory. The largest mean monthly air temperature anomalies (higher than 10°C) were recorded in the

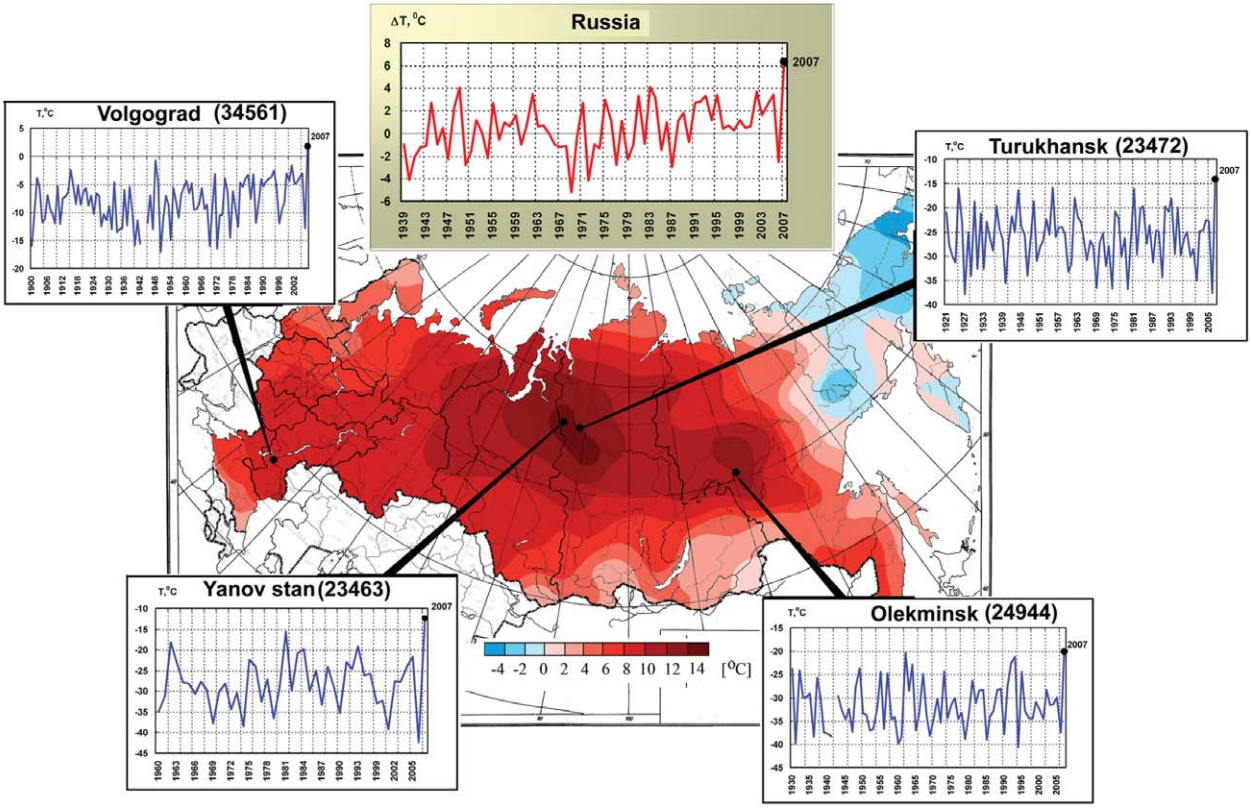

Fig. 6.28. Air temperature anomalies in Jan 2007. Insets show the series of the Jan air temperature anomaly averaged over the Russian territory and the series of mean Jan air temperature at meteorological stations Volgograd, Yanov stan, Turukhansk, and Olekminsk.

north of eastern Siberia and in the Taimyr Autonomous Area. Over virtually all of Russia, except Sakhalin and the Southern Federal District, mean monthly air temperatures were above normal, making April 2007 the second warmest on record. During the last week of May, abnormally hot and dry weather set in over central and southern European Russia. On the last days of the month, the air temperature reached 30°–37°C. Record-breaking daily air temperatures, 38°–39°C, were recorded in the south of the Volgograd Region and in the north of the Astrakhan Region, which were 1°–3°C above the previous records. Hot weather, combined with significant precipitation deficits, low relative air humidity, and strong winds, affected these regions. Beginning on 20 May, soil drought spread into the steppe and submountain regions of the Republic of North Ossetia-Alaniya.

Summer over the Russian territory was also much warmer than normal. In June, the Southern Federal District experienced a precipitation deficit in conjunction with warm temperature anomalies, which contributed to the rapid development of drought that persisted for 30–45 days. Unusually hot weather was recorded in the Southern Federal District during most of July. A vast region of very warm air temperatures formed in Chukotka, where mean monthly air temperature anomalies were greater than +6°C. For the Russian territory as a whole, August was the warmest on record (Fig. 6.30).

The fall in 2007 was also abnormally warm, particularly on the Arctic coast of Asian Russia. September brought above-average air temperature anomalies nearly everywhere in the Russian territory. The mean September air temperature was only slightly lower than the record-breaking value of 2005. September air temperature records were broken in some parts, such as northern Chukotka (Pevek), where mean monthly air temperature anomalies were higher than +6°C. In October, mean monthly air temperatures were above normal throughout the Russian territory, except the southern regions of western and eastern Siberia and the southwestern coast of Kamchatka. The highest mean monthly temperatures in the Far East were recorded in Chukotka, greater than +7°C above normal. In October, it was very warm on the Arctic coast and in southeastern Yakutia.

The positive temperature anomalies over the Asian territory persisted into November. The center of maximum anomalies (>8°C) remained in the vicinity of Kolyma and

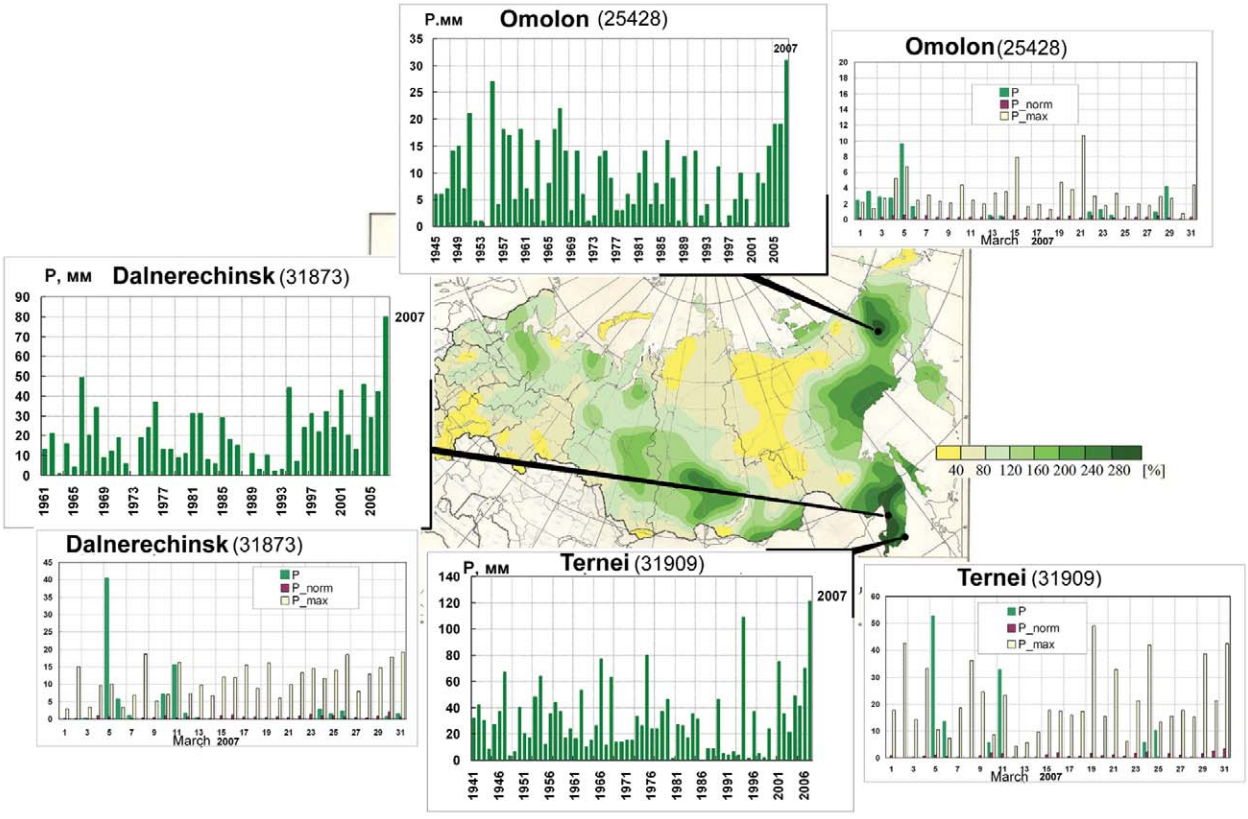

Fig. 6.29. Precipitation total vs the normal value in Mar 2007. Insets show the series of monthly and daily precipitation totals at meteorological stations Dalnerechinsk, Ternei, and Omolon.

in northern Chukotka. In November, record-breaking temperatures were observed in Oimyakon (Yakutia). On 7 November, the maximum air temperature reached –10.5°C, which was nearly 20°C above normal. December also proved to be warmer than usual over most of Russia. Large areas of above average temperatures developed in the north of European Russia and in the northeast of the Asian territory of the country, where monthly means were 8° and 10°C above normal, respectively. In Chukotka, where the monthly mean was warmer than normal for the fourth consecutive month, several stations (Shmidt Cape, Valkarai) had their warmest December on record.

2) East Asia—K. Suda, X. Zou, X. Liang, Y. Chen, Y. Guo, J.-E. Kim, and P. Gomboluudev

(i) Overview

Surface air temperatures over most of East Asia during 2007 were near or above normal (based on the 1971–2000 average), and were significantly above normal in winter (December 2006–February 2007) and spring (March–May 2007). Meanwhile, temperatures in parts of northwestern Mongolia and parts of southern China in autumn (September–November 2007) were slightly below normal. The annual temperature in China for 2007 was 1.3°C above normal (all four seasons were warmer than average), making 2007 the warmest year since reliable records began in 1951. In August, unusually high temperatures hit Japan, breaking the long-term monthly record. Considerable variability in precipitation occurred across East Asia throughout the year. In China, heavy rains caused devastating floods in the Huaihe River Valley in late June and July, while significant droughts affected much of southern China from late September to mid-December. In the Democratic People's Republic of Korea, heavy rains caused severe floods in August. Severe drought conditions persisted across Mongolia.

(ii) Temperature

The average temperature in China for 2007 was 10.1°C, which was 1.3°C above normal, ranking this year as the warmest since reliable national records began in 1951 (Fig. 6.31). Annual mean temperatures for 2007 were above normal over most of China, and 1°–2°C above normal in the northern and eastern

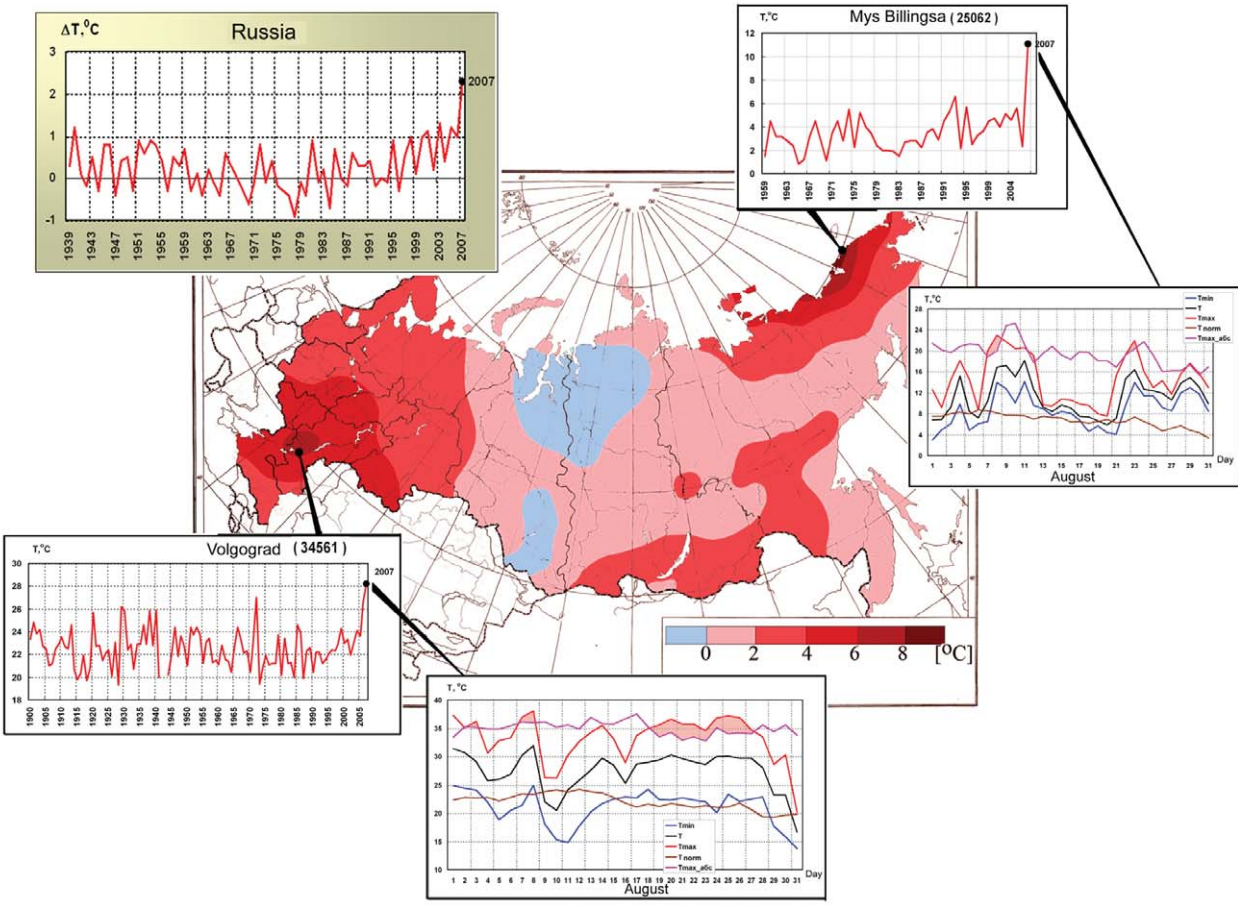

Fig. 6.30. Air temperature anomalies in Aug 2007. Insets show the series of the Aug air temperature anomalies averaged over the Russian territory and the series of mean monthly and daily air temperatures in Aug 2007 at meteorological stations Volgograd and Mys Billingsa.

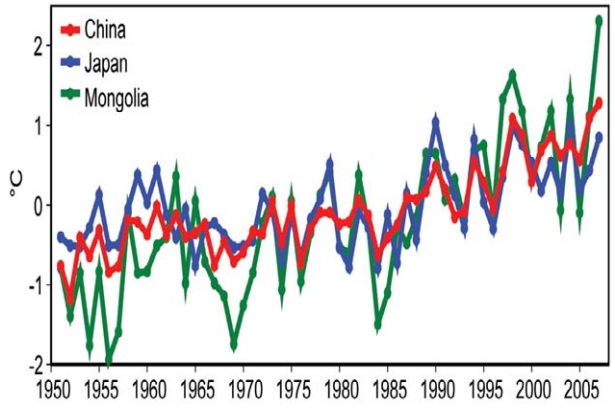

Fig. 6.31. Time series of annual mean temperature anomalies (°C; 1971–2000 base period) in East Asia from 1951 to 2007. [Source: CMA, JMA, and NAMHEM of Mongolia.]

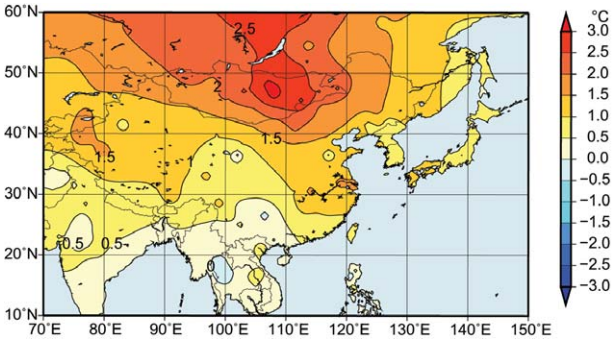

Fig. 6.32. Annual mean temperature anomalies (°C; 1971–2000 base period) over East Asia in 2007. [Source: JMA.]

parts of the country (Fig. 6.32). The 2006/07 winter season was the second warmest winter for China during the past half century. For spring, the average temperature for the whole country was 10.9°C, which was 1.2°C above normal and the warmest spring since 1951. The average temperature for summer (June–August 2007) in China was 21.3°C, which was the second warmest in the 1951–2007 record. The

autumn temperature in 2007 in China was 10.1° and 0.8°C above normal.

The annual mean temperature of the Republic of Korea in 2007 was 13.4°C (1.0°C above normal), making 2007 the second warmest year since 1973. The mean temperature during winter was the highest since 1973. Anomalously warm conditions occurred in September, as daily minimum temperatures did not drop below 25°C in some of the southern parts of the Republic of Korea.

The annual mean temperature in Japan was 0.85°C above normal, the fourth highest on record since 1898. In winter, all-time seasonal mean temperature records were broken at 63 out of 153 observatories. The regional mean temperatures in many parts of Japan were the highest since the winter of 1946/47, when reliable historical records began. In August and September, monthly mean temperatures were significantly above normal in many parts of Japan. A number of stations broke their all-time high temperature records in mid-August. On 16 August 2007, a new national record of 40.9°C was measured concurrently at Kumagaya near Tokyo and Tajimi near Nagoya.

The annual mean temperature in Mongolia was 2.4°C, which was the warmest year since 1940. The winter temperature was –15.4°C, about 3.1°C higher than normal and also the warmest winter in the entire observational record. The summer temperature was the second highest and the spring and autumn temperatures were also above normal.

(iii) Precipitation

Total precipitation for 2007 in China was near normal, ranking as the 27th driest out of 57 yr of nationwide records. The spatial and seasonal precipitation distributions were uneven across the country. Precipitation values were 20%–100% above normal in most of northwest China and the Huaihe River Valley, while deficits of 20%–50% were recorded over Northeast China and the areas south to the Yangtze River (Fig. 6.33). In late June and July, heavy rainfall continued in the Huaihe Valley, which caused the most severe flood since 1954, with more than 1 million evacuees. Anhui province was especially hard hit. During late September to mid-October, successive rains occurred in eastern northwest China and north China, with above-average counts of rainy days, marking the longest autumn rain event on record in northern China. In summer, widespread droughts expanded across much of southern China and northeast China. From late September to mid-December, a 1-in-50-yr drought impacted most of southern China, which rapidly intensified and caused a shortage of potable water for about 3 million people.

The Republic of Korea had an average rainfall of 1,515 mm in 2007, which was 15% above normal. This was punctuated by a very wet September, when Korea received 2.8 times its September normal.

In Japan, annual precipitation amounts were below average in most areas. The amounts were less than 60% of their normal in parts of western Japan, and three observatories reported their driest conditions on record. During winter, the snowfall amounts were significantly less than normal across all of Japan. Some regional mean winter snowfall amounts were the least since the winter of 1961/62, when the historical records began. In a part of eastern Japan, the total snowfall amount was 91% less than normal. In autumn, seasonal precipitation amounts were extremely below average in western Japan.

In Mongolia, a period of dry conditions continued; the annual precipitation was 170 mm, which was 23% lower than normal. Drought persisted from May to July, with the only exceptions of the southwestern and southern parts of the country.

(iv) Atmospheric circulation

In winter, the center of the Aleutian low shifted eastward from its normal position, and the Siberian high was weaker than normal. This type of pattern indicates that the northeastern Asian winter monsoon was weaker than normal with less frequent cold surges. In the upper troposphere, the intensity of the seasonal mean polar front jet was stronger than normal from Europe to Lake Baikal, which brought an extremely warm winter to northeastern Asia. In spring, upper-level ridges over central Asia and troughs from Japan to the western Pacific were observed partly as quasi-stationary Rossby waves

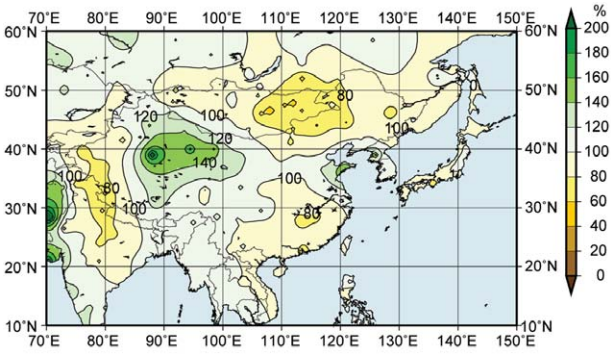

Fig. 6.33. Annual precipitation anomalies (1971–2000 base period) as percentage of normal over East Asia in 2007. [Source: JMA.]

that propagated from Europe. High pressure systems did not develop pesistently in the Sea of Okhotsk in summer, while the North Pacific anticyclone was stronger than normal around Japan in August and September. In the upper troposphere, the Tibetan high was stronger than normal in its northeastern periphery as the Asian jet meandered frequently in August and September. In connection with these synoptic patterns, a barotropic high pressure system brought extremely high temperatures to Japan.

(v) Monsoon

The onset of the SCS summer monsoon began at the end of May, which was later than normal. Subsequently, warm and wet air controlled the SCS as southwesterly flow set in. During mid-June, southwesterlies moved northward to the Jianghuai area together with a northward movement of the northwest Pacific subtropical high. The mei-yu[5] also prevailed in the area, and warm and wet air dominated south of the Huanghuai area. During late July, warm and wet air moved northward to north China. After mid-August, warm and wet air swiftly withdrew southward, and moved back to South China during early September and lingered until late October. At this point, the winds shifted to the northeast, bringing the SCS summer monsoon season to an end. Overall, the SCS summer monsoon index was –1.3 in 2007, which was weaker than average.

The national average of precipitation during the Changma period (the Korean rainy season, roughly 21 June through 29 July) was 322.7 mm, which was close to the climatological normal (346.1 mm). The number of rainy days during the Changma period (20.8 days) was 4.2 days above normal.

The onset of baiu (the rainy season over Japan during the late spring and summer) was later than normal and water shortages occurred in parts of western Japan, due to migratory anticyclones and a delay in the northward migration of the baiu front. The baiu front tended to stay near the mainland of Japan through July, which brought rainy and cool days. Monthly precipitation amounts during July were above normal due to the active baiu front enhanced by Super Typhoon Man-Yi (see section 4b for additional details on the west North Pacific typhoon season). The end of baiu season was later than normal in most areas of Japan. However, the North Pacific anticyclone intensified around Japan in August, and hot days continued nationwide with dry weather on the Pacific side of the country.

(vi) Aeolian dust

In spring 2007, China was affected by 15 dust and sand events, which was fewer than in 2006. The average number of dust days in northern China was 2.0 days, which was 3.6 days less than normal. On 30–31 March, a severe dust storm blanketed much of northwest and north China, regarded by some as the worst dust storm in 2007. The Republic of Korea was affected by 13 Asian dust events, and the strongest one peaked on 31 March, affecting most of Korea over a 3-day period. In Japan, the number of days when "yellow sand" (i.e., aeolian dust) was observed was 34 from January to May 2007, which was the eighth most since 1967. The number of stations that observed aeolian dust was 75 on 2 April, and 72 on 26 May, which were the second and third largest counts on record, respectively.

3) South Asia—M. Rajeevan, J. Revadekar, and L. Zubair

(i) Overview

In 2007, South Asia experienced extremes, both in terms of precipitation and temperature. In January, many parts of north India had severely cold conditions, with a few stations reporting minimum temperatures below the freezing point. The cold outbreak also affected northern districts of Bangladesh, where the reported temperatures were the coldest in 38 yr. Heat waves are common in May and June over northern parts of India and Pakistan, before the onset of the summer monsoon. During May and early June, severe heat wave conditions prevailed over parts of Pakistan, northern India, and south peninsular India with temperatures reaching 45°C. The harsh heat wave conditions claimed the lives of at least 100 people in India and Pakistan. During the first week of May, heavy rainfall triggered landslides and flooding along the southwest coast of Sri Lanka, affecting more than 1 million people. Colombo, the capital city of Sri Lanka, received about 10 in. of rain in 48 hr.

(ii) South Asian summer monsoon

Summer monsoon (June to September) contributes 60%–90% of the annual rainfall over major portions of South Asia. The 2007 monsoon was characterized by an early onset over south peninsular India. Immediately after onset, there was a 10 day stall in the monsoon's advancement as a disruption of monsoon flow accompanied the formation of Cyclone Gonu (see tropics chapter) over the Arabian Sea. However, the southwest monsoon ultimately

[5] Mei-yu ("plum rains") refers to the June–July rainy season in southern China, also referred to as baiu in Japan.

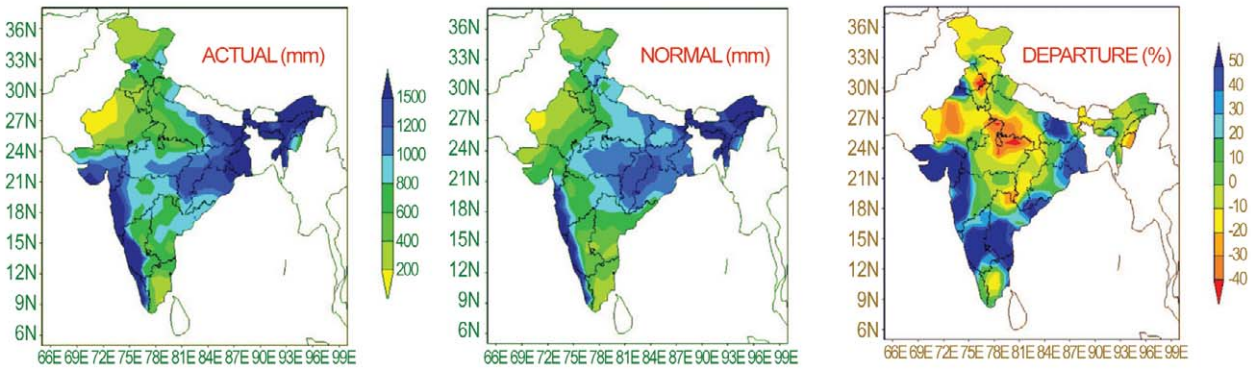

Fig. 6.34. Monsoon rainfall (mm) and anomalies (percentage of normal) over India in 2007.

covered India on 4 July, about 10 days ahead of its normal date.

During the 2007 summer monsoon, storm activity was slightly above normal. The formation of two intense cyclonic storms over the Arabian Sea in the month of June was the unique feature of the season. In addition, 11 low pressure systems, including five deep monsoon depressions, formed over the Bay of Bengal. During the season, the monsoon trough (continental tropical convergence zone) was positioned south of its normal position, causing low pressure systems to move south of their normal tracks and resulting in copious amounts of rainfall and flooding over many southern parts of the peninsula. As a result, severe landslides and floods claimed at least 100 lives. From 21 June to 4 July, three depressions formed over the Bay of Bengal in succession. On 23 June, Kurnool in the semiarid area of the southern peninsula received a record rainfall total of 393 mm in 24 h. The previous record was 81.3 mm, recorded on 4 June 1901.

The India-wide summer monsoon rainfall was 6% above its long-term average of 89 cm. However, rainfall activity was not well distributed over space and time (Fig. 6.34). It exhibited strong intraseasonal activity during the season (Fig. 6.35). Active monsoon conditions prevailed on many days in June, September, and during the first week of July and August. However, monsoon breaks prevailed for several days in July and August. After an early onset, the monsoon was less active until the third week of June, partly due to the disruption of the monsoon circulation by Cyclone Gonu over the Arabian Sea. However, with the formation of a deep depression over the west-central Bay of Bengal on 21 June, monsoon conditions revived and active monsoon conditions continued until 10 July. During the second half of July, a monsoon break prevailed over the country. The monsoon was again less active in August, except for a brief period during the first week of the month. However, with the rapid development of La Niña and the positive Indian Ocean dipole conditions (see tropics chapter), the monsoon revived again during the second week of September causing heavy rains over many parts of the country.

Over the country, the monsoon rainfall was deficient over northwest India and parts of central India. However, it was in excess over the south peninsula, where strong monsoon activity continued throughout the season. Out of 36 meteorological subdivisions, 13 received excess rainfall, 18 received normal rainfall, and 5 received deficient rainfall. Out of 504 meteorological districts for which rainfall data were available, 73% of the meteorological districts received excess rainfall and 27% received deficient rainfall. During the season, 74 districts (15%) experienced moderate drought conditions (a rainfall deficiency of 26% to 50%) and 29 districts (6%) experienced severe drought conditions (a rainfall deficiency of 51% and more).

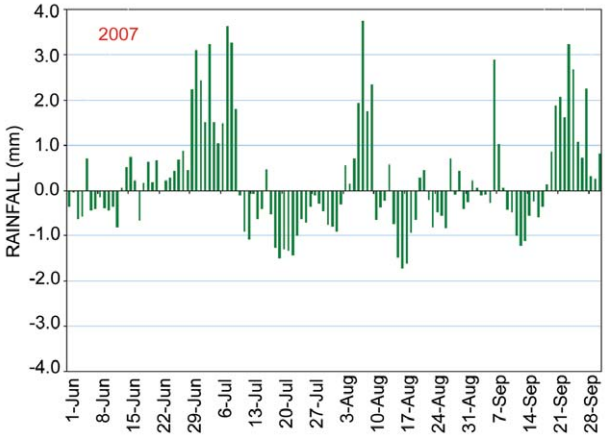

Fig. 6.35. Daily standardized rainfall time series averaged over the monsoon zone (1 Jun–30 Sep 2007).

The 2007 summer monsoon rainfall was deficient over Pakistan. The largest rainfall deficiency was observed in Northwest Frontier Province (–16.4%), followed by Balochistan (–14.1%). In general, normal to above-normal rainfall was recorded in most parts of Nepal, except in the eastern region and the Kathmandu and Dipayal Valleys. As in previous years, many parts of South Asia experienced heavy rainfall and associated floods during the season. More than 25 million people were affected by the floods in South Asia with more than 2,000 fatalities. During August, Bangladesh and Nepal were affected by the heaviest rainfall in decades.

(iii) Northeast monsoon

The NEM sets in over southern peninsular India in October and in Sri Lanka in late November. The NEM contributes 30%–50% of the annual rainfall over southern peninsular India and Sri Lanka as a whole, and up to 70% of the annual rainfall in the dry northern and eastern regions of Sri Lanka. During 2007, the rainfall during NEM over southern peninsular India and Sri Lanka was within 5% of its long-term average. Regionally, the seasonal temperature was near normal. The northern regions of peninsular India of Andhra Pradesh and Karnataka and Eastern Sri Lanka received anomalously lower rainfall. The rainfall from November to mid-December was dramatically low. However, Tamil Nadu experienced above-normal rainfall activity during the second half of December. During the last half of the year, La Niña and positive IOD conditions prevailed (see tropics chapter). This is a rare combination with La Niña typically leading to depressed NEM rainfall and positive IOD enhancing the NEM rainfall. Neither the influence of the La Niña nor the influence of the IOD appears to have been dominant during the 2007 NEM season.

4) Southwest Asia

(i) Iran—F. Rahimzadeh and M. Khoshkam

(a) *Overview*

Most parts of Iran were cooler than average during both winter and summer, while warmer-than-average conditions prevailed in spring and autumn (1°–2°C above average). Spring was wetter than average over much of Iran, while in early June, Super Cyclonic Storm Gonu brought heavy rainfall to Oman and the arid regions of southeastern Iran.

(b) *Seasonal review*

Most of Iran was up to 2°C below normal during winter. Some parts in the east, southeast, and northeast portions of the country were up to 2°C warmer than normal. Areas with near- or above-normal precipitation were the north, northeast, and a narrow band in the northwest. Half of the country experienced precipitation amounts 25% or more below normal during winter 2007. Winter rainfall surpassed 100 mm near the Alborz and Zagros Mountains, and eclipsed 200 mm on the western and southeastern slopes of Zagros. The maximum value of 533 mm was observed in Koohrang. The rest of the country experienced rainfall accumulations between 0 and 50 mm. Winter precipitation across Iran as a whole was 25% below normal and 14% less than in 2006.

Springtime temperatures of up to 2°C above the long-term average were observed over most parts of Iran. The range of spring temperatures varied from 10°C in the northwest to 35°C in the southeast. Precipitation was above normal during spring 2007. Precipitation totals across the southeast (Sistan and Baluchestan Province) were 200% above the long-term mean (Fig. 6.36), primarily due to the impacts of Cyclone Gonu (see below), which first made landfall in Oman and caused severe damage there. Overall, wetter-than-average conditions prevailed over a majority of the country. The Hormozgan Province and some smaller areas received 50%–100% of normal rainfall totals. From a seasonal perspective, the amount of precipitation over Iran was 34% higher than normal.

Summer was cooler than average across much of Iran (up to 2°C below normal), although intraseasonal temperature variability was quite high. During typical summers, the southwest, northeast, and parts of

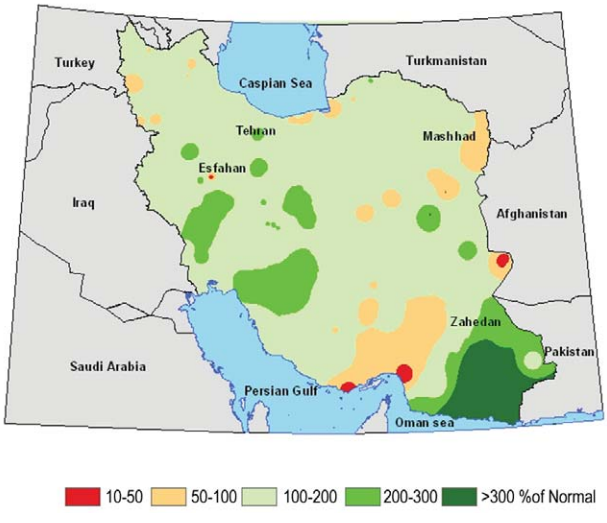

Fig. 6.36. Spring precipitation anomaly (percentage of normal) for Iran. [Source: IRIMO.]

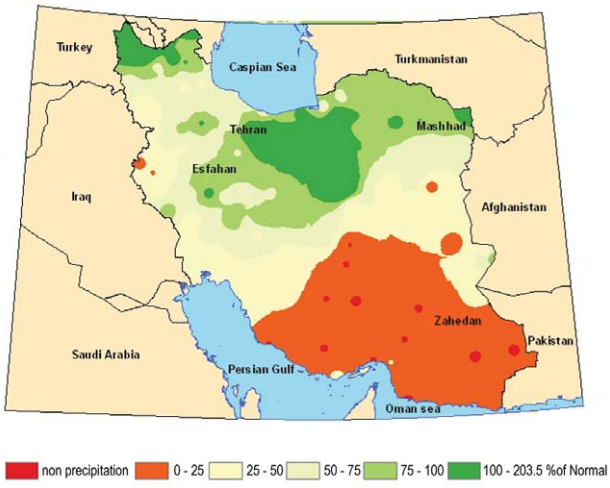

Fig. 6.37. Autumn precipitation anomaly (percentage of normal) for Iran. [Source: IRIMO.]

the south receive limited rainfall. In 2007, however, the Sistan and Baluchestan Province (which experienced drought conditions in association with dust and sand storms in recent summers) received 2 to 3 times their long-term average summer precipitation. Area-averaged precipitation over Iran was above normal in the summer of 2007, 83% higher than the long-term mean and the 2006 summer.

In autumn, warmer-than-average conditions persisted across most of the country; cooler-than-average conditions were limited to the east and northeast of the country. Autumn area-averaged precipitation was 39 mm, 43% less than normal and 52% less than autumn 2006. The southeast and southern regions received very little rainfall. Only parts of northern Iran received near-or above-normal rainfall in autumn (Fig. 6.37).

(c) *Rainfall Impact of Gonu on Iran*

Super Cyclonic Storm Gonu dropped heavy rainfall in early June near the eastern coastline of Iran, causing flooding and heavy damage. Chabahar, Jask, and other stations in Sistan and Baluchestan Province and Hormozgan Province normally receive less than 200 mm annually; rainfall associated with Gonu on 7 June alone brought as much as 60–120 mm to these areas (see Table 6.2). In the aftermath of this very atypical rain event, the southeastern part of Sistan and Baluchestan Province experienced severe problems associated with transportation, telecommunications, and access to drinking water.

(ii) Turkey—S. Sensoy

The annual surface temperature anomaly averaged over Turkey in 2007 was 0.92°C above the 1961–90 average. Only one station (Bingol in the eastern part of Turkey) had an annual temperature anomaly of less than –2.3°C. Generally the western three-fourths of the country had annual temperatures above the mean while the eastern parts were near average (Fig. 6.38). This continued a trend of positive temperature anomalies that have been reported since 1994 (except 1997). Temperatures in April and December were below average, while temperatures were above average in all other months. Significant positive temperature (maximum, minimum, and mean) anomalies ($p \leq 0.05$) occurred between May and October. Recent studies show that the number of summer days (defined as Tmax≥25°C) and tropical nights (Tmin≥20°C) have been increasing all over Turkey while cool nights (Tmin<10th percentile) and cool days (Tmax<10th percentile) have been decreasing (Sensoy et al. 2007; Zhang et al. 2005).

Due to Turkey's topography, rain clouds seldom penetrate the country's interior. Rain clouds deposit most of their water on the slopes facing the sea. For this reason, central Anatolia does not receive very much precipitation. While Rize receives 2,200-mm precipitation annually, Konya receives only 320 mm

Table 6.2. Total precipitation caused by Gonu for several Iranian stations (from Torbali et al. 2007).

Province	Station	Precipitation (mm)
Sistan and Baluchestan	Chanbahr	>160
Hormozgan	Jask	>160
Hormozgan	Bashgerd	>100
Hormozgan	BandarAbas	>11
Hormozgan	Minab and Roudan	>15
Kerman	Kerman	>50

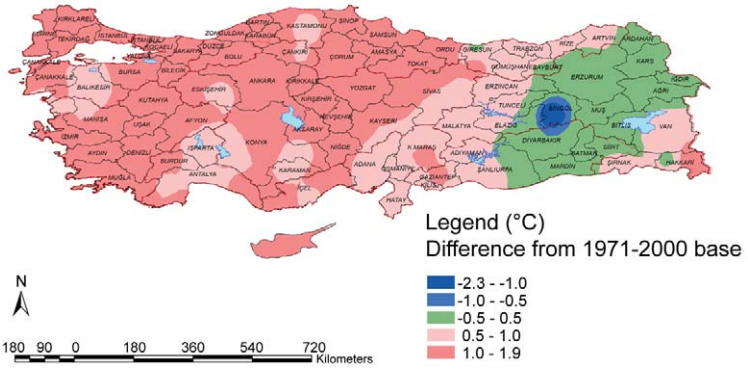

Fig. 6.38. Annual temperature anomalies (°C; 1971–2000 base period) for Turkey in 2007.

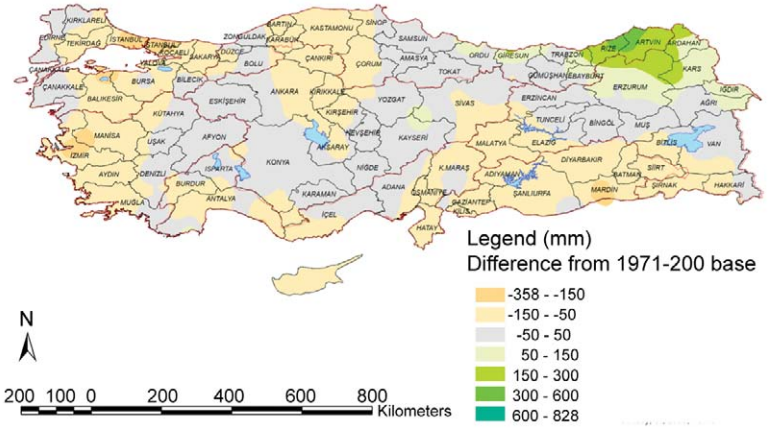

Fig. 6.39. Annual precipitation anomalies (mm; 1971–2000 base period) for Turkey in 2007.

(Arguez et al. 2007; Sensoy 2004). The average annual total precipitation for Turkey is 647.6 mm according to 1961–90 base period. The average total precipitation in 2007 was 618 mm, which was slightly below average. Only northeastern parts of the country (Ordu, Giresun, Rize, Artvin, Erzurum, Kars, Ardahan, and Iğdır) had precipitation surpluses. Western, southern, and north-central regions of Turkey suffered prolonged drought conditions during 2007 (Fig. 6.39). Approximately 60 stations out of 130 across Turkey received below-normal precipitation in 2007, while 20 were above average and about 50 stations were near normal.

g. Europe

1) Overview—A. Obregón, P. Bissolli, J. J. Kennedy, and D. E. Parker

Warmer-than-average conditions covered most of Europe, including the European Arctic, the North Atlantic, and the Middle East, in 2007. Surface air temperature anomalies were 1°–2°C above the 1961–90 average over most of the continent (Figs. 6.40 and 6.41). In the North Atlantic, the warmth was coincident with the continuing warm phase of the Atlantic multidecadal oscillation, which began in the mid-1990s. The annual average land surface temperature derived from the CRUTEM3 dataset (Brohan et al. 2006) was +1.23 ± 0.08°C for the European region between 35°–75°N and 10°W–30°E (Fig. 6.40) and is virtually certain to be one of the five

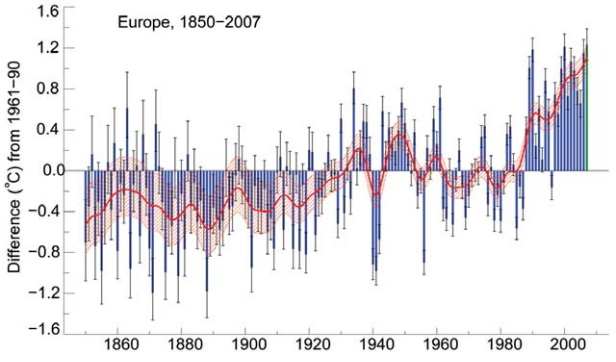

Fig. 6.40. Annual average land surface air temperature anomaly for Europe (35°–75°N, 10°W–30°E). The blue bars show the annual average values and the black error bars indicate the 95% confidence range of the uncertainties. The green bar is the annual value for 2007. The smooth red line shows the annual values after smoothing with a 21-point binomial filter. The hatched red area indicates the 95% confidence range on the smoothed values. Data are taken from the HadCRUT3 dataset (Brohan et al. 2006).

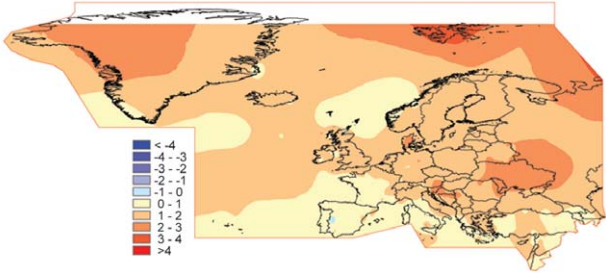

Fig. 6.41. Annual mean temperature anomalies in Europe and over the North Atlantic, 2007 (°C, relative to the 1961–90 average) based on CLIMAT and ship observations. [Source: Deutscher Wetterdienst (DWD).]

warmest years in the 1850–2007 series. The year 2007 was the warmest year on record in the Netherlands, Belgium, the Czech Republic, Denmark, and several countries in eastern and southeastern Europe.

Total precipitation for the year 2007 (Fig 6.42a; Rudolf et al. 2005) was below average in most of Mediterranean Europe. Northwest Italy, the south of France, and parts of Spain received locally less than 60% of the 1961–90 average. Near- or slightly above-average rainfall occurred throughout much of the rest of Europe. Exceptions included central parts of Sweden and Norway, western coastal areas of

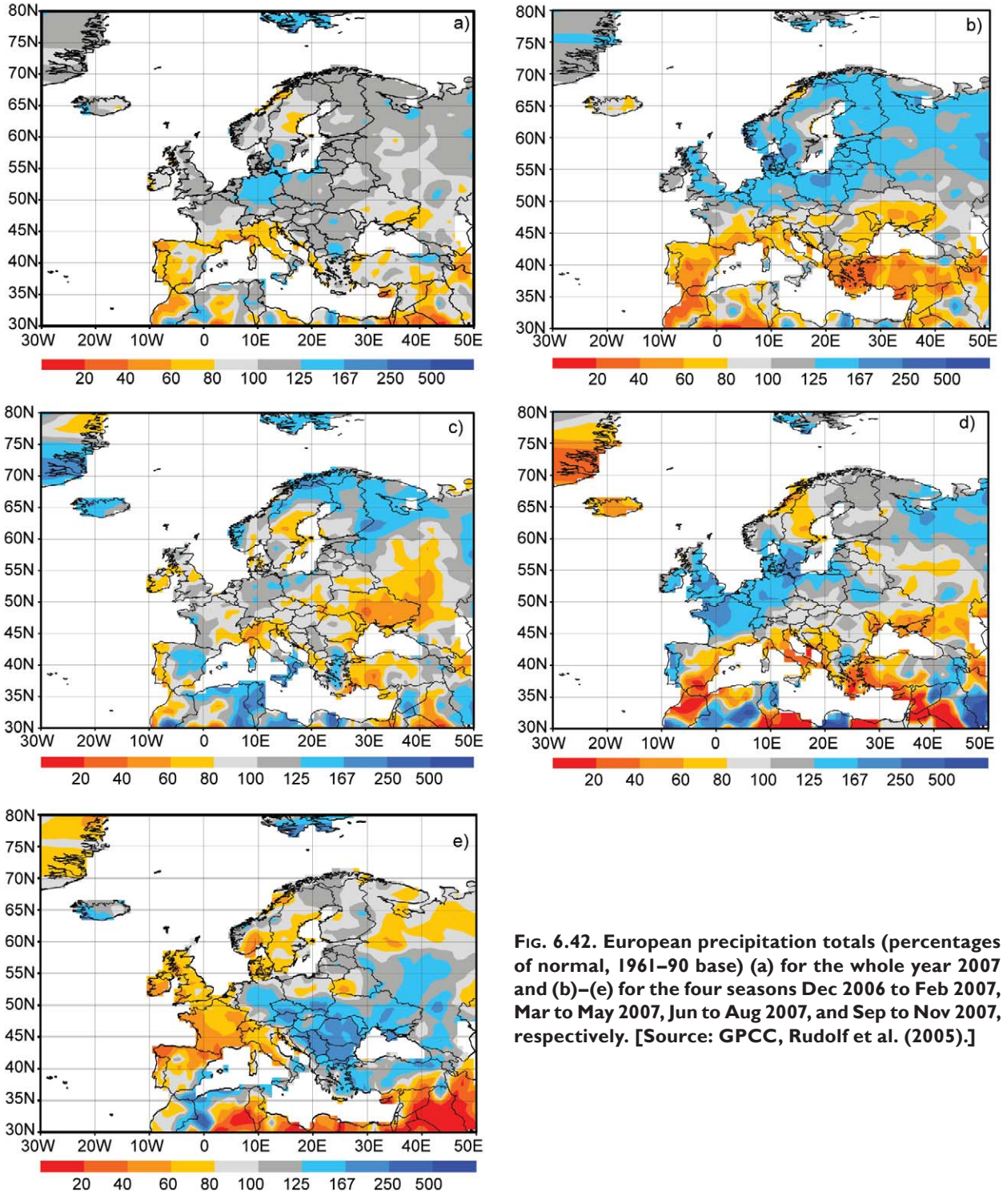

Fig. 6.42. European precipitation totals (percentages of normal, 1961–90 base) (a) for the whole year 2007 and (b)–(e) for the four seasons Dec 2006 to Feb 2007, Mar to May 2007, Jun to Aug 2007, and Sep to Nov 2007, respectively. [Source: GPCC, Rudolf et al. (2005).]

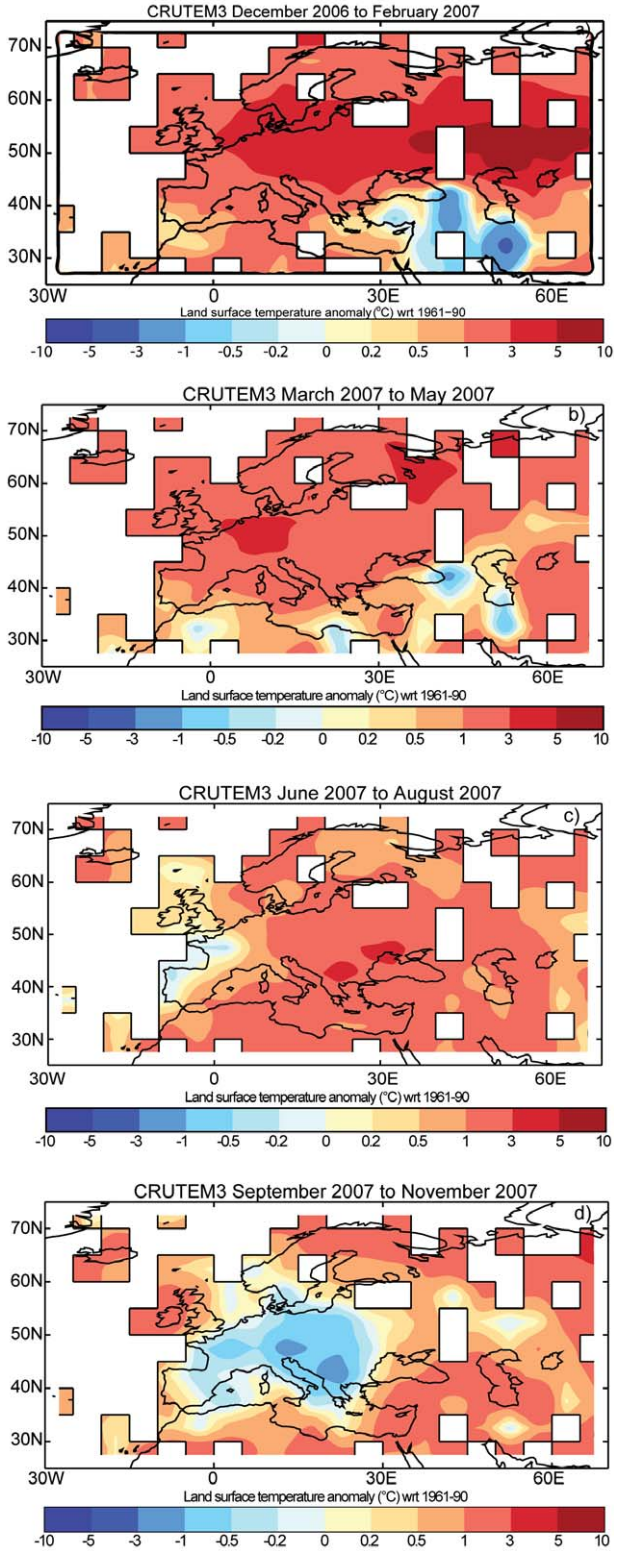

Fig. 6.43. European land surface air temperature anomalies (°C; relative to 1961–90) from the CRUTEM3 dataset (Brohan et al. 2006) for (a) Dec 2006 to Feb 2007, (b) Mar to May 2007, (c) Jun to Aug 2007, and (d) Sep to Nov 2007.

Scotland and Ireland, and some parts of southeastern Europe and the Middle East, where precipitation totals were less than 80% of the average. The highest rainfall anomalies, exceeding 125% of the long-term mean, occurred in northern areas of central Europe, southern Scandinavia, Svalbard, and a few locations in eastern Europe (Fig. 6.42a).

The beginning of 2007 was extraordinarily mild throughout Europe, leading to an early start to the growing season. Several countries experienced their mildest winter (December 2006–February 2007) on record. The winter in central and eastern Europe was unusually warm with anomalies exceeding +3°C (Fig. 6.43a). A recent study (Luterbacher et al. 2007) indicated that the winter of 2006–07 was extremely likely the warmest for more than 500 yr. In January, temperature anomalies reached more than +11°C in far eastern Europe. During the winter season, the 500-hPa height pattern featured positive anomalies (relative to 1971–2000) over southern Europe and negative anomalies over Fennoscandia (Fig. 6.44). This pattern was associated with an almost constant westerly flow that advected mild, marine air from the Atlantic Ocean into Europe. This contributed to exceptionally high surface temperatures in central and eastern Europe and positive rainfall anomalies throughout northern areas of the continent, while

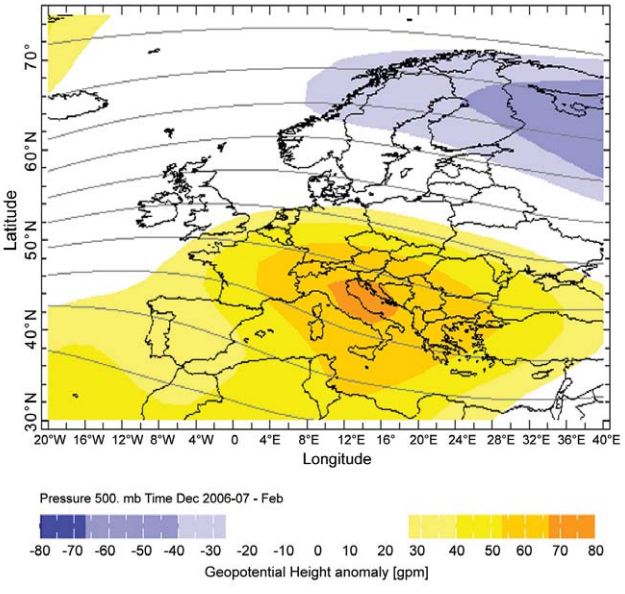

Fig. 6.44. Winter 2006–07 500-hPa geopotential height, seasonal averages (gray contours, contour interval 60 gpm) and anomalies (color-shaded areas, relative to 1971–2000, legend below). Based on NCEP reanalysis data. [Source: IRI Data Library, http://iridl.ldeo.columbia.edu/maproom/.Global/.Atm_Circulation/Seasonal_Height.html.]

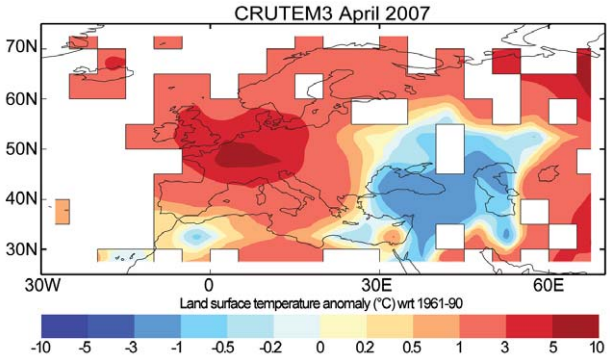

Fig. 6.45. European land surface air temperature anomalies (°C; relative to 1961–90) for Apr 2007 from the CRUTEM3 dataset (Brohan et al. 2006).

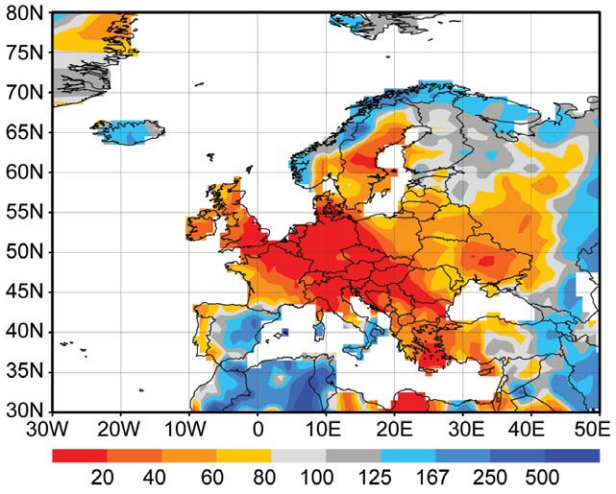

Fig. 6.46. European precipitation anomalies (percentages of normal, 1961–90 base) in Apr 2007. [Source: GPCC, Rudolf et al. (2005).]

southern Europe had a drier-than-average winter (Fig 6.42b). This was consistent with a strong positive phase of the winter NAO (+1.83) for the period December 2006 to March 2007 [based on pressures at Gibraltar and Stykkisholmur (Iceland); Jones et al. 1997]. Other contributing factors included significantly increased cloud cover during winter months and unusually warm SSTs in the North Sea, which developed as a result of the exceptional warmth of summer and autumn 2006. The estimated return period of the extremely high winter temperatures exceeded 100 yr in a large part of Europe.

Temperatures in spring also ranked among the highest ever recorded in several European countries (Fig. 6.43b). Temperature anomalies were unusually high in March (>7°C) with the largest departures over eastern Europe and in Svalbard. April was particularly warm in western and central Europe (>5°C, Fig. 6.45). It was the warmest April on record in some of these areas and many new records of daily mean temperatures were set. In contrast, April was colder than average in southeastern Europe and the Middle East. May was warmer than normal nearly everywhere in Europe, but the anomalies did not exceed +4°C. Spring was drier than average (Fig. 6.42c), and many countries in Europe had their driest April on record (Fig. 6.46), followed by an extremely wet May for all but eastern Europe.

In summer 2007, the jet stream was farther south than normal and low pressure systems were directed to central and southern areas of the United Kingdom, leading to heavy rainfall and severe flooding (Fig. 6.42d) as well as cooler-than-average temperatures (Fig. 6.43c) in much of northwestern Europe. In contrast, southeastern Europe was affected by two severe heat waves in the last weeks of June and July (Fig. 6.47) due to the stronger influence of warm, dry air masses from Africa. Several countries in this part of Europe had their warmest summer since records began, with many new records of daily maximum temperatures exceeding 40°C.

Despite record high SSTs in the North Atlantic, large parts of central Europe were colder than normal in autumn 2007 (September–November; Fig. 6.43d). In contrast, positive mean temperature anomalies in autumn were recorded across the United Kingdom, the southeast, and far northern Scandinavia. Precipitation totals above the long-term mean occurred in southeastern Europe, while western and northern Europe experienced drier-than-normal conditions (Fig. 6.42e). The year ended with a very mild December (anomalies up to +4°C) in the northern half of Europe and colder-than-normal temperatures in

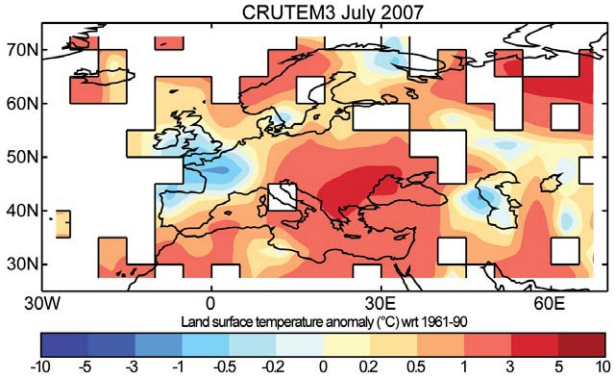

Fig. 6.47. European land surface air temperature anomalies (°C; relative to 1961–90) for Jul 2007 from the CRUTEM3 dataset (Brohan et al. 2006).

the southern half. December precipitation in Europe was mostly below or close to normal.

2) Central and western Europe—A. Obregón, P. Bissolli, J. J. Kennedy, D. E. Parker, S. Bader, M. Beswick, D. Buchel, M. Croci-Maspoli, H. Derka, F. Grooters, J. Hardwick, P. Hechler, E. Hotanova, P. Lennon, G. Müller-Westermeier, M. Perry, J. Prior, O. Svabik, F. Vinit, and J. Zimmer

(i) Temperature

The largest annual 2007 temperature anomalies occurred in Belgium (+2.0°C). The year 2007 was the warmest on record in the Netherlands, Belgium, Luxembourg, eastern Austria, the Czech Republic, and parts of Ireland. The United Kingdom and Germany had their second warmest year on record, and it was also one of the warmest years on record in Austria and the fourth warmest year in Switzerland. However, while the first half of 2007 was exceptionally warmer than normal in all western and central European countries, the last six months were close to or slightly below normal, except in northwestern Europe.

Winter and spring were record-breaking seasons in nearly all central and western European countries, with exceptional warmth in January and April (Fig. 6.45). The winter of 2006–07 was the warmest on record in most of central Europe and the second warmest in the United Kingdom. In the De Bilt, Netherlands, series that begins in 1706, January 2007 was the warmest ever with an average temperature of 6.6°C (3.3°C above average). It was also the warmest January on record in Germany (4.6°C above average), Luxemburg, France, the Alpine region, and the Low Countries. The mean January temperature in Belgium was 7.2°C (+5°C), and monthly anomalies in Austria exceeded +6°C in the east. On the night of 18–19 January, temperatures rose to 20°C in eastern Austria; conditions that are more typical of summer. It was the second warmest January in the United Kingdom as a whole since 1914. February was generally mild but a short period of very cold weather affected northwestern Europe on 5–8 February.

Spring 2007 was the warmest on record in Germany, Switzerland, the Netherlands, Belgium, and France. April was particularly warm with many new temperature and sunshine records established throughout the region. In Germany, which had more than twice the average number of sunshine hours, the monthly mean temperature in April was 11.6°C (+4.2°C). Monthly anomalies of +5.5°C were widespread in Switzerland with larger values (+7.5°C) at higher elevations. In Belgium, the April temperature was 5.8°C above the 1961–90 average of 8.5°C, exceeding the previous record set in 1987 by more than 2°C. The highest anomalies in France, southern England and parts of eastern Scotland were also greater than +5°C. April was also the warmest April in the 349-yr CET (Parker et al. 1992) series (11.2°C, 3.3°C above average).

Most areas in western and central Europe recorded their first negative monthly temperature anomalies of 2007 in July. In contrast, a heat wave affected much of southeast central Europe in mid-July and new daily maximum temperature records were established in many stations in Austria.

(ii) Precipitation

Precipitation totals in 2007 were generally close to or above average in most of central and western Europe (Fig. 6.42a), but southeastern parts of Switzerland received about 75% of normal precipitation and the year 2007 was one of the 10 driest years in Lugano, Switzerland, where regular measurements started in 1864.

January was very wet in north-central Europe and in southwestern and northwestern Austria (up to more than 250% of the normal). A short, but intense, snow storm affected central and western Europe on 22–24 January. Snow depths of 20–30 cm were registered even in the lowlands of southern Germany and France. Another period of heavy snowfall occurred on 19–24 March in the Alpine region due to the formation of a strong low over northern Italy. Fifty centimeters of snow fell within a few hours in southern Austria. More snow fell in this short period in large parts of Austria than in the whole of the preceding winter. Parts of northern Switzerland had almost 30 cm of snow on 22–23 March, while some areas of the northern Alps received 1 m.

April was exceptionally dry throughout the region (Fig. 6.46) due to a blocking high over western Europe. In the England–Wales precipitation series (1766–2007, Alexander and Jones 2001), only 10 mm of rain (15% of the 1961–90 normal) was recorded, the lowest since 1938. Many stations over southeastern England and East Anglia received less than 3 mm (5%–6% of the normal). Some eastern areas of Ireland also had April totals of less than 10 mm. In the Netherlands, little or no precipitation fell during the period from 22 March to 6 May, which was the driest in at least 100 yr. In Uccle, Belgium, no rainfall occurred during the 36 days from 31 March to 5 May. It was the longest period without rainfall on the whole record (for all seasons) since 1833. Only 2 mm of precipitation fell in the city of Luxemburg during the month of April. Germany experienced its driest April since records began in 1901 with a country-wide average

of 4 mm (7% of the 1961–90 normal). In Austria and Switzerland, monthly precipitation amounts were generally below 30% of the normal with some areas receiving no rainfall.

In stark contrast, May 2007 was the wettest May on record in Germany since measurements began in 1901 (126 mm; 177% of average). In northern France, 200% of normal monthly precipitation fell in many places during summer, and Zurich, Switzerland, had its fourth wettest summer since measurements began in 1864. In England and Wales the May–July period was the wettest (406 mm) since records began in 1766, breaking the previous record of 349 mm set in 1789. In June and July (Fig. 6.48) many parts of the United Kingdom were affected by severe flooding. Some stations in northeast England reported totals exceeding 500% of the June average, and the south Midlands and Wales had 300%–400% of the July average. In Ireland, Kilkenny and Dublin Casement Aerodrome had their wettest summer since rainfall records began in 1957 and 1954, respectively. July 2007 was the second wettest July (behind 1942) in the Netherlands since records began in 1906 (155 mm; 200% of normal). Switzerland and Austria experienced unusually heavy thunderstorms in summer with hailstones of up to tennis ball size.

Heavy rains from 5 to 7 September in Austria along the main ridge of the Alps caused flooding. Rainfall rates of up to 245 mm in 72 h were recorded. Autumn precipitation totals exceeded 200% of normal in eastern Austria. The beginning of winter 2007/08 brought early snow cover to the Alps. During November, Switzerland experienced its heaviest snowfall in more than 50 yr. In Davos, 62 cm of snow fell in 24 h, setting a new record.

(iii) Notable events

Winter storm "Kyrill" hit the Irish and British coasts on 17 January, then made landfall on the coasts of Germany and the Netherlands on 18 January and moved toward Poland and the Baltic Sea (also affecting the Czech Republic along the way). Precipitation amounts of 80–90 mm fell on the Harz Mountains in Germany. A gust of 56 m s^{-1} was recorded at Wendelstein (southern Germany), and gusts of more than 38 m s^{-1} occurred in the lowlands. A rare winter tornado was observed in Wittenberg, Germany, near the cold front. The United Kingdom had its strongest measured winds since 1990. In Ireland, a gust of 41 m s^{-1} was measured at Dublin Airport on 18 January, the highest at the station since it opened in 1941.

On 8–9 November, a heavy winter storm caused a storm surge in the North Sea. The coastlines of the

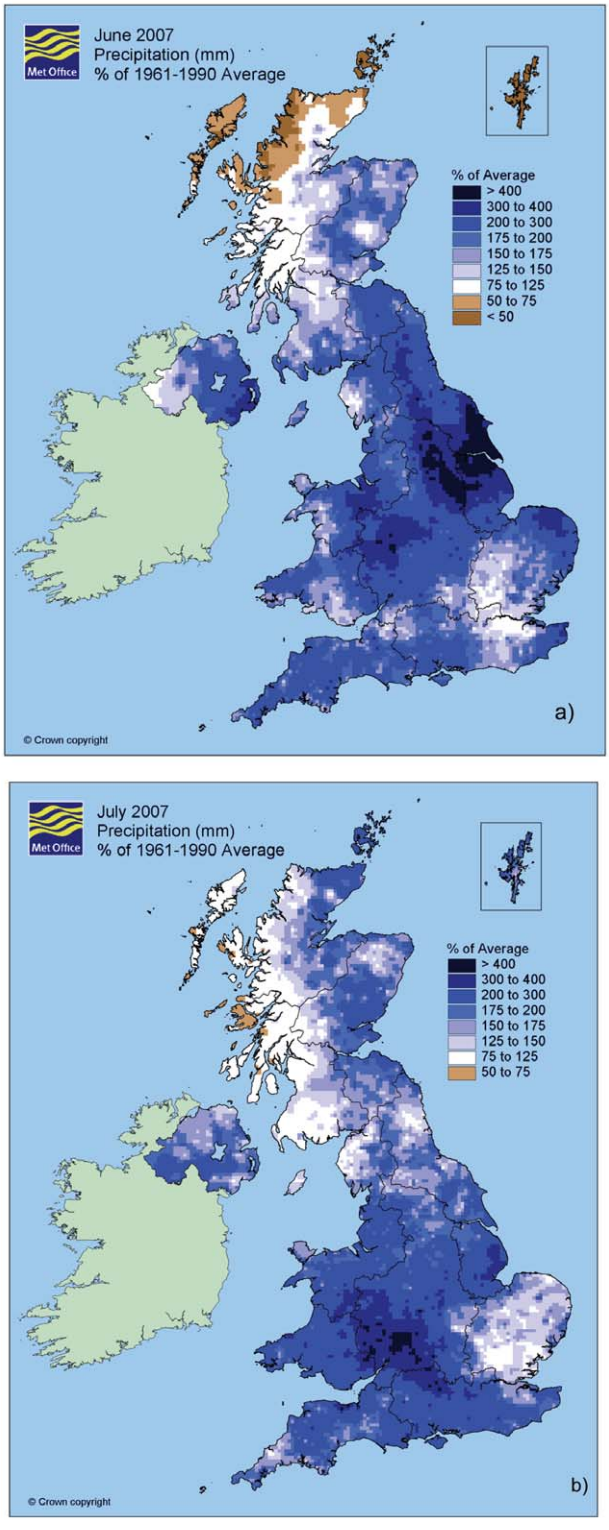

Fig. 6.48. Precipitation anomalies (percentages of normal, 1961–90 base) in the United Kingdom during Jun and Jul 2007. [Source: Met Office.]

United Kingdom, the Netherlands, Belgium, and Germany were most affected. Damage was relatively minor because the flooding did not coincide with high tide. However, at the East Anglian coast, the storm surge was one of the highest since 1953.

On 9 December, just after midnight, a slow-moving depression (966-hPa central pressure) brought stormy conditions and an exceptionally high wave of over 17 m to the west coast of Ireland. It was the highest wave ever measured by the Irish buoy network.

3) The Nordic countries—C. Achberger, D. Chen, J. Cappelen, S. Hellström, K. A. Iden, M. Jonsson, and S. Saku

(i) Temperature

Annual temperatures over the Nordic region (Sweden, Norway, Denmark, Finland, and Iceland) were above the 1961–90 long-term mean in 2007 (Fig. 6.41). Denmark had its warmest and sunniest year on record, 1.8°C above the 1961–90 mean and 0.1°C above the 2006 annual mean. Since 1870, Danish temperatures (low-pass filtered) have increased by 1.5°C. In addition, the number of sunshine hours (low-pass filtered) in Denmark has increased considerably since 1980. Annual mean temperatures in Sweden exceeded the long-term mean by 1.5°–2°C, making 2007 the seventh warmest year. In Norway the annual temperature was 1.3°C above normal, making 2007 the 10th warmest year since 1900. Furthermore, on the Svalbard Archipelago, annual mean temperatures were an extremely high –2.5°C, which is 4.2°C above normal. Finland reported annual mean temperatures ranging from 1.0°–1.6°C above the 1971–90 long-term mean, with the strongest positive anomalies in northern areas of the country. For Iceland, the spell of warm years dominating its climate since the turn of the century continued in 2007.

The positive annual temperature deviations over the Nordic region are to a considerable extent explained by the mild winter December 2006 to February 2007 (Fig. 6.43a). Around Svalbard, winter temperatures were 9°–10°C above normal. For the Scandinavian countries, winter temperature anomalies ranged between 1° and 4°C, with the highest anomalies over southern Sweden and Denmark. These anomalies followed the extremely warm autumn of 2006. On the Swedish west coast, the first frost of the season was reported as late as 22 January, which is the latest date for a first frost ever reported by a Swedish station. Furthermore, the Finnish winter was characterized by a mild January (2°–3°C above normal). Although February was generally colder than normal in Finland, spring started at the beginning of March, about one month earlier than usual. Spring was generally warm throughout the Nordic region (Fig. 6.43b). Due to the mild winter conditions, the Baltic Sea ice season started very late (Vainio et al. 2008). Only near the end of January did ice begin to form in all sea areas. The largest ice extent was reached on 23 February, and two months later the Baltic Sea was ice free.

On average, summer temperatures over the Nordic region were 0.5°–2.0°C above the long-term mean in 2007 (Fig. 6.43c). In Denmark and Sweden, summer started with a very warm and sunny spell in the first half of June, but the rest of the summer was dominated by unsettled weather. Summer temperatures in Norway were 1°C above normal, making summer 2007 the 19th warmest since 1900. Large positive deviations from the long-term mean occurred locally in the northernmost part of the Nordic region. At the airport of Svalbard, the summer mean temperature was more than 2°C higher than normal and resulted in the warmest summer since the start of measurements in 1912. In many parts of Finland, the spring season was unusually warm (mean spring temperature ranked as the fifth warmest since 1900), while unsettled weather dominated the Finnish summer. Still, mean summer temperatures were 0.5°–1.5°C above normal there, mainly due to unusually high temperatures in early August.

December 2007 was the warmest December in more than 70 yr locally in the northernmost parts of Norway and Sweden. An extensive high over southern Scandinavia maintained strong and persistent westerly winds that transported warm and humid air masses into northern Fennoscandia.

(ii) Precipitation

On average, annual precipitation over the Nordic region in 2007 was close to or slightly above normal, but large deviations from the long-term mean occurred in some regions and seasons, especially during the summer (Fig. 6.42d). In Iceland, an extended period of warm and dry weather in June and July caused local water shortages and the southeastern region of the country had its driest summer since 1873. This unusual dry spell was followed by an exceptional wet period beginning in the second half of August. The rest of the year was the wettest ever registered in southern and western Iceland. Annual precipitation in Denmark was 155 mm above the normal amount of 712 mm. Much of the annual surplus was due to an extraordinarily wet summer, which ranked third since 1874. Station records in Denmark show that annual precipitation (low-pass filtered) has increased approximately 100 mm since measurements started in 1870.

Annual precipitation for Sweden as a whole was not exceptional, but large regional deviations from the long-term mean occurred. In southern Sweden, several stations reported the rainiest summer since records began, and some records for monthly and annual precipitation were broken. Norwegian annual precipitation was about 15% above normal, making 2007 the fifth wettest year since 1900. Considerable positive deviations occurred in the southern part of Norway's west coast where annual precipitation in 2007 exceeded the long-term mean by 25%–50%. However, central parts of the west coast had less than 80% of normal rainfall in 2007 (Fig. 6.42a). In contrast to Sweden and Denmark, the wettest seasons (relative to normals) in Norway were winter and spring with seasonal precipitation amounts 40%–50% above the normal value. Annual precipitation amounts in Finland were close to or slightly above normal. However, large regional precipitation deviations occurred during the summer season when the southeastern part of the country received 383 mm, 50% more than usual. Due to higher-than-normal winter temperatures, only the northern and eastern parts of Finland had persistent snow cover.

(iii) Atmospheric circulation

Large-scale atmospheric circulation over northern Europe and the North Atlantic control the regional temperature and precipitation patterns. Using Lamb's (1950) synoptic weather typing, the impact of the large-scale atmospheric circulation on the surface weather conditions in this region has been estimated (e.g., Chen 2000). In 2007, the annual frequencies of C days, days with mixed directional and cyclonic flow conditions (CNW, CW, and CE), and W and NW days were higher than the 1961–90 mean. These conditions contributed to the warmer-than-normal conditions in 2007, especially in winter when the frequency of A days, often associated with cold weather conditions, were about 40% lower than normal. In the summer season, C days as well as days with mixed directional and cyclonic flow conditions occurred more frequently at the expense of A days. The seasonal flow conditions were thus consistent with the warmer weather in winter and wetter conditions prevailing in summer in extended parts of Fennoscandia.

(iv) Notable events

On 14 January a severe winter storm named "Per" brought unusually strong winds to coastal areas of Sweden and Norway. In late August, the eastern coast of Sweden was hit by a storm with winds as high as 35 m s^{-1} at the station of Örskär. The storm was the first in August in Swedish coastal areas since 1975. Kiruna, the northernmost city of Sweden, reported a snow depth of 2 cm on 30 August, the first measurable snow depth in August at any Swedish station since 1994. December was very stormy in Iceland, causing interrupted air and land communication on several occasions.

4) Iberia—R. M. Trigo, C. C. Gouveia, R. García-Herrera, A. Obregón, P. Bissolli, J. J. Kennedy, D. E. Parker, and O. Pires

(i) Temperature

On the Iberian Peninsula, warmer-than-average seasonal temperatures occurred in winter (+0.75°C), spring (+0.63°C), and fall (+0.19°C). Only the summer season was cooler than average, −0.19°C below the 1971–2000 mean. For the year as a whole the eastern half of Iberia was generally warmer than average while the western half was near average. The annual temperature averaged over the Spanish mainland and the Balearic Islands was 0.4°C above the 1971–2000 mean. The annual temperature was also above average for Portugal (0.2°C above the 1961–90 mean).

February was a particularly warm month throughout Iberia, ranking as the fourth warmest in Spain. During spring, slight negative anomalies in the 500-hPa geopotential height over northern Africa (not shown) reflected the passage of several low pressure systems that induced relatively high precipitation values over Spain and northern Africa in spring (Fig. 6.49, upper right). Summer was characterized by colder-than-normal temperatures and negative 500-hPa geopotential height anomalies in northern Iberia and adjacent Atlantic areas. These anomalies were associated with summer storms that affected the western and northern sectors of Iberia, particularly in July and August. By contrast, positive 500-hPa geopotential height anomalies were present over the Atlantic region in autumn with a large region of maximum values (above 100 gpm) located west of the British Islands. This pattern contributed to a highly asymmetric 850-hPa temperature anomaly field over Iberia. While the western sector was considerably warmer than normal, the eastern provinces were under the influence of cold air advection.

(ii) Precipitation

Drier-than-average conditions affected the Iberian Peninsula during the 2006–07 winter (DJF), with most of the central, southern, and eastern sectors of Iberia receiving less than 60% of 1961–90 average precipitation (Fig. 6.49, upper left). The winter dryness was consistent with positive SLP anomalies over southwestern Europe and northern Africa, a

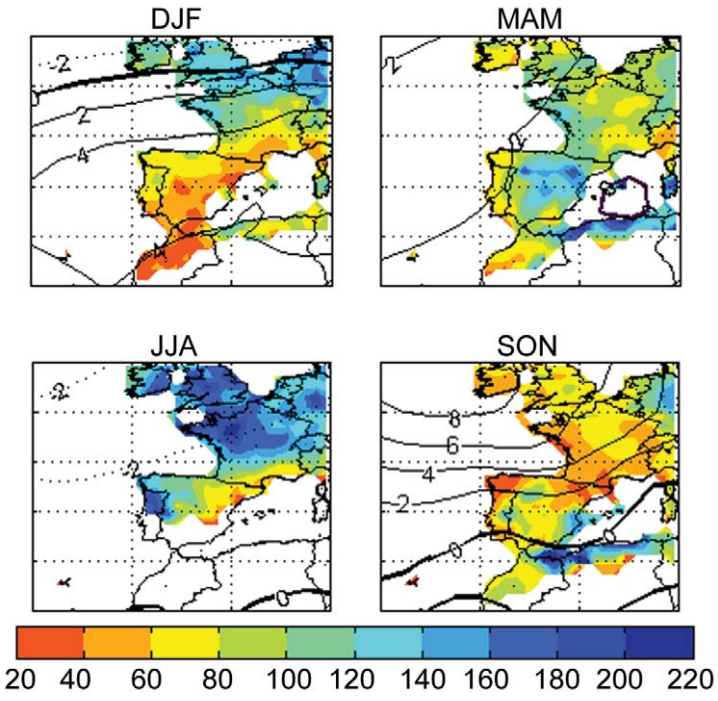

Fig. 6.49. Seasonal anomalies of sea level pressure (contour, hPa) using data from NCAR–NCEP reanalyses. The colored shading represents percentage of accumulated seasonal precipitation compared with climatology using the monthly GPCC precipitation dataset. All climatological averages are computed for the 1961–90 period. Only areas with seasonal rainfall normals above 30 mm are shown. Negative anomalies are dotted while the zero line is bold.

feature that has been shown to limit the progression of Atlantic low pressure systems into southern Europe (Garcia-Herrera et al. 2007). Precipitation was generally above average across Spain and below average in Portugal during spring (Fig. 6.49, upper right). During summer, precipitation totals were above (below) normal in western (eastern) Iberia (Fig. 6.49, lower left). Positive SLP anomalies were predominant during autumn over western Europe, promoting widespread dry conditions over southwestern Europe, with several sectors of northwestern and northeastern Iberia receiving less than 40% of the seasonal average (Fig. 6.49, lower right). December was extraordinarily dry in the northwest with precipitation in most of Portugal and adjacent Spanish regions below the 10th percentile of the 1961–90 distribution. Most of Portugal and also parts of Spain received less than 20% of the normal precipitation.

Summer is a climatologically dry time of year on the Iberian Peninsula. Despite a wetter-than-average summer in western Iberia, the absolute precipitation totals were relatively low. By contrast, the spring and fall seasons are climatologically wetter seasons, and they are the wettest seasons of the year in northern and eastern sectors of Iberia (Trigo and Palutikof 2001). With an anomalously dry winter, spring, and autumn, Iberia received only 75% of annual average rainfall leading to moderate-to-severe drought in several highly populated coastal regions. This was the case for western Iberia, including Portugal and Galicia (Espirito-Santo et al. 2008), as well as Spain's northeastern province of Catalonia. Vigo received only 1038 mm of rainfall (54.4% of the 1971–2000 average), which is the lowest since observations began in 1951. Santiago de Compostela received 58.7% of the annual average precipitation, ranking 2007 as the third driest year since 1944. Overall, Spain received only 80% of the 1971–2000 mean rainfall in 2007. In Portugal, many parts of the country received rainfall amounts below 80%, and for the country as a whole it was the second driest year (behind 2005) since 1931.

(iii) Notable events

On 28 January a rare snowfall occurred in coastal and low altitude regions of Portugal for the second consecutive year. On 21 September, Andalucía (southern Spain) was hit by thunderstorms with severe hail and rainfall producing floods and crop damage. The region around Valencia was also affected by torrential rainfall on 11–12 October. Two-day precipitation totals exceeded 400 mm in the mountainous regions of the Marina Alta Province, more than 50% of the annual average. In Valencia, 170 mm was registered on 11 October alone, making this the second wettest day since records began.

April was exceptionally warm in northern Spain, and in several locations in northeastern parts of the country it was the warmest April on record. A new national record for April daily maximum temperature was set in Oviedo (28.3°C). The month of May was extremely hot for the entire Mediterranean coastal region, with several stations breaking monthly mean temperature (Murcia and Alicante) and monthly maximum temperature records (Valencia, Murcia, Alicante, and Reus). June was also extremely hot throughout the Mediterranean coast and the nearby Balearic Islands, with monthly records broken at several stations in Catalonia and Valencia Provinces. In contrast, for the first time since 1997, there was not a single recorded heat wave (defined as five consecutive

days that exceed the average maximum temperature by 5°C based on the 1961–90 base period) during the summer in Portugal. New records for the lowest mean temperature in November were set in Murcia and Alicante. A new record for the lowest all-time daily minimum temperature in Portugal was set on 18 November in Mirandela (–10.9°C).

5) Mediterranean, Eastern, and Southeastern Europe—A. Obregón, P. Bissolli, J. J. Kennedy, D. E. Parker, A. Busuioc, T. Cegnar, T. Colombo, S. Djordjevic, P. Hechler, J. Karkozas, Z. Katusin, M. Kulbida, I. Lukac, and V. Pavan

(i) Temperature

Parts of Romania and Bulgaria exceeded the 98th percentile of annual temperature in 2007, and anomalies exceeded +2°C in Ukraine, Moldova, and eastern parts of Romania (Fig. 6.41). The winter was extraordinarily warm in the Baltic States, mainly due to an exceptionally warm January (+6.3°C averaged over Lithuania; +4.6°C in Tallinn, Estonia). Romania, Croatia, and Slovenia had their warmest winters on record. In Romania, it was the warmest January on record with local anomalies up to +9°C. There was a record-breaking warm January in Italy, and farmers were surprised by the early flowering of many species of fruit trees. A record January high maximum temperature of 21.3°C was recorded on 21 January in Bologna, where records began in 1948. This warmth was associated with a strong alpine foehn event during the passage of the storm "Kyrill" over central Europe (see section 6g2 above).

In Slovenia and parts of Croatia spring season anomalies exceeded +3°C making it the warmest spring in many regions. Italy and Slovenia, in common with other areas of Europe, experienced their warmest April ever (Fig. 6.45). During summer, exceptional warmth was widespread, with mean air temperatures exceeding the 90th percentile. In northeast Romania, Moldova, and southern Ukraine, departures from normal reached or exceeded +3°C. Extreme heat waves affected much of southeastern Europe in the last 10 days of June and during mid- to late July with many places registering their highest recorded maximum temperatures (Table 6.3).

The July heat wave contributed to an exceptionally warm month in southeastern Europe (Fig. 6.47). The largest anomalies were in Bulgaria (3.7°C in Sofia). The July average maximum temperature for Italy was 34.7°C, the warmest July in at least 30 yr. In Serbia and adjacent countries, temperatures in July were above the 98th percentile of the 1961–90 distribution.

During a warm spell at the end of August, the daily maximum temperature in Bosnia and Herzegovina (Mostar, 43.1°C) exceeded the temperature record set during the July heat wave. August anomalies between 2° and 3°C occurred in the Baltic States, western parts of Belarus and the Ukraine, and eastern Hungary, and anomalies exceeded +3°C in eastern parts of Belarus and Ukraine. In December, temperature anomalies exceeded +5°C in Vilnius and Tallinn, while in Romania, local monthly anomalies were as low as –4°C.

(ii) Precipitation

The northern Balkan Peninsula experienced above-average precipitation in 2007 with the largest anomalies in Romania, Serbia, and Bulgaria (e.g., 148% of average fell in Sofia). In contrast, in the Italian region of Emilia-Romagna (near Bologna), the lowest annual precipitation total since 1925 was recorded, with less than two-thirds of the normal.

Table 6.3. Record temperatures reported in Jun and Jul in southeast Europe.

Location	Date	Temperature
Froggia/Amendola, Southern Italy	25 Jun	47.0°C
Athens, Greece	26 Jun	46.2°C
Negotin, Serbia	26 Jun	41.2°C
Kiskunhalas, Hungary	20 Jul	41.9°C
Hurbanovo, Slovakia	20 Jul	40.3°C
Slobodzya, Moldova	21 Jul	41.9°C
Odessa, Ukraine	23 Jul	39.3°C
Chisinau, Moldova	23 Jul	39.4°C
Prizren, Kosovo	24 Jul	42.0°C
Demir Kapija, Macedonia	24 Jul	45.7°C
Smederevska Palanka, Serbia	24 Jul	44.9°C

Owing to a lack of snow in the Alps and the Apennines and the dry spring, the water level of the Po River reached its lowest level on record on 23 April. It was also a very dry April on the Balkan Peninsula and in Slovenia (Fig. 6.46). In contrast, Sicily had record precipitation during March and was also extraordinarily wet in April and June. Summer brought drought to most of southeastern Europe. There was no rainfall in Athens from July until September. Southern Italy was also affected by severe drought in July and August with water deficits less than 60% of normal. However, the Baltic States had a very wet July, with more than 200% of the average rainfall in Lithuania. Autumn was extraordinarily wet throughout most of the Ukraine, Bulgaria, the Balkan Peninsula, and southern Italy (Fig. 6.42e). Sofia received more than double the average amount of rainfall in every month from August to November.

(iii) Notable events

Intense thunderstorms affected northern Italy in the summer. One west of Bologna on 12 June had a peak rainfall rate of 159 mm h^{-1} and a total accumulation of 59 mm. The extreme heat waves and severe drought in June and July led to massive forest fires across the Balkan Peninsula, Serbia, Croatia, Romania, and Bulgaria. From late June through early September, over 3,000 fires were reported in Greece, causing 79 fatalities and destroying more than 2,700 km^2 of forest and farmland.

6) Middle East—A. Obregón, P. Bissolli, J. J. Kennedy, D. E. Parker, M. Demircan, A. Hovsepyan, H. Ozcan, and S. Pashiardis

(i) Temperature

Winter temperature anomalies exceeded +4°C in western Kazakhstan, but minimum temperatures in January in parts of the Ararat Valley (Armenia) reached record lows near –25°C. Temperatures in spring were generally above average, but significant cold conditions occurred in March (below the 10th percentile) in eastern Turkey and northern Syria. Temperatures in Lebanon, Cyprus, and most of Syria exceeded the 90th percentile during the summer months. Heat waves with temperatures above 40°C on 24–29 June and 24–31 July contributed to several large forest fires. September and October was 2.0°–2.5°C warmer than normal in Armenia, owing to two strong heat waves on 4–9 September and 14–17 October.

(ii) Precipitation

Parts of Cyprus and Azerbaijan received less than 50% of average annual rainfall, but 125%–150% of normal precipitation fell in northeastern parts of Turkey. Winter and spring were particularly wet in western Kazakhstan, while Azerbaijan was drier than normal. In May, precipitation in Georgia and Azerbaijan was below the 10th percentile. In summer, parts of Syria, Lebanon, and Cyprus received less than 50% of the normal rainfall, while Armenia was unusually wet, especially in July. Autumn was very dry in Cyprus (below 25%), while November precipitation exceeded the 90th percentile in Georgia. It was also very wet in Armenia, 200%–270% of normal precipitation. A dry December followed with only 20% of the normal precipitation in the lowlands of Armenia and in the Ararat Valley.

(iii) Notable events

A hailstorm with hailstones of 25 mm in diameter affected central Armenia on 7 June. Tornadoes and severe hailstorms also affected Cyprus in March, May, and in the autumn. On 1 July and 5 December, heavy rainfall with flooding occurred in Cyprus.

h. Oceania

1) Australia—A. B. Watkins and B. C. Trewin

Large parts of Australia were in the grip of both long- and short-term drought leading into 2007. Early trends away from El Niño conditions in the equatorial Pacific led to an Australian area-average rainfall for 2007 of 497 mm, ranking 30th wettest out of the 108 yr of record. The mean for the 1961–90 standard reference period is 472 mm. However, in line with the trends observed over the past 50 yr, the greatest rainfall totals were in Australia's sparsely inhabited northwest. In the densely populated and major agricultural regions, rainfall was generally average to below average. For much of the agricultural sector, promising autumn rains were countered by a severe short-term drought in the crucial late winter and early spring period, greatly reducing crop and pasture growth.

While most areas were generally not as severely dry as they were during 2006, the recovery was only partial and water resources remained very low in most areas. Water demand was high, driven by warm daytime temperatures. Maximum temperatures were the fifth warmest on record,[6] some +0.7°C above

[6] High-quality annual Australia-wide temperature anomalies have been calculated for all years since 1910 (Della-Marta et al. 2004), while high-quality monthly anomalies are available from 1950. High-quality nationwide rainfall measurements commenced in 1900 (Lavery et al. 1997). Anomalies are calculated with respect to the 1961–90 average.

the mean, with just over 37% of the continent in the warmest decile. In terms of mean temperatures it was Australia's sixth warmest year since high quality Australia-wide records commenced in 1950, 0.7°C above the 1961–90 mean.

(i) Temperature

Many of the regions that experienced acute dry conditions during the year, including large areas under long-term drought conditions, were also warmer than average during 2007. Maximum temperatures (Fig. 6.50) over much of the southern half of the continent were at least 1.0°C above normal, with large portions of southern Australia more than 1.5°C above the 1961–90 mean. In decile terms, much of southern Australia was in the highest 10% of recorded temperatures (decile 10), with large parts of southern South Australia and virtually all of Victoria warmest on record. This was reflected in the statewide values. Victorian maximum temperatures were the hottest on record, 1.4°C above the 1961–90 mean, and only the second time (after 1914) that the anomaly surpassed +1°C. Southern Australia as a whole was third warmest on record, only fractionally cooler than 2005. The warmest year remains 2002. For Australia as a whole, the average maximum temperature was the fifth warmest on record behind 2005 (warmest), 2001, 1980, and 1991. Maximum temperatures in 2007 averaged 0.7°C above the mean, with just over 37% of the continent in the warmest decile, and 0% in the coolest decile.

Minimum temperatures were generally 0.5°–1.5°C above average for much of southern, and particularly southeastern, Australia, resulting in southern Australia's warmest nights on record (+0.8°C), marginally above the previous record set in 1973. Conditions were up to 1°C below average in some areas of the north; however, when summed over all of northern Australia, minimum temperatures were still, on average, +0.5°C above average. For Australia as a whole, the average minimum temperature was fifth warmest, 0.6°C above the average. Only 2% of the continent experienced temperatures in the bottom three deciles, yet over 60% of the continent was in the top three deciles.

With warmer-than-average days and nights in the southeastern area of the continent, the states of South Australia (+1.1°C), Victoria (+1.2°C) and New South Wales (+1.1°C), as well as the agriculturally vital Murray–Darling Basin (+1.1°C) region, all recorded their warmest annual mean temperatures on record, while Tasmania (+0.8°C) was second warmest.

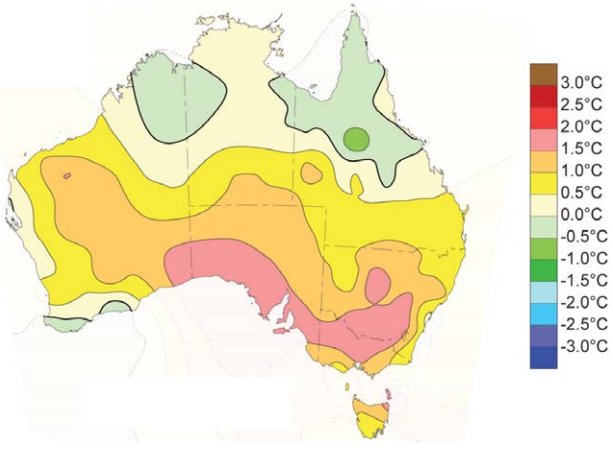

Fig. 6.50. Australian maximum temperature anomalies (°C; 1961–90 base period) for 2007.

(ii) Precipitation

In contrast to the previous year, 2007 started with a wetter-than-average month for much of the continent. Rainfall on just two days (21–22 January) in the South Australian towns of Bedourie (206 mm), Boulia (130 mm), and Hawker (176 mm) were greater than the totals they recorded for the entire 2006 calendar year (54, 95, and 156 mm, respectively). Furthermore, wet months in March, May, and for many areas along the east coast and north, June, heightened expectations of a wetter-than-average year.

However, July–September was particularly dry in the eastern half of the continent, and it was not until November, and the final breakdown of cool conditions to Australia's north and the emergence of La Niña in the equatorial Pacific, that rain returned to much of the continent. December rains again brought flooding in some areas of northern inland New South Wales, with 48-h totals approaching 200 mm.

The result of this varying pattern—from very dry to generally wet months—meant that Australia-wide, the year as a whole was not exceptional (Fig. 6.51). Australian rainfall (497 mm) was 30th wettest out of the 108 yr of record, only 25 mm above the normal 472 mm. In total, 43% of the continent experienced rainfall totals above the 66th percentile for the year. In contrast, only 2.3% of the continent was in the lowest 10% of recorded totals for the year, in stark contrast to 2006 when over 18% of the continent experienced similar conditions.

Despite some rain, long-term dry conditions persisted in southeast Queensland, southwest western Australia, and the southeast corner of the continent. For southeastern Australia (including Tasmania) as a whole, the 11-yr period ending October 2007

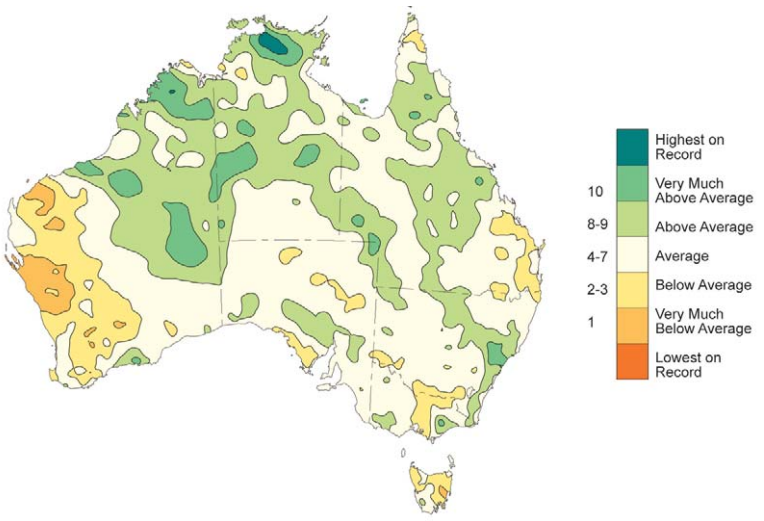

Fig. 6.51. Australian rainfall deciles (1961–90 base period) for 2007.

brought just 6,006 mm of precipitation. Compared to the normal amount of 6,650 mm (605 mm yr^{-1}), southeastern Australia missed out on over one year of normal rainfall when summed over the duration of the 11-yr drought event.

(iii) Notable events

While Australia was consistently warm throughout the year, the average was constrained by its coldest ever June (1.5°C below average). This was almost solely the result of an exceptional cold and wet event in tropical Australia in what is ordinarily the region's dry season. On 20 June, 31% of the land area of Australia experienced its lowest recorded daily maximum temperature for June (over the post-1941 period), with maximum temperatures <10°C observed at 14 tropical stations. Previously there had only been 12 recorded cases of individual tropical stations not reaching 10°C. The low temperatures included maxima of 8.0°C at Tennant Creek (19°39′S), the northernmost ever sub-10°C maximum in Australia.

February was exceptionally hot throughout southern and Western Australia, with western Australia, South Australia, and Tasmania all recording their hottest February on record. For large parts of western Australia, temperatures were >5°C above average. Marble Bar in the western Australian Pilbara region exceeded 40°C on 52 consecutive days from 5 January to 27 February, and had a mean daily maximum of 44.9°C for February, the highest monthly mean ever recorded at an Australian station.

Southeastern Australia was affected by abnormal warmth for late winter in the last week of the season. The South Australian capital of Adelaide reached 30.4°C on 30 August, breaking its previous record for the earliest 30° day by more than two weeks, while Mildura's 29.9°C on the same day equaled the Victorian record for August. The West Australian capital of Perth recorded 44.2°C on Boxing Day, its hottest December day since records began in 1897, exceeding the previous record of 42.3°C on 31 December 1968 by almost 2°C.

A succession of east coast lows developed during June off the New South Wales coast. Major flooding occurred in the Hunter River. Moisture associated with another east coast low brought severe flooding in eastern Victoria at the end of June, with rainfall totals including a 319-mm reading at Mount Wellington on 28 June, the second highest daily rainfall recorded in Victoria. A later event in early November, with daily rainfall of ~100 mm, brought renewed flooding to the same region.

Exceptionally heavy rainfall occurred in the Sunshine Coast region of Queensland on 24–25 August. The most extreme totals occurred on the early morning of the 24th, with 24-h totals of up to 772 mm at Coops Corner, which set a new Australian daily record for August. While these extreme rainfalls were localized, rainfalls in the 100–200-mm range were more widespread, causing significant local flooding, especially in the Noosa area.

Extensive wildfires, which began in early December 2006 in the mountains of northeastern Victoria, continued to burn into early February 2007. It was the most long-lived fire in the state's history. The fire was finally contained on 7 February after 69 days, having burned over 11,000 km^2.

2) New Zealand—M. J. Salinger

(i) General conditions

The national average temperature in 2007 was 12.7°C, 0.1°C above the 1971–2000 normal (Fig. 6.52).[7] The year ended very near the 1971–2000 normal as a consequence of several warm months offsetting some cooler months. Temperatures were near normal in most regions.

Annual rainfall in 2007 was below average throughout much of New Zealand. Annual rain-

[7] New Zealand data are from the National Climate Database archived for New Zealand with NIWA.

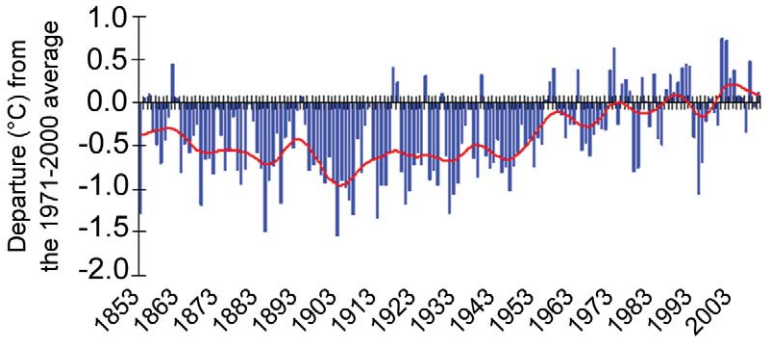

Fig. 6.52. New Zealand annual mean temperature anomalies (°C; 1971–2000 base period) for 1853–2007.

fall was less than 75% of normal in the east from Wairarapa to Otago, as well as eastern Bay of Plenty, Taranaki, Gisborne, Manawatu, Wellington, and Nelson. Rainfall totals were less than 60% of normal in parts of Marlborough, Canterbury, and Central Otago, as many locations recorded their driest year on record. Lauder recorded its driest year in more than 60 yr, with only 291 mm for the year.

Sunshine hours were more than 115% of normal in inland South Canterbury and Otago, with Tekapo, Dunedin, and Invercargill recording one of their sunniest years on record. Totals were at least 110% of normal in eastern Bay of Plenty, Southland, and Westland, and near normal elsewhere. Blenheim was the sunniest location in 2007, recording 2,567 h, followed by Lake Tekapo (2,554 h), and Whakatane (2,551 h).

(ii) Notable events

Notable climate features in various parts of the country were disastrous floods in Northland under very dry conditions, as well as drought in the east of the North Island. There was an unprecedented swarm of tornadoes in Taranaki, as well as destructive windstorms in Northland and in eastern New Zealand in October. There were numerous heavy rainfall events during 2007, of which nine produced flooding. Notable snowfall events occurred on relatively few occasions. There were 14 damaging tornado events for New Zealand for the year, an early autumn and late spring hot spell, two severe hailstorms, and seven damaging electrical storms.

The year began with low rainfall and significant soil moisture deficits, especially in the east, which persisted in the east of the North Island until May. The most disastrous Northland floods for many decades occurred in the Far North and Whangarei districts, especially in the Bay of Islands area at the end of March, due to exceptionally high rainfall ranging from 250 to more than 400 mm in eastern Northland. Warmer-than-normal seas to the west, anticyclones to the east, and frequent warm northwesterlies over New Zealand produced record high mean May temperatures for New Zealand overall and the driest May on record in the northernmost and eastern parts of the country. The national average temperature in May was 12.4°C (1.7°C above normal), the highest for New Zealand as a whole in reliable records dating back to the 1860s.

July was a month of extremes and contrasts with depressions often tracking over, or to the north of, the North Island. They produced floods in parts of Northland (over 400 mm in some areas), Hawke's Bay, coastal South Canterbury, and Otago; damaging windstorms in Northland, Auckland, and the Coromandel; and thunderstorms and damaging tornadoes in Taranaki (severe), Auckland, and Bay of Plenty. More settled, although rather cold, conditions existed for much of the month in Central Otago and inland Southland, often with periods of freezing fog. At Lauder, air temperatures were constantly below zero from 12 to 21 July, and there were 13 days from 7 to 22 July with minimum air temperatures below –10.0°C.

October was rather stormy and generally cold with deep depressions tracking south of New Zealand and frequent westerly gales. This was the fourth windiest October overall with regard to westerlies based on measurements that began in 1966. Wind gusts over 36 m s^{-1} occurred on 13 days (42%) in the month. Many stations had at least 7 more days than average for the time of year with strong winds (gusts to 16 m s^{-1} or more).

Low rainfall totals occurred in many regions in November 2007, especially in the South Island, with totals less than 10 mm throughout much of Nelson, Marlborough, and Central Otago. Severe soil moisture deficits resulted from the lack of rainfall in parts of Hawke's Bay, Marlborough, Canterbury, and Otago. These persisted until the end of the year. Additional extremes included the following:

- Extreme temperatures: The highest recorded extreme temperature of the year was 33.5°C and was recorded at Napier Airport in Hawke's Bay (33.5°C) on 22 January during hot dry northwesterly conditions. The lowest air temperature

for the year was –15.4°C recorded at Lauder on 18 July. This was the lowest reading there since July 1995 (–19.7°C), with numerous other inland South Island locations recording minimum air temperatures below –10.0°C at times between 7 and 22 July.

- Winds and tornadoes: The highest recorded wind gust for the year (as archived in the NIWA climate database) was 47 m s^{-1}. This reading was for a westerly wind at Taiaroa Head (Otago coast) during violent storm conditions on 23 October. A higher wind gust of 50 m s^{-1} was reported on the offshore island of Tititiri Matangi between 9 and 11 July. An extraordinary outbreak of damaging tornadoes caused severe damage throughout Taranaki over 4–5 July.
- Rainfall: The lowest annual precipitation totals occurred in Alexandra in Central Otago (272 mm), followed by Lauder (291 mm), and Clyde (294 mm). Of the regularly reporting gauges, the Cropp River gauge in Westland, inland in the headwaters of the Hokitika River, recorded the highest rainfall with a 2007 annual total of 8,940 mm. This region typically receives on the order of 10,000 mm of rainfall per year as it is situated in an area of moderate uplift of moist westerly air.
- Christchurch was the driest of the five main regions with 510 mm and Auckland the wettest with 1096 mm. Hamilton received 952 mm, Wellington 1070 mm, and Dunedin 599 mm.

3) Southwest Pacific—M. J. Salinger

The first quarter of the year was influenced by decaying El Niño conditions (see chapter 4), followed by a neutral period. La Niña conditions developed by September, and matured in December. There were ENSO-related influences on the location of the SPCZ, with the SPCZ tending to be north of its normal location during the first part of the year, and farther south than usual from July to December. Surface equatorial easterlies became very persistent near the date line from April onward. Above average equatorial SSTs occurred in January around Western and Eastern Kiribati with the decaying warm episode (+1°C anomalies); however, warm anomalies moved south of the equator through October, dissipating after that time. Negative SST anomalies (–0.5°C) developed east of the date line in July, gradually spreading west to reach the date line in October. Temperatures cooled to 1.0°–1.5°C below average in the seas around Eastern Kiribati for the remainder of the year.

Typical of an El Niño event, January's OLR anomalies showed enhanced convection over Kiribati southeast to the Northern Cook Islands, with suppressed convection farther south. However, this was short lived. From June through December a reversal to suppressed convection occurred there in association with La Niña's development. Mean sea level pressures were above average in the subtropics west of the date line until April. Negative anomalies developed in the tropical western Pacific between Papua New Guinea and Fiji from June onward.

For 2007 as a whole, above average SSTs occurred throughout much of the tropical southwest Pacific south and west of the date line (Fig. 6.53), which were at least +1.5°C above average around the Solomon Islands, Vanuatu, Fiji, Samoa, and central French Polynesia. SSTs were below average in the equatorial region near and east of the Line Islands. southwest Pacific island surface air temperature anomalies for 2007 were generally consistent with the SST anomalies throughout the region. It was an extremely warm year in Fiji and Tonga where the mean temperatures were about 1.0°C above historical averages.

OLR anomalies in 2007 (Fig. 6.54) showed a region of enhanced convection over Papua New Guinea and west of the Caroline Islands, as well as between Fiji and central French Polynesia, including Tonga, Samoa, Niue, and the southern Cook Islands. Convection was

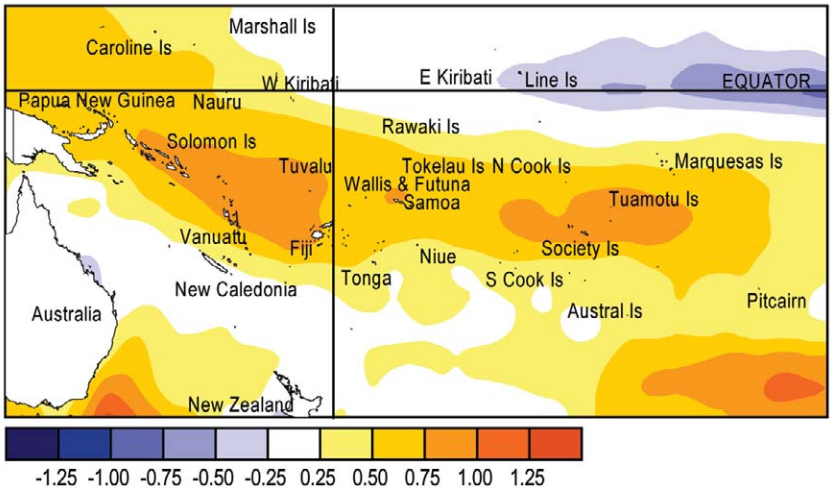

Fig. 6.53. SST anomalies (°C; 1971–2000 base period). Yellow or orange areas represent a warmer-than-average sea surface.

suppressed in 2007 over Kiribati, extending to northern French Polynesia. The year's rainfall anomaly pattern is similar to the OLR pattern, with above-average rainfall between Fiji and central French Polynesia, including Tonga, and below-average rainfall in Kiribati, extending to northern French Polynesia.

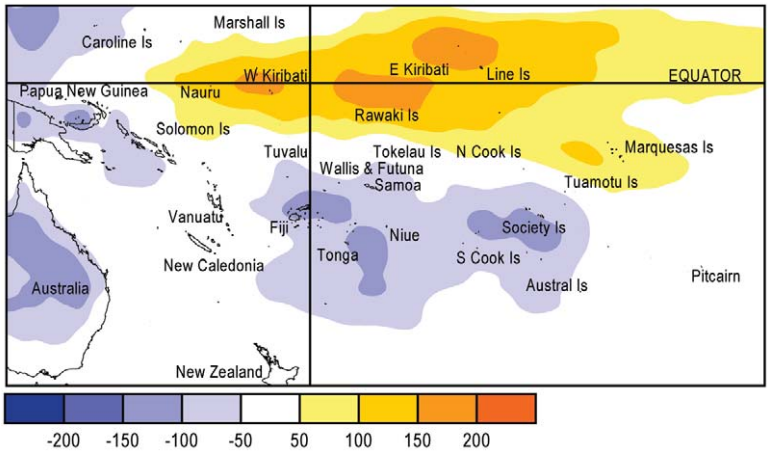

Fig. 6.54. OLR anomalies (W m^{-2}; 1971–2000 base period). High radiation levels (yellow or orange) are typically associated with clearer skies and lower rainfall, while cloudy conditions lower the OLR (blue) and typically mean higher rainfall.

4) Micronesia—C. Guard and M. A. Lander

This assessment covers the area from the date line west to 130°E, between the equator and 20°N. It includes the U.S.-affiliated islands of Micronesia, but excludes the western islands of Kiribati. During 2007, Micronesia was initially dominated by a mild post–El Niño drought and later by the effects of La Niña. In early 2007, the 2006 El Niño waned and gave way to ENSO-neutral conditions. In the middle third of the year, equatorial oceanic conditions vacillated between ENSO-neutral and weak La Niña. Atmospheric conditions, however, had distinct La Niña characteristics in Micronesia during much of the year. Trade winds and low-latitude easterly winds were stronger than normal. The monsoon trough spent most of the boreal summer and fall in the western part of Micronesia, rarely pushing eastward. In fact, it only penetrated to 155°E once during the year and to 145°E 3 times during the year. This caused the tropical cyclone season to start late, with most tropical cyclones developing west of Guam and north of Yap, and not significantly intensifying until they were well on their way to the Philippines, Taiwan, or northeast Asia. In addition, sea levels were significantly higher than normal across all of Micronesia.

(i) Temperature

Average monthly maximum temperatures were higher than normal across most of Micronesia. This was especially the case during the first six months of the year, when many locations were affected by a mild post–El Niño drought (Table 6.4). At the Guam International Airport, monthly average maximum temperature anomalies were +0.8°C for January–June and also +0.8°C for the entire year. All months either had normal or above normal maximum temperatures. For Palau at the western end of the area, the average monthly maximum temperature anomaly was +0.9°C for the first six months and +0.7°C for the entire year, with all months having higher than normal maximum temperatures. At the eastern end of the area, maximum temperatures at Majuro (central Marshall Islands) were warmer than average for 8 of the 12 months, but for the first 6 months and for the entire year, the anomalies only averaged 0.1° and 0.2°C, respectively. Pohnpei in the central part of the Micronesian area had a maximum temperatures anomaly of +0.3°C for the first six months and +0.2°C for the entire year. Only Chuuk, also in the central part of the area, exhibited cooler-than-normal maximum temperatures during 2007, with anomalies of –0.4°C for the first six months and –0.3°C for the entire year. The higher-than-normal maximum temperatures can, for the most part, be attributed to increased incoming solar radiation as a result of increased early year subsidence associated with the post–El Niño drought and reduced monsoon and tropical cyclone activity in the second half of the year.

(ii) Precipitation

Precipitation at the major island stations in Micronesia was drier than normal during the first one to four months of 2007. Widespread subsidence frequently produces drought conditions in the region during the post–El Niño period. The severity of the drought usually corresponds to the severity of the El Niño. Weak El Niño events can produce mixed precipitation patterns with wet and dry areas across the region, as was the case in early 2007. For the most part, rainfall for the first six months of 2007 in Micronesia was between 75% and 125% of average for most locations (Table 6.4). Exceptions occurred

in the Marshall Islands, Palau and Guam, where values were 20%–50%, 40%–60%, and 60%–70% of average, respectively, for at least three of the six months. Extremely dry conditions affected the northern Marshall Islands, where winter rainfall was 20% of normal. Guam was also dry for several months, exacerbating the dry-season wildfire threat. Very dry conditions also affected several of the low islands of Chuuk State. The abrupt change from El Niño to ENSO-neutral conditions and the trend toward La Niña early in the year may have prevented more severe and widespread subsidence and drier conditions early in the year. Despite ENSO-neutral conditions in the boreal spring and summer, the atmospheric patterns over Micronesia were largely La Niña–like and the weather could be described as tranquil, with fewer than normal tropical cyclones, a weak monsoon, and a general suppression of large-scale convective activity.

The stronger-than-normal trade winds and general lack of strong widespread subsidence allowed the convectively active, narrow trade wind trough to develop, keeping the islands between 4° and 8°N wet during most of the months of the first half of the year. Palau at the western edge of the area, Guam on the northern edge of the area, and Kwajalein at the northeast edge of the area had rainfall that was 28%, 14%, and 20% below normal, respectively, for the January–June period. As the trend toward La Niña increased, rainfall increased in the western part of the Micronesian area. Yap maintained its wet pattern during the second half of the year, and Palau was able to make up much of its first half-year deficit (Table 6.4). The high islands of Guam and Pohnpei had sufficient convective activity to produce rainfall values slightly above normal by the end of the year, despite the lack of monsoon and tropical cyclone activity. The La Niña pattern is often accompanied with a strong, persistent TUTT that contains embedded upper cold-core low pressure systems that move east to west. High-level divergent flow equatorward of these low pressure systems produced widespread shower activity over the northern islands (Guam, Yap, Kwajalein) of the area that helped increase rainfall there during the second half of 2007.

(iii) Tropical cyclone impacts

Tropical cyclone activity in 2007 in the western North Pacific and across Micronesia was below normal in almost every category of activity (see chapter 4). Tropical cyclone Kong-rey brought much needed rainfall to parts of Pohnpei and Chuuk States, and to the CNMI. The peak wind recorded in the sparsely populated northern islands of the CNMI was 34.5 m s^{-1}, and it only produced about 91 mm of rain. Yutu passed near Yap as a weak tropical storm. A peak wind of only 18.5 m s^{-1} was recorded on Yap with 115 mm of storm-total rain. In July, Tropical Storm Man-yi passed north of Yap and west of Guam, producing peak winds of about 25 m s^{-1} in Yap State.

Table 6.4. Temperature and precipitation summaries for locations in Micronesia.

Station	Location	Max. temperature anomaly (°C)		Rainfall (mm)			
				Jan–Jun		Annual	
		Jan–Jun	Annual	2007	% Normal	2007	% Normal
Guam	13°N, 145°E	+0.8	–0.8	523.5	86	2,235.7	103
Yap	9°N, 138°E	+0.2	+0.1	1,326.9	114	3,496.3	117
Palau	7°N, 134°E	–0.9	+0.7	1,238.8	72	3,230.1	86
Chuuk	7°N, 152°E	–0.4	–0.3	1,571.8	102	3,216.7	95
Pohnpei	7°N, 158°E	–0.3	+0.2	2,390.1	105	4,921.5	105
Kwajalein	9°N, 168°E	+0.1	–0.1	772.2	80	2,266.4	89
Majuro	7°N, 171°E	+0.1	+0.2	1,419.6	98	3,014.0	90

A strong gradient between the storm and a strong high pressure system several hundred kilometers northeast of Guam produced gale-force winds that battered Guam and the CNMI for 24 h. Tropical Storm Usagi produced peak winds of 21.6 m s^{-1} over the northern islands of the CNMI and a 24-h rainfall total of 236 mm.

(iv) Sea level

The late start of the weak El Niño of 2006 and its abrupt ending near the beginning of February 2007 produced only a small sea level drop over the easternmost parts of Micronesia in the early part of 2007. Western parts of Micronesia never experienced the sea level falls that normally accompany, even weak, El Niño events. With the abrupt demise of El Niño and the trend toward La Niña conditions early in 2007, strong trade winds began to elevate the sea levels across Micronesia. High wave events caused several episodes of coastal flooding in Chuuk State in the boreal spring, fall, and winter. From November 2007 through the end of the year, sea levels averaged 15–20 cm above their normal monthly averages, but during full and new moon phases, the highest sea levels were 60–80 cm above normal heights. The high astronomical tides coupled with the affect of La Niña caused considerable coastal inundation in Chuuk and Pohnpei States.

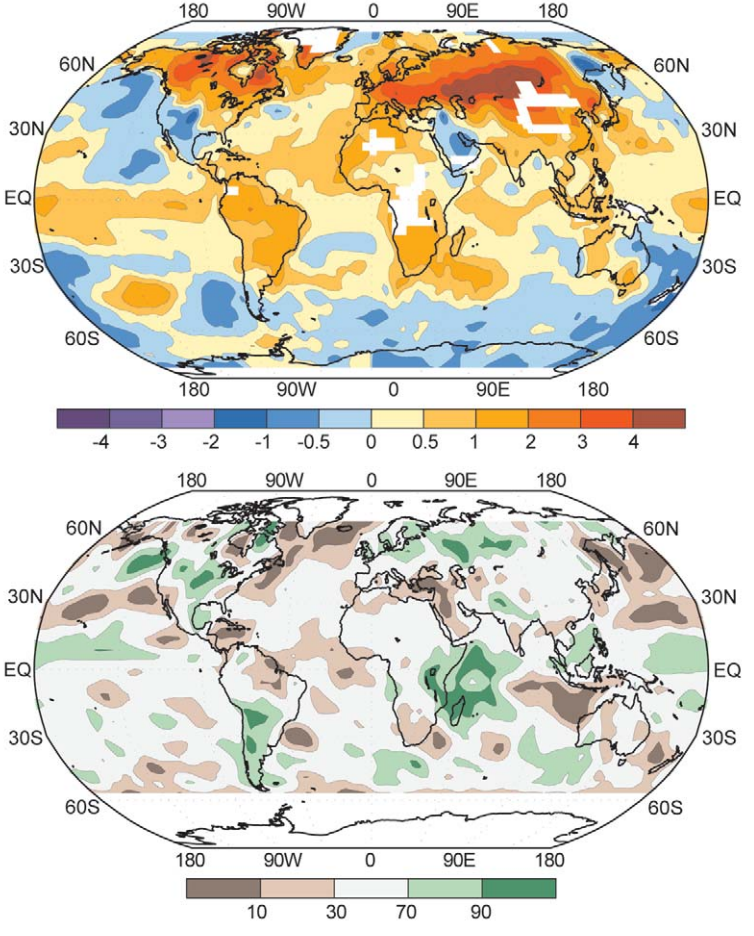

Fig. 7.1. Dec 2006–Feb 2007 (top) surface temperature anomalies (°C) and (bottom) precipitation percentiles based on a gamma distribution fit to the 1979–2000 base period. Temperature anomalies (1971–2000 base period) are based on station data over land and sea surface temperature over water. Precipitation data were obtained from the CAMS-OPI dataset that is a combination of rain gauge observations and satellite-derived estimates (Janowiak and Xie 1999). Analysis was omitted in data-sparse regions (white areas).

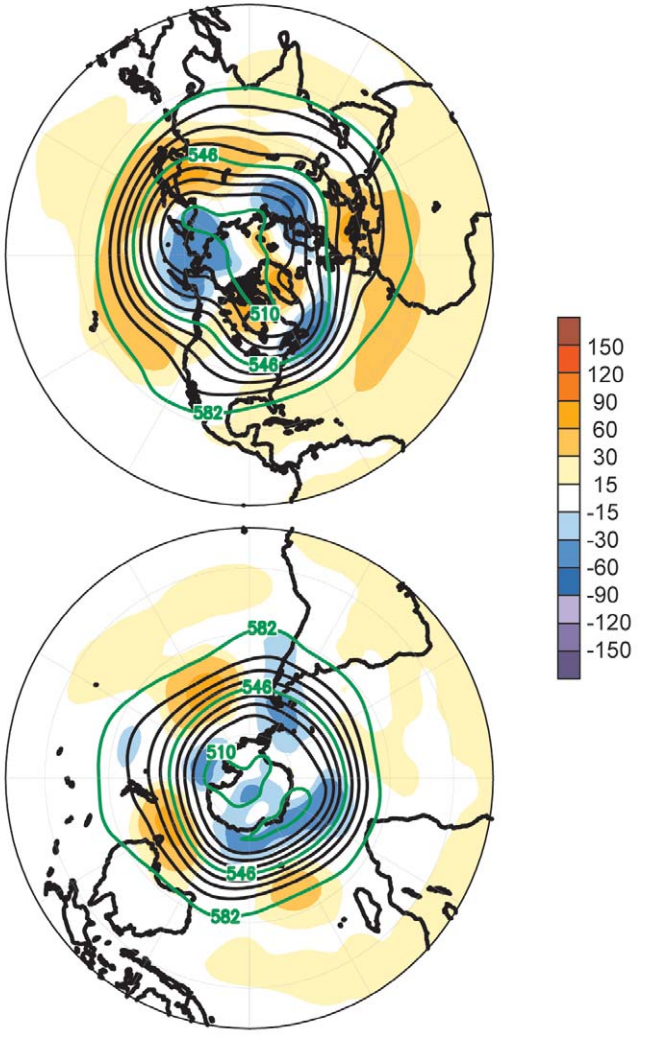

Fig. 7.2. Dec 2006–Feb 2007 (top) Northern Hemisphere and (bottom) Southern Hemisphere 500-hPa geopotential heights (9-dam contour interval) and anomalies (shading) determined from the 1979–2000 base period mean.

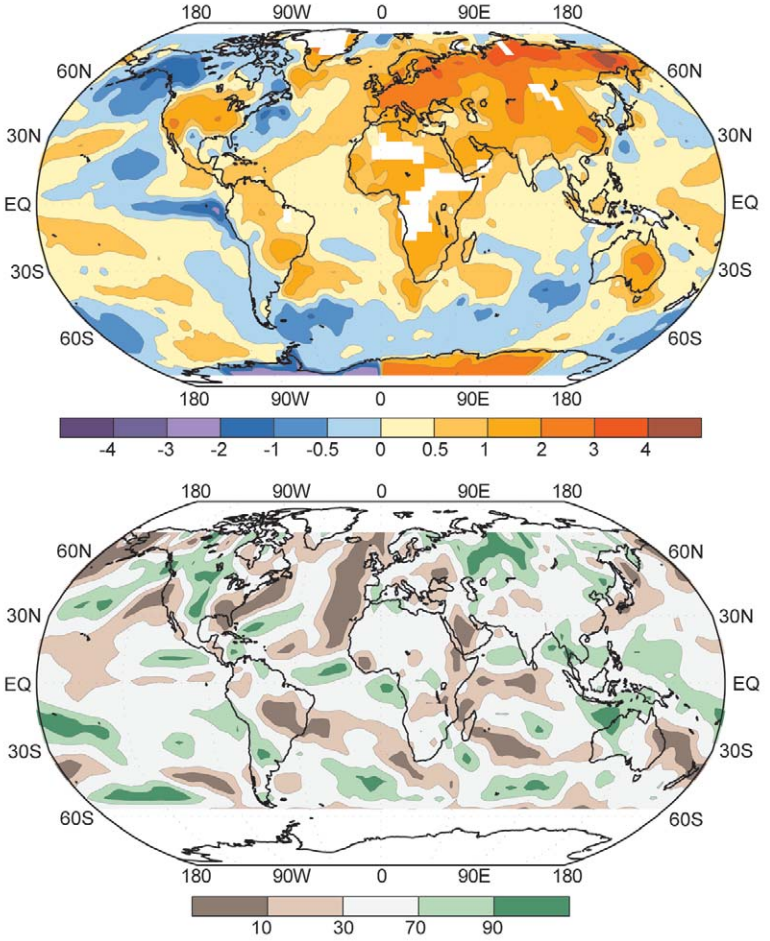

Fig. 7.3. Mar–May 2007 (top) surface temperature anomalies (°C) and (bottom) precipitation percentiles based on a gamma distribution fit to the 1979–2000 base period. Temperature anomalies (1971–2000 base period) are based on station data over land and sea surface temperature over water. Precipitation data were obtained from the CAMS-OPI dataset that is a combination of rain gauge observations and satellite-derived estimates (Janowiak and Xie 1999). Analysis was omitted in data-sparse regions (white areas).

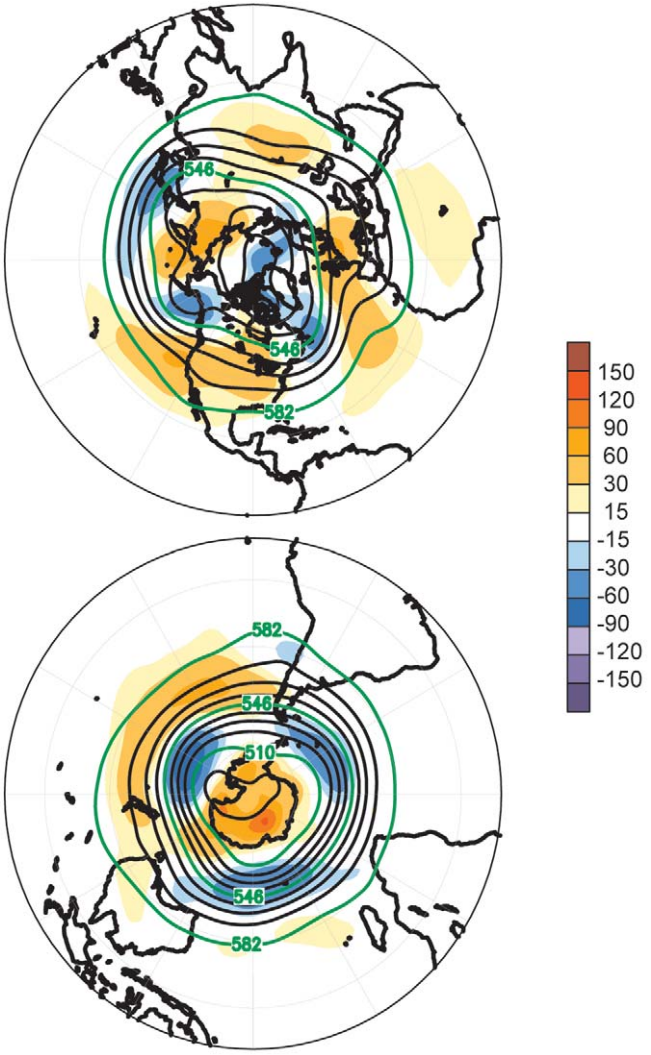

Fig. 7.4. Mar–May 2007 (top) Northern Hemisphere and (bottom) Southern Hemisphere 500-hPa geopotential heights (9-dam contour interval) and anomalies (shading) determined from the 1979–2000 base period mean.

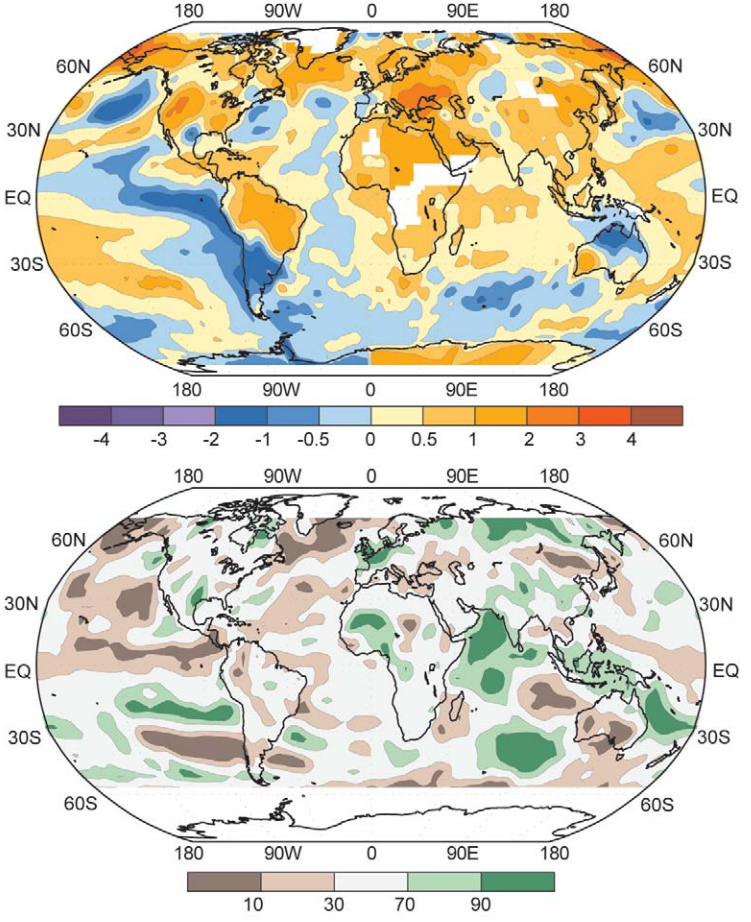

Fig. 7.5. Jun–Aug 2007 (top) surface temperature anomalies (°C) and (bottom) precipitation percentiles based on a gamma distribution fit to the 1979–2000 base period. Temperature anomalies (1971–2000 base period) are based on station data over land and sea surface temperature over water. Precipitation data were obtained from the CAMS-OPI dataset that is a combination of rain gauge observations and satellite-derived estimates (Janowiak and Xie 1999). Analysis was omitted in data-sparse regions (white areas).

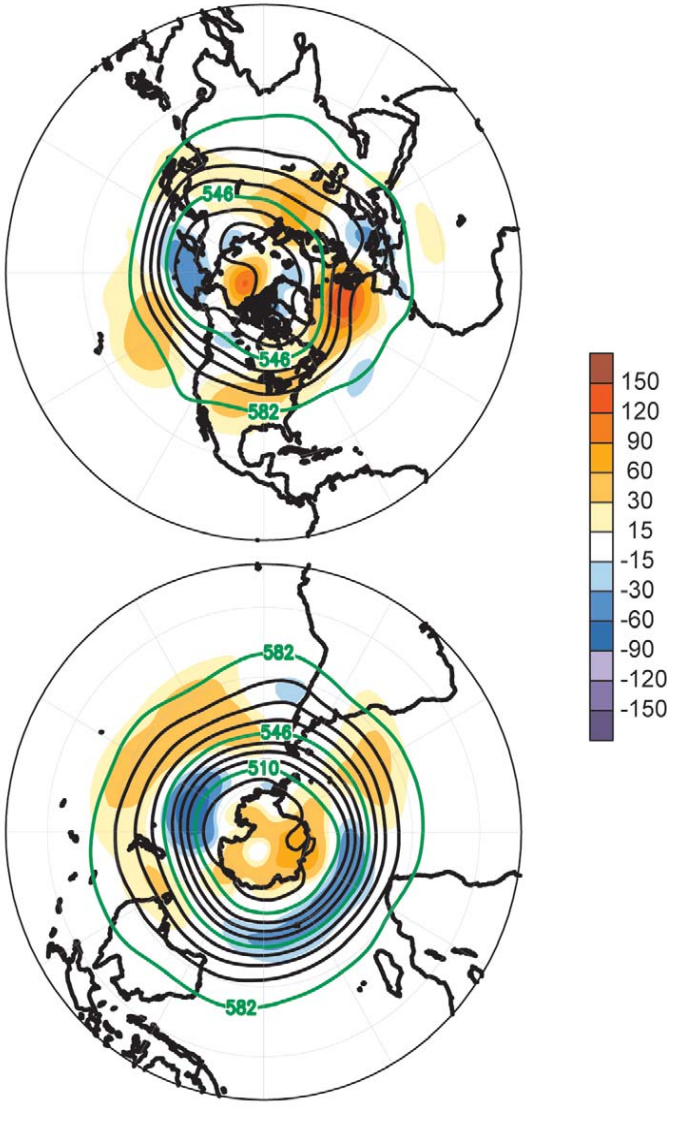

Fig. 7.6. Jun–Aug 2007 (top) Northern Hemisphere and (bottom) Southern Hemisphere 500-hPa geopotential heights (9-dam contour interval) and anomalies (shading) determined from the 1979–2000 base period mean.

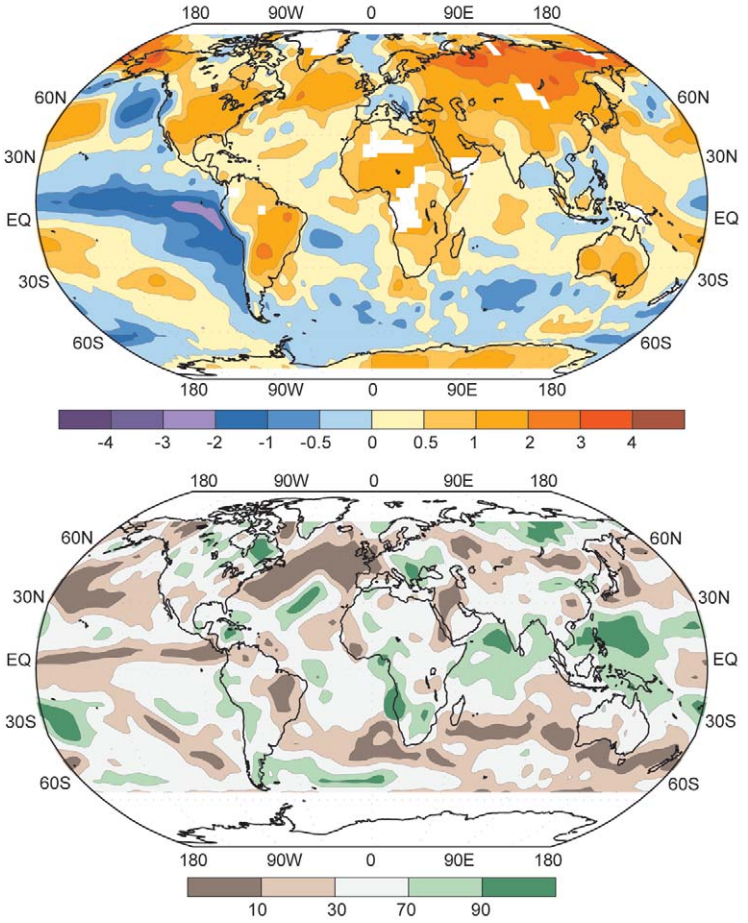

FIG. 7.7. Sep–Nov 2007 (top) surface temperature anomalies (°C) and (bottom) precipitation percentiles based on a gamma distribution fit to the 1979–2000 base period. Temperature anomalies (1971–2000 base period) are based on station data over land and sea surface temperature over water. Precipitation data were obtained from the CAMS-OPI dataset that is a combination of rain gauge observations and satellite-derived estimates (Janowiak and Xie 1999). Analysis was omitted in data-sparse regions (white areas).

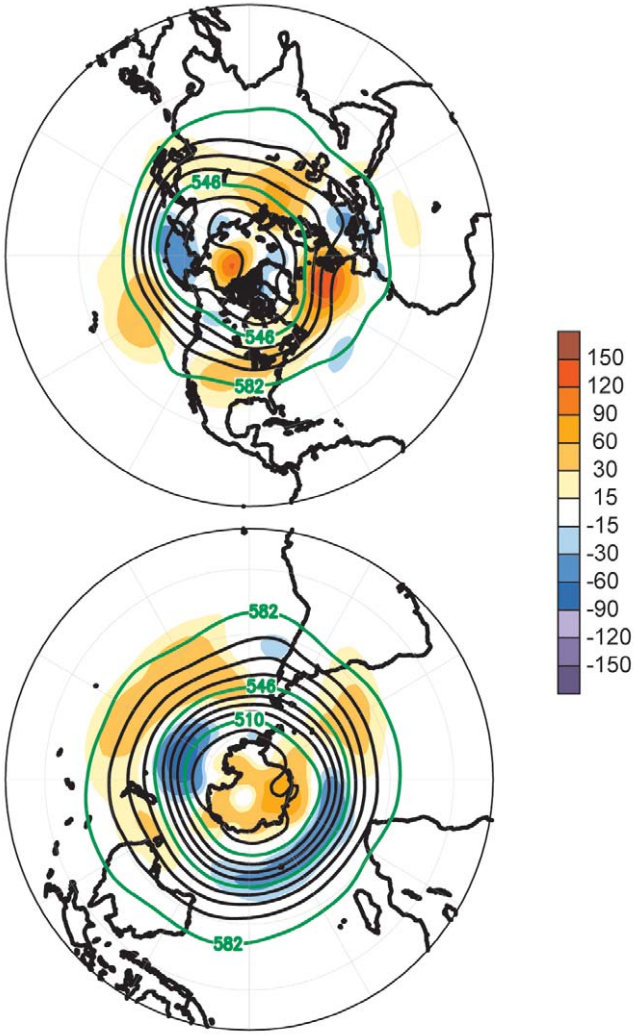

FIG. 7.8. Sep–Nov 2007 (top) Northern Hemisphere and (bottom) Southern Hemisphere 500-hPa geopotential heights (9-dam contour interval) and anomalies (shading) determined from the 1979–2000 base period mean.

ACKNOWLEDGMENTS. Over 300 individuals from more than 50 countries participated in this report, including authors, reviewers, graphics specialists, and various facilitators. The editors acknowledge the graphics team at NOAA's NCDC for their devotion to the report: Glenn Hyatt, Deborah Riddle, Sara Veasey, Deborah Misch, and Christian Zamarra. NCDC's Mara Sprain also provided invaluable assistance in the development of the hundreds of references included in this report. We also kindly thank Omar Baddour of the WMO, and Dick Thigpen, on contract to the GCOS Secretariat at the WMO. John Kennedy and David Parker were supported by the Defra and MoD Integrated Climate Programme GA01101, CBC/2B/0417_Annex C5. The Contribution from the University of Gothenburg is taken as Contribution No. 12 from TELLUS, the Centre for Earth System Science at University of Gothenburg. This report was partially supported by the NOAA Climate Program Office Climate Change Data and Detection Program Element.

We also gratefully acknowledge the following individuals:

- Julie Bartynski, American Meteorological Society, Boston, MA
- Lawrence E. Flynn, NOAA/NESDIS/ORA, Camp Springs, MD
- Carlos Fuller, National Meteorological Service of Belize
- Laura Furgione, NOAA/NWS, Anchorage, AK
- Bryan Hanssen, American Meteorological Society, Boston, MA
- Ken Heideman, American Meteorological Society, Boston, MA
- Dave Hofmann, NOAA/ESRL, Boulder, CO
- Bryan Johnson, NOAA/ESRL, Boulder, CO
- Ralph Kahn, NASA GSFC, Greenbelt, MD
- Ken Knapp, NOAA/NCDC, Asheville, NC
- Mike Kruk, NOAA/NCDC, Asheville, NC
- Ken Kunkel, Midwest Regional Climate Center, Champaign, IL
- Israel Matos, NOAA/NWS, San Juan, Puerto Rico
- Rich McPeters, NASA GSFC, Greenbelt, MD
- Carl Mears, Remote Sensing Systems, Santa Rosa, CA
- Christopher Miller, NOAA Climate Program Office, Silver Spring, MD
- Samuel J. Oltmans, NOAA/ESRL, Boulder, CO
- Joel Perez, CATHALAC, Panama City, Panama
- Steve Piotrowicz, Ocean.US, Silver Spring, MD
- Michael C. Pitts, NASA LaRC, Langley, VA
- Guillermo Podestá, University of Miami, Miami, FL
- Kelly Redmond, Western Regional Climate Center, Reno, NV
- Jeff Rosenfeld, American Meteorological Society, Boston, MA
- Michelle Santee, NASA JPL, Pasadena, CA
- Carven Scott, NOAA/NWS, Anchorage, AK
- Derrick Snowden, NOAA Climate Program Office, Silver Spring, MD
- Diane Stanitski, Geocation, LLC, Boulder, CO
- Kathy Tedesco, U.S. Geological Survey, St. Petersburg, FL
- Jim Todd, NOAA Climate Program Office, Silver Spring, MD
- B. Mete Uz, NOAA Climate Program Office, Silver Spring, MD
- Chris Velden, CIMSS, University of Wisconsin; Madison, WI
- Jeff Waldstreicher, NOAA/NWS, Bohemia, NY

APPENDIX: ACRONYMS

A	Anticyclonic days
ACC	Antarctic Circumpolar Current
ACE	NOAA's Accumulated Cyclone Energy Index
AEJ	African Easterly Jet
AGCM	Atmospheric general circulation model
AGGI	NOAA's Annual Greenhouse Gas Index
AMIP	Atmospheric Model Intercomparison Project
ALT	Active layer thickness
AMM	Atlantic Multidecadal Mode
AMO	Atlantic Multidecadal Oscillation
AMSR-E	Advanced Microwave Scanning Radiometer for Earth Observing System
AMSU	Advanced Microwave Sounding Unit
ANEEL	Agência Nacional de Energia Eléctrica
AO	Arctic Oscillation
AOD	Aerosol optical depth
AOML	Atlantic Oceanographic and Meteorological Laboratory
ASO	August–September–October
ASTER	Advanced Spaceborne Thermal Emission and Reflection Radiometer
ATLAS	Autonomous Temperature Line Acquisition System
AVHRR	Advanced Very High Resolution Radiometer
AVISO	Archiving, Validating, and Interpretation of Satellite Oceanographic data
AW	Atlantic Water

AWS	Automatic weather station
BC	British Columbia
BGOS	Beaufort Gyre Observing System
BI	Balleny Islands
Br	Bromine
C	Cyclonic days
CALIPSO	Cloud-Aerosol Lidar and Infrared Pathfinder Satellite Observation
CAMS	Climate Anomaly Monitoring System
CCM3	NCAR Community Climate Model version 3
CDAS	Climate Data Assimilation System
cDOM	Colored dissolved organic matter
CE	Cyclonic easterly days
CEMIG/SIMGE/MG	Companhia Energética de Minas Gerais
CET	Central England Temperature
CFC	Chlorofluorocarbon
CFC-11	Trichlorofluoromethane
CFC-12	Dichlorodifluoromethane
CH_4	Methane
Chlsat	Surface-layer chlorophyll concentration
CIIFEN	International Research Center on El Niño
CIMSS	University of Wisconsin—Madison Cooperative Institute for Meteorological Satellite Studies
CIRES	Cooperative Institute for Research in Environmental Sciences
Cl	Chlorine
CLIVAR	Climate Variability and Predictability
ClO	Chlorine monoxide
$ClONO_2$	Chlorine nitrate
CLS	Collecte Localisation Satellites
CMA	China Meteorology Administration
CMCD/INPE	Data Collection Mission Center/ National Institute for Space Research
CMIP	Coupled Model Intercomparison Project
CMRH/SE	Centro Estadual de Meteorologia e dos Recursos Hídricos/ Superitendência de Recursos Hídricos de Sergipe
CNES	Centre National d'Etudes Spatiales
CNMI	Commonwealth of the Northern Mariana Islands
CNW	Cyclonic north-westerly days
CO	Carbon monoxide
CO_2	Carbon dioxide
COARE	Coupled Ocean–Atmosphere Response Experiment
CPC	Climate Prediction Center
CPHC	NOAA's Central Pacific Hurricane Center
CPTEC	Center for Weather Forecasting and Climate Studies
CRU	Climate Research Unit
CSI	NOAA Climate Scene Investigation
CW	Cyclonic westerly days
CYC	Cyclone
D1	Moderate drought
DIC	Dissolved inorganic carbon
DISC	Data and Information Services Center
DJF	December–January–February
DJFM	December–January–February–March
DM	Drift-Age Model
DOE	Department of Energy
DT-MSLA	Delayed Time-Merged Sea Level Anomaly
DU	Dobson units
DWBC	Deep western boundary current
DWD	Deutscher Wetterdienst
EASE	Equal-Area Scalable Earth
ECl	Equivalent chlorine
ECMWF	European Centre for Medium-Range Weather Forecasts
EECl	Effective equivalent chlorine
EESC	Effective equivalent stratospheric chlorine
EF	Enhanced Fujita
EKE	Eddy kinetic energy
EMPARN	Empresa de Pesquisa Agropecuária do Rio Grande do Norte
ENACT	Enhanced ocean data assimilation and climate prediction
ENP	Eastern North Pacific (basin)
ENSO	El Niño–Southern Oscillation
EOF	Empirical orthogonal function
EPAC	East Pacific
EPOGA	East Pacific Ocean–Global Atmosphere
ESRL	Earth System Research Laboratory
ET	Equatorial trough
ETC	Extratropical cyclone
EU	European Union
EWG	Environmental Working Group
FUNCEME/CE	Fundação Cearense de Meteorologia e Recursos Hídricos/ Estado do Ceara
GC	Gas chromatograph

GCM	General circulation model
GCOS	Global Climate Observing System
GEOSECS	Geochemical Ocean Section Study
GES	Goddard Earth Sciences
GFDL AM2.1	Geophysical Fluid Dynamics Laboratory Atmosphere Model version 2.1
GFS	NCEP Global Forecast System
GHA	Greater Horn of Africa
GHCN	Global Historical Climatology Network
GHG	Greenhouse gas
GIA	Glacial isostatic adjustment
GISS	NASA's Goddard Institute of Space Studies
GLOSS	Global Sea Level Observing System
GMD	Global Monitoring Division
GOGA	Global Ocean–Global Atmosphere
GOM	Gulf of Mexico
GPCC	Global Precipitation Climatology Centre
GPI	Genesis potential index
GRACE	Gravity Recovery and Climate Experiment
GSM	Garver–Siegel–Maritorena
H	Hurricane
HadAT2	Hadley Centre gridded free-atmosphere temperatures from radiosondes dataset
HadCRUT3	Hadley Centre/CRU gridded monthly temperatures dataset
HCFC	Hydrochlorofluorocarbon
HCl	Hydrogen chloride
HFC	Hydrofluorocarbon
HOTS	Hawaiian Ocean Time Series
hPa	Hectopascal (1 mb)
HTC	Hurricanes/typhoons/cyclones
HURDAT	Atlantic Hurricane Database
ICESat	Ice, Cloud, and Land Elevation Satellite
IGRA	Integrated Global Radiosonde Archive
INMET	Instituto Nacional de Meteorologia
INPO	International Network of Permafrost Observatories
IO	Indian Ocean
IOCCG	International Ocean Colour Coordinating Group
IOD	Indian Ocean dipole
IOP	Intensive observing period
IPCC	Intergovernmental Panel on Climate Change
IPCC AR4	IPCC Fourth Assessment report (published in 2007)
IPCC FAR	IPCC First Assessment Report (published in 1996)
IPY	International Polar Year
IR	Infrared
IRI	International Research Institute for Climate and Society
IRIMO	Islamic Republic of Iran Meteorological Organization
ITCZ	Intertropical convergence zone
ITEP/LAMEPE/PE	Instituto Tecnológico de Pernambuco/Laboratório de Meteorologia de Pernambuco
JAMSTEC	Japan Agency for Marine–Earth Science and Technology
JAS	July–August–September
JASO	July–August–September–October
J-CAD	JAMSTEC Compact Arctic Drifter
JGOFS	Joint Global Ocean Flux Study
JJA	June–July–August
JMA	Japanese Meteorological Agency
JPL	Jet Propulsion Laboratory
JTWC	U.S. Navy's Joint Typhoon Warning Center
KNMI	Royal Netherlands Meteorological Institute
LaRC	Langley Research Center
LHF	Latent heat flux
LLJ	Low-level jet
LMRS/PB	Laboratório de Meteorologia, Recursos/Remoto da Paraíba
LS	Lower stratosphere
LT	Lower troposphere
LTM	Long-term mean
MAM	March–April–May
MCC	Mesoscale convective complex
MCYC	Major cyclone
MDR	Main Development Region
MEI	Multivariate ENSO Index
MH	Major hurricane
MJO	Madden–Julian oscillation
MLO	Mauna Loa Observatory
MLS	Microwave Limb Sounder
MM5	Fifth-generation Pennsylvania State University–National Center for Atmospheric Research Mesoscale Model
MOC	Meridional overturning current
MOCHA	Meridional Overturning Circulation Heat Transport Array
MODIS	Moderate Resolution Imaging Specroradiometer

MPI	Maximum potential intensity
MSU	Microwave Sounding Unit
MT	Midtroposphere
MTC	Major tropical cyclone
N_2O	Nitrous oxide
NAMHEM	National Agency for Meteorology, Hydrology and Environmental Monitoring
NAM	Northern annular mode
NAO	North Atlantic Oscillation
NARR	North American Regional Reanalysis
NASA	National Aeronautics and Space Administration
NBC	North Brazil Current
NCAR	National Center for Atmospheric Research
NCDC	National Climatic Data Center
NCEP	National Center for Environmental Prediction
NDVI	Normalized difference vegetation index
NEC	North Equatorial Current
NECC	North Equatorial Countercurrent
NEM	Northeast monsoon
NERC	National Environmental Research Council
NESIS	Northeast Snowfall Impact Scale
NH	Northern Hemisphere
NHC	National Hurricane Center
NIFC	National Interagency Fire Center
NIND	North Indian
NIO	Northern Indian Ocean
NIWA	National Institute of Water and Atmospheric Research
NN2	NOAA/NWS/NCEP/DOE Reanalysis II
NO	Nitric oxide
NOAA	National Oceanic and Atmospheric Administration
NOMADS	National Operational Model Archive and Distribution System
NP	North Pole
NPEO	North Pole Environmental Observatory
NPP	Net primary production
NS	Named storm
NSIDC	National Snow and Ice Data Center
NSW	New South Wales, Australia
NW	North-westerly days
NWS	National Weather Service
O_3	Ozone
OAFlux	Objectively Analyzed Air–Sea Fluxes
OBPG	Ocean Biology Processing Group
ODGI	Ozone Depleting Gas Index
ODS	Ozone-depleting substance
OH	Hydroxide anion
OHCA	Ocean Heat Content Anomaly
OI	Optimal interpolation
OLR	Outgoing longwave radiation
OMI	Ozone Monitoring Instrument
ONI	Oceanic Niño Index
OPI	OLR precipitation index
PATMOS (-x)	Pathfinder Atmospheres (Extended Product)
pCO_2	Carbon dioxide partial pressure
PDF	Probability distribution function
PDO	Pacific decadal oscillation
PDSI	Palmer Drought Severity Index
Pg	Petagram (1015 g)
pIOD	Positive phase of the IOD
PIRATA	Pilot Research Array in the Tropical Atlantic
PMEL	Pacific Marine Environmental Laboratory
PNA	Pacific–North American pattern
ppb	Parts per billion
ppbv	Parts per billion by volume
ppm	Parts per million
ppt	Parts per trillion
PSC	Polar stratospheric cloud
PSS	Practical salinity scale
psu	Practical salinity unit
QBO	Quasi-biennial oscillation
QuikSCAT	Quick Scatterometer
QSCAT	QuikSCAT satellite
RAOBCORE	Radiosonde Observation Correction
RATPAC	Radiosonde Atmospheric Temperature Products for Assessing Climate
RMB	Renminbi
RPCA	Rotated principal component analysis
RSL	Relative sea level
RSMC	Regional Specialized Meteorological Center Tokyo
RSS	Remote Sensing Systems
SACZ	South Atlantic convergence zone
SAM	Southern annular mode
SAT	surface air temperature
SCA	Snow-covered area
SCE	Snow cover extent
SCS	South China Sea

SEAAB/PI	Secretaria do Agricultura, Abastecimiento e Irrigacao of the Government of Piauí
SEAG/ES	Secretaria de Agricultura do Estado do Espírito Santo
SeaWiFS	Sea-viewing Wide Field of View
SEC	South Equatorial Current
SEIND	Southeast Indian
SENAMHI	Bolivian Meteorological Service
ΣChl	Photic zone chlorophyll
SF_6	Sulfur hexafluoride
SH	Southern Hemisphere
SHF	Sensible heat flux
SIO	Southern Indian Ocean
SITCZ	Southern intertropical convergence zone
SL	Sea level
LA	Sea level anomaly
SLE	Sea level equivalent
SLP	Sea level pressure
SMD	Surface melt duration
SMMR	Scanning Multichannel Microwave Radiometer
SMN	Mexico's National Meteorological Service
SON	September–October–November
SOI	Southern Oscillation index
SPA	South Pacific anticyclone
SPAC	South Pacific
SPCZ	South Pacific convergence zone
SPI	Standardized Precipitation Index
SRH/BA	Superintendência de Recursos Hídricos da Bahia
SSA	Southern South America
SSM/I	Special Sensor Microwave Imager
SSS	Sea surface salinity
SST	Sea surface temperature
SSTA	Sea surface temperature anomaly
STY	Supertyphoon
SUDENE	Superintendência do Desenvolvimento do Nordeste
Sv	Sverdrups (1 Sv ≡ 10^6 m^3 s^{-1})
SWI	Summer warmth index
SWIND	Southwest Indian
SWJ	Subtropical westerly jet
SWP	Southwest Pacific
TATL	Tropical Atlantic
TC	Tropical cyclone
TCHP	Tropical cyclone heat potential
TD	Tropical depression
TEJ	Tropical easterly jet
TMI	Tropical Rainfall Measuring Mission Microwave Imager
TOMS	Total Ozone Mapping Spectrometer
TRMM	Tropical Rainfall Measuring Mission
TS	Tropical storm
TSP	Thermal state of permafrost
TMI	Tropical Rainfall Measuring Mission Microwave Imager
TY	Typhoon
UAH	University of Alabama Huntsville
UKMO	Met Office
UMD	University of Maryland
USDA	U.S. Department of Agriculture
W	Westerly days
WBC	Western boundary current
WHOI	Woods Hole Oceanographic Institute
WMO	World Meteorological Organization
WOA	*World Ocean Atlas*
WOCE	World Ocean Circulation Experiment
WP	west Pacific (teleconnection pattern)
WPAC	West Pacific
WPO	west Pacific Ocean
XBT	Expendable bathythermograph

REFERENCES

Alexander, L. V., and P. D. Jones, 2001: Updated precipitation series for the U.K. and discussion of recent extremes. *Atmos. Sci. Lett.,* **1,** doi:10.1006/asle.2001.0025.

Arblaster, J. M., and G. A. Meehl, 2006: Contributions of external forcings to southern annual mode trends. *J. Climate,* **19,** 2896–2905.

Arguez, A., and Coauthors, 2007: State of the Climate in 2006. *Bull. Amer. Meteor. Soc.*, **88** (6), S8–S132.

Armstrong, R. L., and M. J. Brodzik, 2001: Recent Northern Hemisphere snow extent: A comparison of data derived from visible and microwave sensors. *Geophys. Res. Lett.,* **28,** 3673–3676.

——, ——, K. Knowles, and M. Savoie, 2005a: Global monthly EASE-Grid snow water equivalent climatology. National Snow and Ice Data Center, Boulder, CO, digital media. [Available online at http://nsidc.org/data/nsidc-0271.html.]

——, B. Raup, S. J. S. Khalsa, R. Barry, J. Kargel, C. Helm, and H. Kiefer, 2005b: GLIMS glacier database. National Snow and Ice Data Center, Boulder, CO, digital media. [Available online at http://nsidc.org/data/nsidc-0272.html.]

Atkinson, G. D., 1971: Forecasters' guide to tropical meteorology. U.S. Air Force Tech. Rep. 240, 360 pp.

Baehr, J., H. Haak, S. Alderson, S. A. Cunningham, J. H. Jungclaus, and J. Marotzke, 2008: Timely detection of changes in the meridional overturning circulation at 26°N in the Atlantic. *J. Climate,* **20,** 5827–5841.

Bales, R. C., E. Mosley-Thompson, and J. R. McConnell, 2001: Variability of accumulation in northwest Greenland over the past 250 years. *Geophys. Res. Lett.,* **28,** 2679–2682.

Baringer, M. O., and J. Larsen, 2001: Sixteen years of Florida current transport at 27°N. *Geophys. Res. Lett.,* **28,** 3179–3182.

——, and C. S. Meinen, 2007: Thermohaline circulation [in "State of the Climate in 2006"]. *Bull. Amer. Meteor. Soc.,* **88** (6), S1–S135.

Behera, S. K., J.-J. Luo, S. Masson, S. A. Rao, H. Sakuma, and T. Yamagata, 2006: A CGCM study on the interaction between IOD and ENSO. *J. Climate*, **19**, 1688–1705.

Behrenfeld, M. J., and P. G. Falkowski, 1997: Photosynthetic rates derived from satellite-based chlorophyll concentration. *Limnol. Oceanogr.,* **42,** 1–20.

——, E. Boss, D. A. Siegel, and D. M. Shea, 2005: Carbon-based ocean productivity and phytoplankton physiology from space. *Global Biogeochem. Cycles,* **19,** GB1006, doi:10.1029/2004GB002299.

——, K. Halsey, and A. Milligan, 2008: Evolved physiological responses of phytoplankton to their integrated growth environment. *Philos. Trans. Roy. Soc. London,* **363,** doi:10.1098/rstb.2008.0019.

Behringer, D. W., M. Ji, and A. Leetmaa, 1998: An improved coupled model for ENSO prediction and implications for ocean initialization. Part I: The ocean data assimilation system. *Mon. Wea. Rev.,* **126,** 1013–1021.

Bell, G. D., and M. Chelliah, 2006: Leading tropical modes associated with interannual and multidecadal fluctuations in North Atlantic hurricane activity. *J. Climate,* **19,** 590–612.

——, and Coauthors, 2000: Climate assessment for 1999. *Bull. Amer. Meteor. Soc.,* **81,** S1–S50.

——, and Coauthors, 2007: The 2006 North Atlantic hurricane season: A climate perspective [in "State of the Climate in 2006"]. *Bull. Amer. Meteor. Soc.,* **87** (6), S1–S68.

Beránger, K., L. Siefridt, B. Barnier, E. Garnier, and H. Roquet, 1999: Evaluation of operational ECMWF surface freshwater fluxes of oceans during 1991-1997. *J. Mar. Syst.,* **22,** 13–36.

Bindoff, N. L., and Coauthors, 2007: Observations: Oceanic climate change and sea level. *Climate Change 2007: The Physical Science Basis*, S. Solomon, et al., Eds., Cambridge University Press, 385–431.

Bonjean, F., and G. S. E. Lagerloef, 2002: Diagnostic model and analysis of the surface currents in the tropical Pacific Ocean. *J. Phys. Oceanogr.,* **32,** 2938–2954.

Bopp, L., P. Monfray, O. Aumont, J.-L. Dufresne, H. Treut, G. Madec, L. Terray, and J. Orr, 2001: Potential impact of climate change on marine export production. *Global Biogeochem. Cycles,* **15,** 81–99.

Bousquet, P., and Coauthors, 2006: Contribution of anthropogenic and natural sources to atmospheric methane variability. *Nature,* **443,** 439–443.

Box, J. E., and A. E. Cohen, 2006: Upper-air temperatures around Greenland: 1964-2005. *Geophys. Res. Lett.,* **33,** L12706, doi:10.1029/2006GL025723.

——, and Coauthors, 2006: Greenland ice sheet surface mass balance variability (1988–2004) from calibrated Polar MM5 output. *J. Climate,* **19,** 2783–2800.

Boyd, P. W., and S. C. Doney, 2002: Modelling regional responses by marine pelagic ecosystems to global climate change. *Geophys. Res. Lett.,* **29,** 1806, doi:10.1029/2001GL014130.

Boyer, T. P., C. Stephens, J. I. Antonov, M. E. Conkright, R. A. Locarnini, T. D. O'Brien, and H. E. Garcia, 2002: *Salinity.* Vol. 2, *World Ocean Atlas 2001,* NOAA Atlas NESDIS 50, 165 pp.

Bretherton, F. P., R. E. Davis, and C. Fandry, 1976: A technique for objective analysis and design of oceanographic instruments applied to MODE-73. *Deep-Sea Res.,* **23,** 559–582.

Brodzik, M. J., R. L. Armstrong, E. C. Weatherhead, M. H. Savoie, K. W. Knowles, and D. A. Robinson, 2006: Regional trend analysis of satellite-derived snow extent and global temperature anomalies. *Eos, Trans. Amer. Geophys. Union,* **87** (Fall Meeting Suppl.), Abstract U33A-0011.

Brohan, P., J. J. Kennedy, I. Haris, S. F. B. Tett, and P. D. Jones, 2006: Uncertainty estimates in regional and global observed temperature changes: A new dataset from 1850. *J. Geophys. Res.,* **111,** D12106, doi:10.1029/2005JD006548.

Bromwich, D. H., 1988: Snowfall in high southern latitudes. *Rev. Geophys.,* **26,** 149–168.

——, Z. Guo, L. Bai, and Q.-S. Chen, 2004: Modeled Antarctic precipitation. Part I: Spatial and temporal variability. *J. Climate,* **17,** 427–447.

Bryden, H. L., H. R. Longworth, and S. A. Cunningham, 2005: Slowing of the Atlantic meridional overturning circulation at 25°N. *Nature,* **438,** 655–657.

Bunn, A. G., S. J. Goetz, J. S. Kimball, and K. Zhang, 2007: Northern high-latitude ecosystems respond to climate change. *Eos, Trans. Amer. Geophys. Union,* **88,** 333–334.

Camargo, S. J., and A. H. Sobel, 2005: Western North Pacific tropical cyclone intensity and ENSO. *J. Climate,* **18,** 2996–3006.

——, A. W. Robertson, S. J. Gaffney, P. Smyth, and M. Ghil, 2007a: Cluster analysis of typhoon tracks. Part II: Large-scale circulation and ENSO. *J. Climate,* **20,** 3654–3676.

——, K. A. Emanuel, and A. H. Sobel, 2007b: Use of a genesis potential index to diagnose ENSO effects on tropical cyclone genesis. *J. Climate,* **20**, 4819–4834.

Cappelen, J., E. V. Laursen, P. V. Jørgensen, and C. Kern-Hansen, 2007: DMI monthly Climate Data Collection 1768-2006, Denmark, The Faroe Islands and Greenland. Danish Meteorological Institute, Tech. Rep. 07-06, 53 pp.

——, ——, ——, and ——, 2008: DMI monthly Climate Data Collection 1768-2006, Denmark, The Faroe Islands and Greenland. Danish Meteorological Institute, Tech. Rep. 07-06, 53 pp.

Carr, M.-E., and Coauthors, 2006: A comparison of global estimates of marine primary production from ocean color. *Deep-Sea Res.,* **53,** 741–770.

Chaggar, T. S., 1984: Reunion sets new rainfall records. *Weather,* **39,** 12–14.

Chan, J. C. L., 1985: Tropical cyclone activity in the northwest Pacific in relation to El Niño/Southern Oscillation phenomenon. *Mon. Wea. Rev.,* **113,** 599–606.

——, cited 2008: Verification of forecasts of tropical cyclone activity over the western North Pacific in 2007. Laboratory for Atmospheric Research, City University of Hong Kong. [Available online at http://aposf02.cityu.edu.hk/~mcg/tc_forecast/2007_Verification.htm.]

Chapman, W. L., and J. E. Walsh, 2007a: Simulations of Arctic temperature and pressure by global coupled models. *J. Climate,* **20,** 609–632.

——, and ——, 2007b: A synthesis of Antarctic temperatures. *J. Climate,* **20,** 4096–4117.

Chen, D., 2000: A monthly circulation climatology for Sweden and its application to a winter temperature case study. *Int. J. Climatol.,* **20,** 1067–1076.

Chia, H. H., and C. F. Ropelewski, 2002: Interannual variability in the genesis location of tropical cyclones in the northwest Pacific. *J. Climate,* **15,** 2934–2944.

Christensen, J. H., and Coauthors, 2007: Regional climate projections. *Climate Change 2007: The Physical Science Basis,* S. Solomon, et al., Eds., Cambridge University Press, 847–939.

Christy, J. R., and S. J. Drouilhet, 1994: Variability in daily, zonal mean lower-stratospheric temperatures. *J. Climate,* **7,** 106–120.

——, R. W. Spencer, W. B. Norris, W. D. Braswell, and D. E. Parker, 2003: Error estimates of version 5.0 of MSU/AMSU bulk atmospheric temperatures. *J. Atmos. Oceanic Technol.,* **20,** 613–629.

Chu, P.-S., 2002: Large-scale circulation features associated with decadal variations of tropical cyclone activity over the central North Pacific. *J. Climate,* **15,** 2678–2689.

Church, J. A., and N. J. White, 2006: A 20th century acceleration in global sea-level rise. *Geophys. Res. Lett.,* **33,** L01602, doi:10.1029/2005GL024826.

——, ——, R. Coleman, K. Lambeck, and J. X. Mitrovica, 2004: Estimates of the regional distribution of sea level rise over the 1950–2000 period. *J. Climate,* **17,** 2609–2625.

Clerbaux, C., and D. Cunnold, 2007: Long-lived compounds. Scientific Assessment of Ozone Depletion: 2006, Global Ozone Research and Monitoring Project Rep. 50, World Meteorological Organization, 1.1–1.63.

Climate Prediction Center, 2007: *Climate Diagnostics Bulletin*, October 2007. [Available from U.S. Dept. of Commerce, NOAA, NWS, Climate Prediction Center, 5200 Auth Road, Camp Springs, MD 20746–4304.]

——, 2008: *Climate Diagnostics Bulletin*, April 2008. [Available online at http://www.cpc.ncep.noaa.gov/products/CDB.]

Cogley, G. J., 2005: Mass and energy balances of glaciers and ice sheets. *Encyclopedia of Hydrological Sciences*, M. Anderson, Ed., John Wiley and Sons, 2555–2573.

Comiso, J. C., C. L. Parkinson, R. Gersten, and L. Stock, 2008: Accelerated decline in the Arctic sea ice cover. *Geophys. Res. Lett.,* **35,** L01703, doi:10.1029/2007GL031972.

Conway, T. J., P. P. Tans, L. S. Waterman, K. W. Thoning, D. R. Kitzis, K. A. Masarie, and N. Zhang, 1994: Evidence for interannual variability of the carbon cycle from the NOAA CMDL global air sampling network. *J. Geophys. Res.,* **99,** 22 831–22 855.

Cooper, T. F., G. De'Ath, K. E. Fabricius, and J. Lough, 2008: Declining coral calcification in massive Porites in two nearshore regions of the northern Great Barrier Reef. *Global Change Biol.,* **14,** 529–538.

Cosca, C. E., R. A. Feely, J. Boutin, J. Etcheto, M. J. McPhaden, F. P. Chavez, and P. G. Strutton, 2003: Seasonal and interannual CO_2 fluxes for the central and eastern equatorial Pacific Ocean as determined from fCO_2-SST relationships. *J. Geophys. Res.,* **108,** 3278, doi:10.1029/2000JC000677.

Couture, R., S. Smith, S. D. Robinson, M. M. Burgess, and S. Solomon, 2003: On the hazards to infra-

structure in the Canadian North associated with thawing of permafrost. *Proc. Geohazards (2003), Third Canadian Conf. on Geotechnique and Natural Hazards,* Edmonton, Alberta, Canada, The Canadian Geotechnical Society, 97–104.

Cunninghman, S. A., and Coauthors, 2007: Temporal variability of the Atlantic meridional overturning circulation at 26.5ºN. *Science,* **317,** 935–938.

Curry, R. G., and M. S. McCartney, 2001: Ocean gyre circulation changes associated with the North Atlantic oscillation. *J. Phys. Oceanogr.,* **31,** 3374–3400.

Curtis, S., and R. Adler, 2000: ENSO indexes based on patterns of satellite-derived precipitation. *J. Climate,* **13,** 2786–2793.

Daniel, J. S., and S. Solomon, 1998: On the climate forcing of carbon monoxide. *J. Geophys. Res.,* **103,** 13 249–13 260.

Della-Marta, P. M., D. A. Collins, and K. Braganza, 2004: Updating Australia's high-quality annual temperature dataset. *Aust. Meteor. Mag.,* **53,** 75–93.

DeMaria, M., M. J. Baik, and J. Kaplan, 1993: Upper-level eddy angular momentum fluxes and tropical cyclone intensity change. *J. Atmos. Sci.,* **50,** 1133–1147.

Denman, K. L., and Coauthors, 2007: Couplings between changes in the climate system and biogeochemistry. *Climate Change 2007: The Physical Science Basis,* S. Solomon et al., Eds., Cambridge University Press, 499–588.

Dlugokencky, E. J., S. Houweling, L. Bruhwiler, K. A. Masarie, P. M. Lang, J. B. Miller, and P. P. Tans, 2003: Atmospheric methane levels off: Temporary pause or new steady state? *Geophys. Res. Lett.,* **30,** 1992, doi:10.1029/2003GL018126.

Dmitrenko, I. A., and Coauthors, 2008: Toward a warmer Arctic Ocean: Spreading of the early 21st century Atlantic Water warm anomaly along the Eurasian Basin margins. *J. Geophys. Res.*, **113,** C05023, doi:10.1029/2007JC004158.

Durre, I., R. S. Vose, and D. B. Wuertz, 2006: Overview of the integrated global radiosonde archive. *J. Climate,* **19,** 53–68.

Dyurgerov, M. B., and M. F. Meier, 2005: Glaciers and the changing earth system: A 2004 snapshot. Institute of Arctic and Alpine Research, University of Colorado Occasional Paper 58, 117 pp.

Emanuel, K. A., 2005: Increasing destructiveness of tropical cyclones over the past 30 years. *Nature,* **436,** 686–688.

——, and D. S. Nolan, 2004: Tropical cyclone activity and the global climate system. *Proc. 26th Conf. on Hurricanes and Tropical Meteorology*, Miami, FL, Amer. Meteor. Soc., 240–241. [Available online at http://ams.confex.com/ams/pdfpapers/75463.pdf.]

Enfield, D. B., and A. M. Mestas-Nuñez, 1999: Multiscale variabilities in global sea surface temperatures and their relationships with tropospheric climate patterns. *J. Climate,* **12,** 2719–2733.

Espirito-Santo, F. E., V. Pires, A. Silva, S. Moita, T. Cota, and L. Mendes, 2008: *Characterization of the Climate in Portugal during 2007* (in Portuguese). Instituto de Meteorologia, 47 pp.

Evan, A. T., 2008: Global aerosols [in "State of the Climate in 2007"]. *Bull. Amer. Meteor. Soc.,* **89,** S31–S32.

——, N. Mahowald, and L. Remer, 2007: Aerosols [in "State of the Climate in 2006"]. *Bull. Amer. Meteor. Soc.,* **88** (6), S23–S25.

Fairall, C. W., E. F. Bradley, J. E. Hare, A. A. Grachev, and J. B. Edson, 2003: Bulk parameterization on air–sea fluxes: Updates and verification for the COARE algorithm. *J. Climate,* **16,** 571–591.

Feely, R. A., and Coauthors, 2002: Seasonal and interannual variability of CO_2 in the equatorial Pacific. *Deep-Sea Res. II,* **49,** 2443–2469.

——, C. L. Sabine, K. Lee, W. Berrelson, J. Kleypas, V. J. Fabry, and F. J. Millero, 2004: Impact of anthropogenic CO_2 on the $CaCO_3$ system in the oceans. *Science,* **305,** 362–366.

——, T. Takahashi, R. Wanninkhof, M. J. McPhaden, C. E. Cosca, and S. C. Sutherland, 2006: Decadal variability of the air-sea CO_2 fluxes in the equatorial Pacific Ocean. *J. Geophys. Res.,* **111,** C08S90, doi:10.1029/2005JC003129.

——, V. J. Fabry, and J. M. Guinotte, 2008: Ocean acidification of the North Pacific Ocean. *PICES Press,* **16** (1), 22–26.

Fetterer, F., K. Knowles, W. Meier, and M. Savoie, 2002: Sea ice index. National Snow and Ice Data Center, Boulder, CO, digital media. [Available online at http://nsidc.org/data/seaice_index/.]

Fiore, A. M., L. W. Horowitz, E. J. Dlugokencky, and J. J. West, 2006: Impact of meteorology and emissions on methane trends, 1990–2004. *Geophys. Res. Lett.,* **33,** L12809, doi:10.1029/2006GL026199.

Fogt, R. L., and D. Bromwich, 2006: Decadal variability of the ENSO teleconnection to the high-latitude South Pacific governed by coupling with the southern annular mode. *J. Climate,* **19,** 979–997.

Forster, P., and Coauthors, 2007: Changes in atmospheric constituents and in radiative forcing. *Climate Change 2007: The Physical Science Basis,* S. Solomon et al., Eds., Cambridge University Press, 129–234.

Free, M., D. J. Seidel, and J. K. Angell, 2005: Radiosonde Atmospheric Temperature Products for Assessing Climate (RATPAC): A new data set of large-area

anomaly time series . *J. Geophys. Res.,* **110,** D22101, doi:10.1029/2005/D006169.

Frei, A., and D. A. Robinson, 1999: Northern Hemisphere snow extent: Regional variability 1972-1994. *Int. J. Climatol.,* **19,** 1535–1560.

Ganachaud, A., and C. Wunsch, 2003: Large-scale ocean heat and freshwater transports during the World Ocean Circulation Experiment. *J. Climate,* **16,** 696–705.

Garcia-Herrera, R., D. Paredes, R. M. Trigo, I. F. Trigo, H. Hernández, D. Barriopedro, and M. T. Mendes, 2007: The outstanding 2004/05 drought in the Iberian Peninsula: Associated atmospheric circulation. *J. Hydrometeor.,* **8,** 483–498.

Gascard, J. C., and Coauthors, 2008: Exploring Arctic transpolar drift during dramatic sea ice retreat. *Eos, Trans. Amer. Geophys. Union,* **89,** 21–28.

Gates, W. L., 1992: AMIP: The Atmospheric Model Intercomparison Project. *Bull. Amer. Meteor. Soc.,* **73,** 1962–1970.

Genthon, C., 2004: Space-time Antarctic surface mass balance variability from climate models. *Ann. Glaciol.,* **39,** 271–275.

GLOBALVIEW-CO2, 2007: *Cooperative Atmospheric Data Integration Project—Carbon Dioxide.* NOAA/ESRL, Boulder, CO, CD-ROM. [Available online at ftp.cmdl.noaa.gov/ccg/co2/GLOBALVIEW.]

Goetz, S. J., A. G. Bunn, G. J. Friske, and R. A. Houghton, 2005: Satellite-observed photosynthetic trends across boreal North America associated with climate and fire disturbance. *Proc. Natl. Acad. Sci. USA,* **102,** 13 521–13 525.

Goldenberg, S. B., and L. J. Shapiro, 1996: Physical mechanisms for the association of El Niño and West African rainfall with Atlantic major hurricane activity. *J. Climate,* **9,** 1169–1187.

——, C. W. Landsea, A. M. Mestas-Nuñez, and W. M. Gray, 2001: The recent increase in Atlantic hurricane activity: Causes and implications. *Science,* **293,** 474–479.

Goni, G., S. Kamholz, S. Garzoli, and D. Olson, 1996: Dynamics of the Brazil-Malvinas confluence based on inverted echo sounders and altimetry. *J. Geophys. Res.,* **101,** 16 273–16 289.

Goswami, B. N., V. Krishnamurthy, and H. Annamalai, 1999: A broad scale circulation index for the interannual variability of Indian summer monsoon. *Quart. J. Roy. Meteor. Soc.,* **125,** 611–633.

Gray, W. M., 1984: Atlantic seasonal hurricane frequency. Part I: El Niño and 30 mb quasi-biennial oscillation influences. *Mon. Wea. Rev.,* **112,** 1649–1668.

Groisman, P. Ya., R. W. Knight, T. R. Karl, D. R. Easterling, B. Sun, and J. H. Lawrimore, 2004: Contemporary changes of the hydrological cycle over the contiguous United States, trends derived from in situ observations. *J. Hydrometeor.,* **5,** 64–85.

——, ——, D. R. Easterling, T. R. Karl, G. C. Hegerl, and V. N. Razuvaev, 2005: Trends in intense precipitation in the climate record. *J. Climate,* **18,** 1326–1350.

Gurney, K. R., R. M. Law, A. S. Denning, P. J. Rayner, B. Pak, and the TransCom-3L2 modelers, 2004: Transcom-3 inversion intercomparison: Control results for the estimation of seasonal carbon sources and sinks. *Global Biogeochem. Cycles,* **18,** GB1010, doi:10.1029/2003GB002111.

Haas, C., 2004: Late-summer sea ice thickness variability in the Arctic Transpolar Drift 1991-2001 derived from ground-based electromagnetic sounding. *Geophys. Res. Lett.,* **31,** L09402, doi:10.1029/2003GL019394.

Haimberger, L., 2007: Homogenization of radiosonde temperature time series using innovation statistics. *J. Climate,* **20,** 1377–1403.

Haine, T. W. N., and S. L. Gray, 2001: Quantifying mesoscale variability in ocean transient tracer fields. *J. Geophys. Res.,* **106,** 13 861–13 878.

Hanna, E., J. McConnell, S. Das, J. Cappelen, and A. Stephens, 2006: Observed and modeled Greenland Ice Sheet snow accumulation, 1958–2003, and links with regional climate forcing. *J. Climate,* **19,** 344–358.

Hansen, J., R. Ruedy, M. Sato, M. Imhoff, W. Lawrence, D. Easterling, T. Peterson, and T. Karl, 2001: A closer look at United States and global surface temperature change. *J. Geophys. Res.,* **106,** 23 947–23 963.

——, and Coauthors, 2005: Earth's energy imbalance: Confirmation and implications. *Science,* **308,** 1431–1435.

Harris, C., and Coauthors, 2003: Warming permafrost in European mountains. *Global Planet. Change,* **39,** 215–225.

Hátún, H., A. B. Sandø, H. Drange, B. Hansen, and H. Valdimarsson, 2005: Influence of the Atlantic subpolar gyre on the thermohaline circulation. *Science,* **309,** 1841–1844.

Held, I. M., and B. J. Soden, 2006: Robust response of the hydrological cycle to global warming. *J. Climate,* **19,** 5686–5699.

Hendon, H., C. Zhang, and J. Glick, 1999: Interannual variation of the Madden–Julian oscillation during austral summer. *J. Climate,* **12,** 2538–2550.

Hoegh-Guldberg, O., and Coauthors, 2007: Coral reefs under rapid climatic and ocean acidification. *Science,* **318,** 1737–1742.

Hofmann, D. J., J. H. Butler, E. J. Dlugokencky, J. W. Elkins, K. Masarie, S. A. Montzka, and P. Tans, 2006: The role of carbon dioxide in climate forcing from 1979-2004. *Tellus,* **58B,** 614–619.

Holgate, S., 2007: On the decadal rates of sea level change during the twentieth century. *Geophys. Res. Lett.,* **34,** L01602, doi:10.1029/2006GL028492.

Holland, G. J., 1993: Ready Reckoner. Global Guide to Tropical Cyclone Forecasting, WMO/TC 560, Rep. TCP-31. [Available online at http://www.bom.gov.au/bmrc/pubs/tcguide/ch9/ggch9.htm.]

Ignatov, A., and L. Stowe, 2002a: Aerosol retrievals from individual AVHRR channels. Part I: Retrieval algorithm and transition from Dave to 6S radiative transfer model. *J. Atmos. Sci.,* **59,** 313–334.

——, and ——, 2002b: Aerosol retrievals from individual AVHRR channels. Part II: Quality control, probability distribution functions, information content, and consistency checks of retrievals. *J. Atmos. Sci.,* **59,** 335–362.

IOCCG, 2006: Remote sensing of inherent optical properties. Fundamentals, tests of algorithms, and applications. Z.-P. Lee, Ed., Reports of the International Ocean-Colour Coordinating Group, No. 5, 122 pp.

Isaksen, K., D. Vonder Mühll, H. Gubler, T. Kohl, and J. L. Sollid, 2000: Ground surface temperature reconstruction based on data from a deep borehole in permafrost at Janssonhaugen, Svalbard. *Ann. Glaciol.,* **31,** 287–294.

Jacobson, A. R., S. E. Mikaloff Fletcher, N. Gruber, J. S. Sarmineto, and M. Gloor, 2007: A joint atmosphere-ocean inversion for surface fluxes of carbon dioxide: 1. Methods and global-scale fluxes. *Global Biogeochem. Cycles,* **21,** GB1019, doi:10.1029/2005GB002556.

Janowiak, J. E., and P. Xie, 1999: CAMS–OPI: A global satellite–rain gauge merged product for real-time precipitation monitoring applications. *J. Climate,* **12,** 3335–3342.

Jauregui, E., 2003: Climatology of landfalling hurricanes and tropical storms in Mexico. *Atmósphera,* **16,** 193–204.

Jia, G. J., H. E. Epstein, and D. A. Walker, 2003: Greening of arctic Alaska, 1981–2001. *Geophys. Res. Lett.,* **30,** 2067, doi:10.1029/2003GL018268.

——, ——, and ——, 2007: Trends in vegetation greenness in the Arctic from 1982-2005. *Eos, Trans. Amer. Geophys. Union,* **88** (Fall Meeting Suppl.), Abstract B21-0041.

Johnson, E. S., F. Bonjean, G. S. E. Lagerloef, J. T. Gunn, and G. T. Mitchum, 2007: Validation and error analysis of OSCAR sea surface currents. *J. Atmos. Oceanic Technol.,* **24,** 688–701.

Jones, P. D., T. Jónsson, and D. Wheeler, 1997: Extension to the North Atlantic Oscillation using early instrumental pressure observations from Gibraltar and South-West Iceland. *Int. J. Climatol.,* **17,** 1433–1450.

Kalnay, E., and Coauthors, 1996: The NCEP/NCAR 40-Year Reanalysis Project. *Bull. Amer. Meteor. Soc.,* **77,** 437–471.

Kanzow, T., and Coauthors, 2007: Observed flow compensation associated with the meridional overturning circulation near 26.5°N in the Atlantic. *Science,* **317,** 938–941.

Karl, T. R., and W. J. Koss, 1984: Regional and national monthly, seasonal and annual temperature weighted by area, 1895-1983. Historical Climatography Series 4-3, NOAA/NESDIS/NCDC.

Kaser, G., J. G. Cogley, M. B. Dyurgerov, M. F. Meier, and A. Ohmura, 2006: Mass balance of glaciers and ice caps: Consensus estimates for 1961–2004. *Geophys. Res. Lett.,* **33**, L19501, doi:10.1029/2006GL027511.

Kasischke, E. S., and Coauthors, 2000: Contributions of 1998 fires in the boreal forest to atmospheric concentrations of carbon monoxide and methane. *Eos, Trans. Amer. Geophys. Union,* **81,** 260.

Kaufman, Y. J., D. Tanre, and O. Boucher, 2002: A satellite view of aerosols in the climate system. *Nature,* **419,** 215–223.

Kayano, M., and V. Kousky, 1999: Intraseasonal (30-60 day) variability in the global tropics: Principal modes and their evolution. *Tellus*, **51A,** 373–386.

Keeley, S. P., N. P. Gillett, D. W. J. Thompson, S. Solomon, and P. M. Forster, 2007: Is Antarctic climate most sensitive to ozone depletion in the middle or lower stratosphere? *Geophys. Res. Lett.,* **34,** L22812, doi:10.1029/2007GL031238.

Keppler, F., J. T. G. Hamilton, M. Brass, and T. Rockmann, 2006: Methane emissions from terrestrial plants under aerobic conditions. *Nature,* **439,** 187–191.

Key, R. M., and Coauthors 2004: A global ocean carbon climatology: Results from Global Data Analysis Project (GLODAP). *Global Biogeochem. Cycles,* **18,** GB4031, doi:10.1029/2004GB002247.

Kidson, J. W., and J. A. Renwick, 2002: The Southern Hemisphere evolution of ENSO during 1981–99. *J. Climate,* **15,** 847–863.

Kiladis, G. N., and H. F. Diaz, 1989: Global climatic anomalies associated with extremes in the Southern Oscillation. *J. Climate,* **2,** 1069–1090.

Kocin, P. J., and L. W. Uccellini, 2004: A snowfall impact scale derived from northeast storm snowfall distributions. *Bull. Amer. Meteor. Soc.,* **85,** 177–194.

Koltermann, K. P., A. V. Sokov, V. P. Tereschenkov, S. A. Dobroliubov, K. Lorbacher, and A. Sy, 1999: Decadal changes on the thermohaline circulation of the North Atlantic. *Deep-Sea Res. II,* **46,** 109–138.

Koren, I., Y. J. Kaufman, L. A. Remer, and J. V. Martins, 2004: Measurement of the effect of Amazon smoke

on inhibition of cloud formation. *Science,* **303,** 1342–1345.

——, L. A. Remer, and K. Longo, 2007: Reversal of trend of biomass burning in the Amazon. *Geophys. Res. Lett.,* **34,** L20404, doi:10.1029/2007GL031530.

Kousky, V., and M. Kayano, 1994: Principal modes of outgoing longwave radiation and 250-mb circulation for the South American sector. *J. Climate,* **7,** 1131–1143.

Kwok, R., 2007: Near zero replenishment of the Arctic multiyear sea ice cover at the end of 2005 summer. *Geophys. Res. Lett.,* **34,** L05501, doi:10.1029/2006GL028737.

——, H. J. Zwally, and D. Yi, 2004: ICESat observations of Arctic sea ice: A first look. *Geophys. Res. Lett.,* **31,** L16401, doi:10.1029/2004GL020309.

Lamb, H. H., 1950: Types and spells of weather around the year in the British Isles. *Quart. J. Roy. Meteor. Soc.,* **76,** 393–438.

Lander, M. A., and C. P. Guard, 1998: A look at global tropical cyclone activity during 1995: Contrasting high Atlantic activity with low activity in other basins. *Mon. Wea. Rev.,* **126,** 1163–1173.

Landsea, C. W., 2007: Counting Atlantic tropical cyclones back to 1900. *Eos, Trans. Amer. Geophys. Union,* **88,** 197–202.

——, and W. M. Gray, 1992: The strong association between Western Sahel monsoon rainfall and intense Atlantic hurricanes. *J. Climate,* **5,** 435–453.

——, G. D. Bell, W. M. Gray, and S. B. Goldenberg, 1998: The extremely active 1995 Atlantic hurricane season: Environmental conditions and verification of seasonal forecasts. *Mon. Wea. Rev.,* **126,** 1174–1193.

——, R. A. Pielke Jr., A. M. Mestas-Nuñez, and J. A. Knaff, 1999: Atlantic basin hurricanes: Indices of climatic changes. *Climatic Change,* **42,** 89–129.

Langenfelds, R. L., R. J. Francey, B. C. Pak, L. P. Steele, J. Lloyd, C. M. Trudinger, and C. E. Allison, 2002: Interannual growth rate variations of atmospheric CO_2 and its $\delta^{13}C$, H_2, CH_4, and CO between 1992 and 1999 linked to biomass burning. *Global Biogeochem. Cycles,* **16,** 1048, doi:10.1029/2001GB001466.

Lavery, B., G. Joung, and N. Nicholls, 1997: An extended high-quality historical rainfall dataset for Australia. *Aust. Meteor. Mag.,* **46,** 27–38.

Laxon, S., N. Peacock, and D. Smith, 2003: High interannual variability of sea ice thickness in the Arctic Region. *Nature,* **425,** 947–950.

Lee, K., R. Wanninkhof, T. Takahashi, S. Doney, and R. A. Feely, 1998: Low interannual variability in recent oceanic uptake of atmospheric carbon dioxide. *Nature,* **396,** 155–159.

Lemke, P., and Coauthors, 2007: Observations: Changes in Snow, Ice and Frozen Ground. *Climate Change 2007: The Physical Science Basis,* S. Solomon et al., Eds., Cambridge University Press, 338–383.

Le Quéré, C., O. Aumont, P. Monfray, and J. Orr, 2003: Propagation of climatic events on ocean stratification, marine biology, and CO_2: Case studies over the 1979-1999 period. *J. Geophys. Res.,* **108,** 3375, doi:10.1029/2001JC000920.

Levitus, S., J. I. Antonov, and T. P. Boyer, 2005: Warming of the World Ocean, 1955–2003. *Geophys. Res. Lett.*, **32**, L02604, doi:10.1029/2004GL021592.

L'Heureux, M. L., and D. W. J. Thompson, 2006: Observed relationships between the El Niño–Southern Oscillation and the extratropical zonal-mean circulation. *J. Climate,* **19,** 276–287.

Liang, S., J. Stroeve, and J. E. Box, 2005: Mapping daily snow/ice shortwave broadband albedo from Moderate Resolution Imaging Spectroradiometer (MODIS): The improved direct retrieval algorithm and validation with Greenland *in situ* measurement. *J. Geophys. Res.,* **110,** D10109, doi:10.1029/2004JD005493.

Liu, H., L. Wang, and K. Jezek, 2005: Wavelet-based edge detection approach to derivation of snow-melt onset, duration and extent from satellite passive microwave measurements. *Int. J. Remote Sens.*, **26,** 4639–4660.

——, L. Wang, and K. Jezek, 2006: Spatiotemporal variations of snowmelt in Antarctica derived from satellite scanning multichannel microwave radiometer and Special Sensor Microwave Imager data (1978–2004). *J. Geophys. Res.,* **111,** F01003, doi:10.1029/2005JF000318.

Liu, Y., J. R. Key, J. A. Francis, and X. Wang, 2007: Possible causes of decreasing cloud cover in the Arctic winter, 1982–2000. *Geophys. Res. Lett.,* **34,** L14705, doi:10.1029/2007GL030042.

Lucht, W., and Coauthors, 2002: Climatic control of the high-latitude vegetation greening trend and Pinatubo effect. *Science,* **296,** 1687–1689.

Lumpkin, R., and S. L. Garzoli, 2005: Near-surface circulation in the Tropical Atlantic Ocean. *Deep-Sea Res. I,* **52,** 495–518.

——, and K. Speer, 2007: Global ocean meridional overturning. *J. Phys. Oceanogr.,* **37**, 2550–2562.

——, K. G. Speer, and K. P. Koltermann, 2008: Transport across 48°N in the Atlantic Ocean. *J. Phys. Oceanogr.,* **38,** 733–752.

Luo, J.-J., S. Masson, S. Behera, and T. Yamagata, 2007: Experimental forecasts of the Indian Ocean Dipole using a coupled OAGCM. *J. Climate,* **20,** 2178–2190.

——, S. Behera, Y. Masumoto, H. Sakuma, and T. Yamagata, 2008: Successful prediction of the con-

secutive IOD in 2006 and 2007. *Geophys. Res. Lett.,* **35,** L14S02, doi:10.1029/2007GL032793.

Luterbacher, J., M. A. Liniger, A. Menzel, N. Estrella, P. M. Della-Marta, C. Pfister, T. Rutishauser, and E. Xoplaki, 2007: Exceptional European warmth of autumn 2006 and winter 2007: Historical context, the underlying dynamics, and its phenological impacts. *Geophys. Res. Lett.,* **34,** L12704, doi:10.1029/2007GL029951.

Madden, R., and P. Julian, 1971: Detection of a 40-50 day oscillation in the zonal wind in the tropical Pacific. *J. Atmos. Sci.,* **28,** 702–708.

——, and ——, 1972: Description of global-scale circulation cells in the tropics with a 40-50 day period. *J. Atmos. Sci.,* **29,** 1109–1123.

——, and ——, 1994: Observations of the 40–50 day tropical oscillation: A review. *Mon. Wea. Rev.,* **122,** 814–837.

Maes, C., K. Ando, T. Delcroix, W. S. Kessler, M. J. McPhaden, and D. Roemmich, 2006: Observed correlation of surface salinity, temperature and barrier layer at the eastern edge of the western Pacific warm pool. *Geophys. Res. Lett.,* **33,** L06601, doi:10.1029/2005GL024772.

Maier-Reimer, E., and K. Hasselmann, 1987: Transport and storage of CO_2 in the ocean—An inorganic ocean-circulation carbon cycle model. *Climate Dyn.,* **2,** 63–90.

Mainelli, M., M. DeMaria, L. Shay, and G. Goni, 2008: Application of oceanic heat content estimation to operational forecasting of recent Atlantic category 5 hurricanes. *Wea. Forecasting,* **23,** 3–16.

Maritorena, S., D. A. Siegel, and A. R. Peterson, 2002: Optimization of a semianalytical ocean color model for global-scale applications. *Appl. Opt.,* **41,** 2705–2714.

Marland, G., T. A. Boden, and R. J. Andres, 2007: Global, regional, and national fossil fuel CO_2 emissions. Trends: A Compendium of Data on Global Change, Carbon Dioxide Information Analysis Center, Oak Ridge National Laboratory, U.S. Department of Energy, Oak Ridge, TN. [Available online at http://cdiac.ornl.gov/trends/emis/tre_glob.htm.]

Marshall, G. J., 2003: Trends in the southern annular mode from observations and reanalyses. *J. Climate,* **16,** 4134–4143.

——, 2007: Half-century seasonal relationships between the southern annular mode and Antarctic temperatures. *Int. J. Climatol.,* **27,** 373–383.

Maslanik, J. A., C. Fowler, J. Stroeve, S. Drobot, J. Zwally, D. Yi, and W. Emery, 2007: A younger, thinner Arctic ice cover: Increased potential for rapid, extensive sea-ice loss. *Geophys. Res. Lett.,* **34,** L24501, doi:10.1029/2007GL032043.

Massom, R., S. Stammerjohn, W. Lefebvre, S. Harangozo, N. Adams, T. Scambos, M. Pook, and C. Fowler, 2008: West Antarctic Peninsula sea ice in 2005: Extreme ice compaction and ice edge retreat due to strong anomaly with respect to climate. *J. Geophys. Res.,* **113,** C02S20, doi:10.1029/2007JC004239.

McLaughlin, F. A., E. C. Carmack, R. W. Macdonald, H. Melling, J. H. Swift, P. A. Wheeler, B. F. Sherr, and E. B. Sherr, 2004: The joint roles of Pacific and Atlantic-origin waters in the Canada Basin, 1997-1998. *Deep-Sea Res. I,* **51,** 107–128.

Mears, C. A., and F. W. Wentz, 2005: The effect of diurnal correction on satellite-derived lower tropospheric temperature. *Science,* **309,** 1548–1551.

——, M. C. Schabel, and F. J. Wentz, 2003: A reanalysis of the MSU channel 2 tropospheric temperature record. *J. Climate,* **16,** 3650–3664.

Meier, M. F., M. B. Dyurgerov, U. K. Rick, S. O'Neel, W. T. Pfeffer, R. Anderson, and S. Anderson, 2007: Glaciers and ice caps to dominate sea level rise through 21st century. *Science,* **317,** 1064–1067.

Melling, H., D. A. Riedel, and Z. Gedalof, 2005: Trends in the draft and extent of seasonal pack ice, Canadian Beaufort Sea. *Geophys. Res. Lett.,* **32,** L24501, doi:10.1029/2005GL024483.

Merrifield, M.A., S. Gill, G.T. Mitchum, and P.L. Woodworth, 2007: Sea level [in "State of the Climate in 2006"]. *Bull. Amer. Meteor. Soc.,* **88** (6), S39–S40.

Mishchenko, M. I., and Coauthors, 2007: Accurate monitoring of terrestrial aerosols and total solar irradiance: Introducing the Glory mission. *Bull. Amer. Meteor. Soc.,* **88,** 677–691.

Mo, K. C., and R. E. Livezey, 1986: Tropical-extratropical geopotential height teleconnections during the northern hemisphere winter. *Mon. Wea. Rev.,* **114,** 2488–2515.

——, and V. E. Kousky, 1993: Further analysis of the relationship between circulation anomaly patterns and tropical convection. *J. Geophys. Res.,* **98,** 5103–5113.

Monaghan, A. J., D. H. Bromwich, and S.-H. Wang, 2006: Recent trends in Antarctic snow accumulation from Polar MM5. *Philos. Trans. Roy. Soc.*, **364,** 1683–1708.

Montzka, S. A., R. C. Myers, J. H. Butler, J. W. Elkins, L. Lock, A. Clarke, and A. H. Goldstein, 1996: Observations of HFC-134a in the remote troposphere. *Geophys. Res. Lett.,* **23,** 169–172.

——, J. H. Butler, J. W. Elkins, T. M. Thompson, A. D. Clarke, and L. T. Lock, 1999: Present and future trends in the atmospheric burden of ozone-depleting halogens. *Nature,* **398,** 690–694.

Morel, A., and J.-F. Berthon, 1989: Surface pigments, algal biomass profiles, and potential production of the

euphotic layer: Relationships reinvestigated in view of remote-sensing applications. *Limnol. Oceanogr.,* **34,** 1545–1562.

Morison, J., K. Aagaard, and M. Steele, 2000: Recent changes in the Arctic: A review. *Arctic,* **53,** 359–371.

——, M. Steele, T. Kikuchi, K. Falkner, and W. Smethie, 2006: Relaxation of central Arctic Ocean hydrography to pre-1990s climatology. *Geophys. Res. Lett.,* **33,** L17604, doi:10.1029/2006GL026826.

Mosley-Thompson, E., and Coauthors, 2001: Local to regional-scale variability of Greenland accumulation from PARCA cores. *J. Geophys. Res.,* **106** (D24), 33 839–33 851.

Mote, P. W., A. F. Hamlet, M. P. Clark, and D. P. Lettenmaier, 2005: Declining mountain snowpack in western North America. *Bull. Amer. Meteor. Soc.,* **86,** 39–49.

Mote, T. L., 2007: Greenland surface melt trends 1973–2007: Evidence of a large increase in 2007. *Geophys. Res. Lett.,* **34,** L22507, doi:10.1029/2007GL031976.

Münnich, M., and J. D. Neelin, 2005: Seasonal influence of ENSO on the Atlantic ITCZ and equatorial South America. *Geophys. Res. Lett.,* **32,** L21709, doi:10.1029/2005GL023900.

Myneni, R. B., C. D. Keeling, C. J. Tucker, G. Asrar, and R. R. Nemani, 1997: Increased plant growth in the northern high latitudes from 1981 to 1991. *Nature,* **38,** 698–702.

Neumann, C. J., 1999: The HURISK model: An adaptation for the Southern Hemisphere (A user's manual). Rep. Science Applications International Corporation, Monterey, CA, 31 pp. [Available from SAIC, 550 Camino El Estero, Suite 205, Monterey, CA 93940, or Naval Research Laboratory, Monterey, CA 93943.]

——, B. R. Jarvinen, C. J. McAdie, and J. D. Elms, 1993: Tropical Cyclones of the North Atlantic Ocean, 1871–1992. National Climatic Data Center in cooperation with the National Hurricane Center, Coral Gables, FL, 193 pp.

Newman, P. A, E. R. Nash, S. R. Kawa, S. A. Montzka, and S. M. Schauffler, 2006: When will the ozone hole recover? *Geophys. Res. Lett.,* **33,** L12814, doi:10.1029/2005GL025232.

Nghiem, S. V, I. G. Rigor, D. K. Perovich, P. Clemente-Colon, J. W. Weatherly, and G. Neumann, 2007: Rapid reduction of Arctic perennial sea ice. *Geophys. Res. Lett.,* **34,** L19504, doi:10.1029/2007GL031138.

Niiler, P. P., N. A. Maximenko, G. G. Panteleev, T. Yamagata, and D. B. Olson, 2003: Near-surface dynamical structure of the Kuroshio Extension. *J. Geophys. Res.,* **108,** 3193, doi:10.1029/2002JC001461.

NOAA, cited 2007: Background information: East Pacific hurricane season. [Available online at http://www.cpc.ncep.noaa.gov/products/Epac_hurr/background_information.html.]

NOAA/NESDIS/OSDPD/SSD, 2006: IMS daily Northern Hemisphere snow and ice analysis at 4 km and 24 km resolution. National Snow and Ice Data Center, Boulder, CO, digital media. [Available online at http://nsidc.org/data/g02156.html.]

Nobre, P., and J. Shukla, 1996: Variations of sea surface temperature, wind stress and rainfall over the tropical Atlantic and South America. *J. Climate,* **9,** 2464–2479.

Novelli, P. C., K. A. Masarie, P. M. Lang, B. D. Hall, R. C. Myers, and J. C. Elkins, 2003: Reanalysis of tropospheric CO trends: Effects of the 1997-1998 wildfires. *J. Geophys. Res.,* **108,** 4464, doi:10.1029/2002JD003031.

Oberman, N. G., and G. G. Mazhitova, 2001: Permafrost dynamics in the north-east of European Russia at the end of the 20th century. *Norw. J. Geogr.*, **55**, 241–244.

Ogi, M., and J. M. Wallace, 2007: Summer minimum Arctic sea ice extent and the associated summer atmospheric circulation. *Geophys. Res. Lett.,* **34,** L12705, doi:10.1029/2007GL029897.

Orr, J. C., and Coauthors, 2005: Anthropogenic ocean acidification over the twenty-first century and its impact on calcifying organisms. *Nature,* **437,** 681–686.

Osterkamp, T. E., 2003: A thermal history of permafrost in Alaska. *Permafrost: Proceedings of the 8th International Conference on Permafrost, Zurich, Switzerland, 21-25 July 2003,* M. Phillips, S. M. Springman, and L. U. Arenson, Eds., Vol. 2, A. A. Balkema, 863–868.

——, 2005. The recent warming of permafrost in Alaska. *Global Planet. Change,* **49,** 187–202.

——, and V. E. Romanovsky, 1999: Evidence for warming and thawing of discontinuous permafrost in Alaska. *Permafrost Periglacial Processes,* **10,** 17–37.

Padgett, G., cited 2008: Monthly global tropical cyclone summaries. [Available online at www.metoffice.gov.uk/weather/tropicalcyclone/observations.html.]

Park, G.-H., K. Lee, R. Wanninkhof, and R. A. Feely, 2006: Empirical temperature-based estimates of variability in the oceanic uptake of CO_2 over the past 2 decades. *J. Geophys. Res.,* **111,** C07S07, doi:10.1029/2005JC003090.

Parker, D. E., T. P. Legg, and C. K. Folland, 1992: A new daily Central England Temperature Series, 1772–1991. *Int. J. Climatol.,* **12,** 317–342.

Pavlov, A. V., 1994: Current changes of climate and permafrost in the Arctic and Sub-Arctic of Russia. *Permafrost Periglacial Processes,* **5,** 101–110.

——, and N. G. Moskalenko, 2002: The thermal regime of soils in the north of Western Siberia. *Permafrost Periglacial Processes,* **13,** 43–51.

Peacock, S., M. Maltrud, and R. Bleck, 2005: Putting models to the data test: A case study using Indian Ocean CFC-11 data. *Ocean Modell.,* **9,** 1–22.

Perovich, D. K., B. Light, H. Eicken, K. F. Jones, K. Runciman, and S. V. Nghiem, 2007: Increasing solar heating of the Arctic Ocean and adjacent sea, 1979-2005: Attribution and the role in the ice-albedo feedback. G*eophys. Res. Lett.,* **34,** L19505, doi:10.1029/2007GL031480.

Peters, W., and Coauthors, 2007: An atmospheric perspective on North American carbon dioxide exchange: CarbonTracker. *Proc. Natl. Acad. Sci. USA,* **104,** 18 925–18 930.

Peterson, B. J., R. M. Holmes, J. W. McClelland, C. J. Vorosmarty, R. B. Lammers, A. I. Shiklomanov, I. A. Shiklomanov, and S. Rahmstorf, 2002: Increasing river discharge to the Arctic Ocean. *Science,* **298,** 2171–2173.

Peterson, T. C., and R. S. Vose, 1997: An overview of the Global Historical Climatology Network temperature database. *Bull. Amer. Meteor. Soc.,* **78,** 2837–2849.

Platnick, S., M. D. King, S. A. Ackerman, W. P. Menzel, B. A. Baum, J. C. Riedi, and R. A. Frey, 2003: The MODIS cloud products: Algorithms and examples from Terra. *IEEE Trans. Geosci. Remote Sens.,* **41,** 459–473.

Polovina, J. J., E. A. Howell, and M. Abecassis, 2008: Ocean's least productive waters are expanding. *Geophys. Res. Lett.,* **35,** L03618, doi:10.1029/2007GL031745.

Polyakov, I. V., and Coauthors, 2003: Long-term ice variability in arctic marginal seas. *J. Climate,* **16,** 2078–2085.

——, and Coauthors, 2005: One more step toward a warmer Arctic. *Geophys. Res. Lett.,* **32,** L17605, doi:10.1029/2005GL023740.

——, and Coauthors, 2007: Observational program tracks Arctic Ocean transition to a warmer state. *Eos, Trans. Amer. Geophys. Union,* **88,** 398–399.

——, and Coauthors, 2008: Arctic Ocean freshwater changes over the past 100 years and their causes. *J. Climate,* **21,** 364–384.

Prather, M. J., 1996: Natural modes and time scales in atmospheric chemistry: Theory, GWPs for CH_4 and CO, and runaway growth. *Geophys. Res. Lett.,* **23,** 2597–2600.

Prentice, I. C., and Coauthors, 2001: The carbon cycle and atmospheric carbon dioxide. *Climate Change 2001: The Scientific Basis*, J. T. Houghton et al., Eds., Cambridge University Press, 183–237.

Proshutinsky, A., I. M. Ashik, E. N. Dvorkin, S. Häkkinen, R. A. Krishfield, and W. R. Peltier, 2004: Secular sea level change in the Russian sector of the Arctic Ocean. *J. Geophys. Res.,* **109,** C03042, doi:10.1029/2003JC002007.

Quadfasel, D., A. Sy, D. Wells, and A. Tunik, 1991: Warming in the Arctic. *Nature,* **350,** 385.

Quadrelli, R., and J. M. Wallace, 2004: A simplified linear framework for interpreting patterns of Northern Hemisphere wintertime climate variability. *J. Climate,* **17,** 3728–3744.

Ramsay, B. H., 1998: The Interactive Multisensor Snow and Ice Mapping System. *Hydrol. Processes,* **12,** 1537–1546.

Raphael, M. N., 2004: A zonal wave 3 index for the Southern Hemisphere. *Geophys. Res. Lett.,* **31,** L23212, doi:10.1029/2004GL020365.

——, and M. M. Holland, 2006: Twentieth century simulation of the southern hemisphere climate in coupled models. Part 1: large scale circulation variability. *Climate Dyn.*, **26,** 217–228.

Remer, L. A., and Coauthors, 2005: The MODIS aerosol algorithm, products and validation. *J. Atmos. Sci.,* **62,** 947–973.

Reynolds, R. W., N. A. Rayner, T. M. Smith, D. C. Stokes, and W. Wang, 2002: An improved *in situ* and satellite SST analysis for climate. *J. Climate,* **15,** 1609–1625.

——, T. M. Smith, C. Liu, D. B. Chelton, K. S. Casey, and M. G. Schlax, 2007: Daily high-resolution blended analyses. *J. Climate,* **20,** 5473–5496.

Richter-Menge, J., and Coauthors, 2006: State of the Arctic Report. NOAA OAR Special Rep., NOAA/OAR/PMEL, Seattle, WA, 36 pp.

Rignot, E., 2008: Changes in West Antarctic ice stream dynamics observed with ALOS PALSAR data. *Geophys. Res. Lett.*, doi:10.1029/2008GL033365, in press.

Rigor, I. G., and J. M. Wallace, 2004: Variations in the age of Arctic sea ice and summer sea-ice extent. *Geophys. Res. Lett.,* **31,** L09401, doi:10.1029/2004GL019492.

Robinson, D. A., and A. Frei, 2000: Seasonal variability of northern hemisphere snow extent using visible satellite data. *Prof. Geogr.,* **51,** 307–314.

Roemmich, D., S. Riser, R. Davis, and Y. Desaubies, 2004: Autonomous profiling floats: Workhorse for broadscale ocean observations. *J. Mar. Technol. Soc.,* **38,** 31–39.

——, J. Gilson, R. Davis, P. Sutton, S. Wijffels, and S. Riser, 2007: Decadal spin-up of the South Pacific subtropical gyre. *J. Phys. Oceanogr.,* **37,** 162–173.

Romanovsky, V. E., M. Burgess, S. Smith, K. Yoshikawa, and J. Brown, 2002: Permafrost temperature records: Indicators of climate change. *Eos, Trans. Amer. Geophys. Union,* **83,** 589.

——, S. Gruber, A. Instanes, H. Jin, S. S. Marchenko, S. L. Smith, D. Trombotto, and K. M. Walter, 2007a:

Frozen ground. *Global Outlook for Ice and Snow,* United Nations Publications, 181–200.

——, T. S. Sazonova, V. T. Balobaev, N. I. Shender, and D. O. Sergueev, 2007b: Past and recent changes in permafrost and air temperatures in Eastern Siberia. *Global Planet. Change,* **56,** 399–413.

Ronchail, J., G. Cochonneau, M. Molinier, J. L. Guyot, A. Gorreti, V. Guimarães, and E. de Oliveira, 2002: Interannual rainfall variability in the Amazon Basin and sea surface temperatures in the equatorial Pacific and the tropical Atlantic Oceans. *Int. J. Climatol.,* **22,** 1663–1686.

Ropelewski, C. F., and M. S. Halpert, 1987: Global and regional scale precipitation patterns associated with the El Niño/Southern Oscillation. *Mon. Wea. Rev.,* **115,** 1606–1626.

——, and ——, 1989: Precipitation patterns associated with the high index phase of the Southern Oscillation. *J. Climate,* **2,** 268–284.

——, J. E. Janowiak, and M. S. Halpert, 1985: The analysis and display of real time surface climate data. *Mon. Wea. Rev.,* **113,** 1101–1106.

Rothrock, D. A., Y. Yu, and G. A. Maykut, 1999: Thinning of the Arctic sea-ice cover. *Geophys. Res. Lett.,* **26,** 3469–3472.

Rudolf, B., C. Beck, J. Grieser, and U. Schneider, 2005: Global precipitation analysis products. Global Precipitation Climatology Centre (GPCC), DWD Publication, 1–8. [Available online at http://www.dwd.de/en/FundE/Klima/KLIS/int/GPCC/Reports_Publications/QR/GPCC-intro-products-2005.pdf.]

Sabine, C. L., R. M. Key, K. M. Johnson, F. J. Millero, A. Poisson, J. L. Sarmiento, D. W. R. Wallace, and C. D. Winn, 1999: Anthropogenic CO_2 inventory in the Indian Ocean. *Global Biogeochem. Cycles,* **13,** 179–198.

——, and Coauthors, 2004: The oceanic sink for anthropogenic CO_2. *Science,* **305,** 367–371.

Saji, N. H., and T. Yamagata, 2003: Possible impacts of Indian Ocean Dipole mode events on global climate. *Climate Res.,* **25,** 151–169.

——, B. N. Goswami, P. N. Vinayachandran, and T. Yamagata, 1999: A dipole mode in the tropical Indian ocean. *Nature,* **401,** 360–363.

Santer, B. D., and Coauthors, 2006: Forced and unforced ocean temperature changes in Atlantic and Pacific tropical cyclogenesis regions. *Proc. Natl. Acad. Sci. USA,* **103,** 13 905–13 910.

Sarmiento, J. L., and Coauthors, 2004: Response of ocean ecosystems to climate warming. *Global Biogeochem. Cycles,* **18,** GB3003, doi:10.1029/2003GB002134.

Schauer, U., B. Rudels, E. P. Jones, L. G. Anderson, R. D. Muench, G. Björk, J. H. Swift, V. Ivanov, and A.-M. Larsson, 2002: Confluence and redistribution of Atlantic water in the Nansen, Amundsen and Makarov basins. *Ann. Geophys.,* **20,** 257–273.

——, E. Fahrbach, S. Osterhus, and G. Rohardt, 2004: Arctic warming through the Fram Strait: Oceanic heat transport from 3 years of measurements. *J. Geophys. Res.,* **109,** C06026, doi:10.1029/2003JC001823.

Schmittner, A., M. Latif, and B. Schneider, 2005: Model projections of the North Atlantic thermohaline circulation for the 21st century assessed by observations. *Geophys. Res. Lett.,* **32,** L23710, doi:10.1029/2005GL024368.

Sensoy, S., 2004: The mountains influence on Turkey climate. BALWOIS Conf., Ohrid, Macedonia, Water Observation and Information System for Balkan Countries. [Available online at http://balwois.com/balwois/info_sys/publication2008.php?topic=3.]

——, M. Demircan, and I. Alan, 2007: Trends in Turkey climate extreme indices from 1971 to 2004. IUGG Conf., Perugia, Italy, International Union of Geodesy and Geophysics. [Available online at http://balwois.com/balwois/administration/full_paper/ffp-1000.pdf.]

Serreze, M. C., M. M. Holland, and J. Stroeve, 2007: Perspectives on the Arctic's shrinking sea-ice cover. *Science,* **315,** 1533–1536.

Shapiro, L. J., 1989: The relationship of the quasi-biennial oscillation to Atlantic tropical storm activity. *Mon. Wea. Rev.,* **117,** 1545–1552.

——, and S. B. Goldenberg, 1998: Atlantic sea surface temperatures and tropical cyclone formation. *J. Climate,* **11,** 578–590.

Shay, L., G. Goni, and P. Black, 2000: Effects of warm oceanic features on Hurricane Opal. *Mon. Wea. Rev.,* **128,** 131–148.

Shein, K. A., and Coauthors, 2006: State of the Climate in 2005. *Bull. Amer. Meteor. Soc.,* **87** (6), S6–S102.

Shimada, K., F. McLaughlin, E. Carmack, A. Proshutinsky, S. Nishino, and M. Itoh, 2004: Penetration of the 1990s warm temperature anomaly of Atlantic Water in the Canada Basin. *Geophys. Res. Lett.,* **31,** L20301, doi:10.1029/2004GL020860.

——, T. Kamoshida, M. Itoh, S. Nishino, E. Carmack, F. A. McLaughlin, S. Zimmermann, and A. Proshutinsky, 2006: Pacific Ocean inflow: Influence on catastrophic reduction of sea ice cover in the Arctic Ocean. *Geophys. Res. Lett.,* **33,** L08605, doi:10.1029/2005GL025624.

Siegel, D. A., S. Maritorena, N. B. Nelson, and M. J. Behrenfeld, 2005a: Independence and interdependences among global ocean color properties: Reassessing the bio-optical assumption. *J. Geophys. Res.,* **110,** C07011, doi:10.1029/2004JC002527

——, ——, ——, ——, and C. R. McClain, 2005b: Colored dissolved organic matter and its influence on the satellite-based characterization of the ocean biosphere. *Geophys. Res. Lett.,* **32,** L20605, doi:10.1029/2005GL024310.

Simmons, A., J. Wallace, and G. Branstator, 1983: Barotropic wave propagation and instability, and atmospheric teleconnection patterns. *J. Atmos. Sci.,* 40**,** 1363–1392.

Smith, S. L., M. M. Burgess, D. Riseborough, and F. M. Nixon, 2005: Recent trends from Canadian permafrost thermal monitoring network sites. *Permafrost Periglacial Processes,* **16,** 19–30.

Smith, T. M., and R. W. Reynolds, 1998: A high-resolution global sea surface temperature climatology for the 1961–90 base period. *J. Climate,* **11,** 3320–3323.

——, and ——, 2005: A global merged land–air–sea surface temperature reconstruction based on historical observations (1880–1997). *J. Climate,* **18,** 2021–2036.

Spencer, R. W., J. R. Christy, W. D. Braswell, and W. B. Norris, 2006: Estimation of tropospheric temperature trends from MSU channels 2 and 4. *J. Atmos. Oceanic Technol.,* **23,** 417–423.

Squires, M. F., and J. H. Lawrimore, 2006: Development of an operational northeast snowfall impact scale. Preprints, *22nd Int. Conf. on Interactive Information Processing Systems for Meteorology, Oceanography, and Hydrology,* Atlanta, GA, Amer. Meteor. Soc., 5.9. [Available online at http://ams.confex.com/ams/pdfpapers/100736.pdf.]

Steele, M., and W. Ermold, 2004: Salinity trends on the Siberian shelves. *Geophys. Res. Lett.,* **31,** L24308, doi:10.1029/2004GL021302.

——, ——, and J. Zhang, 2008: Arctic Ocean surface warming trends over the past 100 years. *Geophys. Res. Lett.,* **35,** L02614, doi:10.1029/2007GL031651.

Stohl, A., and Coauthors, 2006: Arctic smoke—Record high air pollution levels in the European Arctic due to agricultural fires in Eastern Europe. *Atmos. Chem. Phys.,* **6,** 9655–9722.

Straus, D. M., and J. Shukla, 2002: Does ENSO Force the PNA? *J. Climate,* 15**,** 2340–2358.

Stroeve, J., M. Serreze, S. Drobot, S. Gearhead, M. Holland, J. Maslanik, W. Meier, and T. S. Scambo, 2008: Arctic sea ice extent plummets in 2007. *Eos, Trans. Amer. Geophys. Union,* **89,** 13.

Svoboda, M., and Coauthors, 2002: The drought monitor. *Bull. Amer. Meteor. Soc.,* **83,** 1181–1190.

Sweeney, C., E. Gloor, A. R. Jacobson, R. M. Key, G. McKinley, J. L. Sarmiento, and R. Wanninkhof, 2007: Constraining global air-sea gas exchange for CO_2 with recent bomb ^{14}C measurements. *Global Biogeochem. Cycles,* **21,** GB2015, doi:10.1029/2006GB002784.

Takahashi, T., R. A. Feely, R. Weiss, R. Wanninkhof, D. W. Chipman, S. C. Sutherland, and T. T. Takahashi, 1997: Global air-sea flux of CO_2: An estimate based on measurements of sea-air pCO_2 difference. *Proc. Natl. Acad. Sci. USA,* **94,** 8292–8299.

——, and Coauthors, 2002: Global sea-air CO_2 flux based on climatological surface ocean pCO_2, and seasonal biological and temperature effects. *Deep-Sea Res. II,* **49,** 1601–1622.

——, S. C. Sutherland, R. A. Feely, and R. Wanninkhof, 2006: Decadal change of the surface water pCO_2 in the North Pacific: A synthesis of 35 years of observations. *J. Geophys. Res.,* **111,** C07S05, doi:10.1029/2005JC003074.

——, and Coauthors, 2008: Climatological mean and decadal change in surface ocean pCO_2, and net sea-air CO_2 flux over the global oceans. *Deep-Sea Res.*, in press.

Talley, L. D., 2003: Shallow, intermediate, and deep overturning components of the global heat budget. *J. Phys. Oceanogr.,* **33,** 530–560.

Tans, P. P., I. Y. Fung, and T. Takahashi, 1990: Observational constraints on the global atmospheric CO_2 budget. *Science,* **247,** 1431–1439.

Thompson, D. W. J., and J. M. Wallace, 1998: The Arctic Oscillation signature in the wintertime geopotential height and temperature fields. *Geophys. Res. Lett.,* **25,** 1297–1300.

——, and ——, 2000: Annular modes in the extratropical circulation. Part I: Month-to-month variability. *J. Climate,* **13,** 1000–1016.

——, and ——, 2001: Regional climate impacts of the northern hemisphere annular mode. *Science,* **293,** 85–89.

——, and S. Solomon, 2002: Interpretation of recent Southern Hemisphere climate change. *Science,* **296,** 895–899.

——, S. Lee, and M. P. Baldwin, 2003: Atmospheric processes governing the Northern Hemisphere annular mode/North Atlantic Oscillation. *The North Atlantic Oscillation, Geophys. Monogr.*, Vol. 134, Amer. Geophys. Union, 81–112.

Thorne, P. W., D. E. Parker, S. F. B. Tett, P. D. Jones, M. McCarthy, H. Coleman, P. Brohan, and J. R. Knight, 2005: Revisiting radiosonde upper-air temperatures from 1958 to 2002. *J. Geophys. Res.,* **110,** D18105, doi:10.1029/2004JD005753.

Timokhov, L., and F. Tanis, Eds., 1997: *Environmental Working Group Joint U.S.–Russian Atlas of the Arctic Ocean—Winter Period*. Environmental Research Institute of Michigan in association with the National Snow and Ice Data Center, Arctic Climatology Project, CD-ROM.

Torbali, A., A. Mirzaei, M. Hamzenejad, M. Sisipor, S. Malawi, and A. Pour Asgharian, 2007: Report on impacts of Gonu 2007 (in Farsi). Islamic Republic of Iranian Meteorological Organization, Hormozgan office, Iran, 50 pp.

Trenberth, K. E., A. Dai, R. M. Rasmussen, and D. B. Parsons, 2003: The changing character of precipitation. *Bull. Amer. Meteor. Soc.,* **84,** 1205–1217.

Trigo, R. M., and J. P. Palutikof, 2001: Precipitation scenarios over Iberia: a comparison between direct GCM output and different downscaling techniques. *J. Climate,* **14,** 4422–4446.

Turner, J., J. E. Overland, and J. Walsh, 2007: An Arctic and Antarctic perspective on recent climate change. *Int. J. Climatol.,* **27,** 277–293.

Vainio, J., S. Kalliosaari, N. Schmelzer, T. Grafström, G. Ezerskis, E. Komissarov, P. Soloshchuk, N. Fedorenko, and K. Moeller Petersen, cited 2008: The sea ice 2006-2007. HELCOM Indicator Fact Sheets 2007. [Available online at http://www.helcom.fi/environment2/ifs/en_GB/cover/.]

Van de Berg, W. J., M. R. van den Broeke, C. H. Reijmer, and E. van Meijgaard, 2005: Characteristics of the Antarctic surface mass balance (1958-2002) using a regional atmospheric climate model. *Ann. Glaciol.,* **41,** 97–104.

van de Wal, R. S. W., W. Greuell, M. R. van den Broeke, C. H. Reijmer, and J. Oerlemans, 2006: Surface mass-balance observations and automatic weather station data along a transect near Kangerlussuaq, West Greenland. *Ann. Glaciol.,* **42,** 311–316.

van der Werf, G. R., J. T. Randerson, G. J. Collatz, L. Giglio, P. S. Kasibhatla, A. F. Arellano, S. C. Olsen, and E. S. Kasischke, 2004: Continental-scale partitioning of fire emissions during the 1997 to 2001 El Niño/La Niña period. *Science,* **303,** 73–76.

Vose, R. S., R. L. Schmoyer, P. M. Steurer, T. C. Peterson, R. Heim, T. R. Karl, and J. Eischeid, 1992: The Global Historical Climatology Network: long-term monthly temperature, precipitation, sea level pressure, and station pressure data. ORNL/CDIAC-53, NDP-041, Carbon Dioxide Information Analysis Center, Oak Ridge National Laboratory. [Available online at http://cdiac.ornl.gov/epubs/ndp/ndp041/ndp041.html.]

Waliser, D. E., and C. Gautier, 1993: A satellite-derived climatology of the ITCZ. *J. Climate,* **6,** 2162–2174.

Wallace, D. W. R., 1995: *Monitoring Global Ocean Carbon Inventories.* Texas A&M University, 54 pp.

Wallace, J. M., and D. S. Gutzler, 1981: Teleconnections in the geopotential height field during the Northern Hemisphere winter. *Mon. Wea. Rev.,* 109**,** 784–812.

Wang, B., and J. C. L. Chan, 2002: How strong ENSO events affect tropical storm activity over the western North Pacific. *J. Climate,* **15,** 1643–1658.

Wang, M., and J. Overland, 2004: Detecting Arctic climate change using Köppen climate classification. *Climatic Change,* **67,** 43–62.

Wang, X., and J. R. Key, 2003: Recent trends in Arctic surface, cloud, and radiation properties from space. *Science,* **299,** 1725–1728.

Wanninkhof, R., 1992: Relationship between gas exchange and wind speed over the ocean. *J. Geophys. Res.,* **97,** 7373–7381.

Webster, P. J., A. Moore, J. Loschnigg, and M. Leban, 1999: Coupled ocean-atmosphere dynamics in the Indian Ocean during 1997-98. *Nature,* **401,** 356–360.

Weidick, A., and O. Bennike, 2007: Quaternary glaciation history and glaciology of Jakobshavn Isbrae and the Disko Bugt region, West Greenland: A review. Geological Survey of Denmark and Greenland, Bulletin 14, 80 pp.

Westberry, T., M. J. Behrenfeld, D. A. Siegel, and E. Boss, 2008: Carbon-based primary productivity modeling with vertically resolved photophysiology. *Global Biogeochem. Cycles*, in press.

Westerling, A. L., H. G. Hidalgo, D. R. Cayan, and T. W. Swetnam, 2006: Warming and earlier spring increases western U.S. forest wildfire activity. *Science,* **313,** 940–943.

Whitney, L. D., and J. S. Hobgood, 1997: The relationship between sea surface temperatures and maximum intensities of tropical cyclones in the eastern North Pacific Ocean. *J. Climate,* **10,** 2921–2930.

Wijffels, S. E., R. W. Schmitt, H. L. Bryden, and A. Stigebrandt, 1992: Freshwater transport by the ocean. *J. Phys. Oceanogr.,* **22,** 155–162.

——, J. Willis, C. M. Domingues, P. Barker, N. J. White, A. Gronell, K. Ridgway, and J. A. Church, 2008: Changing expendable bathythermograph fall-rates and their impact on estimates of thermosteric sea level rise. *J. Climate*, in press.

Willis, J. K., D. Roemmich, and B. Cornuelle, 2004: Interannual variability in upper ocean heat content, temperature, and thermosteric expansion on global scales. *J. Geophys. Res.,* **109,** C12036, doi:10.1029/2003JC002260.

Woodgate, R. A., K. Aagaard, R. D. Muench, J. Gunn, G. Bjork, B. Rudels, A. T. Roach, and U. Schauer, 2001: The Arctic Ocean boundary current along the Eurasian slope and the adjacent Lomonosov Ridge: Water mass properties, transports and transformations from moored instruments. *Deep-Sea Res. I,* **48,** 1757–1792.

Xie, P., and P. A. Arkin, 1997: Global precipitation: A 17-year monthly analysis based on gauge observations, satellite estimates, and numerical model outputs. *Bull. Amer. Meteor. Soc.,* **78,** 2539–2558.

——, and ——, 1998: Global monthly precipitation estimates from satellite-observed outgoing longwave radiation. *J. Climate,* **11,** 137–164.

——, J. E. Janowiak, P. A. Arkin, R. Adler, A. Gruber, R. Ferraro, G. J. Huffman, and S. Curtis, 2003: GPCP pentad precipitation analyses: An experimental dataset based on gauge observations and satellite estimates. *J. Climate,* **16,** 2197–2214.

Xue, Y., T. M. Smith, and R. W. Reynolds, 2003: Interdecadal changes of 30-yr SST normals during 1871–2000. *J. Climate,* **16,** 1601–1612.

Yu, L., and R. A. Weller, 2007: Objectively analyzed air–sea heat fluxes for the global ice-free oceans (1981–2005). *Bull. Amer. Meteor. Soc.,* **88,** 527–539.

——, J. Xin, and R. A. Weller, 2008: Multidecade global flux datasets from the Objectively Analyzed Air-sea Fluxes (OAFlux) project: Latent and sensible heat fluxes, ocean evaporation, and related surface meteorological variables. Woods Hole Oceanographic Institution, OAFlux Project Tech. Rep. OA-2008-01, 64 pp.

Zebiak, S. E., 1989: Oceanic heat content variability and El Niño cycles. *J. Phys. Oceanogr.*, **19,** 475–486.

Zhang, C., 2005: Madden-Julian Oscillation. *Rev. Geophys.*, **43,** 1–36.

——, and J. Gottschalck, 2002: SST anomalies of ENSO and the Madden–Julian oscillation in the equatorial Pacific. *J. Climate,* **15,** 2429–2445.

Zhang, X., and Coauthors, 2005: Trends in Middle East climate extreme indices from 1950 to 2003. *J. Geophys. Res.,* **110,** D22104, doi:10.1029/2005JD006181.

Zhou, L., C. J. Tucker, R. K. Kaufmann, D. Slayback, N. V. Shabanov, I. Fung, and R. B. Myneni, 2001: Variations in northern vegetation activity inferred from satellite data of vegetation index during 1981 to 1999. *J. Geophys. Res.,* **106** (D17), 20 069–20 083.